# Enhanced Spatial Metabolomics Enabled by On-Tissue Chemistry, Computational Metabolome Mining and Mass Spectrometry Imaging

Cumulative dissertation

by

Domenic Dreisbach

Submitted to the

Faculty of Biology and Chemistry (FB08)

and prepared at the

Institute of Inorganic and Analytical Chemistry

for the degree of

*Doctor rerum naturalium* (*Dr. rer. nat.*)

Justus Liebig University Giessen, Germany

Giessen 2024

This thesis was accepted as a doctoral dissertation in fulfillment of the requirements for the degree of *Doctor rerum naturalium* by the Faculty of Biology and Chemistry, Justus Liebig University Giessen, Germany

1. Referee: Prof. Dr. Bernhard Spengler

2. Referee: Prof. Dr. Georg Petschenka

# Contents

## List of Publications

This thesis is based on the following publications in peer-reviewed scientific journals.

1) Dreisbach, D., Bhandari, D. R., Betz, A., Tenbusch, L., Vilcinskas, A., Spengler, B., Petschenka, G., Spatial metabolomics reveal divergent cardenolide processing in the monarch (*Danaus plexippus*) and the common crow butterfly (*Euploea core*), *Mol. Ecol. Resour*. **2023**; 00:1-16

2) Dreisbach, D., Heiles, S., Bhandari, D. R., Petschenka, G., Spengler, B., Molecular Networking and On-Tissue Chemical Derivatization for Enhanced Identification and Visualization of Steroid Glycosides by MALDI Mass Spectrometry Imaging, *Anal. Chem*. **2022**, 94, 46, 15971-15979

# List of Abbreviations

| Abbreviation | Explanation |
|---|---|
| 9-AA | 9-aminoacridine |
| ACN | Acetonitrile |
| AI | Artificial intelligence |
| AP-SMALDI | Atmospheric pressure scanning microprobe matrix-assisted laser desorption/ionization |
| AUP | Area under peak |
| CD | Chemical derivatization |
| CHCA | α-cyano-4-hydroxycinnamic acid |
| DAN | 1,5-diaminonaphthalene |
| DDA | Data-dependent acquisition |
| *D. plexippus* | *Danaus plexippus* |
| DESI | Desorption electrospray ionization |
| DHB | 2,5-dihydroxybenzoic acid |
| *E. core* | *Euploea core* |
| ESI | Electrospray ionization |
| FBMN | Feature-based molecular networking |
| FDR | False discovery rate |
| FTICR | Fourier transform ion cyclotron resonance |
| GE | Gut epithelium |
| GirT | Girard's reagent T |
| GNPS | Global Natural Products Social Molecular Networking |
| H&E | Haematoxylin & eosin staining |
| HPLC | High-performance liquid chromatography |
| LAESI | Laser ablation electrospray ionization |
| MALDI | Matrix-assisted laser desorption/ionization |
| MS | Mass spectrometry |
| $MS^2$ | Tandem mass spectrometry |
| *m/z* | Mass-to-charge ratio |
| MSI | Mass spectrometry imaging |
| OTCD | On-tissue chemical derivatization |
| PC | Phosphatidylcholine |
| PE | Phosphatidylethanolamine |
| RGB | Red-green-blue |
| ROI | Region of interest |
| SVM | Support vector machine |
| TFA | Trifluoroacetic acid |
| TIC | Total ion current |
| TOF | Time-of-flight |
| UV | Ultraviolet |

## Abstract

Spatial metabolomics is an emerging field of research and provides deep insight into biochemical pathways and transport processes for low-molecular-weight chemical compounds in tissues and cells. Yet, current approaches predominantly focused on analyzing a limited number of previously known molecules of interest in mammalian tissues. In the first part of this thesis, we set out to apply mass spectrometry imaging (MSI)-based spatial metabolomics for investigating complex metabolic networks in the delicate sample system of insects. Specifically, we acquired spatially-resolved metabolomes related to plant toxin sequestration in milkweed butterflies. Despite being famous for sequestering milkweed steroidal glycosides (i.e. cardenolides), the underlying mechanism of uptake and toxin distribution in caterpillars of the monarch butterfly (*Danaus plexippus*) is still unknown. We revealed cardenolide distributions at unprecedent detail across the whole body of monarch caterpillars and the closely related nonsequestering common crow butterfly (*Euploea core*) to determine at which physiological scale quantitative and qualitative differences between both species manifest: while monarchs retain and accumulate cardenolides above plant concentrations, the toxins are degraded in the gut lumen of *E. core*. We visualized cardenolide transport over the monarch midgut epithelium at the low-micrometer-scale and identified integument cells as the final site of storage to provide chemical defenses against predators. Collectively, these results provided novel insight into the selectivity and the mechanism of cardenolide sequestration. Yet, we encountered significant challenges in terms of visualizing and identifying the complex metabolic network of steroid glycosides. In the second part of this thesis, we therefore enhanced our spatial metabolomic approach with liquid chromatography mass spectrometry (LC-MS)-based computational metabolome mining and on-tissue chemistry to counteract the absence of respective databases and low intrinsic ionization efficiency for steroidal glycosides. We conducted feature-based molecular networking in combination with artificial intelligence (AI)-driven molecular characterization to characterize and annotate 32 different cardenolides. This comprehensive database guided matrix-assisted laser desorption/ionization (MALDI) MSI of cardenolide sequestration in *D. plexippus*. We developed a spatial-context preserving on-tissue chemical derivatization (OTCD) protocol, which improved ion yields for cardenolides by at least 1 order of magnitude compared to untreated samples. Empowered by this approach, we visualized previously inaccessible cardenolide distributions with 2 µm and 5 µm pixel size across complex insect organs, such as Malpighian tubules. In addition to unraveling intricate details regarding cardenolide sequestration, the results underscore the potential of OTCD MALDI MSI for deeper spatial metabolomic research.

## Zusammenfassung

Die räumlich aufgelöste Metabolomik ist ein aufstrebendes Forschungsfeld, welches umfassende Einblicke in biochemische Wege und Transportprozesse von niedermolekularen chemischen Verbindungen in Geweben und Zellen ermöglicht. Gegenwärtige Ansätze konzentrieren sich jedoch vorwiegend darauf, eine begrenze Anzahl bereits bekannter Moleküle in Säugetiergewebe zu analysieren. Der erste Teil dieser Arbeit beschäftigt sich daher mit der Anwendung der massenspektrometrie-basierten räumlich aufgelösten Metabolomik zur Untersuchung komplexer Stoffwechselnetzwerke für das anspruchsvolle Probensystem von Insektengewebe. Obwohl Monarchfalter (*Danaus plexippus*) bekannt für die Sequestrierung von Herzglykosiden sind, ist der zugrunde liegende Mechanismus hinsichtlich Aufnahme und Lokalisierung der Toxine noch unbekannt. Der verwendete Ansatz ermöglichte die Visualisierung von Herzglykosiden im gesamten Körper der Raupen des Monarchfalters und den direkten Vergleich hinsichtlich qualitativen and quantitativen Unterschieden zur nicht-sequestrierenden Krähenraupe (*Euploea core*). Während die Toxine im Darm von *E. core* abgebaut wurden, akkumulierten die Raupen des Monarchfalters Herzglykoside im Darm über dem Konzentrationsniveau der Wirtspflanze (*Asclepias curassavica*). Des Weiteren konnte mit Hilfe von hochauflösenden Analysen der Transport von Cardenoliden über das Mitteldarmepithel visualisiert und Integumentzellen als finalen Speicherort der Toxine identifiziert werden. Zusammenfassend lieferte dieser Ansatz erstmalig umfangreiche Informationen bezüglich Selektivität und Mechanismus hinsichtlich der Sequestrierung von Herzglykosiden. Nichtsdestotrotz wurde aufgrund der molekularen Komplexität, eine signifikante Herausforderung für die Visualisierung und Identifizierung von Herzglykosiden festgestellt. Dementsprechend wurde im zweiten Teil dieser Arbeit das experimentelle Design durch die Integration von computergestützter Metabolomik-Analyse basierend auf Flüssigkeitschromatographie mit Massenspektrometrie-Kopplung (LC-MS) und chemischer Derivatisierung am Gewebe (OTCD) weiterentwickelt. Dies diente dazu, die fehlende Datenbank und der niedrigen Ionisierungseffizienz von Herzglykoside entgegenzuwirken. Die erstellten molekularen Netzwerke ermöglichten die Charakterisierung von 32 verschiedenen Herzglykosiden. Diese umfassende Datenbank unterstütze die räumliche Analyse von Herzglykosid-Sequestierung in *D. plexippus* mittels bildgebender Massenspektrometrie. Das entwickelte OTCD Protokoll verbesserte die Ionenausbeute für Herzglykoside um mindestens eine Größenordnung und bewahrte dabei die räumliche Verteilung im Gewebe. Diese Verbesserung ermöglichte die Visualisierung von Herzglykosiden in komplexen Gewebestrukturen mit einer Pixelgröße von 2 und 5 µm und demonstriert das Potenzial von OTCD MSI für tiefere räumlich aufgelöste Metabolomik.

# CHAPTER I

## 1.1 Introduction

Metabolic networks describe interconnected pathways of biochemical reactions and transport processes of low-molecular-weight chemical species (e.g. metabolic intermediates, hormones, secondary metabolites) within living organisms.[1,2] Spatial metabolomics is a rapidly emerging field of omics research focused on the mapping and interpretation of low-molecular-weight chemical species in their native spatial context of cells, tissues, organs and organisms.[3] However, the identification and spatial characterization at the cellular level in an untargeted fashion remains challenging. Traditional methods, such as immunofluorescence, require the labelling of analytes of interest with fluorophores, which can be time-consuming, inefficient and restricted to individual compounds.[4] In addition, labelling of molecules can alter their physiochemical properties and hence influence their native tissue distributions.[5] In contrast, mass spectrometry imaging (MSI) emerged as one of the fastest growing mass spectrometry (MS) fields over the past decade providing for spatially-resolved, qualitative and semi-quantitative analysis of molecular species in tissues and cells.[6] Importantly, not only the analytes of interest but also thousands of other chemical species can be detected, visualized, and identified simultaneously – thereby aiming to link chemical structures to biological functions and origins. The following introduction covers the fundamentals of mass spectrometry and describes the biological context required for interpreting the MSI research presented in this thesis.

### Mass Spectrometry

Mass spectrometry is a central bioanalytical technique in life sciences due to its unprecedented characteristics in limits of detection, depth of information, accuracy, time of acquisition and broad applicability. The general principle is to generate ions from either inorganic or organic compounds, utilizing a suitable ionization technique, and to detect these ions qualitatively and quantitatively by their respective mass-to-charge-number ratio ($m/z$) and abundance. In general, a mass spectrometer consists of an ion source, a mass analyzer and a detector. Whereas the ion source can be operated at atmospheric pressure or under various vacuum conditions, mass analyzer and detector are generally operated under high vacuum conditions.[7]

The fundamental work for mass spectrometry was conducted in 1898 by analyzing anode rays via magnetic deflection and determining their respective positive charges.[8] In 1912, the first mass spectrometer (called parabola spectrograph) was constructed and mass spectra of $O_2$, $N_2$, CO, $CO_2$ and $COCl_2$ were obtained.[9] Further early developments

included the electron ionization source coupled to a spectrometer with a sector-shaped magnet with direct focusing in 1918[10] and the first mass spectrometer with velocity focusing to measure mass defects in 1919[11].

In the ion source, molecular species are volatilized and ionized prior to mass analysis in the mass spectrometer. A plethora of ionization techniques were developed, which can be differentiated into hard (very energetic, extensive fragmentation) and soft ionization (generating intact ions of the molecular species) based on the internal energy transfer during the ionization process and the physico-chemical properties of the analyte.[10,12–19] Electron ionization, chemical ionization and field ionization allow for gas-phase ionization, thus, are restricted to compounds that are sufficiently volatile and thermally stable. In contrast, chemical compounds that are thermally labile or do not have sufficient vapor pressure have to be extracted directly from the condensed to the gas phase via a direct ion source. These direct ion sources can be divided into two types: liquid-phase ion sources and solid-phase ion sources. For liquid-phase ion sources (e.g. electrospray ionization (ESI)), the analyte is in solution and introduced by nebulization into the ion source and subsequently, ions are generated at atmospheric pressure and focused into the mass spectrometer.[12] In contrast, for solid-phase ion sources (e.g. matrix-assisted laser desorption/ionization (MALDI)), analytes are deposited in an involatile matrix (that can be native or applied), which is irradiated by energetic particles or photons. Next, the analytes of interest are desorbed and ionized and can be extracted by an electric field or gas stream and focused towards the inlet of the mass spectrometer.[13] For both types, ion production is based on the ionization of neutral molecules in the gas phase including processes such as electron ejection, electron capture, protonation, deprotonation, adduct formation or by the transfer of charged species from a condensed phase into the gas phase, or by combinations of both.[20]

In the next step, the mass-to-charge-number ratio ($m/z$) of the generated ions is measured and determined via the mass analyzer. Several types of mass analyzers (e.g. Quadrupole[21], time-of-flight (TOF)[22], Fourier transform ion cyclotron resonance (FT-ICR)[23,24] and orbital trapping devices (Orbitrap)[25–27]) have been developed, each having their own advantages and limitations for the main performance characteristics of mass range, acquisition speed, ion transmission, mass accuracy and mass resolution. For this thesis, orbital trapping mass spectrometers were employed. The general principle of an electrostatic axially-harmonic orbital trap (“Orbitrap”) that utilizes Fourier transformation to obtain mass spectra was introduced in 2000.[27] The Orbitrap consists of an outer barrel-shaped electrode, split into two equal parts with a small interval and of a central electrode that has a spindle-like shape. While the outer electrode remains at ground potential, an electrostatic potential is applied to the inner electrode resulting in an electrostatic field

with a quadro-logarithmic potential distribution, based on the DC voltage and the specific geometry of the trap. The ions are injected off-axis and start to rotate on stable trajectories around the central electrode and oscillate in axial direction. The frequency of axial oscillation is directly linked to the *m*/*z* ratio while being independent of the kinetic energy of the injected ions. The electric current (induced by the oscillating ions) at the outer electrode is measured and converted by a Fourier transformation to the individual frequencies and intensities – thereby yielding the mass spectra.[27]

The generated mass spectrum is a two-dimensional plot of the relative abundance (ordinate) versus the scale of atomic mass per number of elementary charges (abscissa), which is called mass-to-charge number ratio *m*/*z* (as often called "mass-to-charge ratio"). Since 1961, the *unified atomic mass* [u] has been defined as $^{1}/_{12}$ of the mass of one single atom of the nuclide $^{12}C$, which by definition has been set to exactly 12 u.
Depending on the ionization method and experimental conditions (e.g. large molecules), doubly, triply or highly charged ions can be generated. Importantly, there are different ways to define and to calculate the mass of an atom, molecule or ion. For instance, in chemical stoichiometry, the weighted average of the atomic masses of the different isotopes of each element in the molecule is utilized. However, in mass spectrometry, the monoisotopic mass is used, which is calculated based on the exact mass of the most abundant isotope of each constituent element.[7] The obtained mass spectra are normalized to the base peak, which is the signal with the highest abundance for the corresponding spectrum (100% relative intensity). The individual peak intensities in absolute values can be determined by extracting the area under peak (AUP).

## Mass Spectrometry Imaging

Mass spectrometry imaging (MSI) is a powerful method, which provides for the untargeted spatially-resolved analysis of molecular species in the spatial context of, for example, cells, tissues or organs. In contrast to microscopy-based methods (e.g. immunofluorescence microscopy), no prior knowledge or labeling of the analytes of interest is required.[6,28,29] Since its introduction in 1994[30], matrix-assisted laser desorption/ionization (MALDI) MSI is the predominant bioanalytical MSI method in life sciences due to its applicability for a wide range of chemical classes and molecular masses while providing lateral resolutions at the low-micrometer-scale.[6,31] The general experimental design for a MALDI MSI experiment is a multi-step process involving sample preparation, analyte desorption, mass analysis and image generation. Notably, sample preparation is one of the most crucial steps and has to be robust and reproducible for the analytical success of MALDI MSI experiments. To obtain snap-shots for in vivo biochemical processes, samples (e.g. complete organs) have to be flash-frozen or

chemically-fixed (e.g. FFPE preparation = “Formalin Fixed Paraffin Embedded”) to stop enzyme activity and to reduce degradation and delocalization of molecular species. Next, cryo-sectioning is performed to obtain thin tissue sections. These protocols have to consider sample stabilization, section thickness, orientation of fixation and optimized temperature and cutting-angle. In particular, for fragile and delicate sample specimens, embedding material (e.g. carboxymethyl cellulose, gelatin) is necessary to preserve tissue morphology. Next, analytes of interest are extracted from the tissue and embedded in a matrix of highly light absorbing, low-molecular-weight molecules. Typically, matrix-analyte crystallization is performed via pneumatic spraying or sublimation. Despite causing larger matrix crystal-sizes, the solvent of the sprayed matrix solution significantly improves analyte extraction and the development of automated sprayer systems enabled reproducible matrix application methods of high quality.[32] Importantly, the physico-chemical properties of MALDI matrices have to enable strong absorbance at the laser wavelength (typically UV, 337-344 nm), vacuum stability, solubility in solvents compatible to analytes of interest, low chemical reactivity and the potential to promote analyte ionization.[33] However, the large degree of molecular heterogeneity in bioanalytical research (e.g. metabolites, peptides, proteins) precludes an universal MALDI matrix. Instead, the experimental design, including the choice of matrix and analyte extraction process, has to be developed and optimized for the individual bioanalytical framework. The development of rationally-designed MALDI matrices represents an active field of research. Yet, the first generation archetype MALDI matrices 2,5-dihydroxybenzoic acid (DHB)[34], *alpha*-cyano-4-hydroxycinnamic acid (CHCA)[35] for positive-ion mode and 9-aminoacridine (9-AA)[36], 1,5-diaminonaphthalene (DAN)[37] for negative-ion mode are still the most utilized compounds due to their relatively broad applicability regarding molecular coverage.

In the next step, analyte-doped matrix crystals are irradiated by intense laser pulses of nanosecond duration resulting in rapid heating, localized ablation and subsequent sublimation of matrix crystals with intact analytes ejecting in the expanding matrix plume. The ejected material contains both, neutral and charged molecular species and although the MALDI ionization mechanism is not completely elucidated, several chemical- and physical ionization pathways, such as gas-phase photoionization, excited state proton transfer, ion-molecule reactions and the desorption of preformed ions (e.g. proton-transfer in the solid phase) are suggested.[38–40] Notably, the intrinsic ionization efficiency and matrix/analyte integration efficiency varies for different chemical classes and molecular structures. As a consequence, very abundant and/or easily ionizable analyte molecules (e.g. phosphatidylcholine-lipids) are predominantly formed and detected.[40,41] Yet, various strategies can be applied to overcome and to limit the effect of “suppression

effects" (e.g. on-tissue chemical derivatization, which is described later in this introduction). In the last step of the measurement, ions are accelerated and focused by an electrostatic field (and/or a gas pressure gradient) towards the inlet of the mass spectrometer, followed by the transmission and the analysis in the mass analyzer.

For conventional MALDI, the ionization process takes place under vacuum conditions. However, various developments in 2000 led to the advent of atmospheric pressure (AP) MALDI ion sources with ionization occurring at atmospheric pressure conditions outside the vacuum of the mass spectrometer.[42–44] To assist the ion transport from the atmospheric pressure ionization region towards the high vacuum of the mass spectrometer, a high voltage (3-4 kV) is applied on the MALDI probe (e.g. metal target plate). AP-MALDI allows for experimental flexibility by enabling the analysis of vacuum-sensitive samples, volatile compounds and does not require sample fixation and/or -drying. In addition, low-energy collisions of analyte ions with residual gas molecules result in a reduction of internal energy, thus preventing fragmentation and making it a softer ionization technique relative to conventional vacuum MALDI. In particular, atmospheric-pressure scanning microprobe matrix-assisted laser desorption/ionization (AP-SMALDI) MSI emerged as the high end in MALDI MSI instrumentation due to its unmatched performance regarding mass resolution, spatial resolution, sensitivity and experimental flexibility.[45–48] Moreover, the implemented pixel-wise autofocusing method utilizes laser-triangulation to keep the MALDI focus, fluence and ablation spot-size constant for the whole MSI experiment. This technical feature enables 3D-surface analysis and improves the sensitivity for decreasing sampling areas (subsequently reduced numbers of desorbed/ionized analytes of interest) of MSI experiments performed with pixel-sizes at the low-micrometer-scale (≤ 10 µm).[47]

For typical MSI experiments, the region of interest (i.e. grid in x- and y-dimension) is analyzed with a defined step size between each measurement event. A mass spectrum is obtained for each separate measurement event and by utilizing computational software, individual *m*/*z* values can be extracted with their corresponding intensities (i.e. relative abundancies). Next, the chemical information is combined with the spatial information (based on the x,y-grid) into a heat map image depicting the relative distribution of the selected ion for the analyzed region of interest.

Molecular identification and structural elucidation of specific ions remains as one of the key challenges for MSI. Recently, methods for automated data-dependent acquisition of structurally diagnostic $MS^2$ data in parallel with MSI data were reported.[49,50] However these approaches were restricted to highly abundant lipids while providing a spatial resolution of 40 µm. Also, performing on-tissue MALDI $MS^2$ experiments of lowly

abundant chemical species or various metabolite classes (e.g. steroids, carboxylic acids) is challenging due to low intrinsic ionization efficiencies, thus, require additional method development to selectively improve the ion yield (e.g. on-tissue chemical derivatization). As an alternative that does not rely on $MS^2$ data, METASPACE[51], a community-populated knowledge base for annotating high-mass-resolution MSI data was developed. The applied bioinformatic framework performs database-driven annotation at the sum-formula level combined with metabolite-signal match scoring (integrating spectral and spatial isotopic information), and target-decoy false-discovery-rate (FDR) estimation – thereby providing automated and high-confidence annotation of MSI data.[52] Yet, the most prominent approach relies on separate LC-$MS^2$ analysis of the respective tissue homogenate for the targeted structural characterization and confirmation of annotations related to the MSI experiment. In particular for untargeted workflows, thousands of $MS^2$ spectra can be acquired within a single LC-$MS^2$ experiment. The complexity of these datasets hinders manual analysis and, instead, fuels the development of various computational tools, which are discussed in the next chapter 'Computational Metabolome Mining".

## Computational Metabolome Mining

To comprehensively explore and interpret metabolic networks, the corresponding individual chemical species have to be discovered and identified. As a highly sensitive and precise analytical platform, LC-MS enables routine analysis of these complex metabolic mixtures with the omission of spatial information. Notably, a single LC-MS experiment can collect thousands of $MS^1$ and $MS^2$ spectra, resulting into data sets which are too large for manual analysis. Also, decomposing complex metabolic networks into chemical compound classes and molecular identifications remains a major bottleneck due to the absence of repository-scaled databases. Instead, the majority of mass spectrometric reference data in spectral libraries are based on commercially available chemicals.[53–55] To tackle the chemical complexity, advances in bioinformatics tools have enhanced the field of MS-based metabolomics over the last decade by efficiently speeding up the discovery process of novel metabolites and their corresponding chemical structures.[56,57] For example, Global Natural Products Social Molecular Networking (GNPS) is a data-driven infrastructure for the storage, analysis, and knowledge dissemination of $MS^2$ spectra that enables community sharing of raw spectra, continuous annotation of deposited data, and collaborative curation of reference spectra and experimental data.[58] The integrated molecular networking workflow has become an essential tool to organize, annotate and visualize the chemical space for untargeted mass spectrometry data and, uniquely, goes beyond spectral matching against reference

spectra. In detail, each $MS^2$ spectrum is simplified as a vector in a multidimensional space with each dimension correlating to the *m*/*z* value of a fragment ion and its peak abundance. Next, for comparison, the angle between two spectral vectors in the multidimensional space is calculated and the similarity is determined via a cosine score. Importantly, fragment peaks between two spectra are not only aligned and compared based on their original *m*/*z* ratio, but also based on *m*/*z* shifts according to the difference in the precursor *m*/*z* of the two molecules (e.g. water loss which results in Δ(*m*/*z)* of 18.0105 for a subset of fragment peaks). The resulting matrix of spectral similarities can be visualized as molecular networks with each node representing an $MS^2$ spectrum, and edges between nodes displaying the calculated cosine score (which is above the user-defined threshold).[56,59,60] In nature, similar molecular building blocks are often reused to form increasingly complex structures. Thus, metabolites of the same molecular family share common substructures, which transpires into similar spectral patterns. Therefore, related molecules form molecular networks and spectral library annotations can be propagated to facilitate the process of structural elucidation and to discover novel metabolites of similar molecular families.[56]

Chemical compound classes represent molecular species with similar sub-structural features and biological activities (e.g. flavonoids, polyketides, peptides). Over the last five years, various approaches have been developed to annotate metabolite features at the chemical-compound-class level for large-scale metabolomics analyses. In particular, the introduction of chemical ontologies allowed to train machine- and deep-learning methods for recognizing the links between $MS^2$ spectra and chemical classes.[61] For instance, the computational tool class assignment and ontology prediction using mass spectrometry (CANOPUS) uses a deep neural network to predict 2,497 compound classes (including all biologically relevant classes) from $MS^2$ spectra. Remarkably, CANOPUS does not rely on annotated candidate structures and, instead, can assign compound classes to molecular species that are not recorded in any spectral- or structural database.[62,63]

The annotation of $MS^2$ spectra at the structural level remains the biggest challenge and is generally restricted to compounds present in spectral libraries. Introduced in 2015, Compound Structure Identification (CSI):FingerID tackles this major bottleneck and emerged as the state-of-the-art tool for *in silico* annotation of $MS^2$ spectra.[64] In the first step, putative fragmentation pathways (i.e. fragmentation trees) based on small chemical modifications are calculated, which subsequently form the input to a machine learning method for molecular fingerprint prediction. For this process, multiple support-vector machines (SVM) classifiers predict the presence or absence of several thousand fingerprint elements (e.g., aromatic ring, hydroxyl-function, nitrogen atom) resulting in a

vector of the probabilities regarding the presence of each fingerprint element. Next, the experimental molecular fingerprint is compared to calculated fingerprints based on molecular structure databases (which are substantially larger compared to spectral databases) and putative annotations are listed according to the similarity of the respective fingerprint vectors.[56,64]

### On-tissue Chemical Derivatization

To detect and visualize the spatial distribution of molecular species directly from tissue sections and other samples via MALDI MSI, the analytes of interest have to be present at concentrations relevant to MALDI MSI and must be ionized efficiently. However, not all molecules are amenable to ionization, for example because of the absence of chargeable chemical functions or because of intrinsically low ionization efficiencies (e.g. steroids, carboxylic acids).[65] In addition, the problem of generally low MALDI ionization efficiencies (ion yields of $10^{-6}$ for various chemical classes[40,41]) is exacerbated by the decreasing amount of ablated molecular material in high-resolution MSI. To increase the MALDI ion yield, multiple approaches have been reported, including optimized MALDI laser wavelength[66,67] and laser-induced post-ionization.[68] For example, the analytical sensitivity for phospho- and glycolipids was improved by post-ionization by several orders of magnitude with pixel sizes of 1 µm to 2 µm.[69] However, this approach requires novel and complex instrumentation and the limited availability of commercial MALDI MSI instruments capable of post-ionization prevents broader applicability.[70]

In 1997, chemical derivatization (CD) was performed to increase the sensitivity and to facilitate sequence analysis of peptides by post-source decay MALDI mass spectrometry.[71] In 2005, CD has been used to improve the detection of poorly ionizable molecules in the context of ESI-LC-MS experiments.[72,73] Both approaches utilized pre-charged derivatization reagents that selectively reacted with functional chemical groups (e.g. amines) in the sample solution – thereby increasing the intrinsic ionization of analytes of interest. On-tissue chemical derivatization (OTCD) describes the transfer of CD to biological tissues. Therefore, in the context of MALDI MSI experiments, OTCD provides for counteracting low intrinsic ionization efficiencies, ion suppression and isobaric matrix interferences. Nevertheless, OTCD methods have to be specifically developed in accordance with the analytes of interest and desired spatial resolution of the MSI experiment. First, the choice of reagent, matrix compatibility and optimal application method has to be determined. In general, the OTCD reagent is applied to the sample surface before matrix application, using the same technique (e.g. pneumatic spraying). Hence, experimental parameters, such as reagent concentration, solvent composition, coverage density and physical parameters, including flow rate, velocity,

ambient temperature and distance to the sample surface, have to evaluated. Next, incubating the sample for several hours at increased humidity and temperature increases the ion yield with the drawback of potentially causing analyte delocalization.[65] Therefore, all the additional sample preparation steps have to be optimized to selectively increase the ion yield while preserving the spatial information.

As an alternative, recent developments also include reactive matrices, which combine the properties of derivatization reagents and physico-chemical MALDI matrix characteristics into one compound – thereby overcoming undesired side effects or additional sample preparation steps.[74,75]

Utilizing different reagents, various different functional groups can be targeted via OTCD, such as aliphatic alcohols[76], phenols[77], alkenes[75,78], carboxylic acids[79], amines[80,81], ketones and aldehydes[82–84]. For instance, Girard's T (GirT) and Girard's P (GirP) are hydrazine-based reagents that form stable hydrazones with aldehyde- and carbonyl groups. In 2013, GirT was utilized for the first time to detect substrate and product of glucocorticoid-amplifying enzyme 11β-HSD1 in rat adrenal gland and mouse brain.[85] In the following, GirT enabled the spatially-resolved analysis of various other steroidal compounds in mouse, rat and human tissue.[82,83] All of these studies demonstrated that OTCD is a powerful method to selectively enhance ion yields for MSI-based bioanalytical research. Yet, limitations in sample preparation (that cause analyte diffusion) and instrumentation hindered the visualization of metabolite distributions with pixel sizes below 20 µm.

### *Danaus plexippus*, Sequestration and Cardenolides

Over the course of the co-evolutionary arms race, plants evolved a plethora of defense traits against herbivorous insects and other antagonists. These traits include the production of low-molecular-weight chemicals (i.e. secondary plant metabolites), which affect herbivores directly, impair their growth and development, or lower the digestibility of the plant diet.[86–89] Remarkably, insects have developed sophisticated morphological, behavioral, and physiological adaptions to overcome plant defense mechanisms. Sequestration is the most complex phenomenon of insect adaptions and represents the selective accumulation of plant toxins in the insect body for defense against natural predators.[90–95] Monarch butterflies (*Danaus plexippus*) and its host plant milkweed (*Asclepias* spp., Apocynaceae) serve as royal representatives in deciphering insect-plant coevolution and are famous for the sequestration of cardenolides (i.e. steroid glycosides).[96–100] Cardenolides are specific inhibitors of $Na^+/K^+$-ATPase, a ubiquitously expressed animal enzyme that is involved in various essential physiological functions.[101,102] Remarkably, the monarch butterfly has evolved resistant $Na^+/K^+$-ATPase

based on amino acid substitutions, which increase the target site insensitivity to cardenolides (i.e. lowering the binding-potential to the enzyme).[98,103–107] Interestingly, other milkweed butterfly species (e.g. *Euploea core*) can tolerate dietary-cardenolides but are not able to cope with these steroidal glycosides once dispersed in the hemolymph of the caterpillar.[98,108,109] This finding suggests that the $Na^+/K^+$-ATPase resistance to cardenolides for monarch butterflies represents an adaption, which is linked to the ability to sequester these plant toxins as chemical defense.

The general structure of cardenolides consists of a steroidal core composed of 23 carbon atoms linked to a five-membered lactone ring at carbon 17 and exist either as glycosides (mostly mono-,bi- and triglycosides) or as free genins.[101] For *Asclepias curassavica* (*A. curassavica*), which represents a critical host plant for monarch butterflies, 21 different cardenolides were identified using nuclear magnetic resonance spectroscopy (NMR), infrared spectroscopy (IR) and LC-MS.[110] Yet, insect-plant studies of cardenolide sequestration in monarchs are restricted to the predominant toxic glycosides calotropin, calactin, uscharidin and voruscharin. Despite being already described in the 1960s, the molecular- and physical mechanisms underlying sequestration are still largely unknown. This gap of knowledge originates from the lack of analytical methods that enable the comprehensive analysis of the metabolome with its spatial and temporal details for complex sample systems, such as insects.

### Aims of the Thesis

Most spatially-resolved metabolomic approaches have focused on mammalian tissues and were rarely employed to delicate sample systems, such as insect tissues. Taking advantage of recent technical developments for mass spectrometry imaging (MSI), we here set out to acquire spatially-resolved metabolomes related to cardenolide sequestration in *D. plexippus* and *E. core* caterpillars. First, we developed an MSI-compatible sample preparation protocol to obtain high-quality tissue sections while taking snap-shots of in-vivo biochemical processes. Next, we revealed cardenolide distributions across the whole body and demonstrate that quantitative differences between both species already manifest in the gut lumen. While monarchs retain and accumulate cardenolides above plant concentrations, the toxins are degraded in the gut lumen of *E. core.* Utilizing dedicated sample preparation in conjunction with maximized analytical performance by the employed instrumental setup, we visualized cardenolide transport across the monarch midgut epithelium at unprecedent detail and identified integument cells as the final site of storage. This work is described in publication 1 (**Chapter II**).

Furthermore, we expanded our experimental design to tackle the two major bottlenecks for the spatially-resolved analysis of cardenolide sequestration and other metabolic networks: the absence of repository-scaled databases and low intrinsic ionization efficiencies of steroidal compounds. Therefore, we integrated an LC-MS-based computational metabolomics pipeline into our MSI workflow to generate a comprehensive ‘in-house” metabolomic database. This database guided subsequent MSI analysis of cardenolide sequestration in tissues and cells of *D. plexippus*. We developed a spatial-context-preserving OTCD method to mitigate the problem of low intrinsic ionization efficiencies by the selective chemical tagging of carbonyl-containing cardenolides with pre-charged moieties. This approach increased the molecular coverage and enabled the visualization of previously inaccessible (sub)-cellular cardenolide distributions in Malpighian tubules, epithelial cells and fat body tissue. Therefore, we demonstrated that expanding experimental designs for MSI studies with advanced computational and chemical tools allows to acquire even further biochemical insight and ultimately enhances spatially-resolved metabolomic research for complex sample systems. This work is described in publication 2 (**Chapter III**).

## 1.2 Results and Discussion

### Spatial metabolomics reveal divergent cardenolide processing in the monarch (*Danaus plexippus*) and the common crow butterfly (*Euploea core*) (Publication 1)

The monarch butterfly (*D. plexippus*) is famous for the sequestration of toxic cardenolides from its host plant milkweed. However, the mechanism of sequestration and the location of cardenolides in the caterpillar body tissues are still unknown. Yet, technical- and methodical limitations hindered accurate and nontargeted analysis of molecular species in the spatial context of insect tissues and cells. Utilizing recent developments in AP-SMALDI MSI, we followed a spatial metabolomics approach to study cardenolide sequestration in *D. plexippus* and the closely-related species *E. core* (**Fig. 1**). First, we established an MSI-compatible sample preparation protocol to obtain transversal- and longitudinal tissue sections of final instar *D. plexippus* and *E. core* caterpillars with excellent quality regarding tissue morphology, allowing to snapshot in-vivo biochemical processes in their native environment. Next, we performed whole-body AP-SMALDI MSI (20 µm to 45 µm step size) to reveal the presence of cardenolides in body tissues of *D. plexippus* and *E. core* caterpillars.

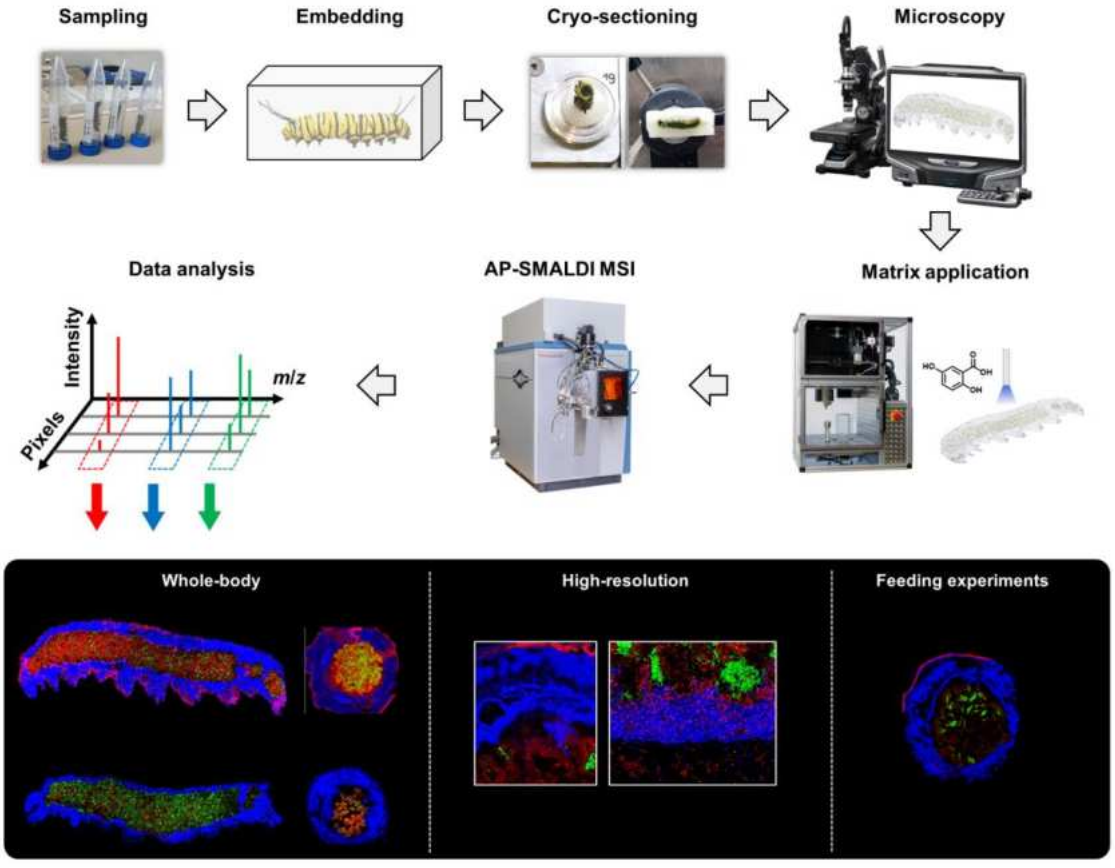


**Figure 1.** Overview of the spatial metabolomics workflow to investigate cardenolide sequestration in *D. plexippus* and *E. core* via AP-SMALDI MSI

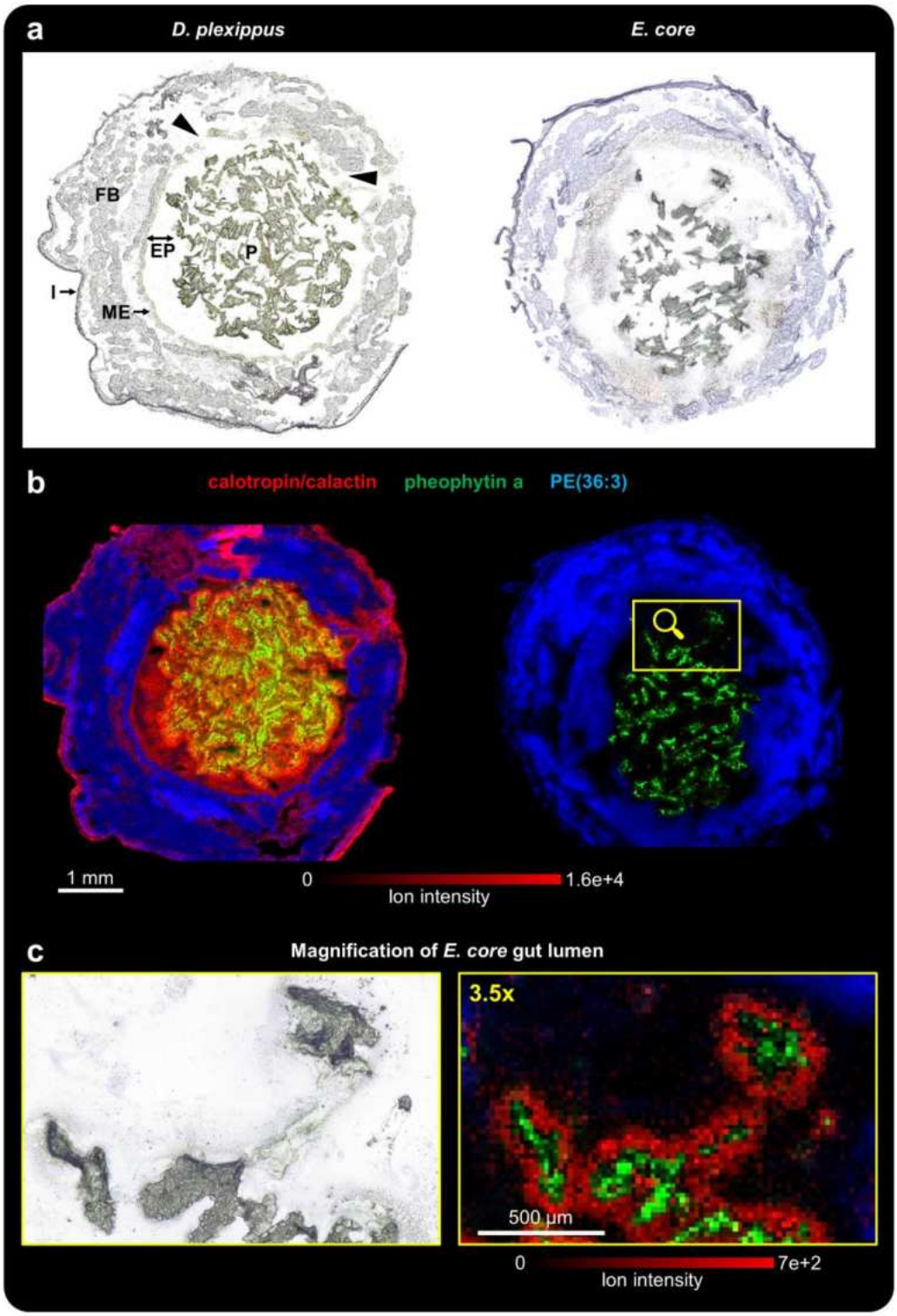


**Figure 2.** AP-SMALDI MSI of transversal sections of caterpillars of *D. plexippus* and *E. core*. (**a**) Optical image of the transversal section of a fifth instar caterpillar of *D. plexippus* (left) and *E. core* (right) before matrix application. P: plant material, EP: ectoperitrophic space, ME: midgut epithelium, FB: fat body, I: integument. (**b**) Corresponding RGB overlay images obtained with 35 µm (*D. plexippus*) and 20 µm (*E. core*) step size, showing the spatial distribution of the cardenolide calotropin and/or its isomer calactin ($[M+K]^+$, red) at *m*/*z* 571.2304, the chlorophyll derivative pheophytin a at *m*/*z* 909.5288 ($[M+K]^+$, green) as a chemical marker for plant tissue, and the animal lipid PE(36:3) ($[M+K]^+$, blue) as a chemical marker for animal tissues. Both RGB overlay images are normalized to the same intensity scale. The *D. plexippus* gut epithelium was damaged at two areas (highlighted in the optical image), causing potential analyte delocalization in the corresponding hemolymph area. (**c**) Magnification of the optical image and RGB overlay image for the highlighted area of the *E. core* gut lumen. For this ion image, the intensity scale of calotropin/calactin was adjusted to highlight the cardenolide distribution at the fringes of leaf pieces in the gut lumen of *E. core*.

To overcome the technical challenges of the delicate and heterogeneous sample characteristics of caterpillar sections (e.g. fragile integument, various tissue types and ingested plant material), we utilized the recently implemented pixel-wise autofocusing method (3D-surface mode) of the AP-SMALDI$^5$ AF ion source to keep the laser focus, fluence and ablation spot-size constant for the whole MSI experiment. Due to the high mass resolution and mass accuracy provided by the Orbitrap mass analyzer, we were able to assign and annotate cardenolides, lipids and other metabolites based on accurate mass measurements, which were subsequently confirmed by complementary HPLC-MS/MS experiments.

Utilizing whole-body MSI, we were able to reveal diverging strategies of the two closely-related milkweed butterfly species regarding the processing and uptake of plant toxins in the gut as well as the storage of sequestered compounds for defense. In particular, our data demonstrated that the gut lumen was the first physiological layer, mediating selectivity and playing a vital role in coping with a toxic diet in both species. For *D. plexippus*, cardenolides were distributed in the entire body, including the integument as the location of storage, fat body, hemolymph and gut lumen including the ectoperitrophic space (i.e. the region between the peritrophic envelope surrounding the food bolus and the midgut epithelium) (**Fig. 2b**). In contrast, for *E. core* caterpillars, cardenolides were absent from body tissues (i.e. no sequestration) and exclusively detected at the fringes of *A. curassavica* leaf pieces and not in the liquid phase in the gut lumen (**Fig. 2c**).

In addition to transversal sections, we performed whole-body MSI (45 µm step size) of longitudinal sections and found similar patterns of cardenolide distributions along the entire gut passage (**Fig. 3a,b**). According to the visual differences (in **Figs. 2,3**), we determined that cardenolides were up to 6.8 times more abundant (for comparable regions at leaf fringes) in the gut lumen of *D. plexippus*. For the in-depth quantitative analysis of the entire gut passage, we conducted complementary HPLC-MS and HPLC-DAD experiments based on freeze-dried gut segments (foregut: FG, four sequential midgut portions: MG1-4, and hindgut: HG) and determined heterogeneous total cardenolide concentrations along the gut passage of *D. plexippus* ($F_{5,38}$ = 8.312, $p < 0.001$; n = 7-9) with higher cardenolide concentrations in midgut portions 2 and 3 compared to milkweed leaves ($F_{4,32}$ = 5.622, p = 0.002) (**Fig. 3c**). In contrast, total cardenolide concentrations were constant across all gut regions of *E. core* caterpillars ($F_{5,25}$ = 1.044, p = 0.414, n = 6) and lower than in plant material except for midgut portion 4 (plant vs. FG, MG1, MG2, MG3, MG4, HG: p = 0.046; 0.023; 0.029; 0.01; 0.228; 0.005; Tukey HSD) (**Fig. 3c**). In addition, the stereoisomer ratio of calotropin/calactin in *E. core* gut lumen (24:1) differed significantly from the isomer ratio found in monarch gut lumen (1.2:1) and *A. curassavica* leaves (1.6:1).

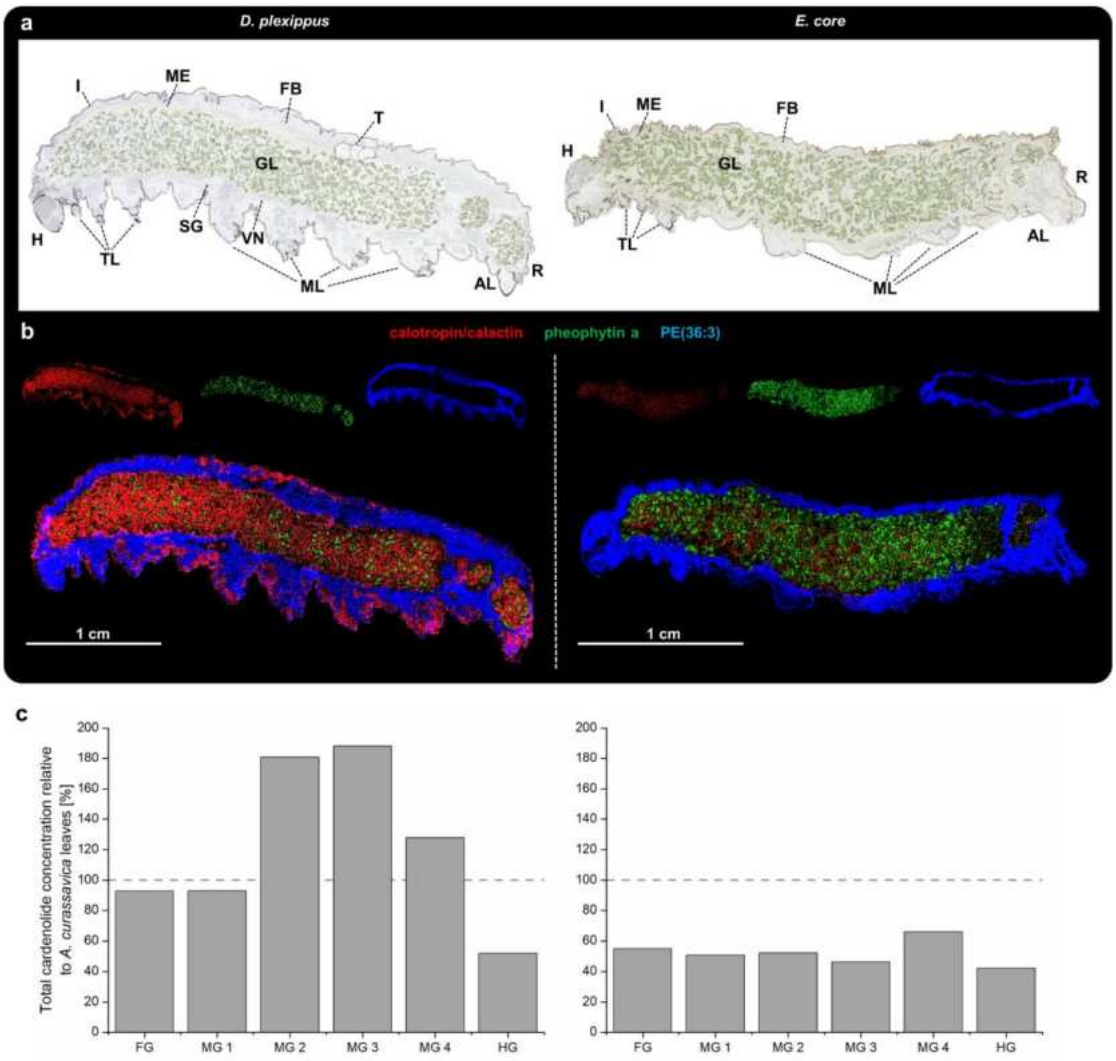


**Figure 3.** Whole-body AP-SMALDI MSI of fifth instar *D. plexippus* and *E. core* caterpillars. (**a**) Optical image of longitudinal *D. plexippus* (left) and *E. core* (right) sections before matrix application. H: head, I: integument, TL: thoracic legs, SG: probably salivary gland, VN: probably ventral nerve code, ML: abdominal prolegs, AL: anal prolegs, R: rectum, T: testis, GL: gut lumen, FB: fat body, ME: midgut epithelium. (**b**) Corresponding RGB overlay images obtained with 45 µm step size, showing the spatial distribution of calactin/calotropin ($[M+K]^+$, at *m*/*z* 571.2304 (red), pheophytin a ($[M+K]^+$, green) at *m*/*z* 909.5292 to highlight ingested *A. curassavica* plant material, and PE(36:3) ($[M+K]^+$, blue) at *m*/*z* 780.4941 serving as a marker for insect tissue, such as gut epithelium and fat body. Both RGB overlay images are normalized to the same intensity scale. (**c**) Schematic representation of total cardenolide concentrations across the gut passage in caterpillars of *D. plexippus* and *E. core* relative to the total cardenolide concentration in *A. curassavica* leaves based on means of six (*E. core*) and nine (*D. plexippus*) dissected caterpillars and milkweed leaves. Horizontal lines indicate the cardenolide concentration in plant material (i.e. 100%).

Previous studies showed that calactin is > 3x more toxic for *E. core* than its stereoisomer calotropin.[111] Hence, we suggested that *E. core* prevents cardenolide intoxication by minimizing the concentration of calactin. Taking together, by revealing the absence of cardenolides in the liquid phase combined with the overall lower cardenolide concentration (relative to *D. plexippus* gut lumen and *A. curassavica* plant material) and striking differences of the stereoisomer ratio in *E. core* gut lumen, our data indicated immediate degradation and/or conversion of toxic steroid glycosides extracted from the plant material.

In contrast, for *D. plexippus*, our results suggested that cardenolides were selectively retained in the monarch gut lumen, resulting in higher local concentrations of preferentially-sequestered cardenolides (e.g. calotropin/calactin, frugoside, calotoxin) to create a steep concentration gradient that supports efficient sequestration. To further address the hypothesis of cardenolide retention in the midgut lumen of *D. plexippus* caterpillars, we conducted MSI experiments with caterpillars raised on *A. curassavica* but fed with the cardenolide-free diet *O. coeruleum* before sampling. Remarkably, even after several rounds of purging with cardenolide-free plant material, preferentially-sequestered cardenolides, such as calotropin/calactin, calotoxin, and frugoside were still located in the interstices between *O. coeruleum* leaf particles with 2.7 x, 1.1 x, 2.1 x lower abundance (t-test, $p < 0.001$ for all comparisons) compared to previous MSI experiments (**Fig. 4**). Notably, the dominant *A. curassavica* leaf cardenolides voruscharin, uscharin and asclepin were not detected anymore. Thus, we demonstrated that preferentially-sequestered cardenolides were retained in the gut lumen and were not moving linearly along with the gut contents. Our MSI data revealed that the spatial distribution of retained cardenolides resembles the shape of the *O. coeruleum* leaf particles (**Fig. 4a**). Therefore, we propose a mechanism analogous to adsorption chromatography to retain cardenolides in the gut lumen while the food contents are passing by and are defecated. Whether the observed selectivity is related to the retention mechanism and/or enzymatic activities in the gut environment remains an open question.

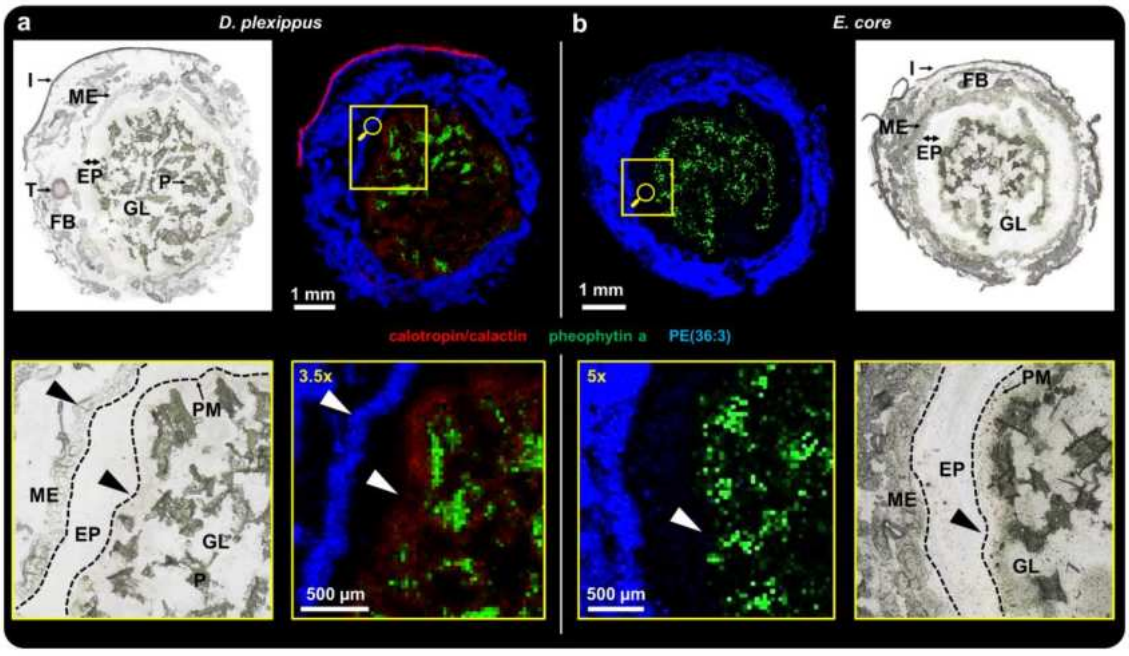


**Figure 4.** AP-SMALDI MSI (25 µm step size) of *D. plexippus* and *E. core* fed with the non-toxic plant *Oxypetalum coeruleum* before sampling. Optical image, RGB overlay and magnified view of transversal (**a**) *D. plexippus* and (**b**) *E. core* section. P: *O. coeruleum* plant material, EP: ectoperitrophic space, PM: peritrophic matrix, ME: midgut epithelium, T: testis, FB: fat body, I: integument. Both RGB overlay images and magnified views show calactin/calotropin ($[M+K]^+$, red) at *m/z* 571.2304, pheophytin a ($[M+K]^+$, green) at *m/z* 909.5292 as a chemical marker for plant tissue and PE(36:3) ($[M+K]^+$, blue) at *m/z* 780.4942 as a chemical marker for insect tissue.

In contrast to previous MSI experiments based on caterpillars actively feeding on *A. curassavica* before sampling, we did not detect cardenolides in the ectoperitrophic space and body cavity of *D. plexippus* caterpillars, thus, suggesting rapid clearance once the supply from the gut lumen is halted (**Fig. 4a**). For *E. core*, we did not detect any cardenolides after purging the gut lumen overnight with *O. coeruleum* (**Fig. 4b**).

We complemented our whole-body MSI with high-resolution AP-SMALDI MSI experiments (5 µm and 10 µm step size) of particular regions of interest (e.g. epithelia of the midgut and integument) for in-depth analysis of the selectivity of sequestration as well as transportation and storage of cardenolides in *D. plexippus* (**Fig. 5**). Despite being lowly abundant compounds in *A. curassavica* leaves (**Fig. 5a**), calotropin/calactin, frugoside and calotoxin were the most abundant cardenolides in the gut lumen and integument of monarch caterpillars (**Fig. 5a-c**). In contrast, the predominant cardenolides in *A. curassavica* leaves, uscharidin, asclepin, voruscharin and uscharin did not belong to the preferentially-sequestered steroid glycosides of the monarch. In particular, asclepin being 5.8 times more abundant in *A. curassavica* leaves relative to calotropin (**Fig. 5a**), was not sequestered and by utilizing the high spatial resolution (5 µm pixel size) provided by the AP-SMALDI MSI platform, we were able to reveal that asclepin was exclusively abundant at fringes of ingested *A. curassavica* leaf material (**Fig. 5d**). Considering the high structural similarity to calotropin/calactin (i.e. acetoxy-group (-OAc) instead of hydroxyl-group (-OH) in the sugar moiety), it seems puzzling that the molecular mechanism underlying sequestration prohibits the uptake of asclepin. Based on our high-resolution MSI data, we hypothesized that asclepin was rapidly converted into calactin and/or calotropin instead of being not sequestered (**Fig. 5e**). Similar observations regarding the metabolic conversion of structurally-related cardenolides into calotropin/calactin by *D. plexippus* were already made for uscharidin and voruscharin.[112–114] Notably, uscharidin occurred at similar concentration (compared to asclepin) in *A. curassavica* leaves (**Fig. 5a**), but was very abundant in the monarch gut lumen (**Figure 5f**). Hence, we hypothesized that the conversion rate of asclepin into calotropin/calactin is significantly higher compared to uscharidin, suggesting a passive mechanism (e.g. gut pH; similar to the observations for voruscharin) and not an involvement of enzymes as it was shown for uscharidin.

Previous studies showed that for the thiazolidine-ring containing cardenolide voruscharin, monarch $Na^+/K^+$-ATPases was less than twofold more resistant compared to non-adapted porcine $Na^+/K^+$-ATPases (for other cardenolides, monarch $Na^+/K^+$-ATPases showed 50- to 94-fold higher resistance) and was also not detected in *D. plexippus* caterpillar bodies via LC-MS.[111,114]

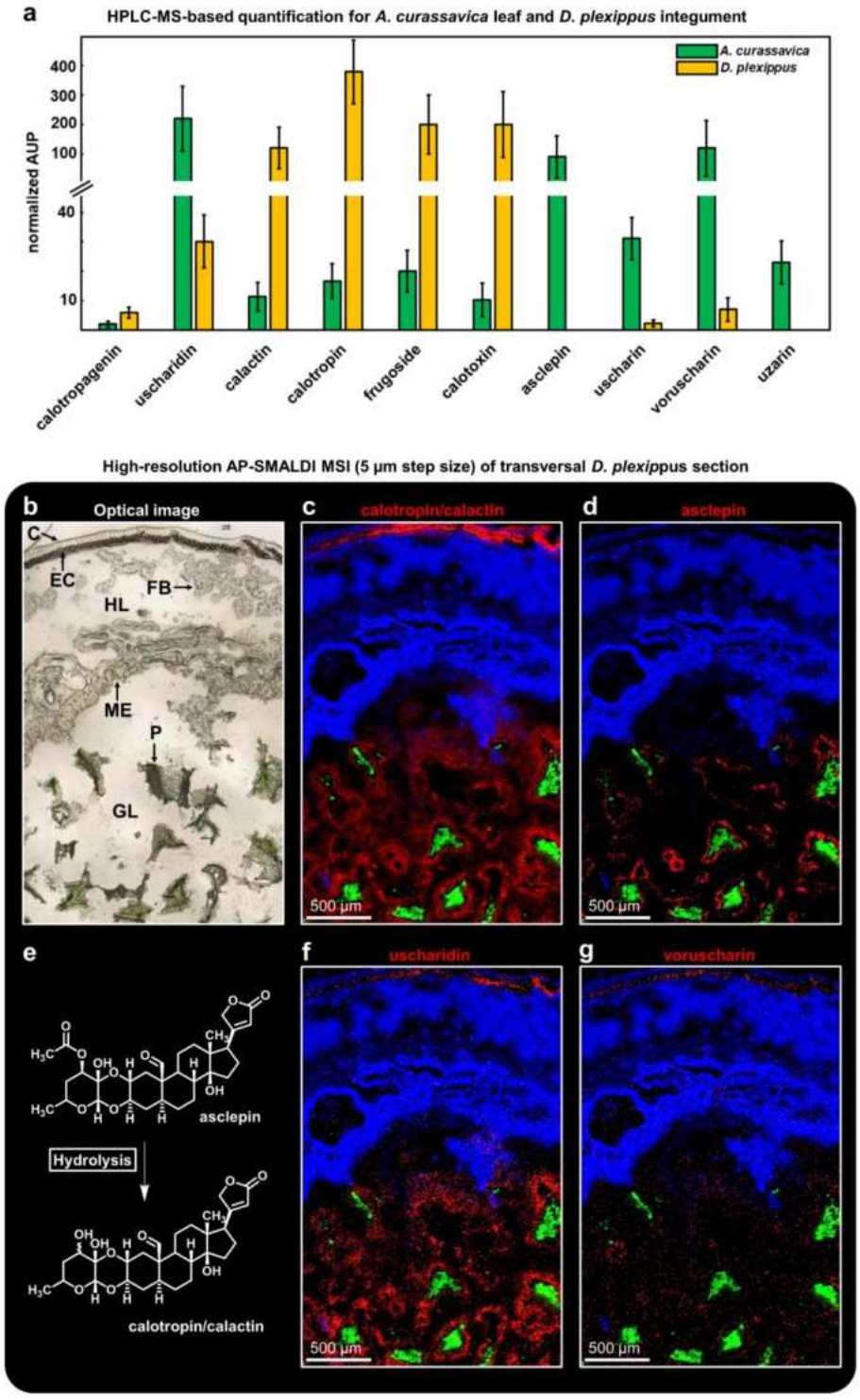


**Figure 5**. Bulk quantification of cardenolides for *A. curassavica* leaf and *D. plexippus* integument and high-resolution AP-SMALDI MSI (5 µm step size) of a transversal *D. plexippus* section. (**a**) HPLC-MS-based quantification for 10 detected cardenolides in *Asclepias curassavica* leaf material and *D. plexippus* integument. Each bar represents the mean of three biological replicates and error bars indicate standard deviation. The area under peak (AUP) was normalized to the internal standard (digitoxin). Note that quantities between leaf material and caterpillar tissue may not be compared in absolute terms since sample dry masses were different. (**b**) Optical image of the analyzed region of interest. C: cuticle, EC: epidermal cells, HL: hemolymph, FB: fat body, ME: midgut epithelium, GL: gut lumen, P: *A. curassavica* plant material. (**c**,**d**) RGB overlay images showing the spatial distribution of (**c**) calactin/calotropin ($[M+K]^+$, red) at *m*/*z* 571.2304, (**d**) asclepin ($[M+K]^+$, red) at *m*/*z* 613.2427, and (**c,d**) pheophytin a ($[M+K]^+$, green) at *m*/*z* 909.5290 and PE(36:3) ($[M+K]^+$, blue) at *m*/*z* 780.4940. (**e**) Putative degradation pathway of asclepin in *D. plexippus* gut. (**f**,**g**) RGB overlay images showing the spatial distribution of (**f**) uscharidin ($[M+K]^+$, red) at *m*/*z* 569.2146, (**g**) voruscharin ($[M+H]^+$, red) at *m*/*z* 590.2770, and (**f,g**) pheophytin a ($[M+K]^+$, green) at *m*/*z* 909.5290 and PE(36:3) ($[M+K]^+$, blue) at *m*/*z* 780.4940.

Consequently, the results were interpreted as an adaption to avoid toxicity. However, due to the high sensitivity of the employed MSI system, we were able to detect and visualize low amounts of voruscharin in the gut lumen and epidermal cells of the integument (**Fig. 5g**; LC-MS-based quantification revealed 160 x lower concentration compared to calotropin in the integument). Hence, our data indicated that rapid degradation of voruscharin in the caterpillar gut results in reduced sequestration and limited resistance by not exerting selection pressure on monarch $Na^+/K^+$-ATPase.

To investigate the role of the midgut epithelium as the transport organ for sequestered toxins mediating selectivity, we also analyzed the distribution of cardenolides at the interface gut lumen, midgut epithelium, and hemolymph. We were able to detect calotropin/calactin with low abundance in the midgut epithelium tissue of transversal monarch sections **(Fig. 6a**). To address the molecular transport process in a larger spatial environment, we also performed high-resolution AP-SMALDI MSI (10 µm pixel size) of longitudinal sections. In line with the previous results, we were able to reveal calotropin/calactin and other dominant sequestered cardenolides (calotoxin and frugoside) within the epithelial tissue of the monarch gut (**Fig. 6b,c**). In contrast, the cardenolides uzarin and asclepin, which were absent from the body cavity (i.e. not sequestered), were also not detected within the layer of midgut cells (**Figs. 6d** and **7b**). For uzarin, metabolism can be ruled out as a factor preventing sequestration due to being extensively abundant in the gut lumen and being in direct contact with the apical surface of the midgut epithelium. Hence, our MSI data provided proof that the midgut epithelium discriminates against individual compounds with molecular size and/or polarity being important determinants (uzarin had the highest mass out of all detected cardenolides). To this point, the phenomenon of plant toxin sequestration, involving various chemical classes, is described for more than 275 insect species.[90] Yet, the underlying mechanism of how plant toxins are transported across the insect gut epithelium (i.e. from the gut lumen into the body cavity) is still largely unknown. Our high-resolution MSI data revealed a discrete granular pattern of cardenolides in the midgut epithelial tissue (**Fig.6c**), which might indicate a vesicular transport via transcytosis, similar to albumin uptake in the midgut of the silkworm (*Bombyx mori*).[115] In addition, other secondary plant metabolites, such as polysaccharides, and flavonoids, as well as primary metabolites (e.g. guanosine) appeared in the same granular pattern, thus suggesting that vesicular uptake is a universal mode of uptake for various metabolites (**Fig. 7c-f**). Micelles, formed by the aggregation of phospholipids, galactosyl glycerides, long chain fatty acids, and other amphiphilic and lipophilic compounds, are known to represent the primary constituents of the non-aqueous phase of the midgut fluid in insect herbivores.[116]

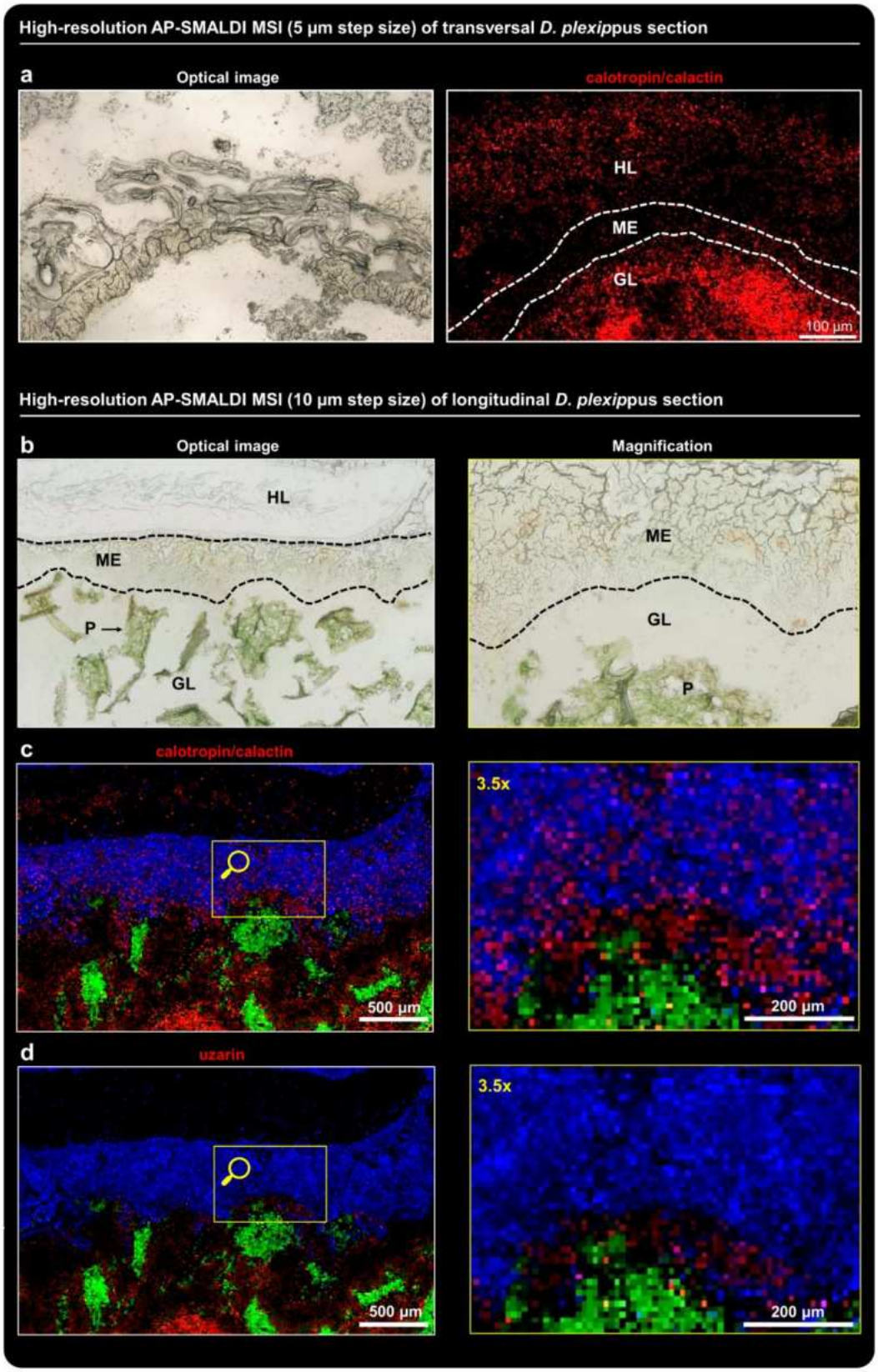


**Figure 6**. High-resolution AP-SMALDI MSI of the interface gut lumen, midgut epithelium and hemolymph for transversal and longitudinal *D. plexippus* sections. (**a**) Optical image of the analyzed region of interest and corresponding single ion image for calactin/calotropin ($[M+K]^+$, red) at *m*/*z* 571.2304. P: *A. curassavica* plant material, GL: gut lumen, ME: midgut epithelium, HL: hemolymph. (**b**) Optical image of the analyzed region of interest and magnified view (3.5x) of the outlined region in **c**,**d**. (**c**,**d**) RGB overlay images and magnified view of the outlined region showing the spatial distribution of calactin/calotropin ($[M+K]^+$, red) at *m*/*z* 571.2304 in (**c**), uzarin ($[M+K]^+$, red) at *m*/*z* 737.3149 in (**d**), pheophytin a ($[M+K]^+$, green) at *m*/*z* 909.5290 and PE(36:3) ($[M+K]^+$, blue) at *m*/*z* 780.4940.

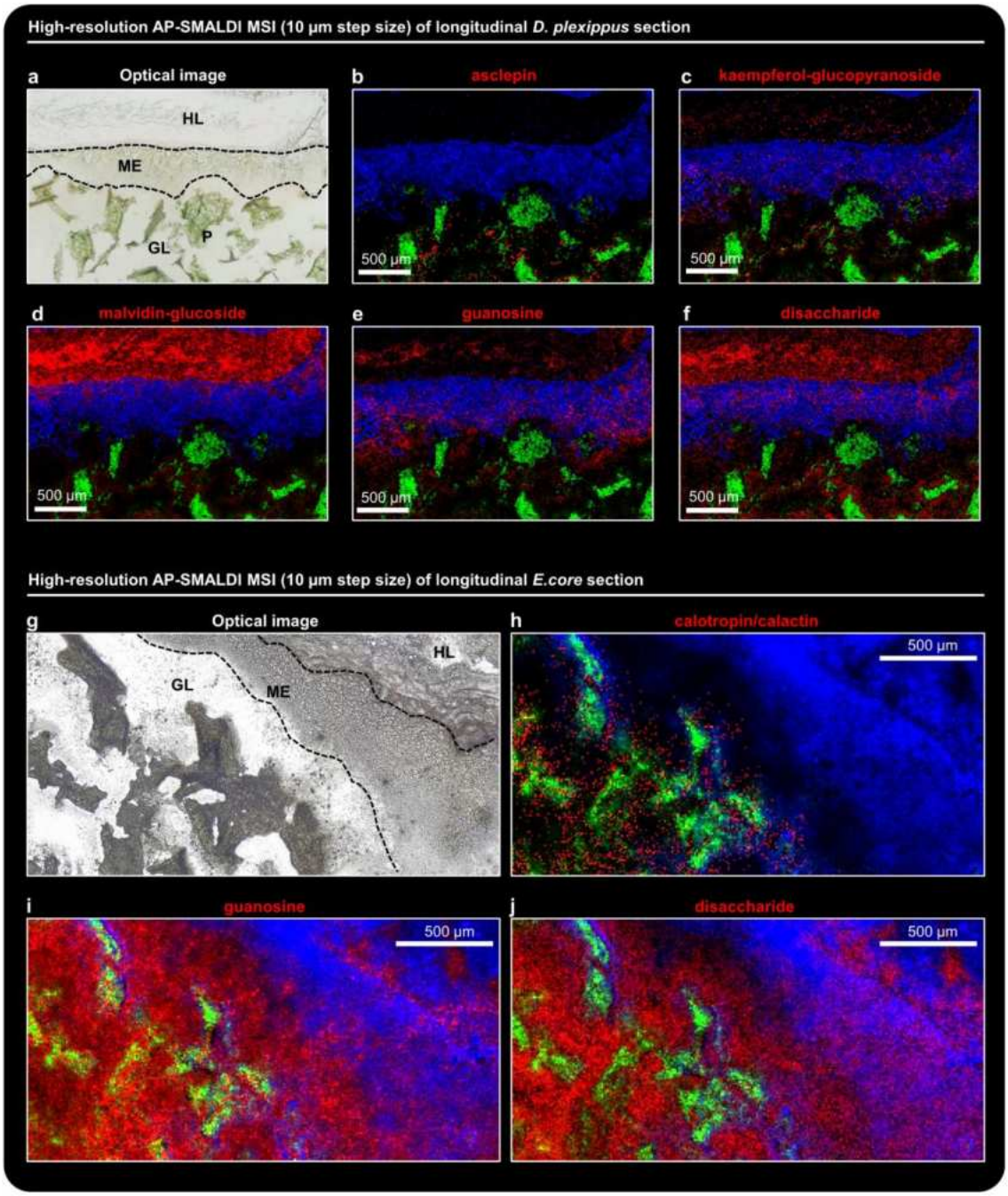


**Figure 7**. High-resolution AP-SMALDI MSI (10 µm step size) of midgut epithelium tissue for longitudinal *D.plexippus* and *Euploea core* section to investigate the transport of cardenolides and other primary- and secondary metabolites. (**a**) Optical image of the analyzed region of interest for *D. plexippus*. GL: gut lumen, ME: midgut epithelium tissue, HL: hemolymph. (**b-f**) RGB overlay images showing the spatial distribution for (**b**) asclepin ($[M+K]^+$, red) at *m*/*z* 613.2415, (**c**) kaempferol-glucopyranoside ($[M+Na]^+$, red) at *m*/*z* 471.0898, (**d**) malvidin-glucoside ($[M+Na]^+$, red) at *m*/*z* 515.1160, (**e**) guanosine ($[M+K]^+$, red) at *m*/*z* 322.0548, (**f**) disaccharide ($[M+K]^+$, red) at *m*/*z* 381.0793. (**g**) Optical image of the analyzed region of interest for *E. core.* (**h-j**) RGB overlay images showing the spatial distribution for (**h**) calotropin/calactin ($[M+K]^+$, red) at *m*/*z* 571.2305, (**i**) guanosine ($[M+K]^+$, red) at *m*/*z* 322.0547, (**j**) disaccharide ($[M+K]^+$, red) at *m*/*z* 381.0792. For all RGB images, pheophytin a ($[M+K]^+$, green) at *m*/*z* 909.5290 and PE(36:3) ($[M+K]^+$, blue) at *m*/*z* 780.4940 were used to highlight ingested plant tissue and midgut epithelium tissue.

Previous studies showed that amphiphilic allelochemicals are expected to be absorbed into micelles in the fluid phase of the insect's gut.[116] Therefore, we hypothesized that the observed granular distribution was related to micelles, composed of plant lipids and cardenolides, crossing the midgut epithelium by diffusion – thereby representing the mode of transport by which cardenolides were sequestered.

We followed the same experimental design for *E. core*, and found comparable patterns for various metabolites but remarkably, cardenolides were not detected in the midgut epithelium (**Fig. 7g-j**). Therefore, it is unclear, how caterpillars of *E. core* discriminated against the uptake of cardenolides while apparently taking up other metabolites in a similar fashion compared to *D. plexippus*. The peritrophic membrane (i.e. semi-permeable, non-cellular structure surrounding the food bolus) of grasshoppers prevents the uptake of micelles containing various plant toxins (including the cardenolide digitoxin) by ultrafiltration.[116] However, our MSI data showed that cardenolides were able to cross the peritrophic membrane and were in close contact with the midgut epithelium. Therefore, our study suggests that degradation of cardenolides in the fluid-phase of the gut prevents the sequestration of cardenolides in *E. core*.

## Molecular Networking and On-Tissue Chemical Derivatization for Enhanced Identification and Visualization of Steroid Glycosides by MALDI Mass Spectrometry Imaging (Publication 2)

First, we utilized non-targeted LC-$MS^2$ experiments of *A. curassavica* leaf extracts to acquire an 'in-house' metabolomic database of the host plant (**Fig. 8a**). However, molecular identification and elucidation of chemical structures is generally restricted to compounds for which mass spectrometric reference data are archived in spectral databases (e.g. commercially available chemicals). Thus, the metabolomics-related aspects of our workflow are built in state-of-the-art molecular networking tools as well as *in silico* molecular characterization methods based on machine learning and deep learning. We performed feature-based molecular networking (FBMN) from the GNPS ecosystem to push the boundaries of database search. The underlying idea of molecular networking utilizes spectral similarity to group metabolites with the implicit assumption that similar molecular structures will generate similar $MS^2$ fragmentation spectra. Thus, spectral library annotations can be propagated throughout the molecular network and facilitate structural elucidation of unknown chemical compounds. In total, our FBMN results for *A. curassavica* consisted of 1175 mass spectral nodes ($MS^2$ spectra), which were organized into 89 independent molecular families (**Fig. 8b**). By utilizing 145 spectral library hits, we were able to classify the corresponding molecular networks, such as fatty acids, phosphatidylcholines, sphingomyelins, flavonoid glycosides, carotenoids, polysaccharides and cardiac glycosides, which are potent inhibitors for Na+/K+-ATPase, a cation carrier ubiquitously expressed in animal cells. **Figure 8c** shows the enlarged steroidal glycoside molecular networks with the node size proportionally representing the LC-MS feature abundance (i.e. peak area) and increased edge thickness correlating to higher spectral similarity. In addition, our AI-driven molecular characterization approach classified 12 additional nodes ($MS^2$ spectra) as cardiac glycosides, which were not part of the molecular networks due to different fragments in the $MS^2$ spectra. In total, 32 different cardiac glycosides were identified based on eight GNPS spectral library hits (red nodes) and 24 *in-silico* annotations (grey nodes), which were evaluated by analysing the respective fragmentation spectra. Compared to most recent studies regarding steroidal glycoside composition in *A. curassavica*, we, therefore, found 20 additional cardiac glycosides that were also absent from mass spectral libraries. Computational substructure predictions facilitated detailed structural characterization – thereby revealing structural diversity along cardiac glycosides in *A. curassavica*. Besides digitoxin and two derivatives, all cardiac glycosides were 19-oxosteroids with either an aldehyde or hydroxyl group at C19.

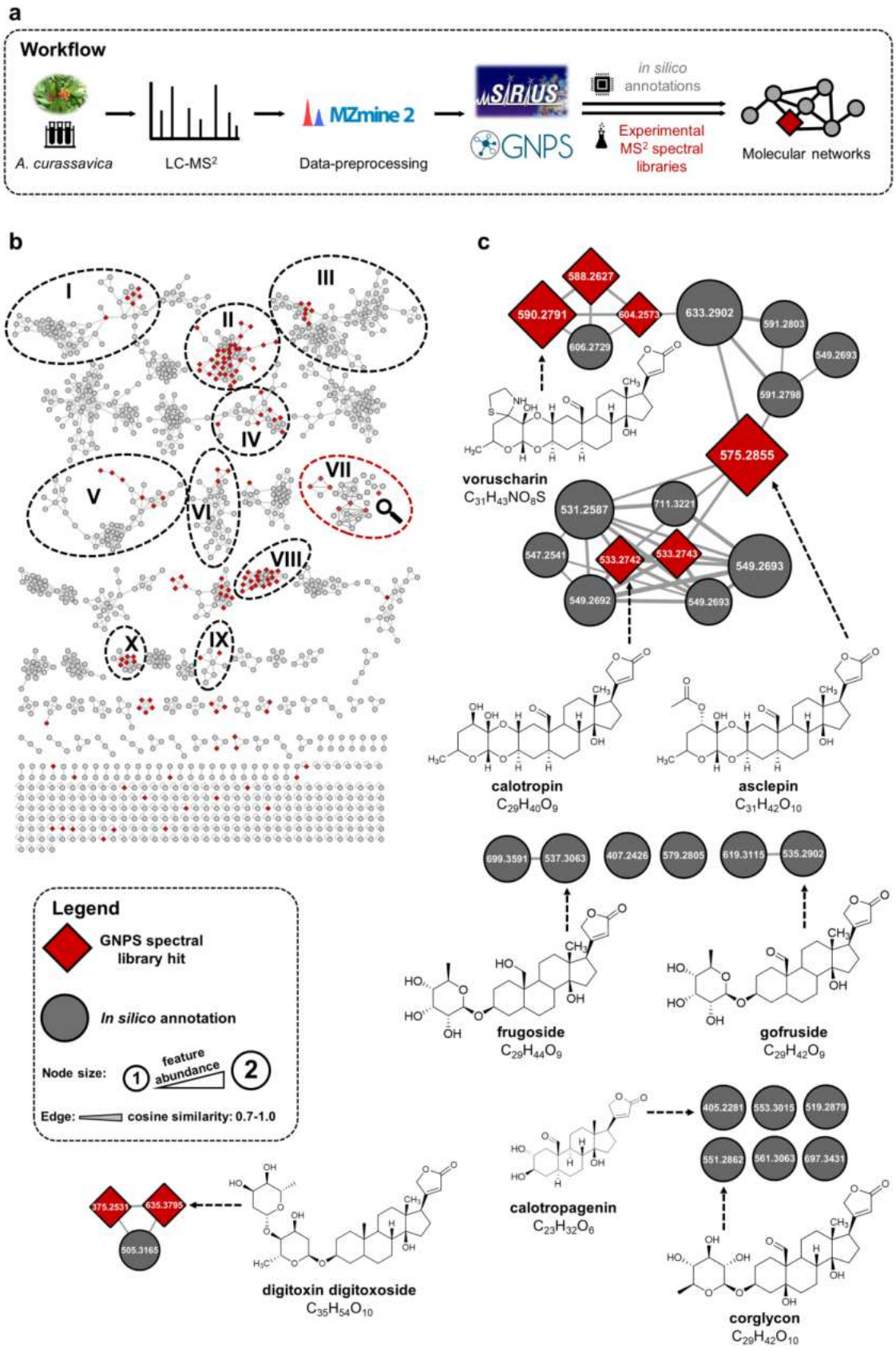


**Figure 8. Feature-based molecular networking and AI-driven molecular classification, substructure prediction and annotation of cardiac glycosides in *A. curassavica*.** (**a**) Overview of the workflow for generating an 'in-house' metabolomic database. (**b**) Comprehensive FBMN results consisting of 1175 mass spectral nodes, that were organized into 89 independent molecular families. In total, 145 spectral library hits (red nodes) were obtained allowing to classify the corresponding molecular networks. For instance, the molecular networks I to III (MN I-III) were composed of fatty acids, phosphatidylcholines (PC),

sphingomyelins (SM) and arachidonoylthio-PCs; MN IV contains flavonoid glycosides, MN V contains phosphatidylethanolamines (PE), MN VI contains carotenoids, MN VII contains cardiac glycosides, MN VIII contains flavonoids, MN IX contains polysaccharides and MN X contains isoflavonoids. (**c**) Magnified view of the molecular networks related to cardiac glycosides. Node size proportionally represents the LC-MS feature abundance (peak area) and increased edge thickness corresponds to higher cosine similarity (0.7 to 1.0). AI-driven molecular classification and compound annotation was utilized to discover additional steroid glycosides that were not part of the original molecular network. In total, 32 different cardiac glycosides were identified based on 8 GNPS spectral library hits (red nodes) and 24 *in silico* annotations (grey nodes).

In addition, we determined differences regarding the linkage between the glycoside unit and the steroidal-backbone, which either consisted of ether-bond linkage or 1,4-dioxane linkage. Furthermore, the highlighted spectral library annotations in **Figure 8c** demonstrate different chemical subgroups (e.g. thiazolidine-/thiazoline-, acetyloxy- and hydroxy-/ketone-group) in the glycoside unit. In contrast to classical molecular networking, the feature-based molecular networking workflow (including pre-processing of chromatographic features) resolved structural isomers for *m*/*z* 533.2741, *m*/*z* 549.2693 and *m*/*z* 591.2803 and enables quantitative analysis, thus, showing that asclepin, acetoxyasclepin, uscharidin and voruscharin are the most abundant cardiac glycosides in *A. curassavica* (**Fig. 8c**).

Next, we used our metabolomic 'in-house' database to guide the spatial characterization of metabolic networks related to cardiac glycoside sequestration in *D. plexippus*. However, previous studies showed that a broad range of metabolite classes, including steroids[82,85], show low intrinsic ionization efficiencies in MSI experiments, thus restricting the spatial characterization of metabolic networks in the context of tissues and cells. Thus, sensitivity is a significant barrier in spatial metabolomics research, in particular for high-resolution MSI experiments (i.e. decreasing amount of ablated material for smaller spot sizes). Therefore, we developed an ultrafine OTCD method using Girard's reagent T (GirT) to selectively increase the ion yield for steroidal glycosides. Importantly, OTCD methods have to overcome several challenges including incomplete derivatization, interferences due to excess of derivatization reagents and analyte delocalization caused by additional spraying- and incubation steps. Hence, we optimized the sample preparation protocol to achieve high sensitivity for derivatized molecular species at (sub)-cellular resolution. In summary, the solvent composition of methanol/water (7:3) v/v enabled high GirT reagent concentration (15 mg/mL), which subsequently allowed a low spray volume (35 µL), preventing analyte delocalization. Between OTCD and matrix application, the sample tissue was transferred into a desiccator for two hours at room temperature to increase reaction yield (**Fig. 9a**) and to prevent spatial artefacts due to hydroscopic properties of the GirT reagent. Any further incubation step that included increased humidity and temperature resulted in analyte delocalization and wash-out effects and was thus avoided (**Fig. 9b**).

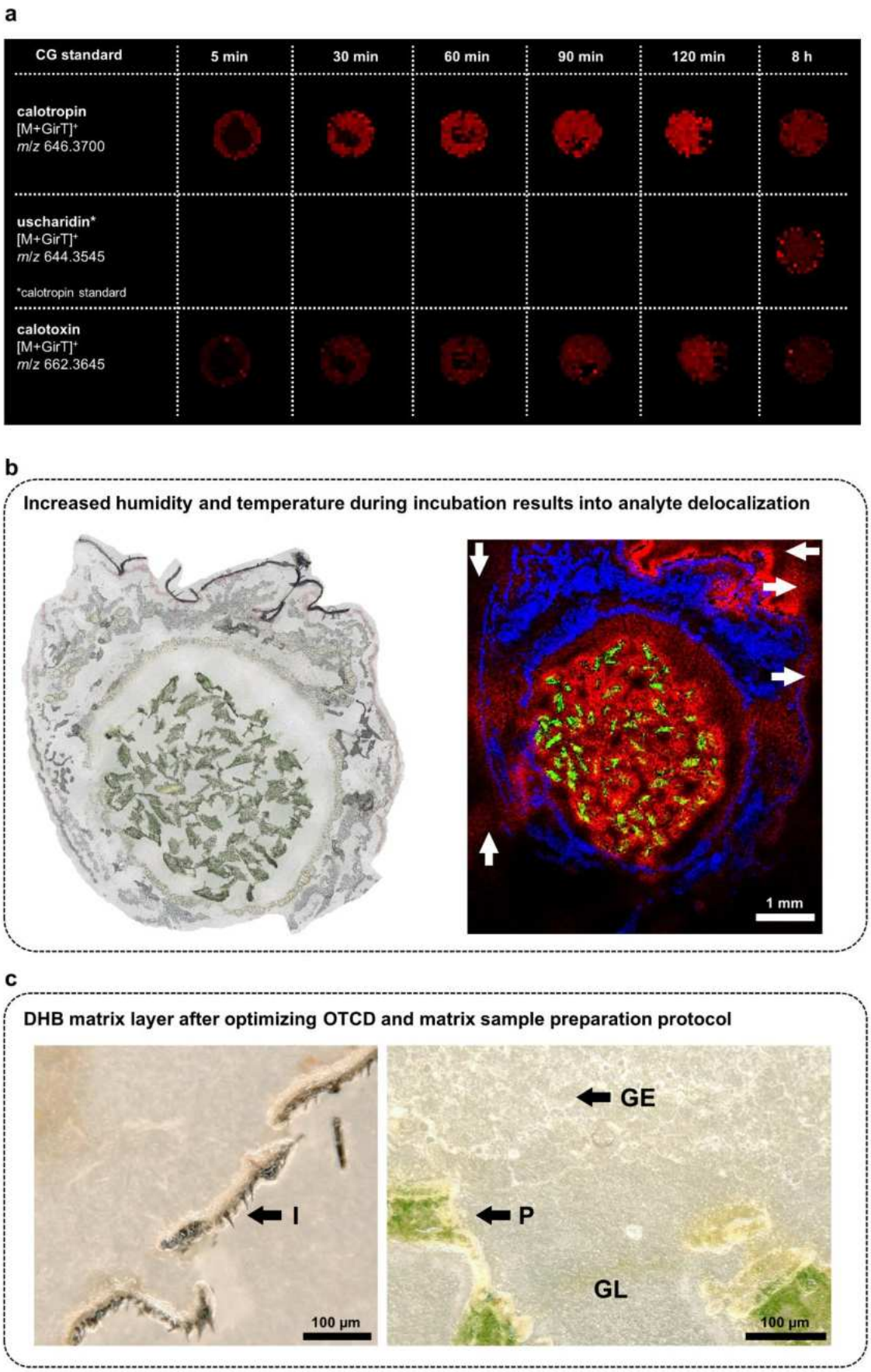


**Figure 9. Method development for high-resolution OTCD MALDI MSI of steroid glycosides.** (**a**) Dried-droplet MALDI MSI experiments of two derivatized cardiac glycoside standards (calotropin and calotoxin). A volume of 1 µL cardiac glycoside standard was spotted into reaction holes of a PTFE-coated glass slide. Subsequently, 1 µL of GirT-reagent (15 mg/mL) was added. After specific time intervals, the reaction was

quenched by adding 1 µL of DHB-matrix solution (30 mg/mL). The highest reaction yield was obtained after 120 minutes of incubation. After 8 hours, uscharidin was detected for the calotropin standard measurement, indicating oxidation of the respective species. Note that all reaction holes were measured simultaneously after the longest incubation time interval (8 hours). Thus, our data suggests that the chemical reaction is successfully quenched by adding the DHB matrix solution, which subsequently provides chemical preservation and inhibits the oxidation of derivatized cardiac glycosides (see time incubation intervals of ≤ 2 hours). (**b**) OTCD MALDI MSI of derivatized cardiac glycosides in *D. plexippus*. After GirT-reagent application (10 mg/ml in MeOH/water 7:3 v/v, 50 µL spray volume, 10 µL/min flowrate), the sample was incubated in a cell culture incubator (38°C, 100% relative humidity) for 2 hours. Optical image of transversal *D. plexippus* section before OTCD and matrix application and the corresponding RGB overlay image obtained with 25 µm step size shows the spatial distribution of calotropin/calactin in red ($[M+GirT]^+$ at *m*/*z* 646.3699), pheophytin a ($[M+K]^+$ at *m*/*z* 909.5291) in green and PS(18:1/18:2) ($[M+K]^+$ at *m*/*z* 810.5046) in blue. The extensive and leaked-out cardiac glycoside distribution at the integument indicates wash-out effects and analyte delocalization. (**c**) Optical images of longitudinal *D. plexippus* section (**a**) after OTCD and (b) after OTCD and matrix application. The optimized sample preparation protocol for OTCD (15 mg/ml GirT in MeOH/water 7:3 v/v, 35 µL spray volume, 7 µL/min flowrate) and matrix application (30 mg/ml DHB in MeOH/water 1:1 v/v, 100 µL spray volume, 5 µL/min flowrate) provides a homogenous matrix layer with crystal sizes of ≤ 10 µm, which is demonstrated for different surface characteristics including integument (I) plant material (P), gut lumen (GL) and gut epithelium (GE).

Using an ultrafine pneumatic spraying protocol for DHB as the MALDI matrix with methanol/water (1:1) v/v as solvent showed excellent results regarding homogenous matrix crystallization (crystal sizes ≤ 10 µm) for different surface characteristics of *D. plexippus* tissue sections, including fat tissue, digested plant material and integument (**Fig.9c**).

The applied workflow for OTCD MALDI MSI of cardiac glycosides for longitudinal *D. plexippus* sections is depicted in **Figure 10a**. As previously determined in the process of structural elucidation, the majority of detected cardiac glycosides are 19-oxosteroids having an aldehyde function at C19. Girard's reagent T is a quaternary ammonium salt that reacts with carbonyl-functions, resulting in hydrazine formation (**Fig.10b**). Subsequently, the derivatized analyte of interest contains a positively charged trimethylamine, which facilitates MSI analysis by increasing the ion yield and, thus, the sensitivity. To analyze and demonstrate the ion signal boost in detail, we also performed MSI experiments without OTCD, but with identical experimental parameters of the adjacent section. **Figure 10c** displays the optical images of the analyzed area consisting of gut lumen (GL) that contains *A. curassavica* plant material, surrounded by the gut epithelium (GE), fat tissue (FT), and integument (I). The corresponding MSI results for three selected ion signals are shown in red-green-blue (RGB) overlay images obtained with 25 µm step size. The toxic cardiac glycosides isomers calotropin and calactin are shown in red ($[M+K]^+$ for control, $[M+GirT]^+$ for OTCD). The green color channel highlights pheophytin a ($[M+K]^+$), which is characterized as a chlorophyll A molecule without the central $Mg^{2+}$ cation and is serving as a marker for plant material in the gut lumen. The spatial distribution of PS(36:3) ($[M+K]^+$) is shown in blue to highlight the gut epithelium and fat body tissue of the caterpillar. For OTCD, no additional adducts ($H^+$,$Na^+$,$K^+$) of cardiac glycosides were detected and derivatized ions were exclusively detected as GirT-carrying ions. Both RGB images are normalized to the same intensity scale to demonstrate that the average signal intensity of calotropin/calactin ($[M+GirT]^+$)

was increased by 16-fold relative to the [M+K]+ adduct, which was the dominant adduct for the control MSI experiment.

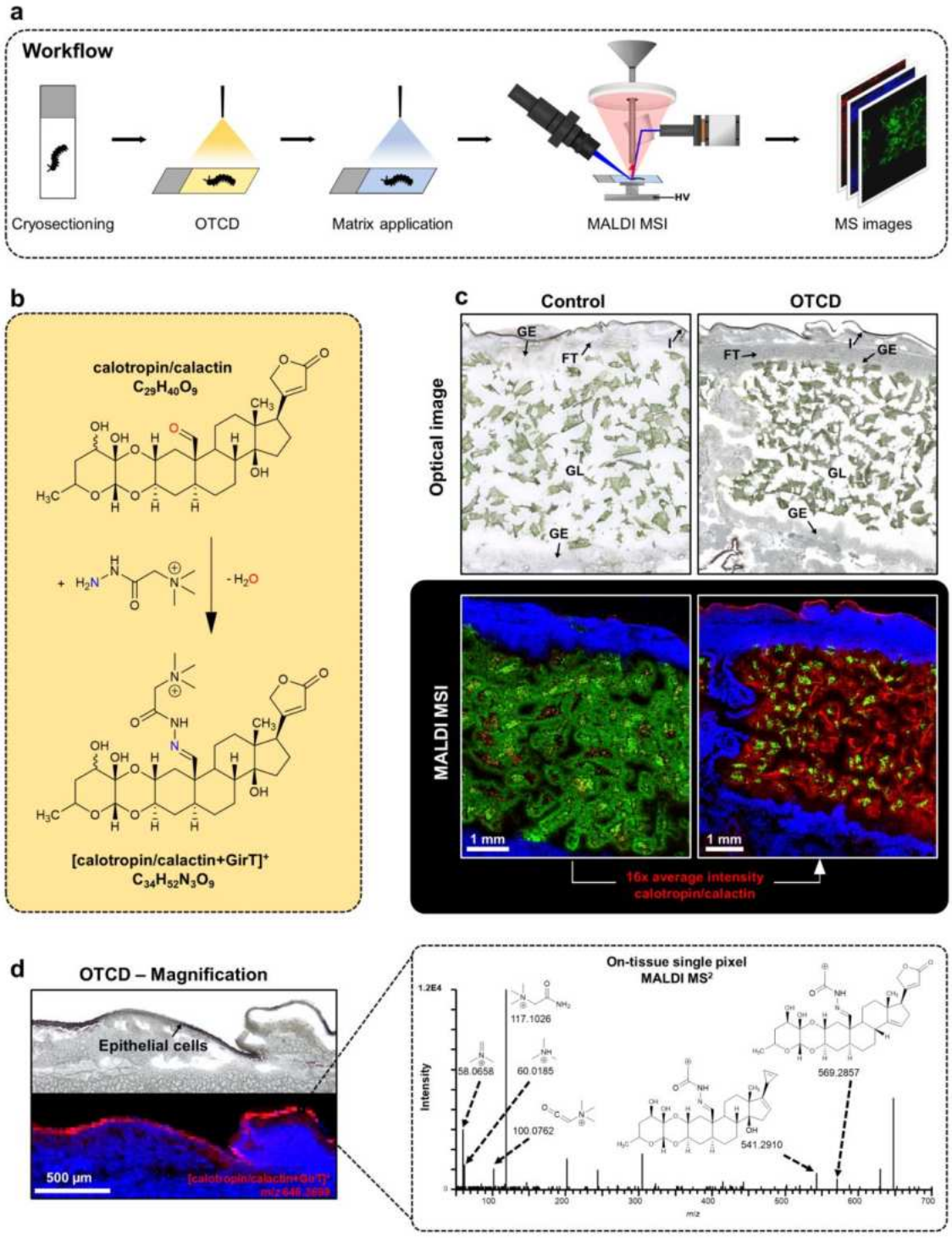


**Figure 10. High-resolution OTCD MALDI MSI of cardiac glycosides in longitudinal *D. plexippus* sections.** (**a**) Overview of the workflow for OTCD MALDI MSI (**b**) Schematic of the reaction between calotropin/calactin and GirT reagent. (**c**) Optical images of the analysed area showing the analysed area for conventional MALDI (left) and OTCD MALDI MSI (right). The corresponding RGB overlay images are normalized to the same intensity scale and show the spatial distribution of calotropin/calactin in red as $[M+K]^+$ at *m*/*z* 571.2306) for control (left) and $[M+GirT]^+$ at *m*/*z* 646.3699 for OTCD (right), pheophytin a as $[M+K]^+$ at *m*/*z* 909.5291) in green and PS(36:3) as $[M+K]^+$ at *m*/*z* 810.5046) in blue. (**d**) Magnified view for the integument area of the OTCD experiment highlighting the accumulation of the toxin in the epithelial cells of the integument. Corresponding OTCD MALDI $MS^2$ spectrum of calotropin/calactin as $[M+GirT]^+$ at *m*/*z* 646.3699) acquired from a single pixel at the *D. plexippus* integument. Six characteristic fragments are highlighted.

Consequently, OTCD MALDI MSI lowered the limit of detection for calotropin/calactin and increased the pixel coverage to 58% (14% for control). Therefore, OTCD MALDI MSI significantly improved the extracted biological information and vividly revealed that cardiac glycosides are extracted from the ingested plant material, absorbed into the gut epithelium and stored in the integument of the caterpillar. Importantly, derivatized cardiac glycosides preserved their spatial integrity, thus, allowing us to spatially resolve the fine distribution of the accumulated toxin in the single layer of epithelial cells in the integument (**Fig. 10d**). The enhanced ion signal intensities also enabled *in situ* identification of chemically derivatized cardiac glycosides via on-tissue single pixel MALDI $MS^2$ (**Fig. 10d**). By utilizing our 'in-house' metabolomic database, we annotated and visualized the spatial distribution for 19 derivatized cardiac glycosides – thus, demonstrating that our LC-MS-based molecular networking/AI-classification approach successfully guided and facilitated the spatial molecular characterization using MALDI MSI. The majority of cardiac glycosides are taken up and stored in the integument of the caterpillar (**Fig. 11a-e**). However, asclepin and hydroxyasclepin, which belong to the most abundant steroid glycosides in A. curassavica host plants, were not sequestered and instead were exclusively found in the gut lumen (**Fig.11f,g**). Thus, by utilizing OTCD MALDI MSI, we were able to comprehensively analyze cardiac glycoside distributions in *D. plexippus*, thereby demonstrating that small incremental changes in the chemical structure directly correlate to the selectivity of the underlying uptake- and transport mechanism.

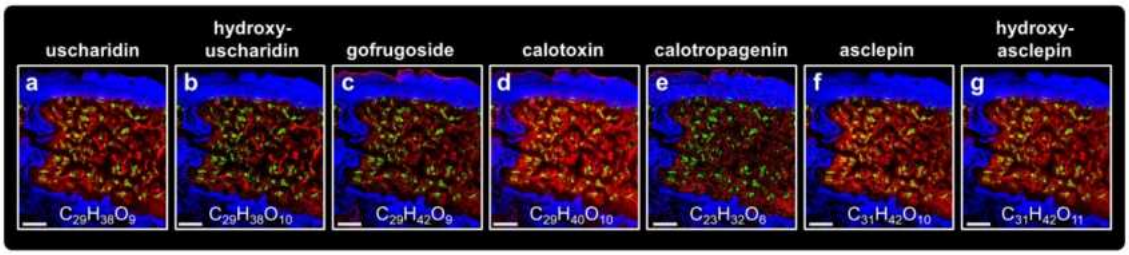


**Figure 11. OTCD MALDI MSI for cardiac glycosides that were annotated based on the 'in-house' metabolomic database.** RGB overlay images showing additional derivatized cardiac glycosides in red. (**a**) uscharidin ($[M+GirT]^+$, *m/z* 644.3541), (**b**) hydroxyuscharidin ($[M+GirT]^+$, *m/z* 660.3489), (**c**) gofrugoside ($[M+GirT]^+$, *m/z* 648.3828), (**d**) calotoxin/hydroxycalactin/hydroxycalotropin ($[M+GirT]^+$, *m/z* 662.3648), (**e**) calotropagenin ($[M+GirT]^+$, *m/z* 518.3233), (**f**) asclepin ($[M+GirT]^+$, *m/z* 688.3806), (**g**) hydroxyasclepin ($[M+GirT]^+$, *m/z* 704.3756). Scale bars, 1 mm.

To reveal specific molecular events and transport processes involved in cardiac glycoside sequestration, the spatially-resolved analysis has to approach (sub)-cellular resolution. However, using a smaller on-tissue laser focus diameter substantially decreases the ablated tissue volume, thus resulting in reduced ion numbers. Utilizing laser-induced post-ionization (MALDI-2) has been shown to enhance ion yields predominantly for lipids and various metabolite classes by several orders of magnitude over those of the used non-post-ionizing instrumentation. Yet, this approach requires

additional instrumentation, and no commercial instrument allows MALDI-2 MSI experiments performed with ≤ 5 µm step size. Therefore, our ultrafine OTCD MALDI MSI method serves as a powerful alternative for visualizing (sub)-cellular metabolite distributions by selectively increasing the ion yield and preserving spatial fidelity. We conducted OTCD MALDI MSI experiments with 5 µm step size of Malpighian tubules, which are multifunctional tissues involved in osmoregulation, renal excretion and the elimination of xenobiotics and metabolic waste from the hemolymph (i.e. body fluid of the caterpillar).[117]

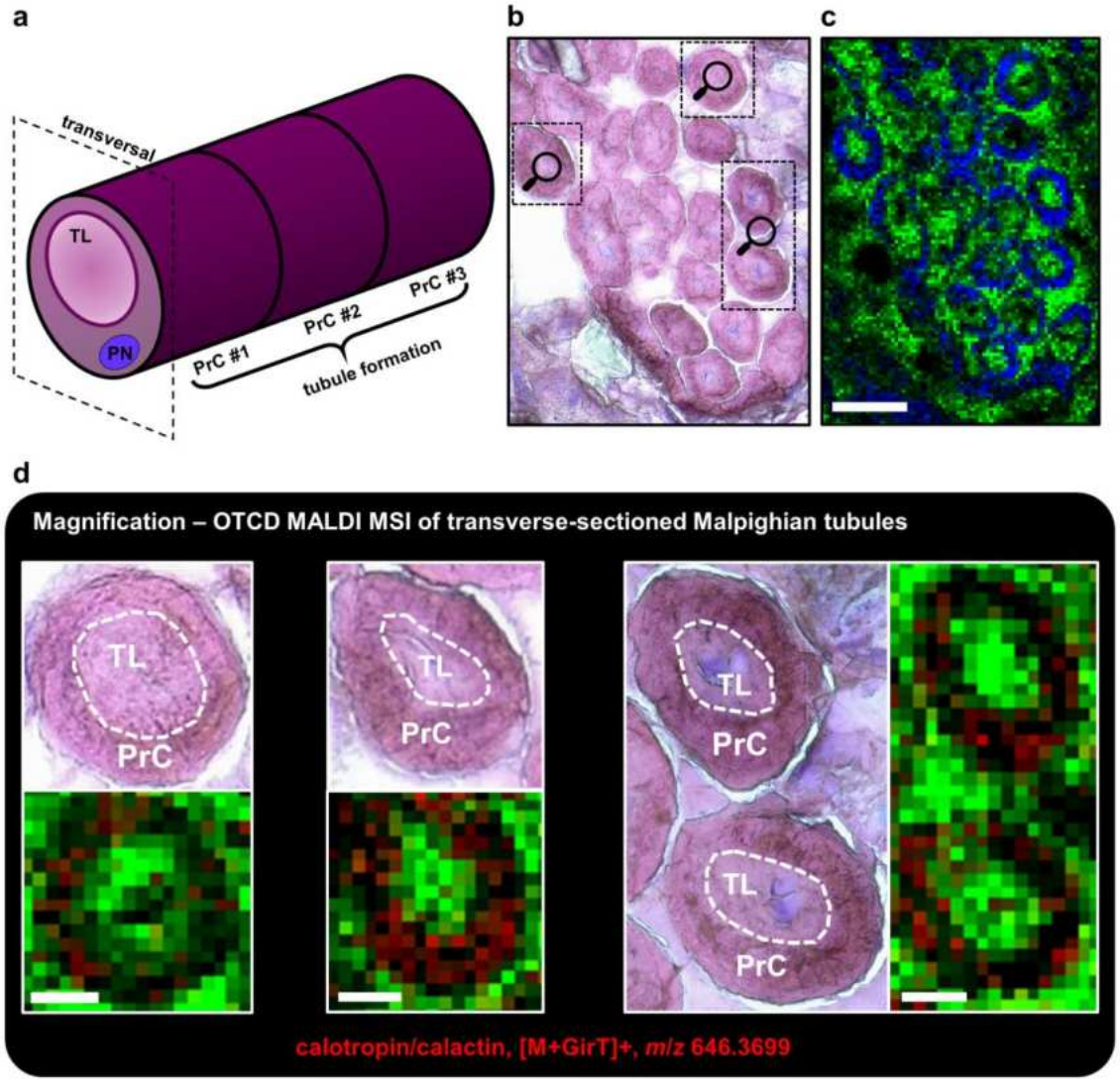


**Figure 12. OTCD MALDI MSI of derivatized cardiac glycosides, nucleotides and lipids at sub-cellular resolution in Malpighian tubules of *D. plexippus*.** (**a**) Simplified schematic showing the morphology of *D. plexippus* malpighian tubules. The principal cells fold upon itself to form a tubule lumen. PrC: principal cell; PN: principal cell nucleus; TL: tubule lumen. (**b**) Optical image of H&E-stained Malpighian tubules after MSI analysis. (**c**) Corresponding green-blue overlay image obtained with 5 µm step size showing the spatial distribution of thymidine 3',5'-hydrogen phosphate ($[M+K]^+$, *m/z* 343.0092, green) in the tubule lumen and GlcCer(47:5;O2) ($[M+H]^+$, *m/z* 874.7130, blue) in the principal cell of the tubule. (**d**) Magnifications of the highlighted areas displaying the morphology for transverse-sectioned Malpighian tubules and their corresponding red-green overlay images obtained with 5 µm step size, showing the spatial distribution of calotropin/calactin ($[M+GirT]^+$, *m/z* 646.3699, red) and thymidine 3',5'-hydrogen phosphate ($[M+K]^+$, *m/z* 343.0092, green). Scale bars, (**c**) 100 µm, (**d**) 25 µm.

Malpighian tubules consist of several principal cells (PrC) that fold upon itself to form a tubule lumen (TL) (**Fig. 12a**). The optical image of H&E-stained Malpighian tubules after MSI analysis is displayed in **Figure 12b**. The morphology of transverse-sectioned tubules can be reproduced by the OTCD MALDI MSI green-blue overlay image, showing the spatial distribution of thymidine 3',5'-hydrogen phosphate ($[M+K]^+$ at *m*/*z* 343.0092) in green and GlcCer(47:5) ($[M+H]^+$ at *m*/*z* 874.7130) in blue (**Fig. 12c**). The nucleotide derivative was primarily located in the tubule lumen and the surrounding tissue, whereas a broad variety of lipids from different lipid classes (e.g. PC, PE, PI, SM) were exclusively detected in the principal cells. **Figure 12d** displays detailed OTCD MALDI MSI results for individual Malpighian tubules (highlighted in **Fig. 12b**) with the red color channel showing the spatial distribution of derivatized calotropin/calactin ($[M+GirT]^+$ at *m*/*z* 646.3699). Interestingly, the cardiac glycoside was exclusively detected in the principal cells and not in the lumen of the tubules. However, the osmotic gradient in the Malpighian tubules causes water-soluble xenobiotics and metabolic waste from the hemolymph to diffuse. Therefore, our data suggests that cardiac glycosides are not part of the excretion pathways and instead are actively transported back to the hemolymph, which subsequently allows accumulation in the integument.

We next analyzed different physiological layers regarding cardiac glycoside uptake with 2 µm step size (**Fig. 13**). The analyzed region of interest consisted of the gut lumen (GL), peritrophic membrane (PM), ectoperitrophic space (EP), gut epithelium (GE) fat body (FB) and hemolymph (HL) (**Fig. 13a**). To highlight the fat body and gut epithelium, we utilized the lipid $[PE(44:1)+H]^+$ at *m*/*z* 858.6927, shown in green. Depicted in blue, we also found various sphingomyelin species (e.g. SM(29:5;O5)) showing specific lipid microdomains, which would most likely remain hidden with higher step sizes. In line with our previous MSI experiments, our data demonstrates that the majority of cardiac glycosides are sequestered (**Fig. 13b**), whereas dominant plant toxins, such as hydroxyasclepin are not taken up by the caterpillar (**Fig. 13c**). However, utilizing 2 µm step size, we were able to spatially-resolve the ectoperitrophic space (i.e. space between the peritrophic membrane and gut epithelium) to demonstrate that the peritrophic membrane, which was shown to restrict cardiac glycosides to the gut lumen of locusts[116], has no function regarding selectivity of cardiac glycosides in *D. plexippus.* In contrast to conventional MALDI MSI experiments, we were able to visualize sequestered cardiac glycosides in the fat body with increased accumulation in the outer layer of fat tissue (**Fig. 13d,e**). This observation was not made for other derivatized metabolites that have different chemical origin but similar polarities (**Fig. 13f**), thus, suggesting that these specific patterns along with other (sub)-cellular cardiac glycoside distributions were not caused by analyte delocalization during sample preparation.

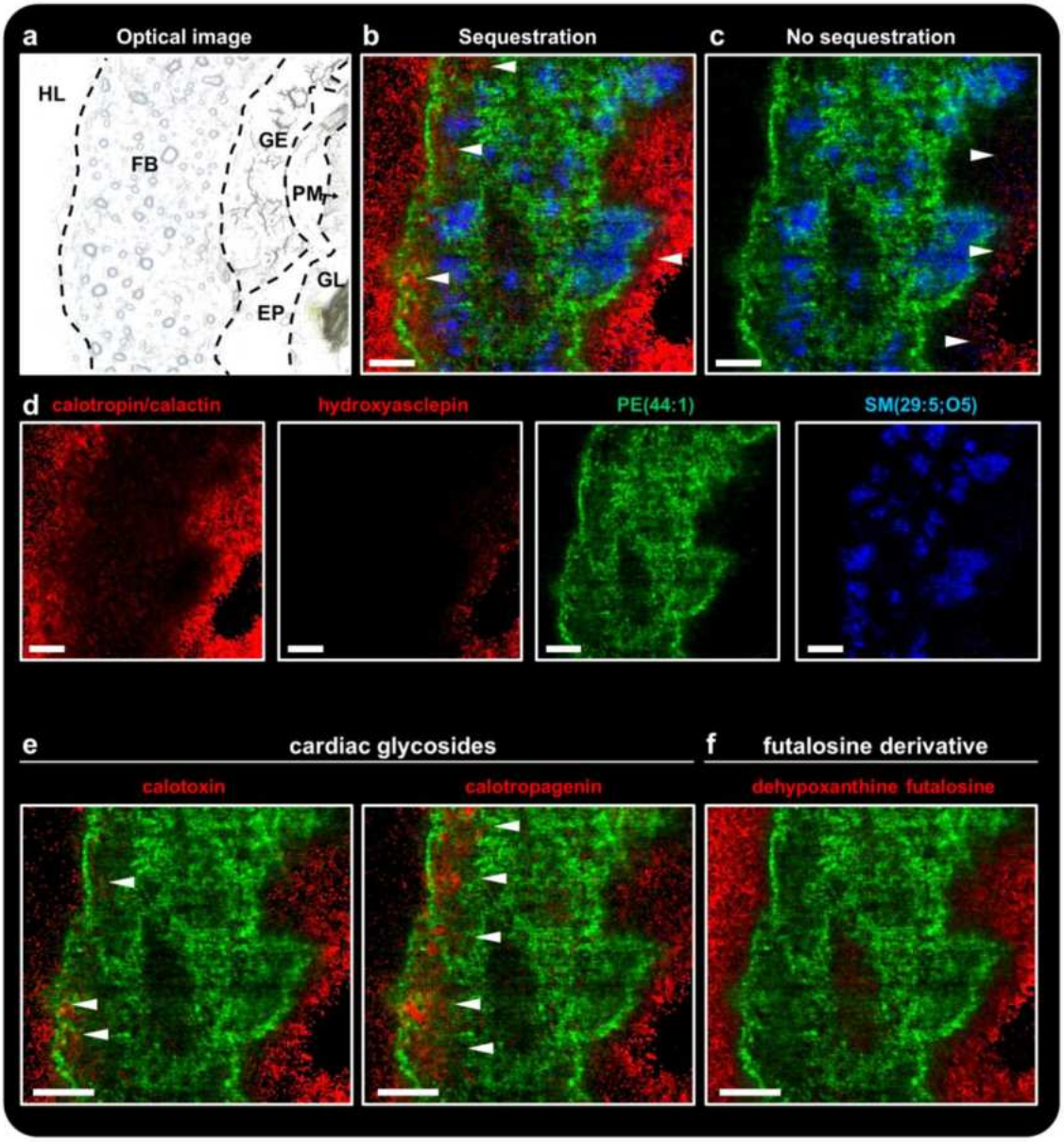


**Figure 13. OTCD MALDI MSI of derivatized metabolites and lipids at (sub)-cellular resolution to analyze cardiac glycoside uptake in *D. plexippus*.** (**a**) Optical image of the region of interest showing the hemolymph (HL), fat body (FB), gut epithelium (GE), ectoperitrophic space (EP), peritrophic membrane (PM) and gut lumen (GL). (**b**,**c**) Corresponding RGB overlay images obtained with 2 µm step size showing the spatial distribution of calotropin/calactin ($[M+GirT]^+$, *m*/*z* 646.3699, red) for (**b**), hydroxyasclepin ($[M+GirT]^+$, *m*/*z* 704.3754, red) for (**c**) and PE(44:1) ($[M+H]^+$, *m*/*z* 858.6927, green) and SM(29:5;O5) ($[M+Na]^+$, *m*/*z* 695.3991, blue) for (**b**,**c**). (**d**) Single ion images for the chemical compounds shown in the RGB overlay. (**e,f**) Red-green overlay images showing the spatial distribution for the derivatized isomers calotoxin/hydroxycalotropin/hydroxycalactin ($[M+GirT]^+$, *m*/*z* 662.3648) and calotropagenin ($[M+GirT]^+$, *m*/*z* 518.3233) in red and dehypoxanthine futalosine ([M+GirT]+, m/z 411.1986) in red; PE(46:3) ($[M+H]^+$, *m*/*z* 882.6922) in green. In contrast to cardiac glycosides, the derivatized futalosine species is not accumulated in the outer layer of the fat body tissue of the caterpillar. Scale bars, (**b**-**d**) 60 µm, (**e**,**f**) 70 µm.

## 1.4 Conclusion

Our spatially-resolved metabolomics approach exhibited diverging strategies regarding cardenolide processing in *D. plexippus* and *E. core*. By utilizing recent developments of the AP-SMALDI MSI technology, we revealed cardenolide distributions at unprecedented detail to provide novel insight into the selectivity and the mechanism of cardenolide sequestration. However, we encountered low intrinsic ionization efficiencies for cardenolides (i.e. steroid glycosides) and the absence of repository-scaled databases hindered comprehensive analysis of the complex metabolic network underlying cardenolide sequestration. We therefore combined LC-MS-based computational metabolome mining with sophisticated on-tissue chemistry MALDI MSI in a robust workflow to comprehensively explore and reveal spatial metabolomes at the cellular level. Our 'in-house' metabolomic database included 32 different cardiac glycosides. To the best of our knowledge, this is the highest number of detected cardiac glycosides for this milkweed species. Hence, we demonstrated the enormous potential of computational metabolomic approaches to decompose metabolic networks into molecular annotations and to successfully guide subsequent MSI analysis. To enhance MSI, we developed a spatial-context-preserving OTCD MSI method, enabling the visualization of previously inaccessible (sub)-cellular cardenolide distributions in various tissues of *D. plexippus*. Although primarily described here for carbonyl-containing steroid glycosides, many functional groups, such as phenols, thiols, amines, carboxylic acids, phosphate monoesters and alkenes can be targeted with different OTCD reagents to achieve increased ion yields and to force specific fragmentation patterns. Hence, our generic workflow represents a customizable method that can be applied to a wide range of spatially-resolved small molecule studies. Collectively, this thesis reports vital conceptual and methodological advances for applying MSI to investigate spatial biochemistry in insects and other complex tissues – thereby paving the way for a plethora of innovative applications, ranging from pharmacokinetic analysis of xenobiotics (e.g. insecticides) to other insect-plant or host-parasite interactions.

## 1.5 Future Work

Spatially-resolved isotope tracing allows to reveal the spatial organization of metabolic activities in tissues.[118] For our experimental design, integrating the spatially-resolved analysis of isotope-labeled cardenolides into the MSI workflow can provide detailed information regarding metabolic activities (e.g. reduced abundance of asclepin in the gut lumen) in monarch caterpillars. For *E. core*, this approach allows to elucidate molecular mechanisms of cardenolide detoxification in qualitative and quantitative fashion by determining degraded molecular products in the gut lumen of the caterpillar. In this

context, open-source software packages to analyze spectral variations of isotopic patterns based on MSI data were recently described.[118]

Developing a new acquisition mode for AP-SMALDI MSI, which enables MSI analysis to be performed in parallel with data-dependent acquisition (DDA) $MS^2$ would deliver deep molecular information for every pixel. Advanced data pre-processing tools, such as MZmine 3[119] already enable multimodal feature detection for DDA $MS^2$ data. Therefore, feature-based molecular networking combined with AI-driven chemical classification and -annotation can be integrated into MSI workflows to significantly increase the analytical depth while retaining spatial information.

In this context, our OTCD method selectively increased the sensitivity and enabled the acquisition of high-quality on-tissue MALDI $MS^2$ spectra for toxic steroid glycosides based on individual 25 $\mu m^2$ pixels. Thus, OTCD may facilitate these *in situ* molecular networking approaches (that rely on spectral similarity) not only by acquiring more $MS^2$ spectra of high quality, but also due to forcing specific fragmentation pathways that are characteristic for derivatized analytes of interest.

In conclusion, the additional work described above not only allows further interrogation of the complex biochemistry underlying plant toxin sequestration, but will also allow molecular identification solely based on MSI data for generating region-specific metabolomic atlases – therefore pushing MSI-based spatial metabolomics closer to the dimension of large-scale, shotgun-based omics approaches.

## References

(1) Jeong, H.; Tombor, B.; Albert, R.; Oltvai, Z. N.; Barabási, A.-L. The Large-Scale Organization of Metabolic Networks. *Nature* **2000**, *407* (6804), 651–654.

(2) Dräger, A.; Planatscher, H. Metabolic Networks BT - Encyclopedia of Systems Biology; Dubitzky, W., Wolkenhauer, O., Cho, K.-H., Yokota, H., Eds.; Springer New York: New York, NY, 2013; pp 1249–1251. https://doi.org/10.1007/978-1-4419-9863-7_1277.

(3) Petras, D.; Jarmusch, A. K.; Dorrestein, P. C. From Single Cells to Our Planet—Recent Advances in Using Mass Spectrometry for Spatially Resolved Metabolomics. *Curr. Opin. Chem. Biol.* **2017**, *36*, 24–31. https://doi.org/https://doi.org/10.1016/j.cbpa.2016.12.018.

(4) Lichtman, J. W.; Conchello, J.-A. Fluorescence Microscopy. *Nat. Methods* **2005**, *2* (12), 910–919. https://doi.org/10.1038/nmeth817.

(5) Zhang, Z.; Cheng, X.; Zhao, Y.; Yang, Y. Lighting up Live-Cell and in Vivo Central Carbon Metabolism with Genetically Encoded Fluorescent Sensors. *Annu. Rev. Anal. Chem* **2020**, *13*, 293–314.

(6) Spengler, B. Mass Spectrometry Imaging of Biomolecular Information. *Anal. Chem.* **2015**, *87* (1), 64–82. https://doi.org/10.1021/ac504543v.

(7) De Hoffmann, E.; Stroobant, V. *Mass Spectrometry: Principles and Applications*; John Wiley & Sons, 2007.

(8) Wien, W. Untersuchungen Über Die Electrische Entladung in Verdünnten Gasen. *Ann. Phys.* **1898**, *301* (6), 440–452.

(9) Thomson, J. J. Rays of Positive Electricity and Their Application to Chemical Analysis. The British Institute of Radiology 1914.

(10) Dempster, A. J. A New Method of Positive Ray Analysis. *Phys. Rev.* **1918**, *11* (4), 316.

(11) Aston, F. W. LXXIV. A Positive Ray Spectrograph. *London, Edinburgh, Dublin Philos. Mag. J. Sci.* **1919**, *38* (228), 707–714.

(12) Fenn, J. B.; Mann, M.; Meng, C. K.; Wong, S. F.; Whitehouse, C. M. Electrospray Ionization for Mass Spectrometry of Large Biomolecules. *Science (80-. ).* **1989**, *246* (4926), 64–71.

(13) Karas, M.; Hillenkamp, F. Laser Desorption Ionization of Proteins with Molecular Masses Exceeding 10,000 Daltons. *Anal. Chem.* **1988**, *60* (20), 2299–2301.

(14) Herzog, R. F. K.; Viehböck, F. P. Ion Source for Mass Spectrography. *Phys. Rev.* **1949**, *76* (6), 855.

(15) Dempster, A. J. Positive Ray Analysis of Lithium and Magnesium. *Phys. Rev.* **1921**, *18* (6), 415.

(16) Bleakney, W. A New Method of Positive Ray Analysis and Its Application to the Measurement of Ionization Potentials in Mercury Vapor. *Phys. Rev.* **1929**, *34* (1), 157.

(17) Widmaier, E. P.; Raff, H.; Strang, K. T. *Vander's Human Physiology*; McGraw-Hill New York, NY, 2006; Vol. 5.

(18) Munson, B. Chemical Ionization Mass Spectrometry. *Anal. Chem.* **1971**, *43* (13), 28A-43a.

(19) Takáts, Z.; Wiseman, J. M.; Gologan, B.; Cooks, R. G. Mass Spectrometry Sampling under Ambient Conditions with Desorption Electrospray Ionization. *Science (80-. ).* **2004**, *306* (5695), 471–473.

(20) Kebarle, P. A Brief Overview of the Present Status of the Mechanisms Involved in Electrospray Mass Spectrometry. *J. Mass Spectrom.* **2000**, *35* (7), 804–817. https://doi.org/https://doi.org/10.1002/1096-9888(200007)35:7<804::AID-JMS22>3.0.CO;2-Q.

(21) Paul, W.; Steinwedel, H. Ein Neues Massenspektrometer Ohne Magnetfeld. *Zeitschrift für Naturforsch. A* **1953**, *8* (7), 448–450.

(22) Stephens, W. E. A Pulsed Mass Spectrometer with Time Disaersion. *Phys. Rev.* **1946**, *69*, 691.

(23) Kofel, P.; Allemann, M.; Kellerhals, H. P.; Wanczek, K. P. External Generation of Ions in ICR Spectrometry. *Int. J. Mass Spectrom. Ion Process.* **1985**, *65* (1–2), 97–103.

(24) Comisarow, M. B.; Marshall, A. G. Fourier Transform Ion Cyclotron Resonance Spectroscopy. *Chem. Phys. Lett.* **1974**, *25* (2), 282–283.

(25) Kingdon, K. H. A Method for the Neutralization of Electron Space Charge by Positive Ionization at Very Low Gas Pressures. *Phys. Rev.* **1923**, *21* (4), 408.

(26) Knight, R. D. Storage of Ions from Laser-produced Plasmas. *Appl. Phys. Lett.* **1981**, *38* (4), 221–223.

(27) Makarov, A. Electrostatic Axially Harmonic Orbital Trapping: A High-Performance Technique of Mass Analysis. *Anal. Chem.* **2000**, *72* (6), 1156–1162.

(28) van Hove, E. R. A.; Smith, D. F.; Heeren, R. M. A. A Concise Review of Mass Spectrometry Imaging. *J. Chromatogr. A* **2010**, *1217* (25), 3946–3954.

(29) Buchberger, A. R.; DeLaney, K.; Johnson, J.; Li, L. Mass Spectrometry Imaging: A Review of Emerging Advancements and Future Insights. *Anal. Chem.* **2018**, *90* (1), 240–265. https://doi.org/10.1021/acs.analchem.7b04733.

(30) Spengler, B.; Hubert, M.; Kaufmann, R. MALDI Ion Imaging and Biological Ion Imaging with a New Scanning UV-Laser Microprobe. In *Proceedings of the 42nd Annual Conference on Mass Spectrometry and Allied Topics*; Chicago, 1994; Vol. 1041, p 1041.

(31) Gilmore, I. S.; Heiles, S.; Pieterse, C. L. Metabolic Imaging at the Single-Cell Scale: Recent Advances in Mass Spectrometry Imaging. *Annu. Rev. Anal. Chem.* **2019**, *12*, 201–224.

(32) Desiderio, D. M.; Nibbering, N. M.; Kraj, A. *Mass Spectrometry: Instrumentation, Interpretation, and Applications*; John Wiley & Sons, 2008.

(33) Calvano, C. D.; Monopoli, A.; Cataldi, T. R. I.; Palmisano, F. MALDI Matrices for Low Molecular Weight Compounds: An Endless Story? *Anal. Bioanal. Chem.* **2018**, *410*, 4015–4038.

(34) Strupat, K.; Karas, M.; Hillenkamp, F. 2, 5-Dihydroxybenzoic Acid: A New Matrix for Laser Desorption—Ionization Mass Spectrometry. *Int. J. Mass Spectrom. Ion Process.* **1991**, *111*, 89–102.

(35) Beavis, R. C.; Chaudhary, T.; Chait, B. T. α-Cyano-4-Hydroxycinnamic Acid as a Matrix for Matrixassisted Laser Desorption Mass Spectromtry. *Org. Mass Spectrom.* **1992**, *27* (2), 156–158. https://doi.org/https://doi.org/10.1002/oms.1210270217.

(36) Vermillion-Salsbury, R. L.; Hercules, D. M. 9-Aminoacridine as a Matrix for Negative Mode Matrix-assisted Laser Desorption/Ionization. *Rapid Commun. mass Spectrom.* **2002**, *16* (16), 1575–1581.

(37) Fukuyama, Y.; Iwamoto, S.; Tanaka, K. Rapid Sequencing and Disulfide Mapping of Peptides Containing Disulfide Bonds by Using 1, 5-diaminonaphthalene as a Reductive Matrix. *J. mass Spectrom.* **2006**, *41* (2), 191–201.

(38) Knochenmuss, R. A Quantitative Model of Ultraviolet Matrix-assisted Laser Desorption/Ionization. *J. Mass Spectrom.* **2002**, *37* (8), 867–877.

(39) Karas, M.; Krüger, R. Ion Formation in MALDI: The Cluster Ionization Mechanism. *Chem. Rev.* **2003**, *103* (2), 427–440.

(40) Dreisewerd, K. The Desorption Process in MALDI. *Chem. Rev.* **2003**, *103* (2), 395–426. https://doi.org/10.1021/cr010375i.

(41) Chu, K. Y.; Lee, S.; Tsai, M.-T.; Lu, I.-C.; Dyakov, Y. A.; Lai, Y. H.; Lee, Y.-T.; Ni, C.-K. Thermal Proton Transfer Reactions in Ultraviolet Matrix-Assisted Laser Desorption/Ionization. *J. Am. Soc. Mass Spectrom.* **2014**, *25* (3), 310–318.

(42) Laiko, V. V; Moyer, S. C.; Cotter, R. J. Atmospheric Pressure MALDI/Ion Trap Mass Spectrometry. *Anal. Chem.* **2000**, *72* (21), 5239–5243.

(43) Laiko, V. V; Baldwin, M. A.; Burlingame, A. L. Atmospheric Pressure Matrix-Assisted Laser Desorption/Ionization Mass Spectrometry. *Anal. Chem.* **2000**, *72* (4), 652–657.

(44) Moyer, S. C.; Cotter, R. J. Peer Reviewed: Atmospheric Pressure MALDI. *Anal. Chem.* **2002**, *74* (17), 468-A.

(45) Spengler, B.; Hubert, M. Scanning Microprobe Matrix-Assisted Laser Desorption Ionization (SMALDI) Mass Spectrometry: Instrumentation for Sub-Micrometer Resolved LDI and MALDI Surface Analysis. *J. Am. Soc. Mass Spectrom.* **2002**, *13* (6), 735–748.

(46) Koestler, M.; Kirsch, D.; Hester, A.; Leisner, A.; Guenther, S.; Spengler, B. A High-resolution Scanning Microprobe Matrix-assisted Laser Desorption/Ionization Ion Source for Imaging Analysis on an Ion Trap/Fourier Transform Ion Cyclotron Resonance Mass Spectrometer. *Rapid Commun. Mass Spectrom. An Int. J. Devoted to Rapid Dissem. Up-to-the-Minute Res. Mass Spectrom.* **2008**, *22* (20), 3275–3285.

(47) Kompauer, M.; Heiles, S.; Spengler, B. Autofocusing MALDI Mass Spectrometry Imaging of Tissue Sections and 3D Chemical Topography of Nonflat Surfaces. *Nat. Methods* **2017**, *14* (12), 1156–1158.

(48) Kompauer, M.; Heiles, S.; Spengler, B. Atmospheric Pressure MALDI Mass Spectrometry Imaging of Tissues and Cells at 1.4-Mm Lateral Resolution. *Nat. Methods* **2017**, *14* (1), 90–96. https://doi.org/10.1038/nmeth.4071.

(49) Ellis, S. R.; Paine, M. R. L.; Eijkel, G. B.; Pauling, J. K.; Husen, P.; Jervelund, M. W.; Hermansson, M.; Ejsing, C. S.; Heeren, R. M. A. Automated, Parallel Mass Spectrometry Imaging and Structural Identification of Lipids. *Nat. Methods* **2018**, *15* (7), 515–518.

(50) Khalil, S. M.; Sprenger, R. R.; Hermansson, M.; Ejsing, C. S. DDA-imaging with Structural Identification of Lipid Molecules on an Orbitrap Velos Pro Mass Spectrometer. *J. Mass Spectrom.* **2022**, *57* (9), e4882.

(51) Alexandrov, T.; Ovchinnikova, K.; Palmer, A.; Kovalev, V.; Tarasov, A.; Stuart, L.; Nigmetzianov, R.; Fay, D.; contributors, K. M.; Gaudin, M. METASPACE: A Community-Populated Knowledge Base of Spatial Metabolomes in Health and Disease. *BioRxiv* **2019**, 539478.

(52) Palmer, A.; Phapale, P.; Chernyavsky, I.; Lavigne, R.; Fay, D.; Tarasov, A.; Kovalev, V.; Fuchser, J.; Nikolenko, S.; Pineau, C. FDR-Controlled Metabolite Annotation for High-Resolution Imaging Mass Spectrometry. *Nat. Methods* **2017**,

*14* (1), 57–60.

(53) Vinaixa, M.; Schymanski, E. L.; Neumann, S.; Navarro, M.; Salek, R. M.; Yanes, O. Mass Spectral Databases for LC/MS-and GC/MS-Based Metabolomics: State of the Field and Future Prospects. *TrAC Trends Anal. Chem.* **2016**, *78*, 23–35.

(54) Kind, T.; Tsugawa, H.; Cajka, T.; Ma, Y.; Lai, Z.; Mehta, S. S.; Wohlgemuth, G.; Barupal, D. K.; Showalter, M. R.; Arita, M. Identification of Small Molecules Using Accurate Mass MS/MS Search. *Mass Spectrom. Rev.* **2018**, *37* (4), 513–532.

(55) Montenegro-Burke, J. R.; Guijas, C.; Siuzdak, G. METLIN: A Tandem Mass Spectral Library of Standards. In *Computational Methods and Data Analysis for Metabolomics*; Springer, 2020; pp 149–163.

(56) Beniddir, M. A.; Kang, K. Bin; Genta-Jouve, G.; Huber, F.; Rogers, S.; Van Der Hooft, J. J. J. Advances in Decomposing Complex Metabolite Mixtures Using Substructure-and Network-Based Computational Metabolomics Approaches. *Nat. Prod. Rep.* **2021**, *38* (11), 1967–1993.

(57) Ramos, A. E. F.; Evanno, L.; Poupon, E.; Champy, P.; Beniddir, M. A. Natural Products Targeting Strategies Involving Molecular Networking: Different Manners, One Goal. *Nat. Prod. Rep.* **2019**, *36* (7), 960–980.

(58) Wang, M.; Carver, J. J.; Phelan, V. V; Sanchez, L. M.; Garg, N.; Peng, Y.; Nguyen, D. D.; Watrous, J.; Kapono, C. A.; Luzzatto-Knaan, T. Sharing and Community Curation of Mass Spectrometry Data with Global Natural Products Social Molecular Networking. *Nat. Biotechnol.* **2016**, *34* (8), 828–837.

(59) Watrous, J.; Roach, P.; Alexandrov, T.; Heath, B. S.; Yang, J. Y.; Kersten, R. D.; van der Voort, M.; Pogliano, K.; Gross, H.; Raaijmakers, J. M. Mass Spectral Molecular Networking of Living Microbial Colonies. *Proc. Natl. Acad. Sci.* **2012**, *109* (26), E1743–E1752.

(60) Nothias, L.-F.; Petras, D.; Schmid, R.; Dührkop, K.; Rainer, J.; Sarvepalli, A.; Protsyuk, I.; Ernst, M.; Tsugawa, H.; Fleischauer, M. Feature-Based Molecular Networking in the GNPS Analysis Environment. *Nat. Methods* **2020**, *17* (9), 905–908.

(61) Feunang, Y. D.; Eisner, R.; Knox, C.; Chepelev, L.; Hastings, J.; Owen, G.; Fahy, E.; Steinbeck, C.; Subramanian, S.; Bolton, E. ClassyFire: Automated Chemical Classification with a Comprehensive, Computable Taxonomy. *J. Cheminform.* **2016**, *8* (1), 1–20.

(62) Dührkop, K.; Fleischauer, M.; Ludwig, M.; Aksenov, A. A.; Melnik, A. V; Meusel, M.; Dorrestein, P. C.; Rousu, J.; Böcker, S. SIRIUS 4: A Rapid Tool for Turning Tandem Mass Spectra into Metabolite Structure Information. *Nat. Methods* **2019**, *16* (4), 299–302.

(63) Dührkop, K.; Nothias, L.-F.; Fleischauer, M.; Reher, R.; Ludwig, M.; Hoffmann, M. A.; Petras, D.; Gerwick, W. H.; Rousu, J.; Dorrestein, P. C. Systematic Classification of Unknown Metabolites Using High-Resolution Fragmentation Mass Spectra. *Nat. Biotechnol.* **2021**, *39* (4), 462–471.

(64) Dührkop, K.; Shen, H.; Meusel, M.; Rousu, J.; Böcker, S. Searching Molecular Structure Databases with Tandem Mass Spectra Using CSI: FingerID. *Proc. Natl. Acad. Sci.* **2015**, *112* (41), 12580–12585.

(65) Harkin, C.; Smith, K. W.; Cruickshank, F. L.; Logan Mackay, C.; Flinders, B.; Heeren, R. M. A.; Moore, T.; Brockbank, S.; Cobice, D. F. On-Tissue Chemical Derivatization in Mass Spectrometry Imaging. *Mass Spectrom. Rev.* **2021**, *n/a* (n/a). https://doi.org/https://doi.org/10.1002/mas.21680.

(66) Soltwisch, J.; Jaskolla, T. W.; Hillenkamp, F.; Karas, M.; Dreisewerd, K. Ion Yields in UV-MALDI Mass Spectrometry as a Function of Excitation Laser Wavelength and Optical and Physico-Chemical Properties of Classical and Halogen-Substituted MALDI Matrixes. *Anal. Chem.* **2012**, *84* (15), 6567–6576.

(67) Niehaus, M.; Schnapp, A.; Koch, A.; Soltwisch, J.; Dreisewerd, K. New Insights into the Wavelength Dependence of MALDI Mass Spectrometry. *Anal. Chem.* **2017**, *89* (14), 7734–7741. https://doi.org/10.1021/acs.analchem.7b01744.

(68) Soltwisch, J.; Kettling, H.; Vens-Cappell, S.; Wiegelmann, M.; Müthing, J.; Dreisewerd, K. Mass Spectrometry Imaging with Laser-Induced Postionization. *Science (80-. ).* **2015**, *348* (6231), 211–215.

(69) Niehaus, M.; Soltwisch, J.; Belov, M. E.; Dreisewerd, K. Transmission-Mode MALDI-2 Mass Spectrometry Imaging of Cells and Tissues at Subcellular Resolution. *Nat. Methods* **2019**, *16* (9), 925–931. https://doi.org/10.1038/s41592-019-0536-2.

(70) Soltwisch, J.; Heijs, B.; Koch, A.; Vens-Cappell, S.; Höhndorf, J.; Dreisewerd, K. MALDI-2 on a Trapped Ion Mobility Quadrupole Time-of-Flight Instrument for Rapid Mass Spectrometry Imaging and Ion Mobility Separation of Complex Lipid Profiles. *Anal. Chem.* **2020**, *92* (13), 8697–8703.

(71) Spengler, B.; Luetzenkirchen, F.; Metzger, S.; Chaurand, P.; Kaufmann, R.; Jeffery, W.; Bartlet-Jones, M.; Pappin, D. J. C. Peptide Sequencing of Charged Derivatives by Postsource Decay MALDI Mass Spectrometry. *Int. J. Mass Spectrom. Ion Process.* **1997**, *169–170*, 127–140. https://doi.org/https://doi.org/10.1016/S0168-1176(97)00218-8.

(72) Higashi, T.; Yamauchi, A.; Shimada, K. 2-Hydrazino-1-Methylpyridine: A Highly Sensitive Derivatization Reagent for Oxosteroids in Liquid Chromatography–Electrospray Ionization-Mass Spectrometry. *J. Chromatogr. B* **2005**, *825* (2), 214–222.

(73) Zaikin, V. G.; Halket, J. M. Derivatization in Mass Spectrometry—8. Soft Ionization Mass Spectrometry of Small Molecules. *Eur. J. Mass Spectrom.* **2006**, *12* (2), 79–115.

(74) Shariatgorji, M.; Nilsson, A.; Fridjonsdottir, E.; Vallianatou, T.; Källback, P.; Katan, L.; Sävmarker, J.; Mantas, I.; Zhang, X.; Bezard, E. Comprehensive Mapping of Neurotransmitter Networks by MALDI–MS Imaging. *Nat. Methods* **2019**, *16* (10), 1021–1028.

(75) Wäldchen, F.; Mohr, F.; Wagner, A. H.; Heiles, S. Multifunctional Reactive MALDI Matrix Enabling High-Lateral Resolution Dual Polarity MS Imaging and Lipid C= C Position-Resolved MS2 Imaging. *Anal. Chem.* **2020**, *92* (20), 14130–14138.

(76) Beasley, E.; Francese, S.; Bassindale, T. Detection and Mapping of Cannabinoids in Single Hair Samples through Rapid Derivatization and Matrix-Assisted Laser Desorption Ionization Mass Spectrometry. *Anal. Chem.* **2016**, *88* (20), 10328–10334.

(77) Chacon, A.; Zagol-Ikapitte, I.; Amarnath, V.; Reyzer, M. L.; Oates, J. A.; Caprioli, R. M.; Boutaud, O. On-Tissue Chemical Derivatization of 3-Methoxysalicylamine for MALDI-Imaging Mass Spectrometry. *J. Mass Spectrom.* **2011**, *46* (8), 840–846. https://doi.org/https://doi.org/10.1002/jms.1958.

(78) Wäldchen, F.; Spengler, B.; Heiles, S. Reactive Matrix-Assisted Laser Desorption/Ionization Mass Spectrometry Imaging Using an Intrinsically Photoreactive Paterno–Buchi Matrix for Double-Bond Localization in Isomeric Phospholipids. *J. Am. Chem. Soc.* **2019**, *141* (30), 11816–11820.

(79) Wu, Q.; Comi, T. J.; Li, B.; Rubakhin, S. S.; Sweedler, J. V. On-Tissue Derivatization via Electrospray Deposition for Matrix-Assisted Laser Desorption/Ionization Mass Spectrometry Imaging of Endogenous Fatty Acids in Rat Brain Tissues. *Anal. Chem.* **2016**, *88* (11), 5988–5995.

(80) Djidja, M.; Francese, S.; Loadman, P. M.; Sutton, C. W.; Scriven, P.; Claude, E.; Snel, M. F.; Franck, J.; Salzet, M.; Clench, M. R. Detergent Addition to Tryptic Digests and Ion Mobility Separation Prior to MS/MS Improves Peptide Yield and Protein Identification for in Situ Proteomic Investigation of Frozen and Formalin-fixed Paraffin-embedded Adenocarcinoma Tissue Sections. *Proteomics* **2009**, *9* (10), 2750–2763.

(81) Shariatgorji, M.; Nilsson, A.; Goodwin, R. J. A.; Källback, P.; Schintu, N.; Zhang, X.; Crossman, A. R.; Bezard, E.; Svenningsson, P.; Andren, P. E. Direct Targeted Quantitative Molecular Imaging of Neurotransmitters in Brain Tissue Sections. *Neuron* **2014**, *84* (4), 697–707.

(82) Cobice, D. F.; Livingstone, D. E. W.; Mackay, C. L.; Goodwin, R. J. A.; Smith, L. B.; Walker, B. R.; Andrew, R. Spatial Localization and Quantitation of Androgens in Mouse Testis by Mass Spectrometry Imaging. *Anal. Chem.* **2016**, *88* (21), 10362–10367. https://doi.org/10.1021/acs.analchem.6b02242.

(83) Takeo, E.; Sugiura, Y.; Uemura, T.; Nishimoto, K.; Yasuda, M.; Sugiyama, E.; Ohtsuki, S.; Higashi, T.; Nishikawa, T.; Suematsu, M.; Fukusaki, E.; Shimma, S. Tandem Mass Spectrometry Imaging Reveals Distinct Accumulation Patterns of Steroid Structural Isomers in Human Adrenal Glands. *Anal. Chem.* **2019**, *91* (14), 8918–8925. https://doi.org/10.1021/acs.analchem.9b00619.

(84) Barré, F. P. Y.; Flinders, B.; Garcia, J. P.; Jansen, I.; Huizing, L. R. S.; Porta, T.; Creemers, L. B.; Heeren, R. M. A.; Cillero-Pastor, B. Derivatization Strategies for the Detection of Triamcinolone Acetonide in Cartilage by Using Matrix-Assisted Laser Desorption/Ionization Mass Spectrometry Imaging. *Anal. Chem.* **2016**, *88* (24), 12051–12059. https://doi.org/10.1021/acs.analchem.6b02491.

(85) Cobice, D. F.; Mackay, C. L.; Goodwin, R. J. A.; McBride, A.; Langridge-Smith, P. R.; Webster, S. P.; Walker, B. R.; Andrew, R. Mass Spectrometry Imaging for Dissecting Steroid Intracrinology within Target Tissues. *Anal. Chem.* **2013**, *85* (23), 11576–11584. https://doi.org/10.1021/ac402777k.

(86) Dussourd, D. E.; Hoyle, A. M. Poisoned Plusiines: Toxicity of Milkweed Latex and Cardenolides to Some Generalist Caterpillars. *Chemoecology* **2000**, *10* (1), 11–16. https://doi.org/10.1007/PL00001810.

(87) Narberhaus, I.; Zintgraf, V.; Dobler, S. Pyrrolizidine Alkaloids on Three Trophic Levels–Evidence for Toxic and Deterrent Effects on Phytophages and Predators. *Chemoecology* **2005**, *15* (2), 121–125.

(88) Cresswell, J. E.; Merritt, S. Z.; Martin, M. M. The Effect of Dietary Nicotine on the Allocation of Assimilated Food to Energy Metabolism and Growth in Fourth-Instar Larvae of the Southern Armyworm, Spodoptera Eridania (Lepidoptera: Noctuidae). *Oecologia* **1992**, *89* (3), 449–453.

(89) Koiwa, H.; Bressan, R. A.; Hasegawa, P. M. Regulation of Protease Inhibitors and Plant Defense. *Trends Plant Sci.* **1997**, *2* (10), 379–384.

(90) Beran, F.; Petschenka, G. Sequestration of Plant Defense Compounds by Insects: From Mechanisms to Insect–Plant Coevolution. *Annu. Rev. Entomol.* **2022**, *67* (1), 163–180. https://doi.org/10.1146/annurev-ento-062821-062319.

(91) Duffey, S. S. Sequestration of Plant Natural Products by Insects. *Annu. Rev. Entomol.* **1980**, *25* (1), 447–477.

(92) Opitz, S. E. W.; Müller, C. Plant Chemistry and Insect Sequestration. *Chemoecology* **2009**, *19* (3), 117–154.

(93) Beran, F.; Pauchet, Y.; Kunert, G.; Reichelt, M.; Wielsch, N.; Vogel, H.; Reinecke, A.; Svatoš, A.; Mewis, I.; Schmid, D.; Ramasamy, S.; Ulrichs, C.; Hansson, B. S.; Gershenzon, J.; Heckel, D. G. <Em>Phyllotreta Striolata</Em> Flea Beetles Use Host Plant Defense Compounds to Create Their Own Glucosinolate-Myrosinase System. *Proc. Natl. Acad. Sci.* **2014**, *111* (20), 7349 LP – 7354. https://doi.org/10.1073/pnas.1321781111.

(94) Kazana, E.; Pope, T. W.; Tibbles, L.; Bridges, M.; Pickett, J. A.; Bones, A. M.; Powell, G.; Rossiter, J. T. The Cabbage Aphid: A Walking Mustard Oil Bomb. *Proc. R. Soc. B Biol. Sci.* **2007**, *274* (1623), 2271–2277. https://doi.org/10.1098/rspb.2007.0237.

(95) Yang, Z.-L.; Nour-Eldin, H. H.; Hänniger, S.; Reichelt, M.; Crocoll, C.; Seitz, F.; Vogel, H.; Beran, F. Sugar Transporters Enable a Leaf Beetle to Accumulate Plant Defense Compounds. *Nat. Commun.* **2021**, *12* (1), 2658. https://doi.org/10.1038/s41467-021-22982-8.

(96) A., A. A.; Katalin, B.; Meena, H.; P., H. A.; A., W. R.; Ren-Wang, J.; Christophe, D. Cardenolides, Toxicity, and the Costs of Sequestration in the Coevolutionary Interaction between Monarchs and Milkweeds. *Proc. Natl. Acad. Sci.* **2021**, *118* (16), e2024463118. https://doi.org/10.1073/pnas.2024463118.

(97) Karageorgi, M.; Groen, S. C.; Sumbul, F.; Pelaez, J. N.; Verster, K. I.; Aguilar, J. M.; Hastings, A. P.; Bernstein, S. L.; Matsunaga, T.; Astourian, M.; Guerra, G.; Rico, F.; Dobler, S.; Agrawal, A. A.; Whiteman, N. K. Genome Editing Retraces the Evolution of Toxin Resistance in the Monarch Butterfly. *Nature* **2019**, *574* (7778), 409–412. https://doi.org/10.1038/s41586-019-1610-8.

(98) Petschenka, G.; Agrawal, A. A. Milkweed Butterfly Resistance to Plant Toxins Is Linked to Sequestration, Not Coping with a Toxic Diet. *Proc. R. Soc. B Biol. Sci.* **2015**, *282* (1818), 20151865.

(99) Brower, L. P.; Ryerson, W. N.; Coppinger, L. L.; Glazier, S. C. Ecological Chemistry and the Palatability Spectrum. *Science (80-. ).* **1968**, *161* (3848), 1349–1350.

(100) Frick, C.; Wink, M. Uptake and Sequestration of Ouabain and Other Cardiac Glycosides in Danaus Plexippus (Lepidoptera: Danaidae): Evidence for a Carrier-Mediated Process. *J. Chem. Ecol.* **1995**, *21* (5), 557–575.

(101) Agrawal, A. A.; Petschenka, G.; Bingham, R. A.; Weber, M. G.; Rasmann, S. Toxic Cardenolides: Chemical Ecology and Coevolution of Specialized Plant–Herbivore Interactions. *New Phytol.* **2012**, *194* (1), 28–45. https://doi.org/https://doi.org/10.1111/j.1469-8137.2011.04049.x.

(102) Schatzmann, H. J. Herzglykoside Als Hemmstoffe Fur Den Activen Kalium Und Natrium-Transport Durch Die Erythrocytemembran. *Helv. physiol. pharmacol. Acta* **1953**, *11*, 346–354.

(103) Petschenka, G.; Offe, J. K.; Dobler, S. Physiological Screening for Target Site Insensitivity and Localization of Na+/K+-ATPase in Cardenolide-Adapted Lepidoptera. *J. Insect Physiol.* **2012**, *58* (5), 607–612. https://doi.org/https://doi.org/10.1016/j.jinsphys.2011.12.012.

(104) Holzinger, F.; Wink, M. Mediation of Cardiac Glycoside Insensitivity in the Monarch Butterfly (Danaus Plexippus): Role of an Amino Acid Substitution in the Ouabain Binding Site of Na+, K+-ATPase. *J. Chem. Ecol.* **1996**, *22* (10), 1921–1937.

(105) Vaughan, G. L.; Jungreis, A. M. Insensitivity of Lepidopteran Tissues to Ouabain: Physiological Mechanisms for Protection from Cardiac Glycosides. *J. Insect Physiol.* **1977**, *23* (5), 585–589.

(106) Petschenka, G.; Fandrich, S.; Sander, N.; Wagschal, V.; Boppré, M.; Dobler, S. Stepwise Evolution of Resistance to Toxic Cardenolides via Genetic Substitutions in the Na+/K+-ATPase of Milkweed Butterflies (Lepidoptera: Danaini). *Evolution (N. Y).* **2013**, *67* (9), 2753–2761.

(107) Dobler, S.; Dalla, S.; Wagschal, V.; Agrawal, A. A. Community-Wide Convergent Evolution in Insect Adaptation to Toxic Cardenolides by Substitutions in the Na, K-ATPase. *Proc. Natl. Acad. Sci.* **2012**, *109* (32), 13040–13045.

(108) Dobler, S.; Petschenka, G.; Wagschal, V.; Flacht, L. Convergent Adaptive Evolution – How Insects Master the Challenge of Cardiac Glycoside-Containing Host Plants. *Entomol. Exp. Appl.* **2015**, *157* (1), 30–39. https://doi.org/https://doi.org/10.1111/eea.12340.

(109) Malcom, S.; Rothschild, M. A Danaid Mullerian Mimic, Euploea Core Amymone (Cramer) Lacking Cardenolides in the Pupal and Adult Stages. *Biol. J. Linn. Soc.* **1983**, *19* (1), 27–33. https://doi.org/10.1111/j.1095-8312.1983.tb00774.x.

(110) Zhang, R.-R.; Tian, H.-Y.; Tan, Y.-F.; Chung, T.-Y.; Sun, X.-H.; Xia, X.; Ye, W.-C.; Middleton, D. A.; Fedosova, N.; Esmann, M.; Tzen, J. T. C.; Jiang, R.-W. Structures, Chemotaxonomic Significance, Cytotoxic and Na+,K+-ATPase Inhibitory Activities of New Cardenolides from Asclepias Curassavica. *Org. Biomol. Chem.* **2014**, *12* (44), 8919–8929. https://doi.org/10.1039/C4OB01545B.

(111) Petschenka, G.; Fei, C. S.; Araya, J. J.; Schröder, S.; Timmermann, B. N.; Agrawal, A. A. Relative Selectivity of Plant Cardenolides for Na+/K+-ATPases from the Monarch Butterfly and Non-Resistant Insects. *Front. Plant Sci.* **2018**, *9*, 1424.

(112) Marty, M. A.; Krieger, R. I. Metabolism of Uscharidin, a Milkweed Cardenolide, by Tissue Homogenates of Monarch Butterfly Larvae, Danaus Plexippus L. *J. Chem. Ecol.* **1984**, *10* (6), 945–956.

(113) Seiber, J. N.; Tuskes, P. M.; Brower, L. P.; Nelson, C. J. Pharmacodynamics of

Some Individual Milkweed Cardenolides Fed to Larvae of the Monarch Butterfly (Danaus Plexippus L.). *J. Chem. Ecol.* **1980**, *6* (2), 321–339.

(114) Agrawal, A. A.; Böröczky, K.; Haribal, M.; Hastings, A. P.; White, R. A.; Jiang, R.-W.; Duplais, C. Cardenolides, Toxicity, and the Costs of Sequestration in the Coevolutionary Interaction between Monarchs and Milkweeds. *Proc. Natl. Acad. Sci.* **2021**, *118* (16), e2024463118. https://doi.org/10.1073/pnas.2024463118.

(115) Casartelli, M.; Corti, P.; Giovanna Leonardi, M.; Fiandra, L.; Burlini, N.; Pennacchio, F.; Giordana, B. Absorption of Albumin by the Midgut of a Lepidopteran Larva. *J. Insect Physiol.* **2005**, *51* (8), 933–940. https://doi.org/https://doi.org/10.1016/j.jinsphys.2005.04.008.

(116) Barbehenn, R. V. Non-Absorption of Ingested Lipophilic and Amphiphilic Allelochemicals by Generalist Grasshoppers: The Role of Extractive Ultrafiltration by the Peritrophic Envelope. *Arch. Insect Biochem. Physiol.* **1999**, *42* (2), 130–137. https://doi.org/https://doi.org/10.1002/(SICI)1520-6327(199910)42:2<130::AID-ARCH3>3.0.CO;2-C.

(117) Beyenbach, K. W.; Skaer, H.; Dow, J. A. T. The Developmental, Molecular, and Transport Biology of Malpighian Tubules. *Annu. Rev. Entomol.* **2010**, *55*, 351–374.

(118) Wang, L.; Xing, X.; Zeng, X.; Jackson, S. R.; TeSlaa, T.; Al-Dalahmah, O.; Samarah, L. Z.; Goodwin, K.; Yang, L.; McReynolds, M. R. Spatially Resolved Isotope Tracing Reveals Tissue Metabolic Activity. *Nat. Methods* **2022**, *19* (2), 223–230.

(119) Schmid, R.; Heuckeroth, S.; Korf, A.; Smirnov, A.; Myers, O.; Dyrlund, T. S.; Bushuiev, R.; Murray, K. J.; Hoffmann, N.; Lu, M. Integrative Analysis of Multimodal Mass Spectrometry Data in MZmine 3. *Nat. Biotechnol.* **2023**, *41* (4), 447–449.

# CHAPTER II

## Spatial metabolomics reveal divergent cardenolide processing in the monarch (*Danaus plexippus*) and the common crow butterfly (*Euploea core*)

**Domenic Dreisbach[1], Dhaka R. Bhandari[1], Anja Betz[2], Linda Tenbusch[3], Andreas Vilcinskas[3,4], Bernhard Spengler[1], Georg Petschenka[2]**

[1]Institute of Inorganic and Analytical Chemistry, Justus Liebig University Giessen, Heinrich-Buff-Ring 17, 35392 Giessen, Germany

[2]Institute of Phytomedicine, University of Hohenheim, Otto-Sander-Straße 5, 70599 Stuttgart, Germany

[3]Institute of Insect Biotechnology, Justus Liebig University Giessen, Heinrich-Buff-Ring 26-32, 35392 Giessen, Germany

[4]Fraunhofer Institute for Molecular Biology and Applied Ecology (IME), Branch for Bioresources, Ohlebergsweg 12, 35392 Giessen, Germany

*Mol. Ecol. Resour*. **2023**; 00:1-16

Received: 4 July 2022 | Revised: 9 March 2023 | Accepted: 16 March 2023
DOI: 10.1111/1755-0998.13786

RESOURCE ARTICLE

MOLECULAR ECOLOGY RESOURCES WILEY

# Spatial metabolomics reveal divergent cardenolide processing in the monarch (*Danaus plexippus*) and the common crow butterfly (*Euploea core*)

Domenic Dreisbach[1] | Dhaka R. Bhandari[1] | Anja Betz[2] | Linda Tenbusch[3] | Andreas Vilcinskas[3,4] | Bernhard Spengler[1] | Georg Petschenka[2]

[1]Institute of Inorganic and Analytical Chemistry, Justus Liebig University Giessen, Giessen, Germany
[2]Institute of Phytomedicine, University of Hohenheim, Stuttgart, Germany
[3]Institute of Insect Biotechnology, Justus Liebig University Giessen, Giessen, Germany
[4]Fraunhofer Institute for Molecular Biology and Applied Ecology (IME), Giessen, Germany

**Correspondence**
Georg Petschenka, Institute of Phytomedicine, University of Hohenheim, Otto-Sander-Straße 5, Stuttgart 70599, Germany.
Email: georg.petschenka@uni-hohenheim.de

**Funding information**
Deutsche Forschungsgemeinschaft, Grant/Award Number: PE 2059/3-1; LOEWE Program of the State of Hesse (LOEWE Center for Insect Biotechnology and Bioresources)

**Handling Editor:** Tatiana Giraud

## Abstract

Although being famous for sequestering milkweed cardenolides, the mechanism of sequestration and where cardenolides are localized in caterpillars of the monarch butterfly (*Danaus plexippus*, Lepidoptera: Danaini) is still unknown. While monarchs tolerate cardenolides by a resistant $Na^+/K^+$-ATPase, it is unclear how closely related species such as the nonsequestering common crow butterfly (*Euploea core*, Lepidoptera: Danaini) cope with these toxins. Using novel atmospheric-pressure scanning microprobe matrix-assisted laser/desorption ionization mass spectrometry imaging, we compared the distribution of cardenolides in caterpillars of *D. plexippus* and *E. core*. Specifically, we tested at which physiological scale quantitative differences between both species are mediated and how cardenolides distribute across body tissues. Whereas *D. plexippus* sequestered most cardenolides from milkweed (*Asclepias curassavica*), no cardenolides were found in the tissues of *E. core*. Remarkably, quantitative differences already manifest in the gut lumen: while monarchs retain and accumulate cardenolides above plant concentrations, the toxins are degraded in the gut lumen of crows. We visualized cardenolide transport over the monarch midgut epithelium and identified integument cells as the final site of storage where defences might be perceived by predators. Our study provides molecular insight into cardenolide sequestration and highlights the great potential of mass spectrometry imaging for understanding the kinetics of multiple compounds including endogenous metabolites, plant toxins, or insecticides in insects.

KEYWORDS
cardenolides, *Danaus plexippus*, MALDI mass spectrometry imaging, sequestration, spatial metabolomics

## 1 | INTRODUCTION

As a product of reciprocal coevolution, plants possess a plethora of defences against herbivorous insects and other antagonists. These traits include the production of toxic secondary plant metabolites, which protect plants by poisoning or deterring herbivores directly (Dussourd & Hoyle, 2000; Narberhaus et al., 2005), impair their growth and development (Ayres et al., 1997; Cresswell et al., 1992), or lower the digestibility of the plant diet (Fraenkel, 1959; Koiwa et al., 1997). Remarkably, many insects are not only able to cope

with a toxic diet, but also sequester (i.e., accumulate and store) plant toxins in their body tissues to defend themselves against predators and parasitoids (Beran & Petschenka, 2022; Duffey, 1980; Opitz & Müller, 2009). Although sequestration is a widespread phenomenon among herbivorous insects including several important pests (Beran et al., 2014; Kazana et al., 2007; Robert et al., 2017; Yang et al., 2021), the underlying physiological mechanisms and especially the transport of toxins across the gut epithelium or the spatial distribution of plant toxins within insect bodies are largely unknown.

The monarch butterfly (*Danaus plexippus*) is an important model for insect-plant coevolution (Agrawal et al., 2021; Karageorgi et al., 2019; Petschenka & Agrawal, 2015) and is famous for the sequestration of toxic cardenolides from its host plant milkweed (*Asclepias* spp., Apocynaceae; Brower et al., 1968; Frick & Wink, 1995; Parsons, 1965; Von Reichstein et al., 1968). Cardenolides are potent inhibitors of $Na^+/K^+$-ATPase (Agrawal et al., 2012; Schatzmann, 1953), an essential cation carrier ubiquitously expressed in animal cells. Remarkably, monarch larvae sequester these toxins in high amounts as a defence against predators and can tolerate them by means of a modified $Na^+/K^+$-ATPase, carrying a few amino acid substitutions in the cardenolide binding site of the enzyme (Dobler et al., 2012; Holzinger & Wink, 1996; Vaughan & Jungreis, 1977).

Despite feeding on cardenolide producing plants as well, the closely-related milkweed butterfly *Euploea core* (the common crow butterfly) possesses a nonresistant $Na^+/K^+$-ATPase and does not sequester cardenolides (Malcom & Rothschild, 1983; Petschenka & Agrawal, 2015). Although it is not yet understood how caterpillars of *E. core* cope with dietary cardenolides, tolerance is potentially mediated on the level of the caterpillars' gut and may involve degradation of the compounds (Petschenka & Agrawal, 2015) or epithelial barriers (Dobler et al., 2015).

Cardenolides consist of a 23-carbon four-ring steroid skeleton bearing a five-membered lactone ring bound to C17 and are frequently attached to a sugar moiety. Approximately 200 cardenolides are known from various milkweed species (Züst et al., 2019), and 21 different cardenolides were identified in *Asclepias curassavica* (Zhang et al., 2014), one of the two most important host plants of the monarch butterfly (Agrawal et al., 2021). Although sequestration in monarch butterflies was already described in the 1960s (Brower et al., 1968; von Reichstein et al., 1968), it is still largely unknown how sequestration is mediated mechanistically and where cardenolides are localized in the caterpillar body. However, a comprehensive view on the spatial distribution and abundance of cardenolides across caterpillar body tissues is a prerequisite to understand the molecular mechanisms of sequestration and the function of stored defences in ecological interactions with predators and parasitoids. Along these lines, comparisons to closely related but nonsequestering species such as *E. core*, are mandatory to reveal specific adaptations related to cardenolide sequestration in the monarch butterfly.

A promising approach to analyse the distribution of plant toxins in insects is matrix-assisted laser desorption/ionization mass spectrometry imaging (MALDI MSI), a method visualizing molecules based on their molecular masses. MALDI MSI allows for the simultaneous and semi-quantitative mapping of hundreds of molecules (e.g., metabolites, lipids, proteins) in tissues and cells. Data are acquired by a laser beam scanning across a matrix-covered tissue section, releasing ionized molecules for subsequent mass spectrometry analysis while also recording their spatial information (Spengler, 2015). By converting spatial signals of selected molecular masses into coloured pixels, images are generated displaying the distribution of compounds of interest. In addition, colour intensities correlate with the local abundance of a molecule.

Among MALDI MSI instrumentation, atmospheric-pressure scanning-microprobe matrix-assisted laser desorption/ionization (AP-SMALDI) MSI is one of the most advanced technologies regarding spatial resolution and sensitivity and therefore is of special interest for the spatial metabolomic characterization of complex molecular systems in the fields of chemistry, biology and medicine (Koestler et al., 2008; Kompauer et al., 2017a, 2017b; Spengler et al., 1994; Spengler & Hubert, 2002). For example, metabolite, lipid and peptide distributions were successfully visualized with spatial resolutions of up to 5 μm on various biological surfaces and within native organisms, thereby linking molecular structures to biological functions and origins (Geier et al., 2020, 2021; Iwama et al., 2021; Kadesch et al., 2019; Kadesch, Hollubarsch, et al., 2020; Kadesch, Quack, et al., 2020; Kompauer et al., 2017b).

In contrast to vacuum-ionization MSI methods such as conventional MALDI and secondary ion mass spectrometry (SIMS), AP-SMALDI MSI allows experiments to be performed under near-physiological conditions (i.e., physiological temperature and pressure). Therefore, AP-SMALDI MSI overcomes vacuum-induced sample damage, loss of volatile compounds and does not require sample fixation and/or sample drying. The most recent instrumental approach in AP-SMALDI MSI eliminates height-related measurement artefacts by utilizing laser triangulation for pixel-wise autofocusing (Kompauer et al., 2017b), thereby enabling the spatially-resolved molecular analysis of delicate and nonplanar sample surfaces, such as the fragile epithelium of the caterpillar integument and heterogeneous tissue types of insects. To this date, the experimental bottlenecks described above had limited the application of high-resolution MSI in the field of insect research (Yang et al., 2020).

Taking advantage of recent AP-SMALDI MSI developments, we here set out to study the distribution of ingested and sequestered cardenolides within their native, spatial context in caterpillars of *D. plexippus* and *E. core*. Using a comparative approach involving caterpillars of both species raised on the same species of milkweed, we tested on which physiological scale the differences in toxin distribution are mediated. Since both caterpillar species are closely related, can be raised on the same host plant, and can cope with the same class of plant toxins (i.e., cardenolides) while possessing diverging ecological strategies (sequestering vs. nonsequestering), they represent a suitable framework to test mechanistic hypothesis about sequestration.

We followed an MSI-based spatial metabolomics approach to study the fate of 10 cardenolides in tissue sections of both species

at high lateral resolution, thus providing novel molecular insight into the process of cardenolide sequestration in *D. plexippus* and cardenolide tolerance in *E. core*. We visualized the chlorophyll derivative pheophytin as a marker for plant material (green), an animal phospholipid (phosphatidylethanolamine; blue) as a marker for animal tissue, and various cardenolides of interest (red). In contrast to previous work on cardenolide sequestration in monarch caterpillars that relied on the extraction of whole individuals or dissected body parts, our approach preserves spatial information and revealed the distribution of individual cardenolides in unprecedent detail across different tissues involved in the process of sequestration, such as the midgut epithelium and the caterpillar integument. We found that, while cardenolides are degraded in the gut lumen of *E. core* caterpillars, they accumulate in the gut lumen of monarch caterpillars representing a novel mechanism of processing plant toxins in herbivorous insects.

Besides providing insight into the process of sequestration in the monarch butterfly and revealing mechanistic differences between two closely related caterpillars coping with the same class of plant toxins but having divergent ecological strategies, our study highlights the potential of high-resolution AP-SMALDI MSI emerging as a powerful platform for researchers to in situ visualize the distribution and kinetics of metabolites in the spatial context of insect tissues and cells, with applications ranging from chemically-mediated plant-insect interactions to insecticide research.

## 2 | MATERIALS AND METHODS

### 2.1 | General experimental design

Our spatial metabolomics approach to study cardenolide sequestration in *D. plexippus* and *E. core* consisted of three major steps. First, we performed whole-body MSI (20 µm to 45 µm pixel size) of transverse- and longitudinal caterpillar tissue sections to obtain a comprehensive overview of cardenolide distributions in both species. Guided by this overview, we selected particular regions of interest for in-depth analysis of cardenolide composition, transport, and storage and carried out high-resolution MSI experiments (5–10 µm pixel size) of these areas using adjacent histological sections. To facilitate and confirm the interpretation of our MSI data (e.g., selectivity of sequestration by comparing cardenolide concentration profiles in the host plant and insects), we conducted complementary HPLC–MS/MS and HPLC-DAD experiments for structural identification and absolute quantification of cardenolides in various caterpillar- and plant tissues.

### 2.2 | Chemicals, plants and insects

If not stated otherwise, all chemicals were purchased from Sigma-Aldrich. Colonies of *D. plexippus* (origin Portugal) and *E. core* (origin Southeast Asia) were maintained in cages in a greenhouse under ambient conditions. Caterpillars from both species were raised on potted *A. curassavica* plants (grown from seeds of commercial origin), grown in the same greenhouse and watered, fertilized and pruned as needed. For MSI experiments, actively feeding final-instar larvae of *D. plexippus* and *E. core* were directly collected from the plants and stored at −80°C for no longer than 2 weeks until sample preparation. For regional gut dissection experiments, caterpillars of *E. core* were raised in the greenhouse as well, while caterpillars of *D. plexippus* were raised in a climate chamber (Fitotron SGC 120, Weiss Technik) at 26°C (day) and 22°C (night) under a 16:8 h day/night cycle at 60% humidity. Caterpillars for these experiments were raised on individual plants and leaf samples from each plant were taken for cardenolide quantification.

To test the hypothesis of cardenolide retention, we performed feeding experiments with cardenolide-free plants. Monarch caterpillars (harvested from *A. curassavica* plants in the greenhouse) were fed with the cardenolide-free Apocynaceae *Oxypetalum coeruleum* (Warashina & Shirota, 2021) for 3 h before sampling. In a preliminary trial, we fed flowers of *A. curassavica* (red and yellow) to a last-instar caterpillar of *D. plexippus* under ambient conditions and coloured faecal pellets observed after 1 h indicated a full gut passage. Since caterpillar feeding activity on *O. coeruleum* was reduced compared to *A. curassavica*, three additional *D. plexippus* caterpillars of similar size were allowed to feed on *O. coeruleum* for 3 h under the same conditions. Caterpillars of *E. core* were quite hesitant to feed on *O. coeruleum* and only one of three caterpillars finally accepted *O. coeruleum* and was left on the leaves overnight. After the trials, caterpillars were frozen at −80°C and treated as described above. Although the time of *O. coeruleum* feeding was different for both caterpillar species, only leaf particles of *O. coeruleum* were visible in the histological sections indicating complete replacement of *A. curassavica* plant material by *O. coeruleum* tissue.

For the LC–MS analyses of isolated caterpillar integuments, we used actively feeding *D. plexippus* caterpillars raised on potted *A. curassavica* plants in the greenhouse under ambient conditions.

### 2.3 | Sample preparation for MALDI mass spectrometry imaging

A schematic overview of the workflow is depicted in Figure S1. Before cryosectioning, caterpillars of *D. plexippus* and *E. core* were transferred to a cryomicrotome (HM525, Thermo Fisher Scientific) and allowed to warm up to −25°C for 60 min. For transverse sectioning, each caterpillar was cut in half and fixed onto a metal target using freezing water as an adhesive medium. Subsequently, transverse sections with 40 µm thickness were obtained at −25°C, thaw-mounted onto glass slides and stored at −80°C until MSI analysis. All transverse sections were obtained between the first and the second pro-leg of the caterpillar to sample the midgut region.

Whole-insect sectioning (i.e., longitudinal sections) is challenging due to the large size of final instar *D. plexippus* and *E.core*

caterpillars (3 to 5 cm in length). Thus, an MSI-compatible sample preparation protocol to obtain longitudinal sections of excellent quality was developed. First, a custom-made cryomold (24 × 50 × 30 mm) was filled to one-third of its volume with aqueous gelatin solution (8% (w/v) for *D. plexippus*, 6% (w/v) for *E. core*) and transferred to −25°C for 20 min. Then, frozen caterpillars were placed onto the solidified gelatin block, covered with fresh gelatin solution and immediately snap-frozen in liquid nitrogen to prevent potential analyte delocalization and tissue damage induced by hot gelatin (45°C).

For sectioning, frozen gelatin blocks were transferred to −25°C for 60 min, subsequently taken out of the cryomold and fixed onto the metal target using freezing water as described above (see Figure S1). Longitudinal sections with 40 µm thickness were obtained at −25°C for *D. plexippus* and −18°C for *E. core*, thaw-mounted onto glass slides and stored at −80°C until MSI analysis. Before matrix application, tissue sections were brought to room temperature in a desiccator for 30 min to avoid condensation of water at the sample surface. Optical images of tissue sections were obtained using a Keyence VHX-5000 digital microscope (Keyence Deutschland GmbH).

Among the MALDI matrices tested (positive-ion mode: 2,5-dihydroxybenzoic acid [2,5-DHB], α-cyano-4-hydroxycinnamic acid [CHCA], 2-mercaptobenzothiazol [MBT]; negative-ion mode: 9-aminoacridine [9-AA], bis(dimethylamino)naphthalene [DMAN]), cardenolides were exclusively detected using 2,5-DHB in positive-ion mode. Before each MSI experiment, a matrix solution of 30 mg/mL 2,5-DHB (2,5-DHB, for synthesis, Merck) in acetone/water at 1:1 (v/v) with 0.1% trifluoroacetic acid (TFA, for spectroscopy, AppliChem GmbH) was freshly prepared. A volume of 100 µL DHB matrix solution for transverse sections, 130 µL for longitudinal sections and 70 µL for high-resolution MSI experiments (≤10 µm pixel size) was sprayed onto the sample surface at a flow rate of 10 µL/min (5 µL/min for high-resolution MSI experiments) using an ultrafine pneumatic sprayer system (SMALDIPrep, TransMIT GmbH). The nebulizing nitrogen gas pressure was 1 bar and the rotation was set to 500 rpm. Crystal sizes (≤10 µm) and homogeneity of the matrix layer on the sample surface were controlled under the microscope before MSI analysis. In total, seven biological replicates of *D. plexippus* and 5 biological replicates of *E. core* were analysed via MSI (see Table S1 for an overview).

After MSI measurement, specific tissue sections were washed for 2 min with ethanol (100%) to remove the matrix layer and stained with haematoxylin and eosin stain (H&E) for histological evaluation (Figure S2).

### 2.4 | Collection of regional gut samples, integuments, and sample preparation for HPLC analysis

For comparison with our whole-body MSI analyses, we assessed the concentration of cardenolides in the food bolus of both caterpillar species along the gut passage by HPLC-DAD and HPLC–MS analyses. To this end, we developed a protocol for dissecting gut portions from freeze-dried caterpillars. Actively feeding last-instar caterpillars (= fifth instar) of *D. plexippus* ($n = 9$) and *E. core* ($n = 6$) were collected from *A. curassavica* plants and immersed in crushed ice for 10 min. In addition, a mature leaf was collected from each plant ($n = 9$ for *D. plexippus* and $n = 6$ for *E. core*), frozen at −80°C and freeze-dried. After chilling, caterpillars were pinned into a dish lined with Sylgard 184 (Dow Corning) under ice-cold PBS (phosphate buffered saline; Roti-CELL, Carl Roth). After decapitation, the integument was opened by a dorsal median cut using microscissors and fixed at both sides. Tissues adhering to the gut or floating in the body cavity were removed (i.e., Malpighian tubules, salivary glands). Subsequently, the preparation was washed with ice-cold PBS while keeping the tissue submersed permanently, frozen at −80°C and eventually freeze-dried for 3 days. Precipitated salts were carefully removed using a soft brush and the caterpillar gut including its contents was separated into foregut, four equally sized portions of mid-, and hindgut (see Figure S3).

Gut portions were weighed and extracted for HPLC-DAD and HPLC–MS analysis. Dry gut portions (i.e., the surrounding epithelium and the gut contents) were transferred into 2 mL screw-cap vials (Sarstedt AG & Co. KG) and 1 mL methanol containing 0.02 mg/mL of the internal standard digitoxin (Sigma-Aldrich) was added. After the addition of c. 900 mg zirconia beads (ø 2.3 mm, BioSpec Products, Inc.), samples were homogenized in a Fast Prep homogenizer (MP Biomedicals) for two 45-s cycles at a speed of 6.5 m/s. After centrifugation at 16,100 *g*, supernatants were transferred into fresh vials. Extraction of the samples was repeated once using 1 mL pure methanol and first and second supernatants were combined. After evaporation under a stream of $N_2$, dry residues were dissolved in 200 µL methanol by agitation in the Fast-Prep-24 instrument. Before HPLC-DAD analysis, samples were filtered via Rotilabo-syringe filters (nylon, 0.45 µm pore size, ø 13 mm, Carl Roth GmbH & Co.).

Leaf samples of *A. curassavica* from the experiment with *D. plexippus* were processed in the same fashion as described for the gut portions using a subset of roughly 50 mg of leaf material for extraction (49.4–52.8 mg). For leaf samples from the experiment with *E. core*, whole freeze-dried leaves were homogenized in 15 mL tubes containing two ceramic sphere beads (MP Biomedicals). We added 2 mL of methanol, containing 0.2 mg/mL of the internal standard digitoxin and samples were homogenized in the Fast-Prep-24 instrument as described above. After centrifugation (10 min at 1000 *g*) and removal of the supernatant, the extraction procedure was repeated with 2 mL pure methanol. Pooled supernatants were dried in a vacuum centrifuge and transferred into a 2-ml tube by washing the original tube with 3 × 500 µL methanol. Finally, the samples were processed as described above for HPLC analysis.

For the analyses of *D. plexippus* caterpillar integuments, three final-instar caterpillars were chilled on ice for 10 min. Subsequently, integuments were dissected, quickly rinsed in PBS, and adhering

PBS was removed by pulling the samples over the edge of a glass beaker. Integument samples were stored at −80°C and extracted as described above for gut portions but resuspended in 100 µL methanol instead.

### 2.5 | Instrumentation for MALDI mass spectrometry imaging

All MSI measurements were performed using an autofocusing AP-SMALDI5 AF ion source (TransMIT GmbH) coupled to a Q Exactive HF Orbitrap mass spectrometer (Thermo Fisher Scientific). For desorption/ionization, 50 laser pulses per pixel at 343 nm and a pulse rate of 100 Hz were focused perpendicular to the sample surface to an effective ablation spot diameter of 5 µm (Figure S4). Whole-body and high-resolution (5 µm to 10 µm pixel size) MSI experiments were performed using the 3D-surface mode ("pixel-wise autofocusing") to keep the MALDI laser focus, fluence and ablation spot size constant for varying sample surface characteristics (Figure S5) and to handle the sample tilt for the longitudinal caterpillar sections (~4 cm in length). The pixel size of the XYZ sample stage was set to the desired pixel size.

For all AP-SMALDI MSI experiments, the mass spectrometer was operated in positive-ion mode in a mass-to-charge-ratio ($m/z$) range of 250–1000 at a mass resolution of 240,000 at $m/z$ 200. Internal lock-mass calibration was performed by using the ion signal from the DHB matrix cluster at $m/z$ 716.12451 ($[5DHB-4H_2O+NH_4]^+$), resulting in a mass accuracy of less than 2 ppm root mean square error (RMSE) for the whole image (Figure S6). The scan speed for MSI experiments was about 1.4 pixel/s. The acceleration voltage was set to 3 kV. The ion injection time was set to 500 ms. The capillary temperature was 250°C, and the S-lens level was set to 100 arbitrary units.

### 2.6 | Instrumentation for HPLC-DAD and HPLC–MS

All HPLC–MS experiments were performed using a Dionex UltiMate 3000 HPLC instrument (Thermo Fisher Scientific) coupled to a Q Exactive HF-X Orbitrap mass spectrometer (Thermo Fisher Scientific). Analytes were separated on a Kinetex C18 reversed-phase column (2.6 µm, 100 × 2.1 mm, Phenomenex). Detailed experimental parameters are provided in Supporting Information Note S1. In total, three biological replicates of every sample type were measured (regional gut samples from *D. plexippus* and *E. core*; *D. plexippus* midgut tissue, integument; *A. curassavica* leaf).

All HPLC-DAD experiments were performed using an Agilent 1100 series HPLC (Agilent Technologies) and compounds were separated on an EC 250/4.6 NUCLEODUR C18 Gravity column (3 µm, 250 × 4.6 mm, Macherey-Nagel). Detailed experimental parameters are provided in Supporting Information Note S1.

### 2.7 | Data processing

Xcalibur (Thermo Fisher Scientific) was used to display mass spectra. Ion images of selected $m/z$ values were generated using MIRION imaging software (Paschke et al., 2013) (TransMIT GmbH, Giessen, Germany). The general principle for image generation is displayed in Figure S7. The ion-selection bin width ($\Delta(m/z)$) of the images, generated from the MS data was set to $\Delta(m/z)=0.01$. Images were normalized to the base pixel (highest intensity of $m/z$ bin) per image if not stated differently. No further data manipulation steps, such as smoothing or interpolation, were used. RGB MS images were obtained by selecting and overlaying three different images for the red-green-blue channels. For consistency in data visualization, selected cardenolides are always displayed in red, the chlorophyll derivative pheophytin a is shown in green to indicate plant tissue, and phosphatidylethanolamine PE (36:3) is depicted in blue as a chemical marker for animal tissue. The resulting images were adjusted in brightness for optimal visualization. MSiReader (Robichaud et al., 2013) was used to extract the ion intensities of specific $m/z$ bins for defined regions of interest in the image. Metabolites and lipids were assigned and identified based on accurate mass measurements with a mass tolerance of less than 2 ppm RMSE for the whole image, MS/MS experiments and database matches (Palmer et al., 2017). For instance, calotropin/calactin ($[M+K]^+$) at $m/z$ 571.2304 was detected with a mass error of 0.5 ppm, and a root mean square error (RMSE) of 1.6 ppm (Figure S6a).

For relative quantification of cardenolides based on MSI data, we defined seven regions of interest in silico (focused on *A. curassavica* leaf material and surrounding cardenolide signals) per biological replicate and extracted the ion intensities for calotropin/calactin, calotoxin, uscharidin, frugoside and asclepin. Throughout all MSI experiments, pheophytin a was homogenously distributed and only marginal variation of intensity across *A. curassavica* leaf pieces in the *D. plexippus* and *E. core* gut lumen was observed. Thus, for better comparability, we utilized the plant tissue marker pheophytin a as an internal standard and normalized the average cardenolide signal abundance to the average pheophytin a signal abundance for the respective region of interest.

For HPLC–MS based quantification, MZmine 2 (Pluskal et al., 2010) was used for preprocessing and extracting the area under the peak (AUP) of cardenolide features in the chromatogram. Subsequently, the respective cardenolide AUP was normalized to the AUP of the internal standard (digitoxin) and the corresponding extracted tissue weight.

Data from HPLC-DAD analyses were evaluated using Agilent ChemStation (Rev. B.04.03, Agilent Technologies). Peaks with symmetrical absorption maxima between 216 and 222 nm (Malcolm & Zalucki, 1996) were interpreted as cardenolides and integrated at 218 nm. For gut samples obtained from dissections of freeze-dried caterpillars, we quantified cardenolides based on the peak area of the known concentration of the internal standard digitoxin. For leaf samples of *A. curassavica*, digitoxin was coeluting with an endogenous cardenolide peak. Therefore, we used the mean of all digitoxin

peak areas from the *E. core* gut samples ($n=36$) which were run in the same batch for calibration of the leaf samples. Leaf samples collected during our experiment with *D. plexippus* were measured several months after the *D. plexippus* gut samples. Hence, cardenolides in these leaf samples were quantified using a digitoxin calibration curve which was measured shortly after the leaf samples were analysed. Cardenolide concentrations of all leaf samples were corrected for the known amount of digitoxin which had been added initially as an internal standard. For caterpillar gut samples and leaf samples of *A. curassavica*, only peaks were considered which were present and had a clear cardenolide spectrum in at least 50% of all samples. The observed pattern of results (see Results section) did not change, when all peaks showing a clear cardenolide spectrum in each sample were considered for quantification.

### 2.8 | Statistical analysis

We compared the cardenolide concentrations of dissected gut portions and leaf material using the standard least squares model in JMP Pro 15 (SAS Institute) including caterpillar individual as a model effect. For the *D. plexippus* data set, data were $\log_{10}$-transformed to achieve normality of residuals and homogeneity of variance. For comparing intensities of cardenolide signals in silico, we calculated means of all seven ROIs for each cardenolide in each caterpillar. Means for each cardenolide were compared between caterpillar species using *t*-tests assuming unequal variances in JMP Pro 15. *p*-values $<.05$ were considered statistically significant.

## 3 | RESULTS

### 3.1 | Spatial distribution of cardenolides in *D. plexippus* and *E. core*

AP-SMALDI MSI experiments (20 and 35 µm pixel size) conducted on transverse caterpillar sections (Figure 1; Figure S8) revealed the presence of cardenolides throughout the body tissues of *D. plexippus* caterpillars (i.e., cardenolides are sequestered), including the midgut epithelium, fat body and haemolymph, and especially the integument from where we obtained the strongest cardenolide signals. In contrast, cardenolides were entirely restricted to the gut lumen in *E. core* caterpillars and were absent from its body tissues (i.e., cardenolides are not sequestered). Remarkably, cardenolides appeared at much higher intensities in guts of *D. plexippus* compared to guts of *E. core* when images were adjusted to the same scale. This pattern was not restricted to the isomers calotropin/calactin but also apparent for uscharidin and voruscharin (Figures S8 and S9, not all cardenolides were compared). In total, we found 10 different cardenolides in both caterpillar species and leaves of *A. curassavica* (Table 1 and Figure S10–S14).

Notably, cardenolides (Figure 1b at the example of [calotropin/calactin+K]$^+$) were visible across the entire gut lumen of *D. plexippus* including the ectoperitrophic space (i.e., the region between the peritrophic envelope surrounding the food bolus and the midgut epithelium). In midguts of *E. core*, in contrast, they were exclusively detected at the fringes of *A. curassavica* leaf pieces (Figure 1c; Figure S8b) and were absent in the liquid phase of the gut lumen. In addition to transverse sections, we carried out whole-body MSI (45 µm pixel size) on longitudinal sections of final instar caterpillars and found according patterns of cardenolide distributions along the entire gut passage (Figure 2; Figure S15).

We compared relative quantities of the five most abundant cardenolides (the isomers calotropin/calactin counted as one) based on MSI data in silico. For this purpose, we selected seven comparable regions of interest (ROI) in transverse and longitudinal sections of *D. plexippus* and *E. core* caterpillars and analysed cardenolide intensities at the fringes of leaf pieces in the gut. According to the visual differences apparent in Figures 1 and 2, the in silico analysis revealed that calotropin/calactin was 6.8×, calotoxin 2.1×, frugoside 2.6×, and uscharidin 1.8× more abundant in *D. plexippus* compared to *E. core* ($p<.001$, $p=.031$, $p=.005$, $p=.02$, no difference for asclepin: 1.15×, $p=.2$; $n=4$, that is, two transverse and two longitudinal sections from individual caterpillars per species; all *t*-tests assuming unequal variances, Figure S16a). Notably, the analysed regions of interest (see Materials and Methods and Figure S16b) included leaf particles and their fringes where cardenolides were detectable. More distantly from the leaf fragments, the difference between the liquid phase of *D. plexippus* and *E. core* would certainly have been even more pronounced.

Besides local quantitative differences between caterpillar species, our total cardenolide estimate based on HPLC-DAD analyses (i.e., all cardenolide peaks integrated) of dissected freeze-dried gut regions (foregut, four segments of the midgut and hindgut) revealed a heterogeneous quantitative distribution of cardenolides along the gut passage in *D. plexippus* but not in *E. core*. Total cardenolide concentrations were constant across all gut regions of *E. core* caterpillars (foregut: FG, four sequential midgut portions: MG1-4, and hindgut: HG; $F_{5,25}=1.044$, $p=.414$, $n=6$; Figures S17 for HPLC-DAD and S18 for HPLC–MS). Contrastingly, in caterpillars of *D. plexippus*, cardenolide concentrations across all gut regions differed substantially ($F_{5,38}=8.312$, $p<.001$; $n=7$–9, see legend of Figure S17) and the cardenolide concentration in the hindgut was lower compared to all other gut regions except of foregut and midgut region 1 (FG vs. HG: $p=.577$; MG1 vs. HG: $p=.085$; MG2-4 vs. HG: $p<.001$; Tukey HSD; Figure S17). Concentrations of gut cardenolides differed across different caterpillar individuals in both species (*E. core*: $F_{5,25}=22.015$, $p<.001$; *D. plexippus*: $F_{8,38}=2.352$, $p<.037$).

When comparing total cardenolide concentrations only across midgut portions (i.e., foregut and hindgut excluded) of monarch caterpillars and leaves of *A. curassavica*, we found higher cardenolide concentrations compared to milkweed leaves in midgut portions 2 and 3 ($F_{4,32}=5.622$, $p=.002$) and a trend of cardenolide accumulation in the central region of the midgut with concentrations of midgut portion 2 and 3 being twice as high compared to midgut portion

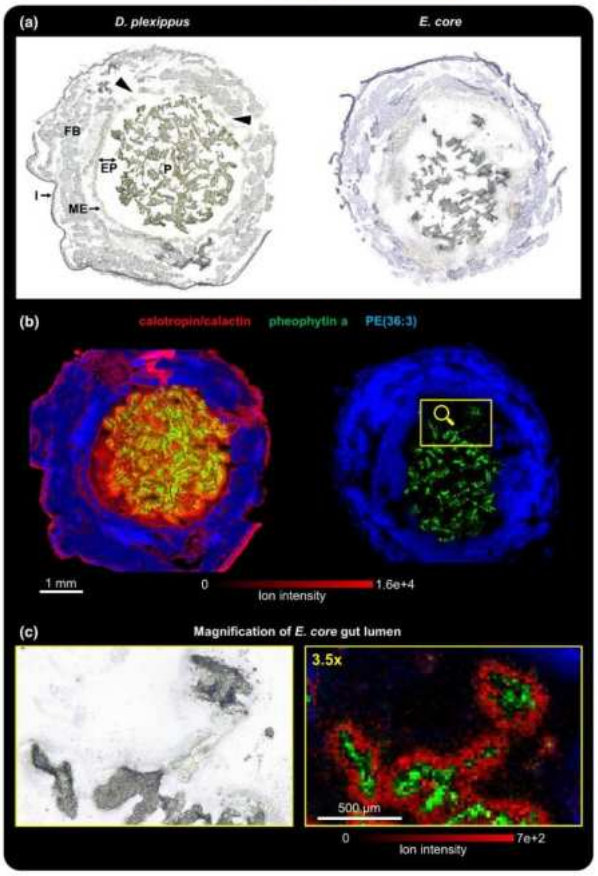


FIGURE 1 AP-SMALDI MSI of transverse sections of caterpillars of *Danaus plexippus* (biological replicate 1) and *Euploea core* (biological replicate 1). (a) Optical image of the transverse section of a fifth instar caterpillar of *D. plexippus* (left) and *E. core* (right) before matrix application. P, plant material; EP, ectoperitrophic space; ME, midgut epithelium; FB, fat body; I, integument. (b) Corresponding RGB overlay images obtained with 35 µm (*D. plexippus*) and 20 µm (*E. core*) pixel size, showing the spatial distribution of the cardenolide calotropin and/or its isomer calactin ($[M+K]^+$, red) at *m/z* 571.2304, the chlorophyll derivative pheophytin a at *m/z* 909.5288 ($[M+K]^+$, green) as a chemical marker for plant tissue, and the animal lipid PE(36:3) ($[M+K]^+$, blue) as a chemical marker for animal tissues. Both RGB overlay images are normalized to the same intensity scale. The *D. plexippus* gut epithelium was damaged at two areas (highlighted in the optical image), causing potential analyte delocalization in the corresponding haemolymph area. (c) Magnification of the optical image and RGB overlay image for the highlighted area of the *E. core* gut lumen. For this ion image, the intensity scale of calotropin/calactin was adjusted to highlight the cardenolide distribution at the fringes of leaf pieces in the gut lumen of *E. core*.

1 ($F_{3,24}$ = 5.121, $p$ = .007; MG1 vs. MG2: $p$ = .018; midgut 1 vs. midgut 3: $p$ = .01; Tukey HSD; Figure S17). In contrast, cardenolide concentrations in gut portions of *E. core* were constantly lower than in plant material except for midgut portion 4 (plant vs. FG, MG1, MG2, MG3, MG4, HG: $p$ = .046; .023; .029; .01; .228; .005; Tukey HSD). Relatively constant toxin concentrations across guts of *E. core* and a heterogeneous distribution in *D. plexippus* were also observed based on absolute quantification of individual cardenolides via HPLC–MS (Figure S18).

Notably, the ratio of the stereoisomers calotropin and calactin in the gut passage differed substantially between both caterpillar species. Across the whole gut passage of *D. plexippus*, ratios of calotropin and calactin concentrations were rather constant (calotropin: calactin = 1.35; *t*-test, $p$ = .15; Figure S19). Contrastingly, in the gut material of *E. core*, the concentration of calotropin had an 8.15× higher concentration relative to calactin (*t*-test, $p$ < .001) (Figure S19). Regionally, the largest difference in the calotropin/calactin ratio between both species was determined in the first portion of the midgut (Figure S20). For comparison, we also analysed the content of both stereoisomers in leaf tissue of the host plant *A. curassavica* (1.61-fold for calotropin relative to calactin, *t*-test, $p$ = .05) and for integument tissue of *D. plexippus* (4.50-fold of calotropin relative to calactin, *t*-test, $p$ < .001; $n$ = 3 for all comparisons; Figure S20).

### 3.2 | Retention of cardenolides in the gut lumen of *D. plexippus*

Based on our observation on cardenolide accumulation in guts of *D. plexippus*, we tested the hypothesis that cardenolides are retained in the midgut lumen of *D. plexippus* caterpillars. For this purpose, we analysed last instar caterpillars of *D. plexippus* which were

TABLE 1 Overview of the 10 different cardenolides (Figure S3 for chemical structures) detected in *Asclepias curassavica* leaves, gut content and various tissue types of *Danaus plexippus* and *Euploea core* (MG: midgut) using AP-SMALDI MSI and complementary LC-MS experiments.

| Compound | *A. curassavica* leaf | *D. plexippus* gut content | *E. core* gut content | *D. plexippus* MG epithelium | *D. plexippus* integument | *E. core* integument |
|---|---|---|---|---|---|---|
| Calotropagenin | ✓† | ✓†,‡ | ✓† | ✓† | ✓†,‡ | –†,‡ |
| Uscharidin | ✓† | ✓†,‡ | ✓†,‡ | ✓† | ✓†,‡ | –†,‡ |
| Calotropin | ✓† | ✓†,‡ | ✓†,‡ | ✓†,‡ | ✓†,‡ | –†,‡ |
| Calactin | ✓† | ✓†,‡ | ✓†,‡ | ✓†,‡ | ✓†,‡ | –†,‡ |
| Frugoside | ✓† | ✓†,‡ | ✓†,‡ | ✓†,‡ | ✓†,‡ | –†,‡ |
| Calotoxin | ✓† | ✓†,‡ | ✓†,‡ | ✓†,‡ | ✓†,‡ | –†,‡ |
| Asclepin | ✓† | ✓†,‡ | ✓†,‡ | –†,‡ | –†,‡ | –†,‡ |
| Uscharin | ✓† | ✓†,‡ | ✓† | ✓† | ✓†,‡ | –†,‡ |
| Voruscharin | ✓† | ✓†,‡ | ✓† | ✓† | ✓†,‡ | –†,‡ |
| Uzarin | ✓† | ✓†,‡ | ✓†,‡ | –†,‡ | –†,‡ | –†,‡ |

*Note*: Native *A. curassavica* leaves were not analysed via AP-SMALDI MSI. Cardenolides detected exclusively with HPLC-MS are marked with ✓† and detected with HPLC-MS and AP-SMALDI MSI are marked with ✓†,‡. Cardenolides that were not detected with HPLC-MS and AP-SMALDI MSI are marked with –†,‡.

raised on *A. curassavica* but were fed with the cardenolide-free plant *Oxypetalum coeruleum* for 3 h before sampling using AP-SMALDI MSI. Remarkably, even after several rounds of purging with cardenolide-free *O. coeruleum*, we still detected cardenolides in the gut lumen. The preferentially-sequestered cardenolides calotropin/calactin (Figure 3b), calotoxin (Figure 3c), calotropagenin (Figure S21a) and frugoside (Figure S21b), as well as uscharidin (Figure S21c), which is the dominant cardenolide in *A. curassavica* leaves, were still present in the interstices between the *O. coeruleum* leaf particles in the gut although at lower abundance compared to a caterpillar freshly harvested from *A. curassavica* (see Figure 1; Figure S22; representative MSI-based relative quantification between biological replicate 1 and biological replicate 5 showed 2.7×, 1.1×, 2.1× reduction for calotropin/calactin, calotoxin, and frugoside, respectively; *t*-test, $p < .001$ for all comparisons; see legend of Figure S22 for details regarding in silico relative quantification). Notably, the dominant *A. curassavica* leaf cardenolides, voruscharin, uscharin and asclepin were no longer detected. In conclusion, our data suggest that sequestered cardenolides are retained in the gut lumen and are not moving linearly along with the gut contents.

In contrast to monarch caterpillars that were analysed directly after feeding on *A. curassavica* (Figure 1), it was not possible to detect any cardenolide signals in the ectoperitrophic space, gut epithelium and haemolymph (see magnified view of the highlighted ROI in Figure 3; Figure S21 and S23), suggesting rapid clearance of cardenolides distributed in the caterpillars' body fluids. For *E. core*, we did not detect any cardenolides after purging the gut lumen overnight with the cardenolide-free plant *O. coeruleum* (Figure S23).

### 3.3 | Selectivity, modification and storage of cardenolides in *D. plexippus*

We studied the selectivity of sequestration as well as the transport and storage of sequestered cardenolides by MSI experiments with a higher spatial resolution (5 μm pixel size) to improve resolution on the tissue level. Despite being minor components in *A. curassavica* leaves (Figure S24 for LC–MS-based quantification), calotropin/calactin (Figure 4b), frugoside (Figure S25b), and calotoxin (Figure S25c) were the most abundant cardenolides in the gut lumen and integument of the monarch caterpillar. In contrast, although being one of the most abundant cardenolides in *A. curassavica* (LC–MS based quantification revealed 5.8× higher concentration relative to calotropin, $n = 3$; Figure S24), asclepin was exclusively detected at the fringes of the leaf particles in the gut lumen and was not sequestered into the body tissues (Figure 4c).

Sequestered cardenolides were primarily stored in the epithelial cells of the integument (Figure 4; Figure S25) and not in the cuticle (see ref. 51 for a histological section of monarch integument). While uscharidin and voruscharin were the dominant cardenolides in *A. curassavica*, their concentration in the integument was 5.2× and 50× lower compared to to the dominant cardenolide calotropin ($n = 3$; Figure S24). However, although only at low amounts, we were able to visualize both toxins in the monarch caterpillar integument (Figure S25e,f). Interestingly while not showing signals in the gut lumen, calotropagenin, which was the cardenolide with the lowest concentration in *A. curassavica* leaves (Figure S24), was detected in the *D. plexippus* integument (Figure S25a). Despite being an abundant compound in *A. curassavica* like asclepin (Figure S24), the biglucoside uzarin was not sequestered by monarch caterpillars (Figure S25f).

Sequestration of plant toxins is generally assumed to be mediated via the epithelium of the midgut (Beran & Petschenka, 2022). In line with this prediction, we were able to detect calotropin/calactin with low abundance in the midgut epithelium of our transverse sections (Figure 4d). We also monitored the distribution of cardenolides at the interface gut lumen, midgut epithelium, and haemolymph based on longitudinal caterpillar sections to address the molecular transport process in a larger spatial context (Figure 5). Here, we were able to visualize the spatial distribution of the dominantly

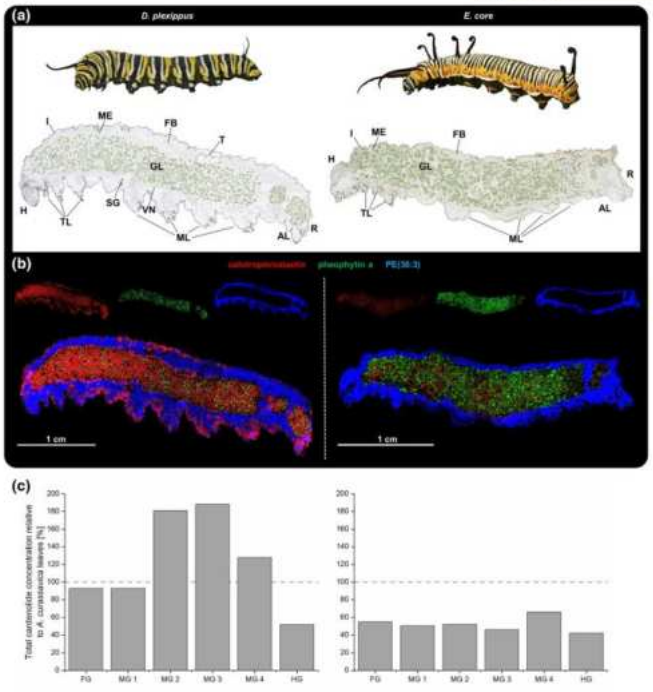


FIGURE 2 Whole-body AP-SMALDI MSI of fifth instar *Danaus plexippus* (biological replicate 3) and *Euploea core* caterpillars (biological replicate 3). (a) Optical image showing live caterpillars and longitudinal *D. plexippus* (left) and *E. core* (right) sections before matrix application. H, head; I, integument; TL, thoracic legs; SG, probably salivary gland; VN, probably ventral nerve code; ML, abdominal prolegs; AL, anal prolegs; R, rectum; T, testis; GL, gut lumen; FB, fat body; ME, midgut epithelium. (b) Corresponding RGB overlay images obtained with 45 µm pixel size, showing the spatial distribution of calactin/calotropin ($[M+K]^+$), at *m/z* 571.2304 (red), pheophytin a ($[M+K]^+$, green) at *m/z* 909.5292 to highlight ingested *Asclepias curassavica* plant material, and PE(36:3) ($[M+K]^+$, blue) at *m/z* 780.4941 serving as a marker for insect tissue, such as gut epithelium and fat body. Both RGB overlay images are normalized to the same intensity scale. (c) Schematic representation of total cardenolide concentrations across the gut passage in caterpillars of *D. plexippus* and *E. core* relative to the total cardenolide concentration in *A. curassavica* leaves based on means of six (*E. core*) and nine (*D. plexippus*) dissected caterpillars and milkweed leaves. Horizontal lines indicate the cardenolide concentration in plant material (i.e., 100%). Please see Figure S17 for a plot based on absolute quantification data.

sequestered cardenolides calactin/calotropin (Figure 5b), frugoside, (Figure S26b) and calotoxin (Figure S26c) within the epithelial tissue of the monarch midgut. In agreement with the putative role of the midgut epithelium as the transport organ for sequestered toxins mediating selectivity, the cardenolides uzarin (Figure 5c) and asclepin (Figure S26d) which were absent from the body cavity (i.e., not sequestered), were also not detected within the layer of midgut cells although they were present in the gut lumen. The cardenolide composition of the midgut epithelium tissue was further validated by LC-MS/MS experiments (Table 1).

In addition, our high-resolution MSI analyses revealed that sequestered cardenolides appear in the monarch gut epithelium in a discrete, granular pattern, which was maintained after dispersion in the haemolymph (Figure 5b; Figure S26b,c). Notably, this pattern does not only apply to the distribution of cardenolides but also to other metabolites (Figure S26, e.g., kaempferol-glucopyranoside, a ubiquitous plant secondary compound also occurring in milkweed).

We compared the distribution of cardenolides with the distribution of primary and other secondary metabolites, such as kaempferol-glucopyranoside (Figure S26e), malvidin-glucoside (Figure S26f), N-(1-deoxy-1-fructosyl)tyrosine (Figure S26g), guanosine (Figure S26h for *D. plexippus* and Figure S27c for *E. core*) and unidentified disaccharides (Figure S26i for *D. plexippus* and Figure S27d for *E. core*) within the midgut epithelial tissue of *D. plexippus* and *E. core*. For both species, we observed spatial distributions similar to sequestered cardenolides in the monarch

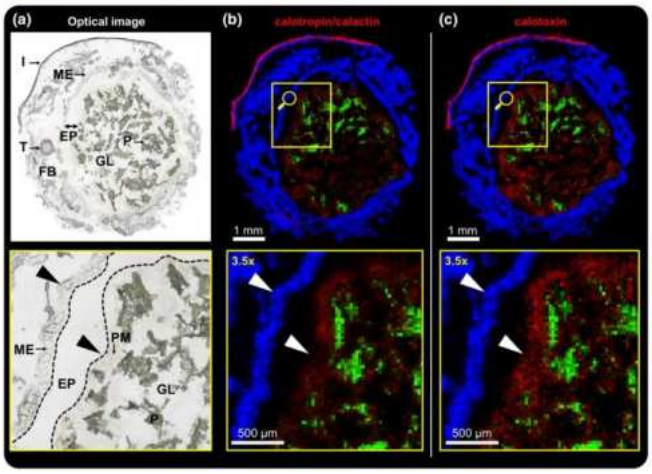


FIGURE 3 AP-SMALDI MSI (25 µm pixel size) of *Danaus plexippus* (biological replicate 5), fed with the nontoxic plant *Oxypetalum coeruleum* for 3 h before sampling. (a) Optical image of transverse *D. plexippus* section and magnified view of the outlined region. P, *O. coeruleum* plant material; EP, ectoperitrophic space; PM, peritrophic matrix; ME, midgut epithelium; T, testis; FB, fat body; I, integument. (b, c) Corresponding RGB overlay images and magnified views of the outlined region in (a) showing (b) calactin/calotropin ($[M+K]^+$, red) at *m/z* 571.2304, (c) calotoxin ($[M+K]^+$, red) at *m/z* 587.2251, (b, c) pheophytin a ($[M+K]^+$) at *m/z* 909.5292 as a chemical marker for plant tissue in green and PE(36:3) ($[M+K]^+$) at *m/z* 780.4942 as a chemical marker for insect tissue in blue.

regarding the extraction from plant material and the transport across the gut epithelium. Therefore, utilizing the high spatial resolution (≤10 µm) provided by the AP-SMALDI MSI system, we were able to reveal the spatial organization of metabolite uptake at the sub-tissue level.

## 4 | DISCUSSION

The demand for spatially-characterized biochemistry and molecular biology has grown rapidly over the recent years (Buchberger et al., 2018; Joo et al., 2008; Kherlopian et al., 2008; Spengler, 2015; van Hove et al., 2010). Traditional methods such as immunofluorescence, require the labelling of biomolecules with fluorophores, which can be time-consuming, inefficient and is restricted to individual preknown compounds (Yang et al., 2020). Moreover, labelling of molecules alters their physicochemical properties and therefore may influence their tissue distribution. Despite its great potential, matrix-assisted laser desorption/ionization (MALDI) MSI was only rarely employed to study sequestration of plant toxins in insects (see Abdalsamee et al., 2014).

Our MSI-based spatial metabolomics approach allows for spatially resolved, qualitative, and semi-quantitative analyses of native metabolites and lipids in an untargeted fashion. We visualized diverging strategies of two closely related milkweed butterfly species regarding the processing and uptake of plant toxins in the gut as well as the storage of sequestered compounds for defence. First, we demonstrated that the midgut lumen is the first physiological layer mediating selectivity and plays a vital role to cope with a toxic diet in *D. plexippus* and *E. core*. In contrast *D. plexippus* where cardenolides were found over the entire lumen, no extracted cardenolides were observed in between the leaf particles in the gut of *E. core*; instead, cardenolides were exclusively detected at the fringes of ingested leaf material. This pattern most likely suggests immediate degradation of cardenolides extracted from plant material. We suggested degradation of cardenolides in *E. core* based on analysed gut contents earlier (Petschenka & Agrawal, 2015) and the visualized lack of cardenolides in the liquid phase of the gut strongly supports our hypothesis and indicates that degradation happens directly in the midgut lumen.

We used whole-body MSI on longitudinal caterpillar sections and complementary HPLC-MS and HPLC-DAD experiments based on freeze-dried gut segments to track cardenolides along the caterpillar gut passage. Specifically, we found that cardenolides accumulated in the midgut of *D. plexippus* while the concentration dropped in the hindgut, suggesting a hitherto undescribed mechanism of toxin partitioning in the monarch gut. In contrast, for *E. core*, we detected constant cardenolide concentrations along the gut passage including the hind gut. These observations indicate that cardenolides are selectively retained in the monarch gut lumen resulting in higher local concentrations of preferentially sequestered cardenolides, such as calotropin, calactin, frugoside. We speculate that the accumulation of cardenolides in the midgut creates a steep concentration gradient supporting efficient sequestration.

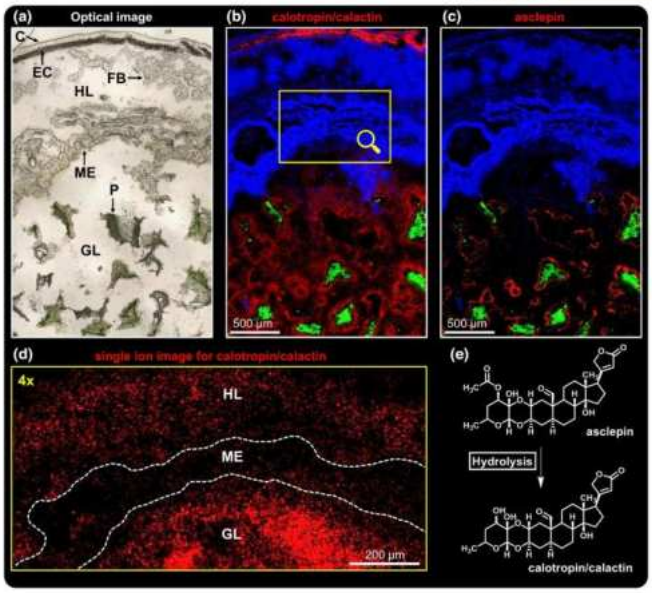


FIGURE 4 High-resolution AP-SMALDI MSI (5 µm pixel size) of a transverse *Danaus plexippus* (biological replicate 7) section. (a) Optical image of the analysed region of interest. C, cuticle; EC, epidermal cells; HL, haemolymph; FB, fat body; ME, midgut epithelium; GL, gut lumen; P, *Asclepias curassavica* plant material. (b, c) RGB overlay images showing the spatial distribution of (b) calactin/calotropin ($[M+K]^+$, red) at *m/z* 571.2304, (c) asclepin ($[M+K]^+$, red) at *m/z* 613.2427, and (b, c) pheophytin a ($[M+K]^+$, green) at *m/z* 909.5290 and PE(36:3) ($[M+K]^+$, blue) at *m/z* 780.4940. (d) Magnified view (4×) of the region outlined in (b) showing the single-ion image for calactin/calotropin ($[M+K]^+$) in red. Due to the high ion intensity in the integument, the intensity scale for this image was adjusted to visualize cardenolides in the midgut epithelium. (e) Putative degradation pathway of asclepin in the *D. plexippus* gut.

We conducted MSI experiments with caterpillars fed with the cardenolide-free diet *O. coeruleum* to purge their guts from milkweed cardenolides to further address the hypothesis of cardenolide retention in the monarch caterpillar gut. Consistent with our prediction, calotropin/calactin, frugoside and calotoxin were still abundant between *O. coeruleum* leaf particles in the gut lumen of monarch caterpillars, while in the gut lumen of *E. core*, no cardenolides were detected anymore after feeding on *O. coeruleum* leaves. We propose a mechanism analogous to adsorption chromatography (i.e., molecules moving in a liquid phase adhering to a stationary phase), retaining cardenolides in the gut lumen while the food contents are passing by and are defaecated. How this could be mediated mechanistically remains an open question and it is interesting to note, that the spatial distribution of cardenolide MSI signals seems to resemble the shape of the *O. coeruleum* leaf particles suggesting adhesion of cardenolides to *O. coeruleum* leaf particles maybe based on physiochemical interactions (e.g., Van der Waals force, hydrogen bonds). Moreover, after purging there were no cardenolides detected anymore in the ectoperitrophic space which showed strong intensities in caterpillars actively feeding on *A. curassavica*. This observation may indicate removal of cardenolides by sequestration via the midgut epithelium. Similarly, the body cavity was free of cardenolides suggesting rapid clearance once the supply from the gut lumen is halted.

Besides differences in the distribution, we also observed striking differences regarding the structural composition of cardenolides in the midgut of both caterpillar species. Remarkably, the stereoisomer ratio of calotropin/calactin in the *E. core* gut lumen (24:1) differed significantly from that found in the monarch gut lumen (1.2:1) and *A. curassavica* leaves (1.6:1). Based on the inhibition of $Na^+/K^+$-ATPase, calactin was reported to be >3× more toxic for *E. core* than its stereoisomer calotropin (Petschenka et al., 2018). Hence, we suggest that *E. core* prevents cardenolide intoxication by minimizing the concentration of calactin in the midgut which could be either mediated by converting calactin into a structurally different cardenolide, by degradation, or by prevention of calactin production from uscharidin contained in the ingested plant material (Seiber et al., 1980). Along the same lines, monarch caterpillars could maintain a high concentration of highly toxic calactin for defence.

Unlike calactin, calotropin, and frugoside, the predominant cardenolides in *A. curassavica* leaves, uscharidin, asclepin, voruscharin and uscharin, do not belong to the preferentially sequestered

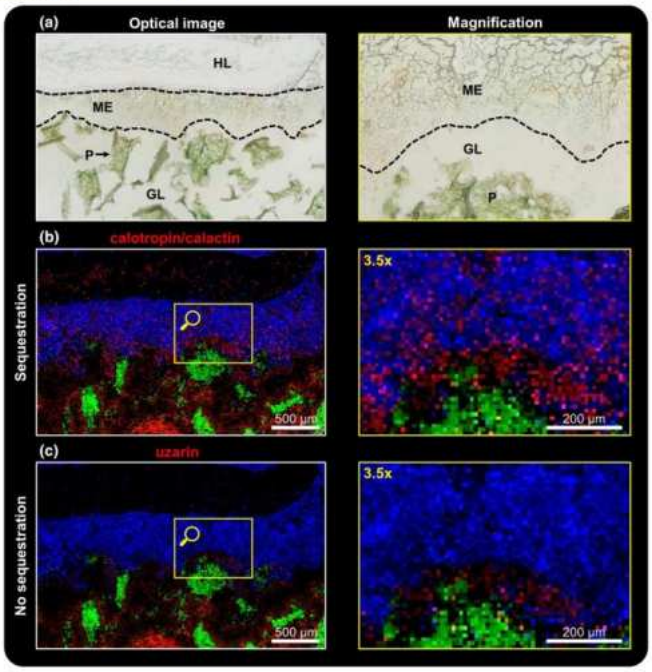


FIGURE 5 High-resolution AP-SMALDI MSI (10 µm pixel size) of a longitudinal *Danaus plexippus* (biological replicate 3) section. (a) Optical image of the analysed region of interest and magnified view (3.5×) of the outlined region in (b, c). P, *Asclepias curassavica* plant material; GL, gut lumen; ME, midgut epithelium; HL, haemolymph. (b, c) RGB overlay images and magnified view of the outlined region showing the spatial distribution of calactin/calotropin ($[M+K]^+$, red) at *m/z* 571.2304 in (b), uzarin ($[M+K]^+$, red) at *m/z* 737.3149 in (c), pheophytin a ($[M+K]^+$, green) at *m/z* 909.5290 and PE(36:3) ($[M+K]^+$, blue) at *m/z* 780.4940.

cardenolides of the monarch, despite having high structural similarity to calotropin and calactin and sharing the same aglycon (calotropagenin). Surprisingly, asclepin, which only differs from calotropin/calactin by having an acetoxy-group (-OAc) instead of a hydroxy-group (-OH) in the sugar moiety, is not sequestered and instead, was exclusively detected at fringes of ingested *A. curassavica* leaf material. Given the high structural similarity to calotropin/calactin, it seems puzzling that the molecular mechanism underlying sequestration prohibits the uptake of asclepin. More likely, asclepin might be rapidly converted into calactin and/or calotropin instead of being not sequestered.

Similar observations regarding the metabolic conversion of structurally-related cardenolides into calotropin and calactin by the monarch caterpillar were already made decades ago for uscharidin (Marty & Krieger, 1984; Seiber et al., 1980) and recently, for voruscharin by Agrawal et al. (2021). Interestingly, both, uscharidin and voruscharin occured at similar concentrations in *A. curassavica* leaves like asclepin but were very abundant in the monarch gut lumen. Consequently, we hypothesize that the conversion rate of asclepin into calactin and/or calotropin is significantly higher compared to uscharidin and voruscharin, suggesting a passive mechanism such as gut pH as observed for voruscharin (Agrawal et al., 2021) and not an involvement of enzymes as it was shown for uscharidin (Marty & Krieger, 1984).

The monarch $Na^+/K^+$-ATPase shows up to 94-fold higher resistance against cardenolides compared to nonadapted $Na^+/K^+$-ATPases (Petschenka et al., 2018). Remarkably, monarch $Na^+/K^+$-ATPase is only less than twofold more resistant to the thiazolidine-ring-containing cardenolides uscharin and voruscharin which dominate the cardenolide spectrum of *A. curassavica* leaves compared to porcine $Na^+/K^+$-ATPase (Agrawal et al., 2021). Consequently, the lack of sequestration of uscharin and voruscharin by monarch caterpillars, observed in this study, was interpreted as an adaptation to avoid toxicity. However, due to the high sensitivity of the employed AP-SMALDI MSI system, we were able to detect and visualize the accumulation of uscharin and voruscharin in the epidermal cells of the integument and LC-MS-based quantification revealed 160× (uscharin) and 50× lower concentrations compared

to the predominantly sequestered calotropin. In conclusion, our data suggest that uscharin and voruscharin are sequestered but to a comparatively low extent. Alternatively to representing plant defence compounds specifically directed against the monarch butterfly, reduced sequestration and limited resistance of monarch $Na^+/K^+$-ATPase towards uscharin and voruscharin might be due to the rapid spontaneous degradation of voruscharin in the caterpillar gut which is also likely for uscharin due to the high structural similarity. Consequently, these compounds would not be available as a substrate for sequestration and not exert selection pressure on monarch $Na^+/K^+$-ATPase.

Our MSI analyses indicate that the midgut epithelium plays a critical role regarding the selectivity of sequestration by prohibiting the uptake of individual cardenolides such as uzarin. For uzarin, metabolism can be ruled out as a factor preventing sequestration, since this compound was found abundantly in the gut lumen and was observed in direct contact with the apical surface of the midgut epithelium. In other words, we suggest that the midgut epithelium discriminates against individual compounds by an unknown mechanism. The nonsequestered biglucoside uzarin was the largest cardenolide detected and is comparatively polar, suggesting that size or polarity could be important determinants. Selective uptake of structurally different nonmilkweed cardenolides was already demonstrated earlier (Frick & Wink, 1995). Here, we show that also milkweed cardenolides that actually occur in the diet of the monarch caterpillar are sequestered selectively.

Although sequestration of plant toxins was described for more than 275 insect species involving different classes of chemical compounds (Beran & Petschenka, 2022; Opitz & Müller, 2009), it is still largely unknown how plant toxins are transported across the insect gut epithelium (i.e. from the gut lumen into the body cavity). Using high-resolution MSI (10 μm pixel size), we were able to detect cardenolides within the midgut epithelium of monarch caterpillars. Notably, cardenolides appeared in a discrete granular pattern, suggesting that cardenolides are transported as aggregates and not as individual molecules. This pattern might indicate a vesicular transport via transcytosis, similar to what was described for the uptake of albumin across the midgut of the silkworm (*Bombyx mori*) (Casartelli et al., 2005). Since this granular pattern of cardenolides was already observed in the midgut lumen, the putative cardenolide vesicles may be plant derived. Although our histological sections were comparatively thick and likely contained several layers of cells complicating interpretation, the uniform distribution of the observed particles suggests that the transport occurs in a trans- and not in a paracellular fashion. It was suggested earlier that a carrier mechanism mediates the transport of cardenolides across the midgut epithelium in monarch caterpillars (Frick & Wink, 1995). How the cardenolide aggregations observed here could be aligned with a carrier-mediated process, however, remains an open question.

Remarkably, also other secondary plant metabolites such as polysaccharides and flavonoids as well as primary metabolites (e.g., guanosine) appeared in the same granular pattern within the midgut epithelium, suggesting that vesicular uptake is a universal mode of uptake for various metabolites. A similar pattern was found for *E. core* regarding these metabolites but remarkably, cardenolides were not detected in the midgut epithelium. Lipophilic and amphiphilic allelochemicals are expected to be sequestered into lipid aggregates (micelles) in the fluid phase of the gut of herbivorous insects proportionately to their lipophilicity (Barbehenn, 1999). Moreover, micelles formed by the aggregation of lysophospholipids, galactosyl glycerides, long chain fatty acids, and other amphiphilic and lipophilic compounds are known to represent the primary constituents of the nonaqueous phase of the midgut fluid in insect herbivores (Barbehenn, 1999). Therefore, it is likely that the granules which we observed represent micelles containing cardenolides and other metabolites. The observation of these putative micelles in the midgut epithelium of monarch caterpillars suggests that micelles composed of plant lipids and cardenolides which may cross the midgut epithelium by diffusion, represent the mode of transport by which cardenolides are sequestered.

It is unclear, however, how caterpillars of *E. core* discriminate against the uptake of cardenolides while apparently taking up other metabolites in a similar fashion. The peritrophic membrane of grasshoppers has been demonstrated to prevent the uptake of micelles containing various plant toxins including the cardenolide digitoxin by ultrafiltration (Barbehenn, 1999). This mechanism, however, is unlikely to explain nonsequestration of cardenolides in *E. core*, since cardenolide granules were observed in close contact with the midgut epithelium and thus were able to cross the peritrophic membrane surrounding the food bolus. It rather seems likely that degradation of cardenolides in the fluid-phase of the gut prevents sequestration of cardenolides in *E. core*.

Our findings indicate that caterpillars of the monarch butterfly possess an entire suite of physiological mechanisms involved in sequestration of cardenolides which may relate to their ecological interactions with predators and parasites at various scales. Accumulation of cardenolides in the gut lumen may not only facilitate sequestration but could also protect larvae against the protozoan parasite *Ophryocystis elektroscirrha* after oral infection (Tan et al., 2018). Similarly, compartmentalization of cardenolides in the epithelial cells of the integument might represent a mechanism to avoid autotoxicity but at the same time cardenolides are located where they will be first perceived by predators. Collectively, our spatially resolved metabolomics approach revealed novel insight into the selectivity and the mechanism of cardenolide sequestration as well as of the location of sequestered cardenolides in monarch butterflies and demonstrates the potential of high-resolution AP-SMALDI MSI to explore insect-plant interaction biochemistry and to unravel the spatiotemporal fate of xenobiotics in insects (e.g., insecticides).

## AUTHOR CONTRIBUTIONS

Georg Petschenka, Bernhard Spengler and Domenic Dreisbach designed research, Domenic Dreisbach, Georg Petschenka, Anja

Betz, Linda Tenbusch and Dhaka R. Bhandari performed research, Domenic Dreisbach and Georg Petschenka analysed data, Domenic Dreisbach, Georg Petschenka, Bernhard Spengler, and Andreas Vilcinskas wrote the manuscript.

## ACKNOWLEDGEMENTS

We thank Hermann Falkenhahn, Johanna Weber, and Sabrina Stiehler for insect rearing, growing of plants and collecting samples. Technical support by Thermo Fisher Scientific GmbH (Bremen, Germany) and TransMIT GmbH (Giessen, Germany) are gratefully acknowledged. This research was funded by DFG grant PE 2059/3-1 to G.P. and the LOEWE Programme of the State of Hesse by funding the LOEWE Centre for Insect Biotechnology and Bioresources. Open Access funding enabled and organized by Projekt DEAL.

## CONFLICT OF INTEREST STATEMENT

B.S. is a consultant, and D.D. is a part-time employee of TransMIT GmbH, Giessen, Germany. All other authors declare no conflicts of interest.

## DATA AVAILABILITY STATEMENT

AP-SMALDI MSI data is publicly accessible in the vendor neutral imzML format at https://metaspace2020.eu/project/Dreisbach_et_al_2023. Raw data on cardenolide quantification along caterpillar gut passages via HPLC-DAD is available as supporting information associated with this article.

## BENEFIT-SHARING STATEMENTS

Biological resources used in this data are not regulated under The Nagoya Protocol on Access and Benefit-sharing.

## ORCID

*Dhaka R. Bhandari* https://orcid.org/0000-0003-2658-6065
*Anja Betz* https://orcid.org/0000-0002-9263-6035
*Andreas Vilcinskas* https://orcid.org/0000-0001-8276-4968
*Bernhard Spengler* https://orcid.org/0000-0003-0179-5653
*Georg Petschenka* https://orcid.org/0000-0002-9639-3042

## REFERENCES

Abdalsamee, M. K., Giampà, M., Niehaus, K., & Müller, C. (2014). Rapid incorporation of glucosinolates as a strategy used by a herbivore to prevent activation by myrosinases. *Insect Biochemistry and Molecular Biology*, *52*, 115–123. https://doi.org/10.1016/j.ibmb.2014.07.002

Agrawal, A. A., Böröczky, K., Haribal, M., Hastings, A. P., White, R. A., Jiang, R.-W., & Duplais, C. (2021). Cardenolides, toxicity, and the costs of sequestration in the coevolutionary interaction between monarchs and milkweeds. *Proceedings of the National Academy of Sciences of the United States of America*, *118*(16), e2024463118. https://doi.org/10.1073/pnas.2024463118

Agrawal, A. A., Petschenka, G., Bingham, R. A., Weber, M. G., & Rasmann, S. (2012). Toxic cardenolides: Chemical ecology and coevolution of specialized plant-herbivore interactions. *New Phytologist*, *194*(1), 28–45. https://doi.org/10.1111/j.1469-8137.2011.04049.x

Ayres, M. P., Clausen, T. P., MacLean, S. F., Jr., Redman, A. M., & Reichardt, P. B. (1997). Diversity of structure and antiherbivore activity in condensed tannins. *Ecology*, *78*(6), 1696–1712.

Barbehenn, R. V. (1999). Non-absorption of ingested lipophilic and amphiphilic allelochemicals by generalist grasshoppers: The role of extractive ultrafiltration by the peritrophic envelope. *Archives of Insect Biochemistry and Physiology*, *42*(2), 130–137. https://doi.org/10.1002/(SICI)1520-6327(199910)42:2<130::AID-ARCH3>3.0.CO;2-C

Beran, F., Pauchet, Y., Kunert, G., Reichelt, M., Wielsch, N., Vogel, H., Reinecke, A., Svatoš, A., Mewis, I., Schmid, D., Ramasamy, S., Ulrichs, C., Hansson, B. S., Gershenzon, J., & Heckel, D. G. (2014). *Phyllotreta striolata* flea beetles use host plant defense compounds to create their own glucosinolate-myrosinase system. *Proceedings of the National Academy of Sciences of the United States of America*, *111*(20), 7349–7354. https://doi.org/10.1073/pnas.1321781111

Beran, F., & Petschenka, G. (2022). Sequestration of plant defense compounds by insects: From mechanisms to insect–plant coevolution. *Annual Review of Entomology*, *67*(1), 163–180. https://doi.org/10.1146/annurev-ento-062821-062319

Brower, L. P., Ryerson, W. N., Coppinger, L. L., & Glazier, S. C. (1968). Ecological chemistry and the palatability spectrum. *Science*, *161*(3848), 1349–1350.

Buchberger, A. R., DeLaney, K., Johnson, J., & Li, L. (2018). Mass spectrometry imaging: A review of emerging advancements and future insights. *Analytical Chemistry*, *90*(1), 240–265. https://doi.org/10.1021/acs.analchem.7b04733

Casartelli, M., Corti, P., Giovanna Leonardi, M., Fiandra, L., Burlini, N., Pennacchio, F., & Giordana, B. (2005). Absorption of albumin by the midgut of a lepidopteran larva. *Journal of Insect Physiology*, *51*(8), 933–940. https://doi.org/10.1016/j.jinsphys.2005.04.008

Cresswell, J. E., Merritt, S. Z., & Martin, M. M. (1992). The effect of dietary nicotine on the allocation of assimilated food to energy metabolism and growth in fourth-instar larvae of the southern armyworm, Spodoptera eridania (lepidoptera: Noctuidae). *Oecologia*, *89*(3), 449–453.

Dobler, S., Dalla, S., Wagschal, V., & Agrawal, A. A. (2012). Community-wide convergent evolution in insect adaptation to toxic cardenolides by substitutions in the Na, K-ATPase. *Proceedings of the National Academy of Sciences of the United States of America*, *109*(32), 13040–13045.

Dobler, S., Petschenka, G., Wagschal, V., & Flacht, L. (2015). Convergent adaptive evolution – How insects master the challenge of cardiac glycoside-containing host plants. *Entomologia Experimentalis et Applicata*, *157*(1), 30–39. https://doi.org/10.1111/eea.12340

Duffey, S. S. (1980). Sequestration of plant natural products by insects. *Annual Review of Entomology*, *25*(1), 447–477.

Dussourd, D. E., & Hoyle, A. M. (2000). Poisoned plusiines: Toxicity of milkweed latex and cardenolides to some generalist caterpillars. *Chemoecology*, *10*(1), 11–16. https://doi.org/10.1007/PL00001810

Fraenkel, G. S. (1959). The raison d'Etre of secondary plant substances: These odd chemicals arose as a means of protecting plants from insects and now guide insects to food. *Science*, *129*(3361), 1466–1470.

Frick, C., & Wink, M. (1995). Uptake and sequestration of ouabain and other cardiac glycosides in Danaus plexippus (lepidoptera: Danaidae): Evidence for a carrier-mediated process. *Journal of Chemical Ecology*, *21*(5), 557–575.

Geier, B., Oetjen, J., Ruthensteiner, B., Polikarpov, M., Gruber-Vodicka, H., & Liebeke, M. (2021). Connecting structure and function from organisms to molecules in small animal symbioses through chemo-histo-tomography. *bioRxiv*. https://doi.org/10.1101/2020.09.28.316802

Geier, B., Sogin, E. M., Michellod, D., Janda, M., Kompauer, M., Spengler, B., Dubilier, N., & Liebeke, M. (2020). Spatial metabolomics of in situ host–microbe interactions at the micrometre scale. *Nature Microbiology*, *5*(3), 498–510.

Holzinger, F., & Wink, M. (1996). Mediation of cardiac glycoside insensitivity in the monarch butterfly (Danaus plexippus): Role of an amino

acid substitution in the ouabain binding site of Na+, K+-ATPase. *Journal of Chemical Ecology*, *22*(10), 1921–1937.

Iwama, T., Kano, K., Saigusa, D., Ekroos, K., van Echten-Deckert, G., Vogt, J., & Aoki, J. (2021). Development of an on-tissue derivatization method for MALDI mass spectrometry imaging of bioactive lipids containing phosphate monoester using Phos-tag. *Analytical Chemistry*, *93*(8), 3867–3875.

Joo, C., Balci, H., Ishitsuka, Y., Buranachai, C., & Ha, T. (2008). Advances in single-molecule fluorescence methods for molecular biology. *Annual Review of Biochemistry*, *77*(1), 51–76. https://doi.org/10.1146/annurev.biochem.77.070606.101543

Kadesch, P., Hollubarsch, T., Gerbig, S., Schneider, L., Silva, L. M. R., Hermosilla, C., Taubert, A., & Spengler, B. (2020). Intracellular parasites toxoplasma gondii and Besnoitia besnoiti, unveiled in single host cells using AP-SMALDI MS imaging. *Journal of the American Society for Mass Spectrometry*, *31*(9), 1815–1824.

Kadesch, P., Quack, T., Gerbig, S., Grevelding, C. G., & Spengler, B. (2019). Lipid topography in *Schistosoma mansoni* Cryosections, revealed by microembedding and high-resolution atmospheric-pressure matrix-assisted laser desorption/ionization (MALDI) mass spectrometry imaging. *Analytical Chemistry*, *91*(7), 4520–4528.

Kadesch, P., Quack, T., Gerbig, S., Grevelding, C. G., & Spengler, B. (2020). Tissue-and sex-specific lipidomic analysis of Schistosoma mansoni using high-resolution atmospheric pressure scanning microprobe matrix-assisted laser desorption/ionization mass spectrometry imaging. *PLoS Neglected Tropical Diseases*, *14*(5), e0008145.

Karageorgi, M., Groen, S. C., Sumbul, F., Pelaez, J. N., Verster, K. I., Aguilar, J. M., Hastings, A. P., Bernstein, S. L., Matsunaga, T., Astourian, M., Guerra, G., Rico, F., Dobler, S., Agrawal, A. A., & Whiteman, N. K. (2019). Genome editing retraces the evolution of toxin resistance in the monarch butterfly. *Nature*, *574*(7778), 409–412. https://doi.org/10.1038/s41586-019-1610-8

Kazana, E., Pope, T. W., Tibbles, L., Bridges, M., Pickett, J. A., Bones, A. M., Powell, G., & Rossiter, J. T. (2007). The cabbage aphid: A walking mustard oil bomb. *Proceedings of the Royal Society B: Biological Sciences*, *274*(1623), 2271–2277. https://doi.org/10.1098/rspb.2007.0237

Kherlopian, A. R., Song, T., Duan, Q., Neimark, M. A., Po, M. J., Gohagan, J. K., & Laine, A. F. (2008). A review of imaging techniques for systems biology. *BMC Systems Biology*, *2*(1), 1–18.

Koestler, M., Kirsch, D., Hester, A., Leisner, A., Guenther, S., & Spengler, B. (2008). A high-resolution scanning microprobe matrix-assisted laser desorption/ionization ion source for imaging analysis on an ion trap/Fourier transform ion cyclotron resonance mass spectrometer. *Rapid Communications in Mass Spectrometry*, *22*(20), 3275–3285.

Koiwa, H., Bressan, R. A., & Hasegawa, P. M. (1997). Regulation of protease inhibitors and plant defense. *Trends in Plant Science*, *2*(10), 379–384.

Kompauer, M., Heiles, S., & Spengler, B. (2017a). Atmospheric pressure MALDI mass spectrometry imaging of tissues and cells at 1.4-μm lateral resolution. *Nature Methods*, *14*(1), 90–96. https://doi.org/10.1038/nmeth.4071

Kompauer, M., Heiles, S., & Spengler, B. (2017b). Autofocusing MALDI mass spectrometry imaging of tissue sections and 3D chemical topography of nonflat surfaces. *Nature Methods*, *14*(12), 1156–1158.

Malcolm, S. B., & Zalucki, M. P. (1996). *Milkweed latex and cardenolide induction may resolve the lethal plant defence paradox*. Proceedings of the 9th international symposium on insect-plant relationships, pp. 193–196.

Malcom, S., & Rothschild, M. (1983). A danaid mullerian mimic, Euploea core amymone (Cramer) lacking cardenolides in the pupal and adult stages. *Biological Journal of the Linnean Society*, *19*(1), 27–33. https://doi.org/10.1111/j.1095-8312.1983.tb00774.x

Marty, M. A., & Krieger, R. I. (1984). Metabolism of uscharidin, a milkweed cardenolide, by tissue homogenates of monarch butterfly larvae, Danaus plexippus L. *Journal of Chemical Ecology*, *10*(6), 945–956.

Narberhaus, I., Zintgraf, V., & Dobler, S. (2005). Pyrrolizidine alkaloids on three trophic levels–evidence for toxic and deterrent effects on phytophages and predators. *Chemoecology*, *15*(2), 121–125.

Opitz, S. E. W., & Müller, C. (2009). Plant chemistry and insect sequestration. *Chemoecology*, *19*(3), 117–154.

Palmer, A., Phapale, P., Chernyavsky, I., Lavigne, R., Fay, D., Tarasov, A., Kovalev, V., Fuchser, J., Nikolenko, S., & Pineau, C. (2017). FDR-controlled metabolite annotation for high-resolution imaging mass spectrometry. *Nature Methods*, *14*(1), 57–60.

Parsons, J. A. (1965). A digitalis-like toxin in the monarch butterfly, Danaus plexippus L. *The Journal of Physiology*, *178*(2), 290–304. https://doi.org/10.1113/jphysiol.1965.sp007628

Paschke, C., Leisner, A., Hester, A., Maass, K., Guenther, S., Bouschen, W., & Spengler, B. (2013). Mirion—A software package for automatic processing of mass spectrometric images. *Journal of the American Society for Mass Spectrometry*, *24*(8), 1296–1306.

Petschenka, G., & Agrawal, A. A. (2015). Milkweed butterfly resistance to plant toxins is linked to sequestration, not coping with a toxic diet. *Proceedings of the Royal Society B: Biological Sciences*, *282*(1818), 20151865.

Petschenka, G., Fei, C. S., Araya, J. J., Schröder, S., Timmermann, B. N., & Agrawal, A. A. (2018). Relative selectivity of plant cardenolides for Na+/K+-ATPases from the monarch butterfly and non-resistant insects. *Frontiers in Plant Science*, *9*, 1424.

Pluskal, T., Castillo, S., Villar-Briones, A., & Orešič, M. (2010). MZmine 2: Modular framework for processing, visualizing, and analyzing mass spectrometry-based molecular profile data. *BMC Bioinformatics*, *11*(1), 395. https://doi.org/10.1186/1471-2105-11-395

Robert, C. A. M., Zhang, X., Machado, R. A. R., Schirmer, S., Lori, M., Mateo, P., Erb, M., & Gershenzon, J. (2017). Sequestration and activation of plant toxins protect the western corn rootworm from enemies at multiple trophic levels. *eLife*, *6*, e29307. https://doi.org/10.7554/eLife.29307

Robichaud, G., Garrard, K. P., Barry, J. A., & Muddiman, D. C. (2013). MSiReader: An open-source interface to view and analyze high resolving power MS imaging files on Matlab platform. *Journal of the American Society for Mass Spectrometry*, *24*(5), 718–721.

Schatzmann, H. J. (1953). Herzglykoside als Hemmstoffe fur den activen Kalium und natrium-transport durch die Erythrocytemembran. *Helvetica Physiologica et Pharmacologica Acta*, *11*, 346–354.

Seiber, J. N., Tuskes, P. M., Brower, L. P., & Nelson, C. J. (1980). Pharmacodynamics of some individual milkweed cardenolides fed to larvae of the monarch butterfly (Danaus plexippus L.). *Journal of Chemical Ecology*, *6*(2), 321–339.

Spengler, B. (2015). Mass spectrometry imaging of biomolecular information. *Analytical Chemistry*, *87*(1), 64–82. https://doi.org/10.1021/ac504543v

Spengler, B., & Hubert, M. (2002). Scanning microprobe matrix-assisted laser desorption ionization (SMALDI) mass spectrometry: Instrumentation for sub-micrometer resolved LDI and MALDI surface analysis. *Journal of the American Society for Mass Spectrometry*, *13*(6), 735–748.

Spengler, B., Hubert, M., & Kaufmann, R. (1994). *MALDI ion imaging and biological ion imaging with a new scanning UV-laser microprobe*. Proceedings of the 42nd annual conference on mass spectrometry and allied topics, 1041.

Tan, W.-H., Tao, L., Hoang, K. M., Hunter, M. D., & de Roode, J. C. (2018). The effects of milkweed induced defense on parasite resistance in monarch butterflies, *Danaus plexippus*. *Journal of Chemical Ecology*, *44*, 1040–1044.

Taylor, C. J., & Yack, J. E. (2019). Hearing in caterpillars of the monarch butterfly (*Danaus plexippus*). *Journal of Experimental Biology*, *222*(22), jeb211862. https://doi.org/10.1242/jeb.211862

van Hove, E. R. A., Smith, D. F., & Heeren, R. M. A. (2010). A concise review of mass spectrometry imaging. *Journal of Chromatography A*, *1217*(25), 3946–3954.

Vaughan, G. L., & Jungreis, A. M. (1977). Insensitivity of lepidopteran tissues to ouabain: Physiological mechanisms for protection from cardiac glycosides. *Journal of Insect Physiology*, *23*(5), 585–589.

Von Reichstein, T., Von Euw, J., Parsons, J. A., & Rothschild, M. (1968). Heart poisons in the monarch butterfly. *Science*, *161*(3844), 861–866.

Warashina, T., & Shirota, O. (2021). Tetracyclic triterpenoids, steroids and Lignanes from the aerial parts of *Oxypetalum caeruleum*. *Chemical and Pharmaceutical Bulletin*, *69*(2), 226–231. https://doi.org/10.1248/cpb.c20-00789

Yang, F., Chen, J., Ruan, Q., Saqib, H. S. A., He, W., & You, M. (2020). Mass spectrometry imaging: An emerging technology for the analysis of metabolites in insects. *Archives of Insect Biochemistry and Physiology*, *103*(4), e21643.

Yang, Z.-L., Nour-Eldin, H. H., Hänniger, S., Reichelt, M., Crocoll, C., Seitz, F., Vogel, H., & Beran, F. (2021). Sugar transporters enable a leaf beetle to accumulate plant defense compounds. *Nature Communications*, *12*(1), 2658. https://doi.org/10.1038/s41467-021-22982-8

Zhang, R.-R., Tian, H.-Y., Tan, Y.-F., Chung, T.-Y., Sun, X.-H., Xia, X., Ye, W.-C., Middleton, D. A., Fedosova, N., Esmann, M., Tzen, J. T. C., & Jiang, R.-W. (2014). Structures, chemotaxonomic significance, cytotoxic and Na+,K+-ATPase inhibitory activities of new cardenolides from Asclepias curassavica. *Organic & Biomolecular Chemistry*, *12*(44), 8919–8929. https://doi.org/10.1039/C4OB01545B

Züst, T., Petschenka, G., Hastings, A. P., & Agrawal, A. A. (2019). Toxicity of milkweed leaves and latex: Chromatographic quantification versus biological activity of cardenolides in 16 *Asclepias species*. *Journal of Chemical Ecology*, *45*(1), 50–60. https://doi.org/10.1007/s10886-018-1040-3

## SUPPORTING INFORMATION

Additional supporting information can be found online in the Supporting Information section at the end of this article.

**How to cite this article:** Dreisbach, D., Bhandari, D. R., Betz, A., Tenbusch, L., Vilcinskas, A., Spengler, B., & Petschenka, G. (2023). Spatial metabolomics reveal divergent cardenolide processing in the monarch (*Danaus plexippus*) and the common crow butterfly (*Euploea core*). *Molecular Ecology Resources*, *00*, 1–16. https://doi.org/10.1111/1755-0998.13786

# SUPPLEMENTARY INFORMATION

## Spatial metabolomics reveal divergent cardenolide processing in the monarch (*Danaus plexippus*) and the common crow butterfly (*Euploea core*)

**Domenic Dreisbach[1], Dhaka R. Bhandari[1], Anja Betz[3], Linda Tenbusch[2], Andreas Vilcinskas[2,4], Bernhard Spengler[1], Georg Petschenka[3]**

[1]Institute of Inorganic and Analytical Chemistry, Justus Liebig University Giessen, Heinrich-Buff-Ring 17, 35392 Giessen, Germany

[2]Institute of Insect Biotechnology, Justus Liebig University Giessen, Heinrich-Buff-Ring 26-32, 35392 Giessen, Germany

[3]Institute of Phytomedicine, University of Hohenheim, Otto-Sander-Straße 5, 70599 Stuttgart, Germany

[4]Fraunhofer Institute for Molecular Biology and Applied Ecology (IME), Branch for Bioresources, Ohlebergsweg 12, 35392 Giessen, Germany

**Supplementary Note 1. Experimental parameters for HPLC-MS and HPLC-DAD**

For HPLC-MS, the injection volume was 15 µL, and the column compartment was set to 30 °C and 50 °C, respectively. The following acetonitrile–H2O (0.1 % FA) gradient gradient was used at a flow rate of 0.5 mL/min: 0–2 min, 10% acetonitrile; 2–20 min, 20–70% acetonitrile; 20–25 min, 70–95% acetonitrile; 25–30 min, 95% acetonitrile; 30–35 min, 95–10% acetonitrile. The mass spectrometer was operated in positive-ion mode in a mass-to-charge-ratio (*m*/*z*) range of 250 to 1000 at a mass resolution of 240,000 at *m*/*z* 200. The following HESI-source parameters were applied: spray voltage (+), 3.5 kV; capillary temperature, 300 °C; sheath gas flow rate, 35 psi; aux gas flowrate, 12 psi; aux gas heater temperature, 150 °C. Normalized collision energy (NCE) of 25% was used for fragmentation with z = 1 as default charge state.
For HPLC-DAD, the injection volume was 15 µL. Cardenolides were eluted at a constant flow of 0.7 ml/min at room temperature with an acetonitrile–H2O gradient as follows: 0–1 min 20% acetonitrile, 31 min 30% acetonitrile, 47 min 50% acetonitrile, 49 min 95% acetonitrile, 54 min 95% acetonitrile, 55 min 20% acetonitrile reconditioning for 10 min at 16% acetonitrile. UV-absorbance spectra were recorded from 200 to 400 nm with a diode array detector.

**Supplementary Table 1**. Overview of the biological replicates of *D. plexippus* and *E. core*, which were analysed via AP-SMALDI MSI. Plant diet, orientation of cryo-sectioning and the figures for the corresponding MSI results are mentioned.

| Biological replicate | Diet | Cryo-sectioning | MSI results |
|---|---|---|---|
| ***Danaus plexippus* 1** | *A. curassavica* | transversal | Figs. 1, S9 |
| ***Danaus plexippus* 2** | *A. curassavica* | transversal | Fig. S8 |
| ***Danaus plexippus* 3** | *A. curassavica* | longitudinal | Figs. 2, 5 |
| ***Danaus plexippus* 4** | *A. curassavica* | longitudinal | Fig. S15 |
| ***Danaus plexippus* 5** | *A. curassavica*, purged with *O. coeruleum* | transversal | Figs. 3, S21 |
| ***Danaus plexippus* 6** | *A. curassavica*, purged with *O. coeruleum* | transversal | Fig. S23 |
| ***Danaus plexippus* 7** | *A. curassavica* | transversal | Figs. 4, S25 |
| ***Euploea core 1*** | *A. curassavica* | transversal | Figs. 1, S9 |
| ***Euploea core 2*** | *A. curassavica* | transversal | Fig. S8 |
| ***Euploea core 3*** | *A. curassavica* | longitudinal | Fig. 2 |
| ***Euploea core 4*** | *A. curassavica* | longitudinal | Fig. S15 |
| ***Euploea core 5*** | *A. curassavica*, purged with *O. coeruleum* | transversal | Fig. S23 |

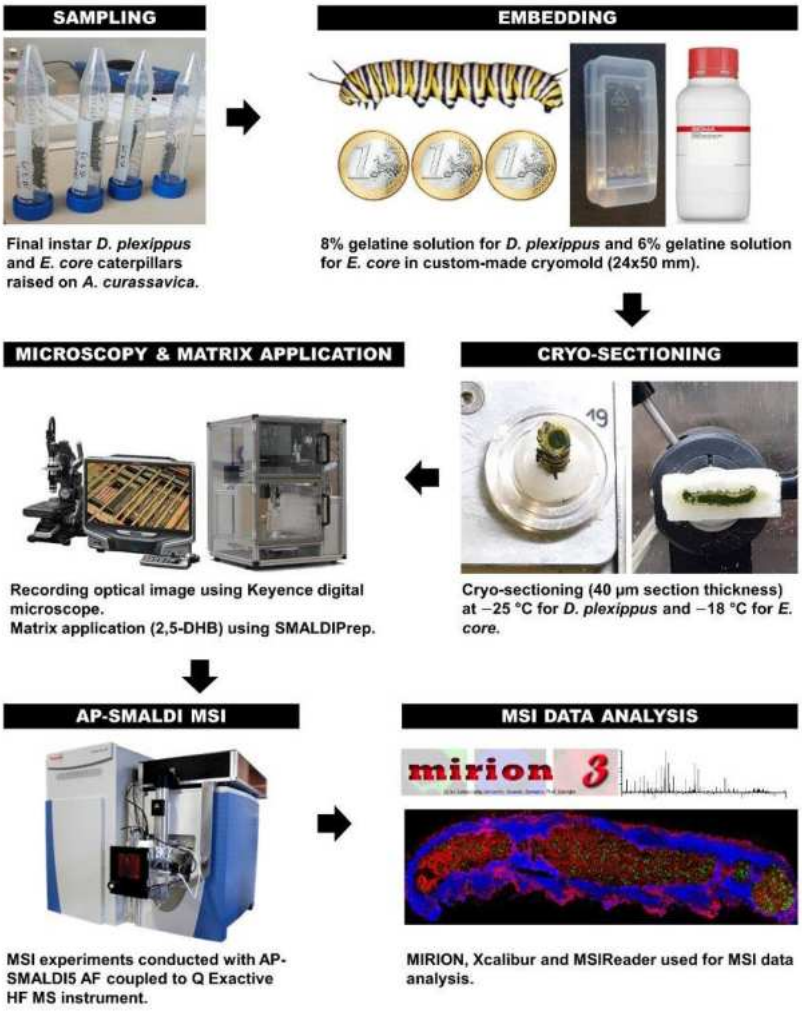


**Figure S1**. MSI-based spatial metabolomics workflow to study the distribution of sequestered cardenolides in milkweed butterflies.

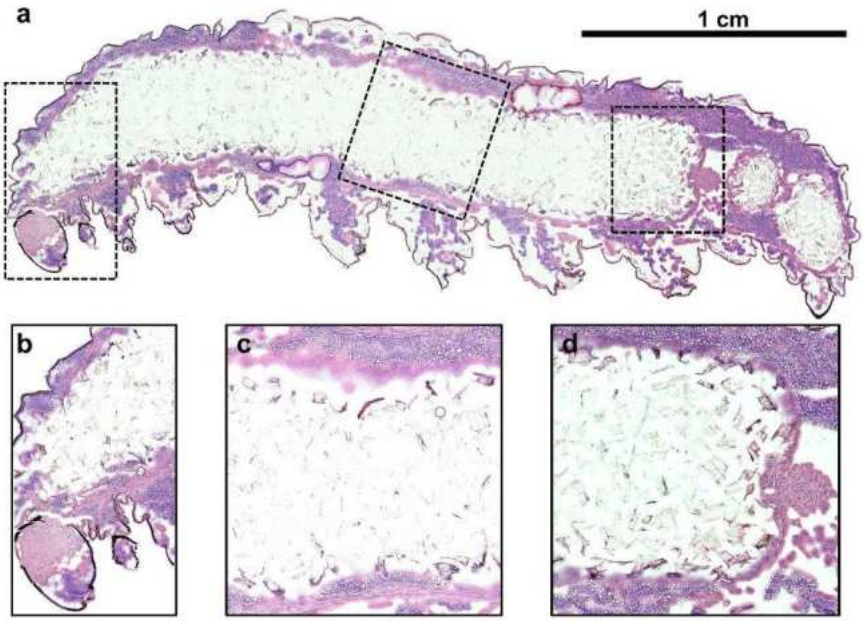


**Figure S2**. Optical image of a longitudinal monarch section (biological replicate 3), which was analysed via AP-SMALDI MSI (see Figure 2). The morphology and different tissue types remain unperturbed during AP-SMALDI MSI analysis, thus allowing to perform classical histology on the same section. The matrix layer was removed with 70% ethanol and H&E-staining was carried out. (**a**) Whole-body of the final instar caterpillar, (**b**) anterior region showing mid gut epithelium tissue, (**c**) central region of the mid gut, (**d**) end of the mid gut.

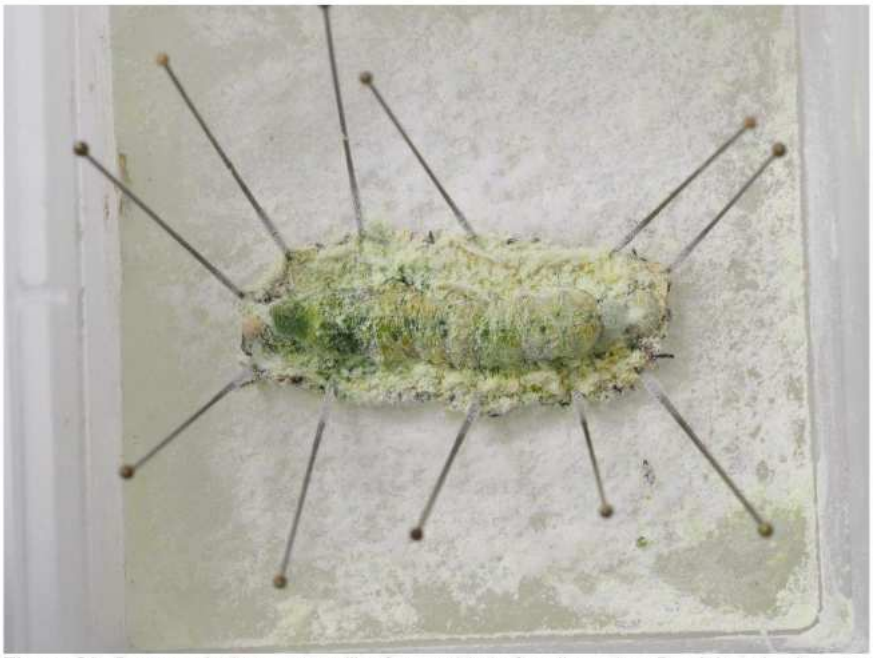

**Figure S3**. *Danaus plexippus* caterpillar freeze dried after dissection. Precipitated salts were removed using a soft brush before the gut was divided into foregut (left), four portions of midgut, and hindgut (right). Please see the methods section of the manuscript for further details.

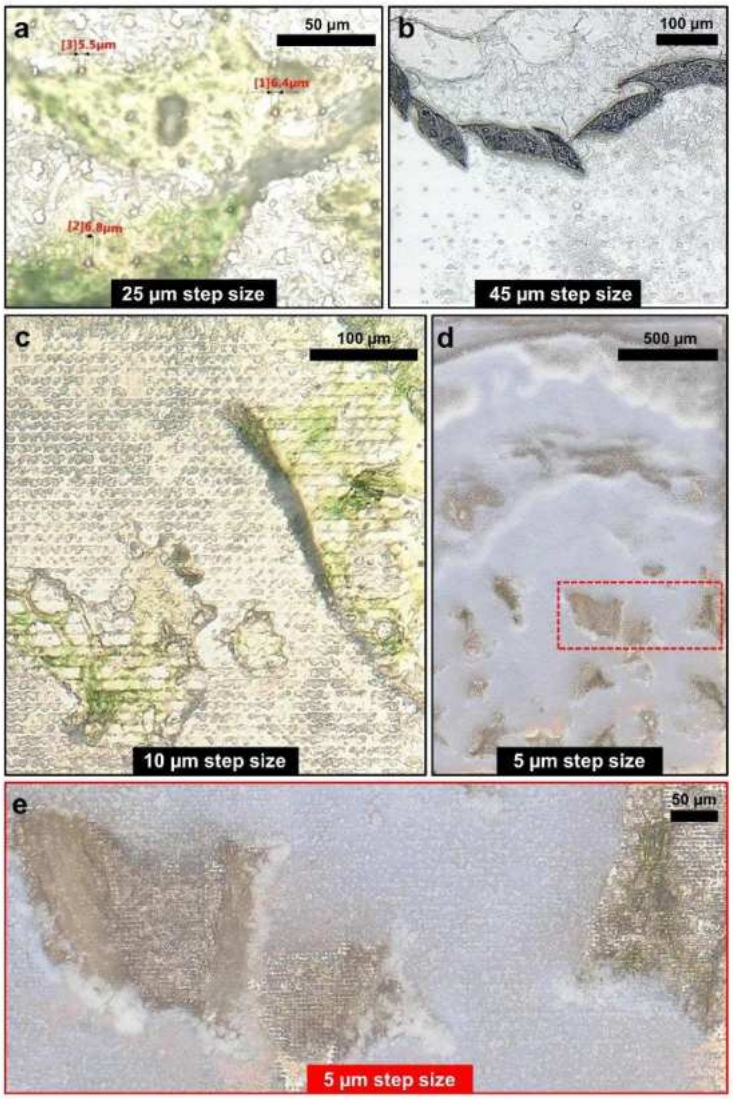


**Figure S4**. Laser ablation spots in the crystalline matrix layer (2,5-DHB) of *D. plexippus* tissue sections for AP-SMALDI MSI experiments conducted with (**a**) 25 µm, (**b**) 45 µm, (**c**) 10 µm and (**d,e**) 5 µm step-size. The laser settings were carefully adjusted in respect to the applied step-size to prevent oversampling (i.e. shooting the same sampling area twice). Of especial importance for low-micrometer-resolution MSI (step-sizes below 10 µm) is that the employed AP-SMALDI5 AF ion source provides a laser focus of 5 µm, thus, allowing us to perform the respective MSI experiments without oversampling.

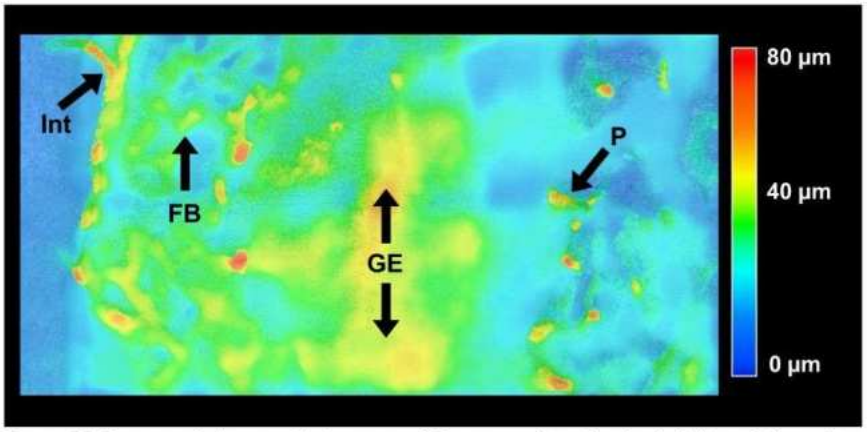


**Figure S5**. Topography image of a transversal *E. core* section showing height variations of up to 80 µm at ingested *A. curassavica* plant material (P) and integument (Int). Across midgut epithelium (GE) and fat body (FB), we found height variations of up to 40 µm. Therefore, we conducted high-resolution MSI experiments (5 µm to 10 µm step size) using the 3D-surface mode (pixelwise autofocusing) of the AP-SMALDI5 AF ion source to keep the MALDI laser focus, fluence and ablation spot size constant for the whole MSI experiment.

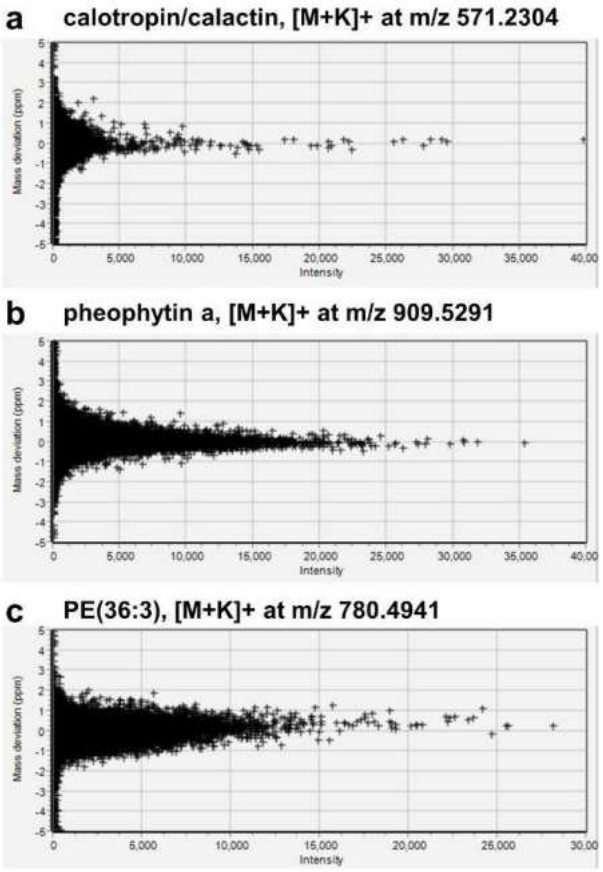


**Figure S6**. Root-mean-square error plots for (**a**) calotropin/calactin ([M+K]+ at *m*/*z* 571.2304), (**b**) pheophytin a ([M+K]+ at *m*/*z* 909.5291) and (**c**) PE(36:3) ([M+K]+ at *m*/*z* 780.4941).

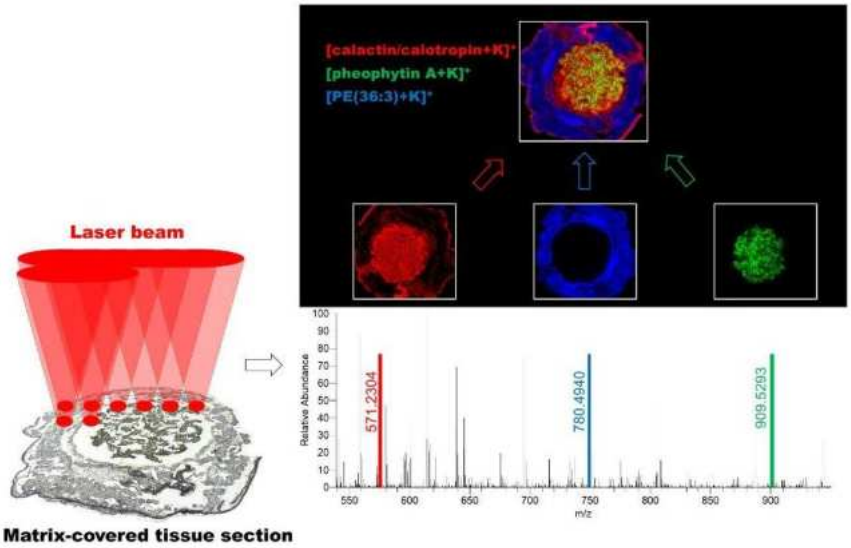


**Figure S7**. General principle to obtain red-green-blue (RGB) overlay ion images using AP-SMALDI MSI. The matrix-covered sample tissue section is scanned by a laser beam for desorption/ionization of analytes with a defined step size between each measurement spot. For image generation, the intensity values of the selected mass-to-charge-number ratio (*m*/*z*) are combined with the spatial information into an image which displays the spatial distribution of the selected signal on the sample surface. For the RGB overlay image, three different signals are assigned to one colour each and superimposed.

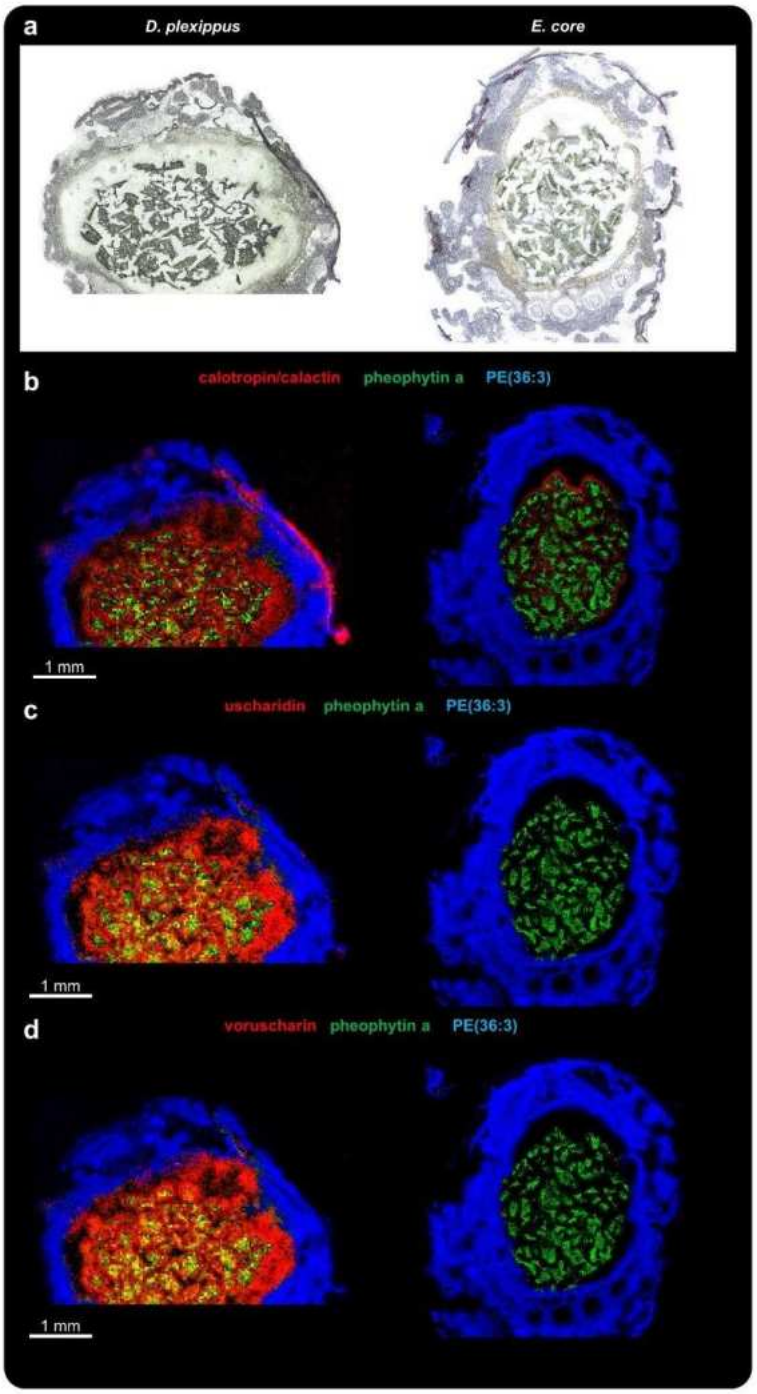


**Figure S8.** AP-SMALDI MSI of transversal sections of caterpillars of *D. plexippus* (biological replicate 2) and *E. core* (biological replicate 2). (**a**) Optical image of the transversal section of a fifth instar caterpillar of *D. plexippus* (left) and *E. core* (right) before matrix application. (**b-d**) Corresponding RGB overlay images obtained with 35 µm (*D. plexippus*) and 20 µm (*E. core*) step size showing the spatial distribution for the cardenolides (**b**) calotropin and/or its isomer calactin ($[M+K]^+$, red) at *m/z* 571.2304, (**c**) uscharidin ($[M+K]^+$, red) at *m/z* 569.2152, (**d**) voruscharin ($[M+K]^+$, red) at *m/z* 628.2346, (**b-d**) the chlorophyll derivative pheophytin a at *m/z* 909.5288 ($[M+K]^+$, green) as a chemical marker for plant tissue and the animal lipid PE(36:3) ($[M+K]^+$, blue) as a chemical marker for animal tissues. To demonstrate the differences regarding the cardenolide content between both species, the respective RGB ion images are normalized to the same intensity scale.

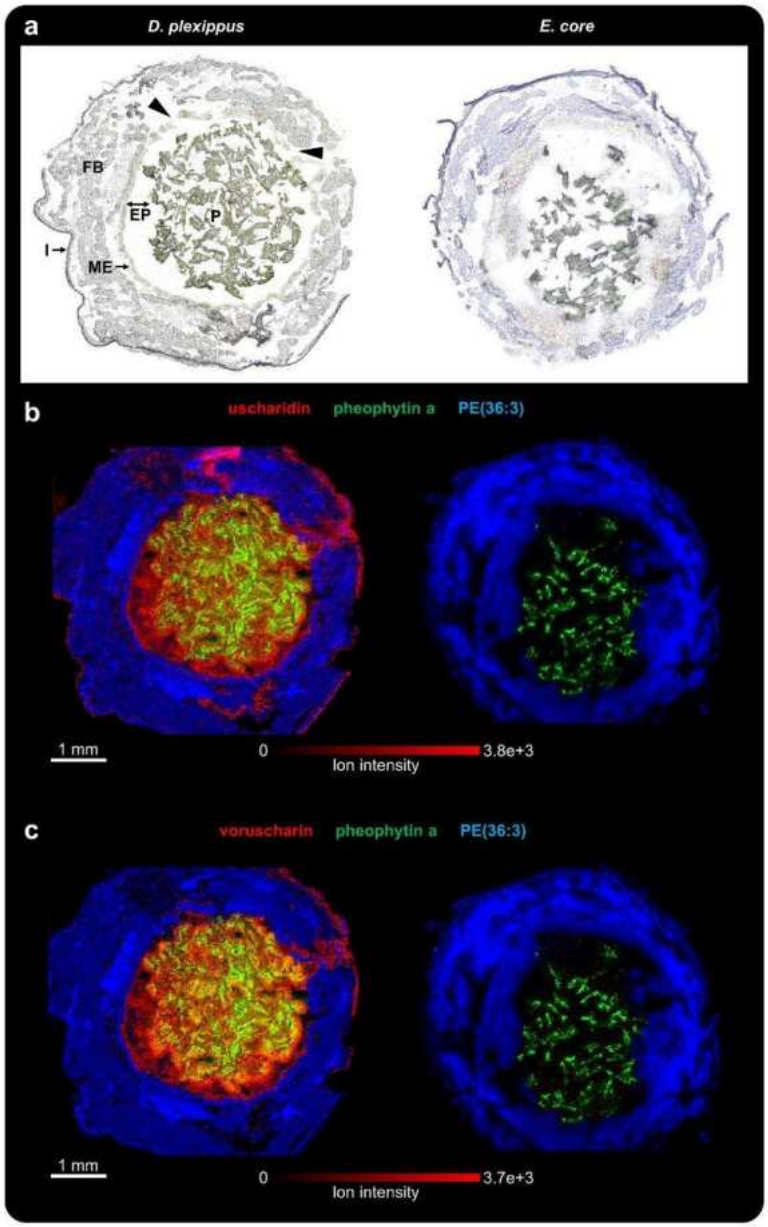


**Figure S9.** AP-SMALDI MSI of transversal sections of caterpillars of *D. plexippus* (biological replicate 1) and *E. core* (biological replicate 1). (**a**) Optical image of the transversal section of a fifth instar caterpillar of *D. plexippus* (left) and *E. core* (right) before matrix application. P:

plant material, EP: ectoperitrophic space, ME: midgut epithelium, FB: fat body, I: integument. (**b**) Corresponding RGB overlay images obtained with 35 µm (*D. plexippus*) and 20 µm (*E. core*) step size, showing the spatial distribution of the cardenolide (**b**) uscharidin ($[M+K]^+$, red) at *m/z* 569.2151, (**c**) voruscharin ($[M+K]^+$, red) at *m/z* 628.2346 and (**b,c**) the chlorophyll derivative pheophytin a at *m/z* 909.5288 ($[M+K]^+$, green) as a chemical marker for plant tissue and the animal lipid PE(36:3) ($[M+K]^+$, blue) as a chemical marker for animal tissues. To demonstrate the differences regarding the cardenolide content between both species, the respective RGB ion images are normalized to the same intensity scale. The *D. plexippus* gut epithelium was damaged at two areas (highlighted in the optical image), causing potential analyte delocalization in the corresponding hemolymph area.

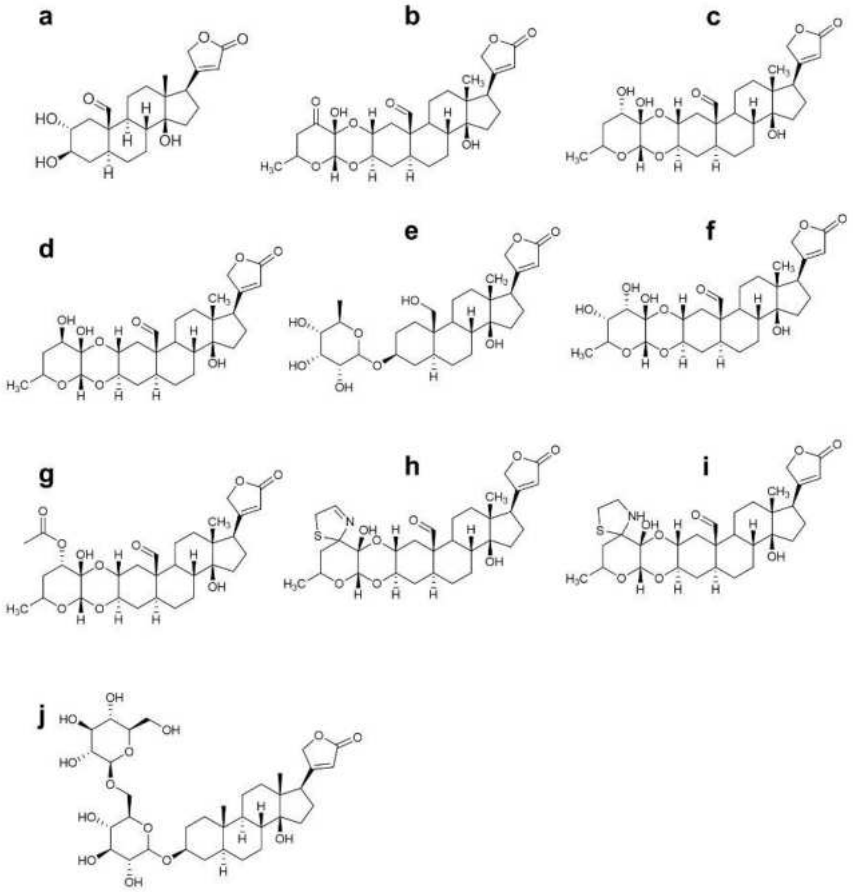


**Figure S10.** Chemical structures for all detected cardenolides. (**a**) calotropagenin, (**b**) uscharidin, (**c**) calotropin, (**d**) calactin, (**e**) frugoside, (**f**) calotoxin, (**g**) asclepin, (**h**) uscharin, (**i**) voruscharin, (**j**) uzarin.

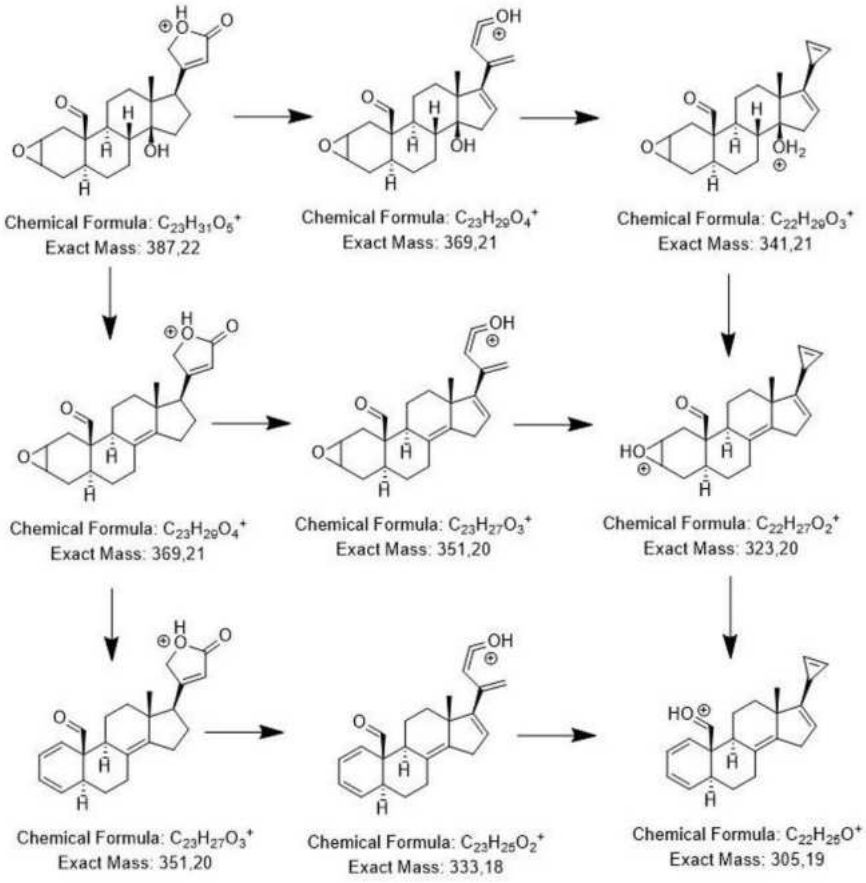


**Figure S11.** Proposed fragmentation pathway for cardenolides having an aldehyde function at C18 and a dioxane-linkage between the glycoside unit and the aglycone (i.e. all cardenolides detected with the exception of frugoside and uzarin). The fragmentation pathways including the chemical structures of the fragments are highlighted in the HPLC-MS/MS spectra of the respective cardenolide (Figs. S5-S7). For asclepin, uscharin and voruscharin, the characteristic fragments based on the glycoside unit are also displayed.

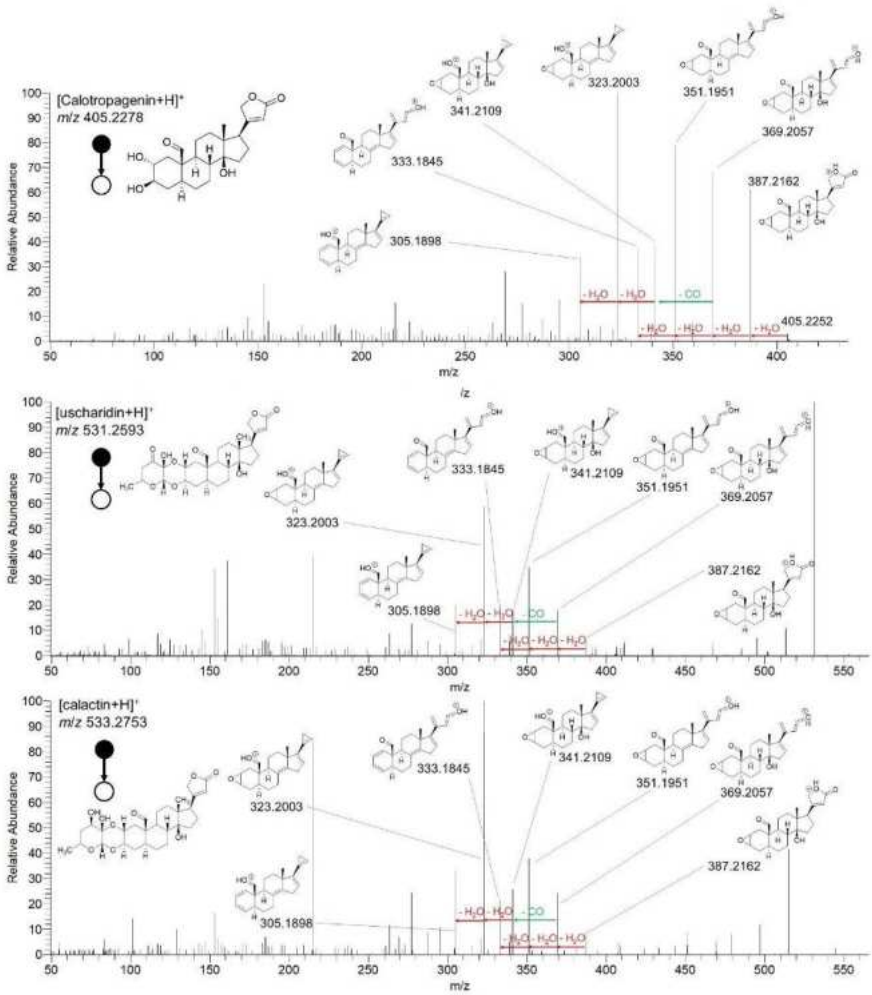


**Figure S12**. HPLC-MS/MS spectra for calotropagenin, uscharidin and calactin to confirm imaging annotations. Fragmentation pathways including characteristic fragments are highlighted.

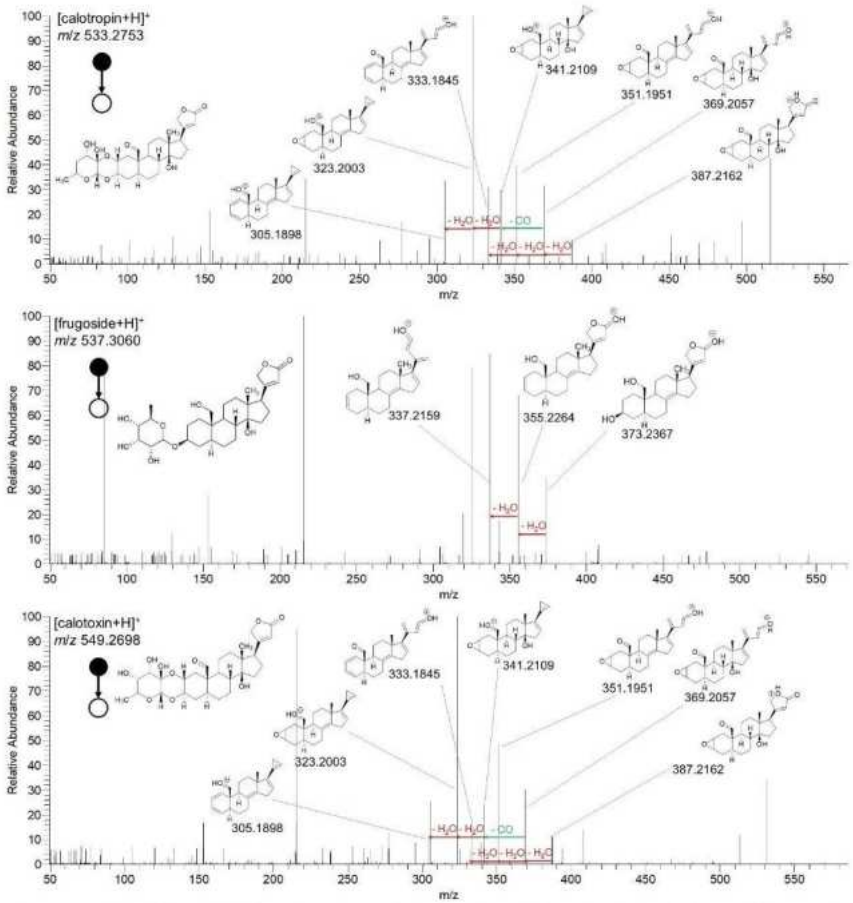


**Figure S13**. HPLC-MS/MS spectra for calotropin, frugoside and calotoxin to confirm imaging annotations. Fragmentation pathways including characteristic fragments are highlighted.

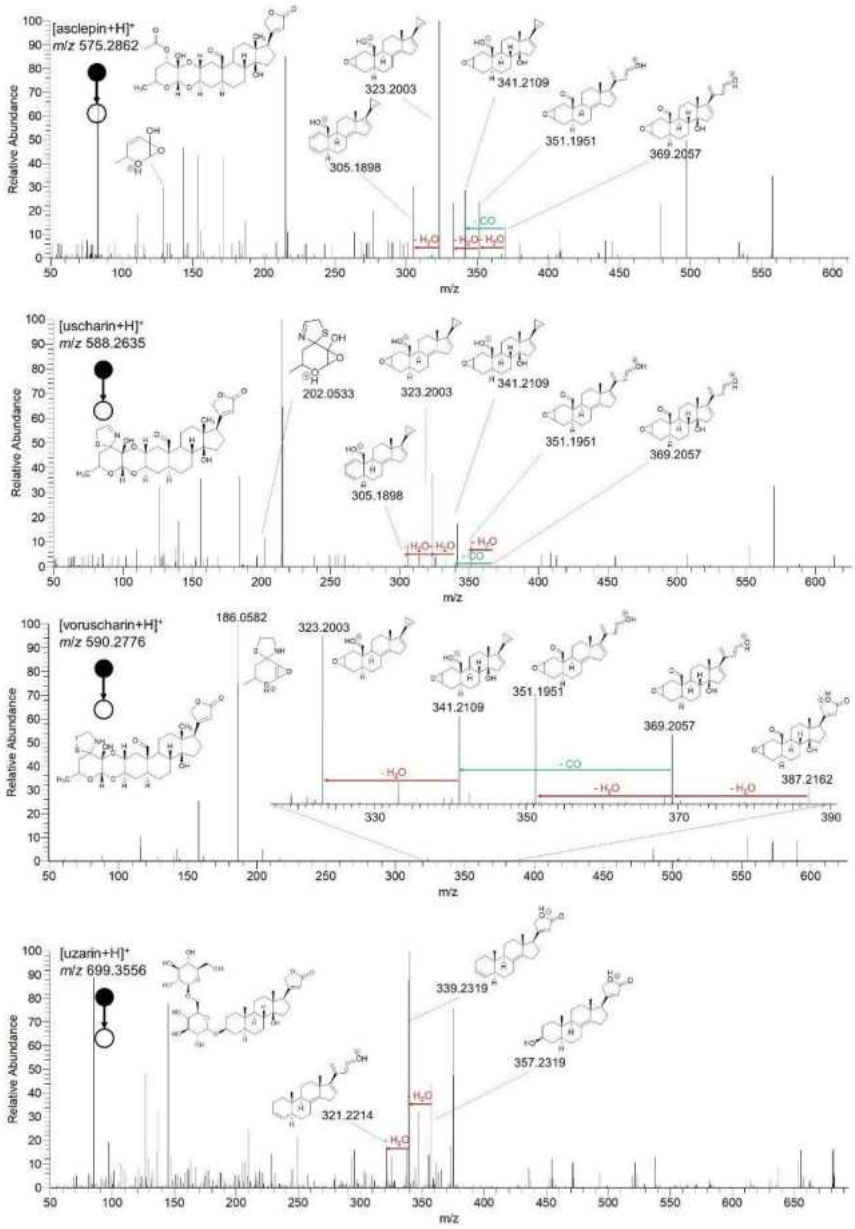


**Figure S14**. HPLC-MS/MS spectra for asclepin, uscharin, and voruscharin to confirm imaging annotations. Fragmentation pathways including characteristic fragments are highlighted.

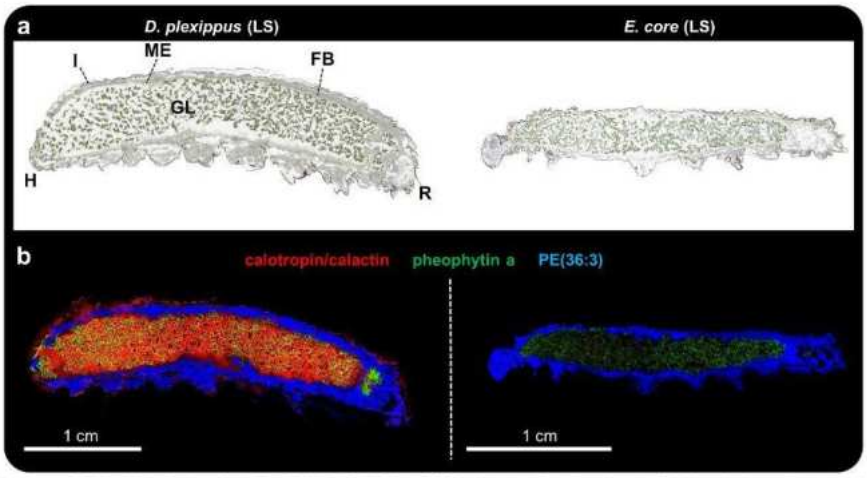


**Figure S15.** Whole-body AP-SMALDI MSI of fifth instar *D. plexippus* (biological replicate 4) and *E. core* caterpillars (biological replicate 4). (**a**) Optical image of longitudinal *D. plexippus* (left) and *E. core* (right) sections before matrix application. H: head, I: integument, R: rectum, GL: gut lumen, FB: fat body, ME: midgut epithelium. (**b**) Corresponding RGB overlay images obtained with 45 µm step size, showing the spatial distribution of calactin/calotropin ($[M+K]^+$, at *m/z* 571.2304 (red), pheophytin a ($[M+K]^+$, green) at *m/z* 909.5292 to highlight ingested *A. curassavica* plant material, and PE(36:3) ($[M+K]^+$, blue) at *m/z* 780.4941 serving as a marker for insect tissue, such as gut epithelium and fat body. Both RGB overlay images are normalized to the same intensity scale.

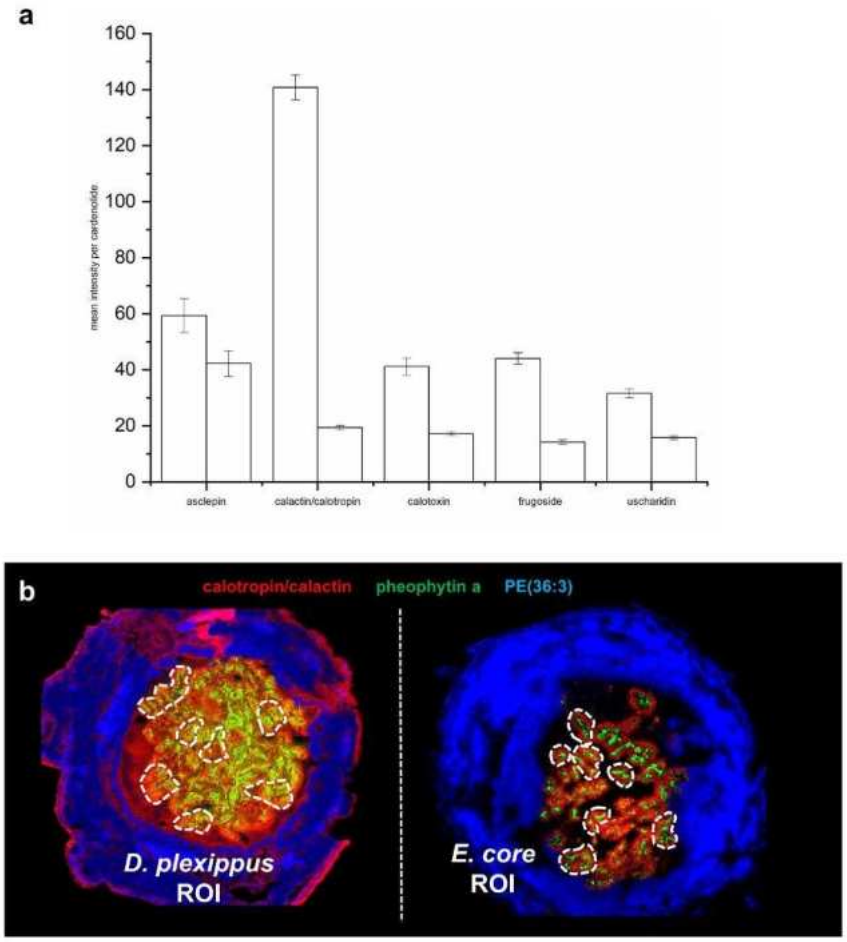


**Figure S16.** (**a**) MSI-based relative quantification for five selected cardenolide signals in the gut lumen of *D. plexippus* (left) and *E. core* (right). Bars represent means ± SE of the respective cardenolide signals based on four biological replicates (two transversal- and two longitudinal sections for each species). For each biological replicate, the mean cardenolide intensity of seven comparable regions of interest (ROI) was calculated. (**b**) Representative *in silico* ROI selection at the example of biological replicate 1 for *D. plexippus* and *E. core*. RGB overlay images showing the spatial distribution of the cardenolide calotropin and/or its isomer calactin ($[M+K]^+$, red) at *m/z* 571.2304, the chlorophyll derivative pheophytin a at *m/z* 909.5288 ($[M+K]^+$, green) as a chemical marker for plant tissue and the animal lipid PE(36:3) ($[M+K]^+$, blue) as a chemical marker for animal tissues. MSiReader was utilized to define the respective regions of interest (n = 7, total amount of pixels: 5134 pixels for *D. plexippus* and 5049 pixels for *E.*

*core*) for both species. Next, ion intensities of the respective cardenolide signal was extracted and for internal normalization and better comparison, normalized to the average pheophytin a signal abundance for the respective region of interest.

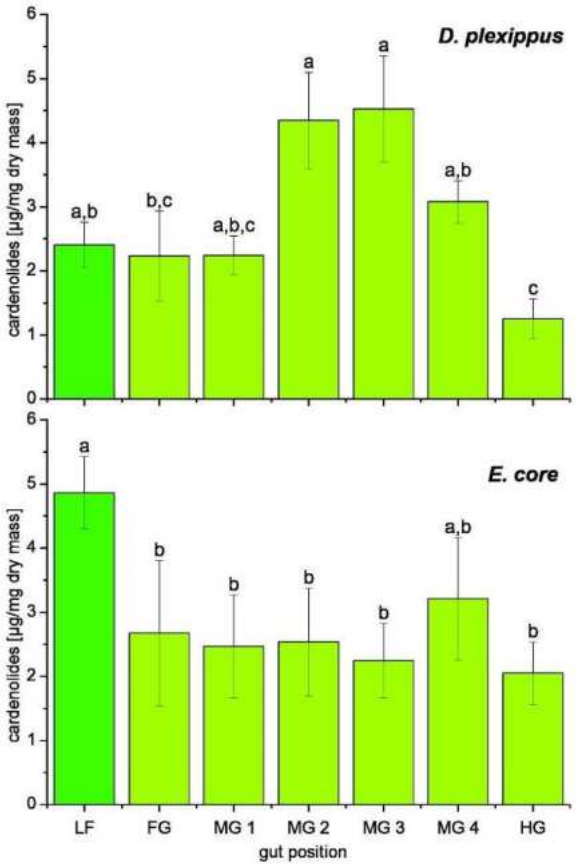


**Figure S17**. Total cardenolide concentrations across the gut passage in caterpillars of *D. plexippus* (DP) and *E. core* (EC). After dissection and freeze drying, guts were divided into foregut (FG), four portions of midgut (MG1-MG4), and hindgut (HG) and analyzed via HPLC-DAD. Samples sizes for *D. plexippus* were: n = 7 for FG, for all other gut portions n = 9; for *E. core*, sample sizes were n = 6 for all gut portions. In addition, we analyzed cardenolides in milkweed (*A. curassavica*) leaves (LF, n = 9 for DP and n = 6 for EC). Bars represent means ± SE, different letters above bars indicate statistically significant differences ($p < 0.05$). Note that cardenolide concentrations in *A. curassavica* leaves were about twice as high in the experiment with *E. core* compared to the experiment with *D. plexippus* which might be due to different environmental conditions for plant growth (greenhouse vs. climate chamber).

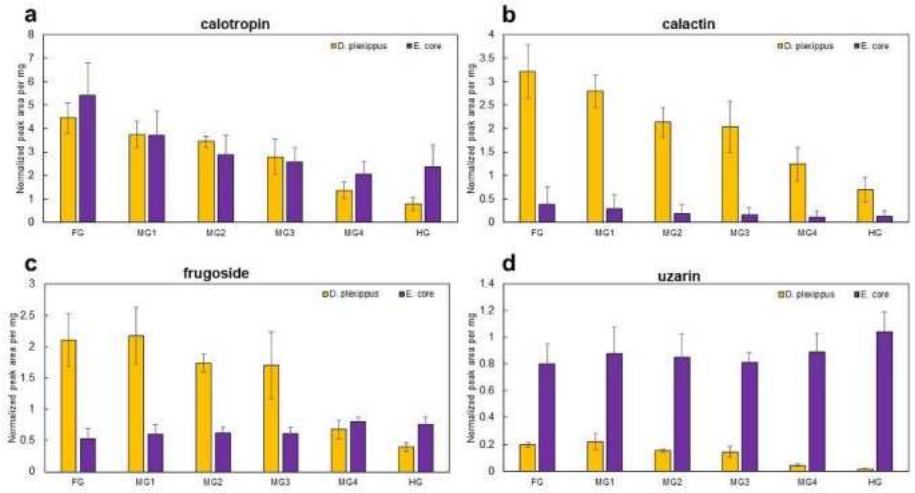


**Figure S18**. HPLC-MS-based absolute quantification of three preferentially sequestered cardenolides (calotropin, calactin, frugoside) and uzarin (not sequestered by *D. plexippus*) for gut material of *D. plexippus* (orange) and *E.core* (purple). The complete gut passage was dissected into six segments, starting with the foregut (FG), followed by 4 segments of the midgut (MG1-MG4), and the hindgut (HG). Each bar represents the mean of three biological replicates and error bars indicate standard deviation. The cardenolide peak area was normalized on the internal standard (digitoxin) and on the extracted tissue weight. (**a**) calotropin ($[M+H]^+$) at *m/z* 533.2755. (**b**) calactin ($[M+H]^+$) at *m/z* 533.2755. (**c**) frugoside ($[M+H]^+$) at *m/z* 537.3061. (**d**) uzarin ($[M+H]^+$) at *m/z* 699.3594.

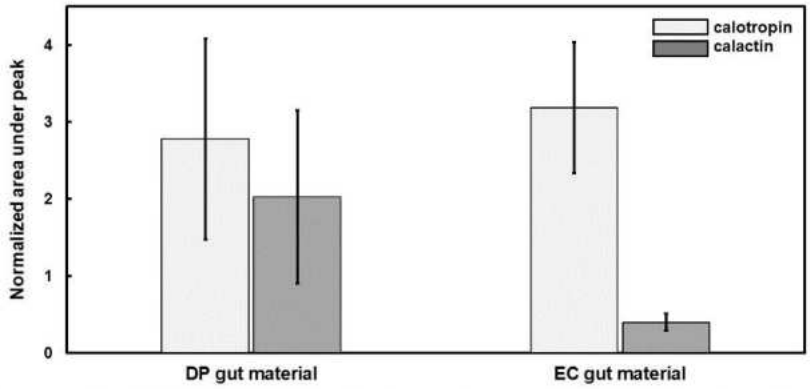


**Figure S19**. HPLC-MS-based quantification of the stereoisomers calotropin and calactin ($[M+H]^+$ at *m*/*z* 533.2751) for ingested plant material for the complete gut passage (foregut, midgut 1-4, and hindgut) of *D. plexippus* (DP) and *E. core* (EC). Each bar is the mean value of three biological replicates and error bars indicate standard deviation. The peak area was normalized on the internal standard (digitoxin) and on the extracted tissue weight of DP-/EC-gut material.

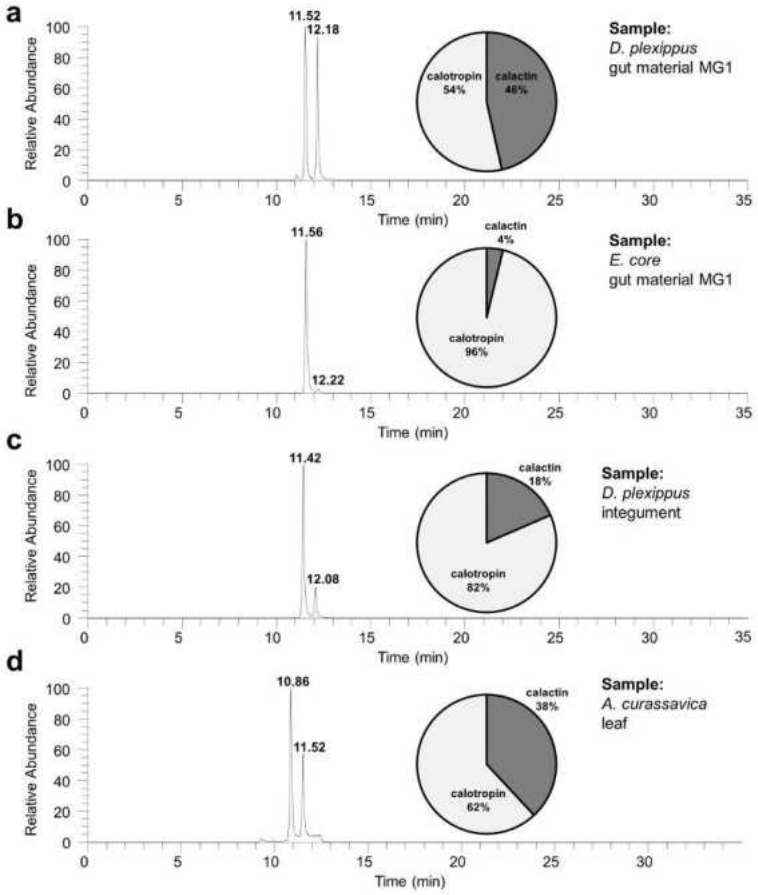


**Figure S20**. Typical HPLC-MS chromatograms for the stereoisomers calotropin and calactin ([M+H]$^+$ at *m*/*z* 533.2751) for (**a**) ingested plant material of *D. plexippus* midgut segment 1 (MG 1), (**b**) ingested plant material of *E. core* midgut segment 1 (MG 1), (**c**) *D. plexippus* integument tissue and (**d**) *A. curassavica* leaf tissue. The pie charts display the calotropin/calactin ratio based on the area under peak (AUP) for each sample type (n = 3).

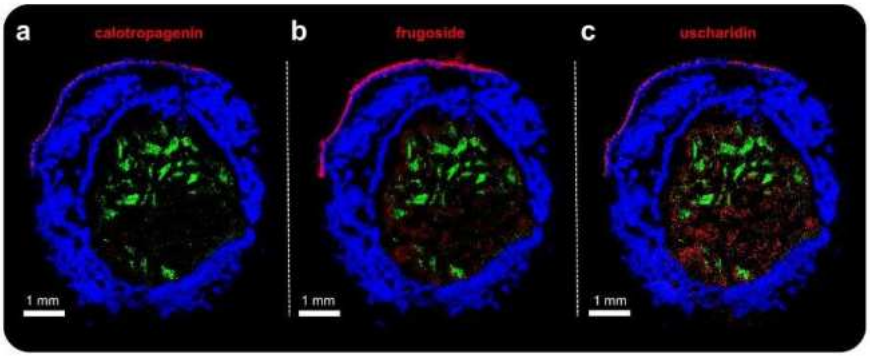


**Figure S21**. AP-SMALDI MSI (25 µm step size) of *Danaus plexippus* (biological replicate 5) fed with the non-toxic plant *Oxypetalum coeruleum* for 3 hours before sampling. (**a-c**) RGB overlay showing (**a**) calotropagenin ($[M+K]^+$, red) at *m/z* 443.1833, (**b**) frugoside ($[M+K]^+$, red) at *m/z* 575.2617, (**c**) uscharidin ($[M+K]^+$, red) at *m/z* 569.2146, and (**a-c**) pheophytin a ($[M+K]^+$, green) at *m/z* 909.5292 and PE(36:3) ($[M+K]^+$, blue) at *m/z* 780.4942.

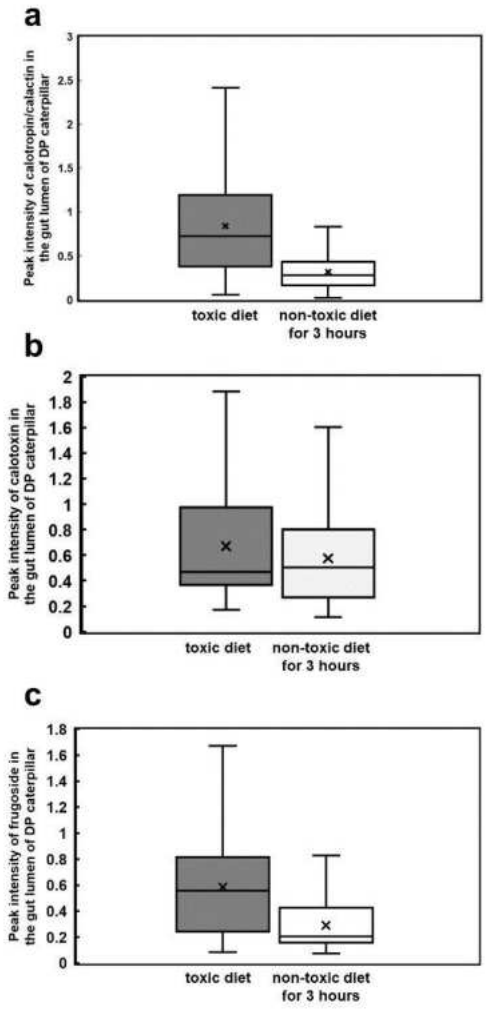


**Figure S22**. MSI-based relative quantification for the preferentially-sequestered cardenolides in the gut lumen of transversally sectioned caterpillars of *Danaus plexippus*. The respective cardenolide abundance was compared between caterpillars fed with *Asclepias curassavica* (deep grey, MSI data from Fig. 1, biological replicate 1) diet and caterpillars raised on *A. curassavica* but purged with a cardenolide-free diet of *Oxypetalum coeruleum* (light grey, MSI data from Fig. 3, biological replicate 5) for 3 hours before sampling. MSiReader was utilized to *in silico* segment the gut lumen and integument and subsequently, cardenolide signal intensities were extracted. Previous LC-MS-based cardenolide quantification for *D. plexippus* integument tissue (Fig. S19) showed no significant variations across biological replicates. For

better comparison, cardenolide signal intensities from the gut lumen were normalized to the average signal abundance of the respective cardenolide at the integument for the same MSI experiment. Box plots for (**a**) calotropin/calactin ($[M+K]^+$ at *m/z* 571.2304) showing 2.7 x less abundance after purging the gut passage with cardenolide-free plant material, (**b**) calotoxin ($[M+K]^+$ at *m/z* 587.2251) showing 1.1 x less abundance after purging the gut passage with cardenolide-free plant material, (**c**) frugoside ($[M+K]^+$ at *m/z* 575.2622) showing 2.1 x less abundance after purging the gut passage with cardenolide-free plant material.

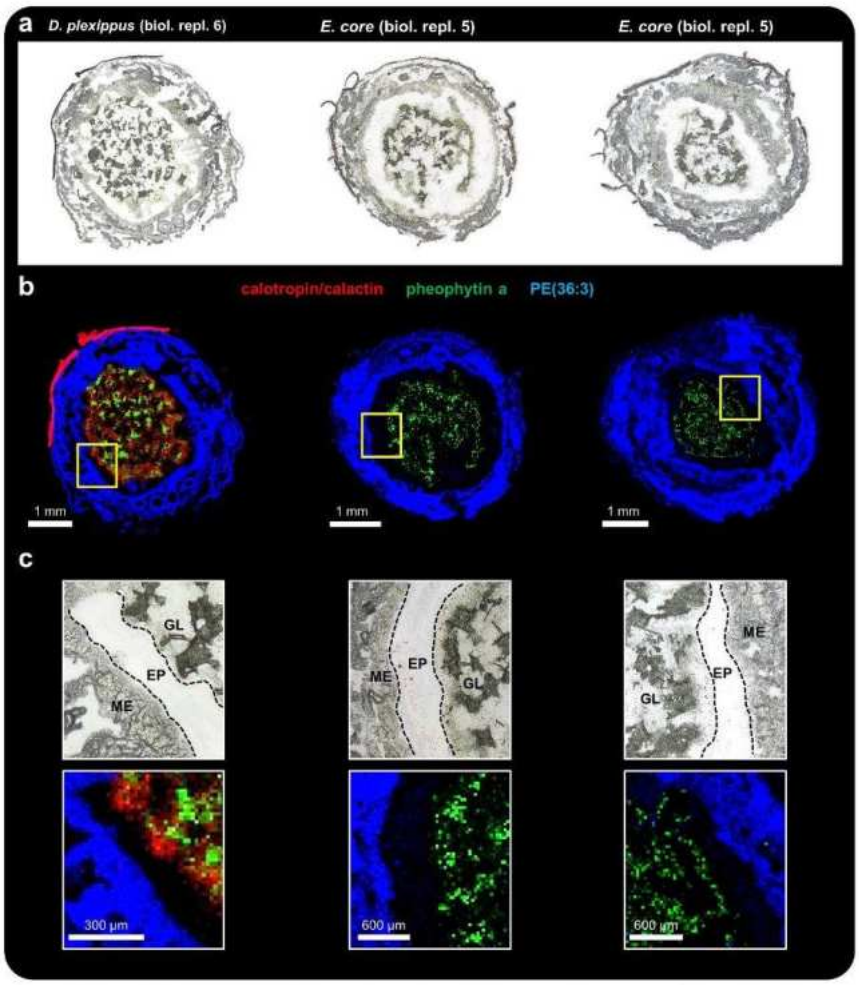


**Figure S23.** AP-SMALDI MSI (25 µm step size) of *Danaus plexippus* (biological replicate 6) and *Euploea core* caterpillars (biological replicate 5) purged with the non-toxic plant *Oxypetalum coeruleum* before sampling. (**a**) Optical images of transversally sectioned last instar *D. plexippus* and *E. core* caterpillars. (**b**) Corresponding RGB overlay images showing calactin/calotropin ($[M+K]^+$, red) at *m/z* 571.2304, pheophytin a ($[M+K]^+$, green) at *m/z* 909.5292 and PE(36:3) ($[M+K]^+$, blue) at *m/z* 780.4942. (**c**) Magnified views of the outlined regions in **b** highlighting midgut epithelium tissue (ME), ectoperitrophic space (EP) and gut lumen (GL).

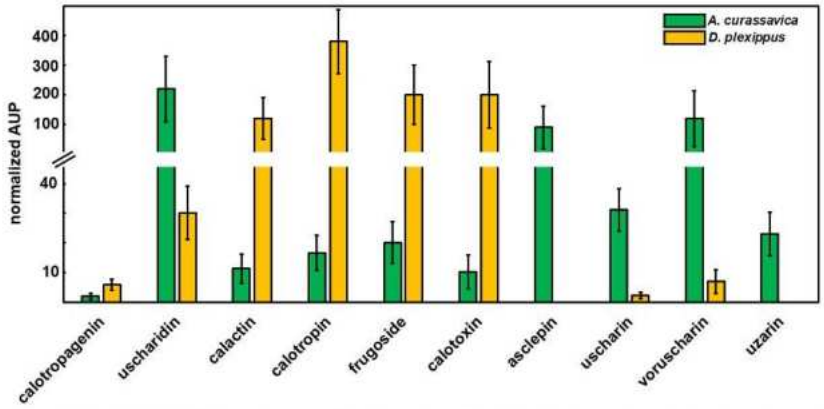


**Figure S24.** HPLC-MS-based quantification for 10 detected cardenolides in *Asclepias curassavica* leaf material and *D. plexippus* integument. Each bar represents the mean of three biological replicates and error bars indicate standard deviation. The area under peak (AUP) was normalized to the internal standard (digitoxin). Please note that quantities between leaf material and caterpillar tissue may not be compared in absolute terms since sample dry masses were different.

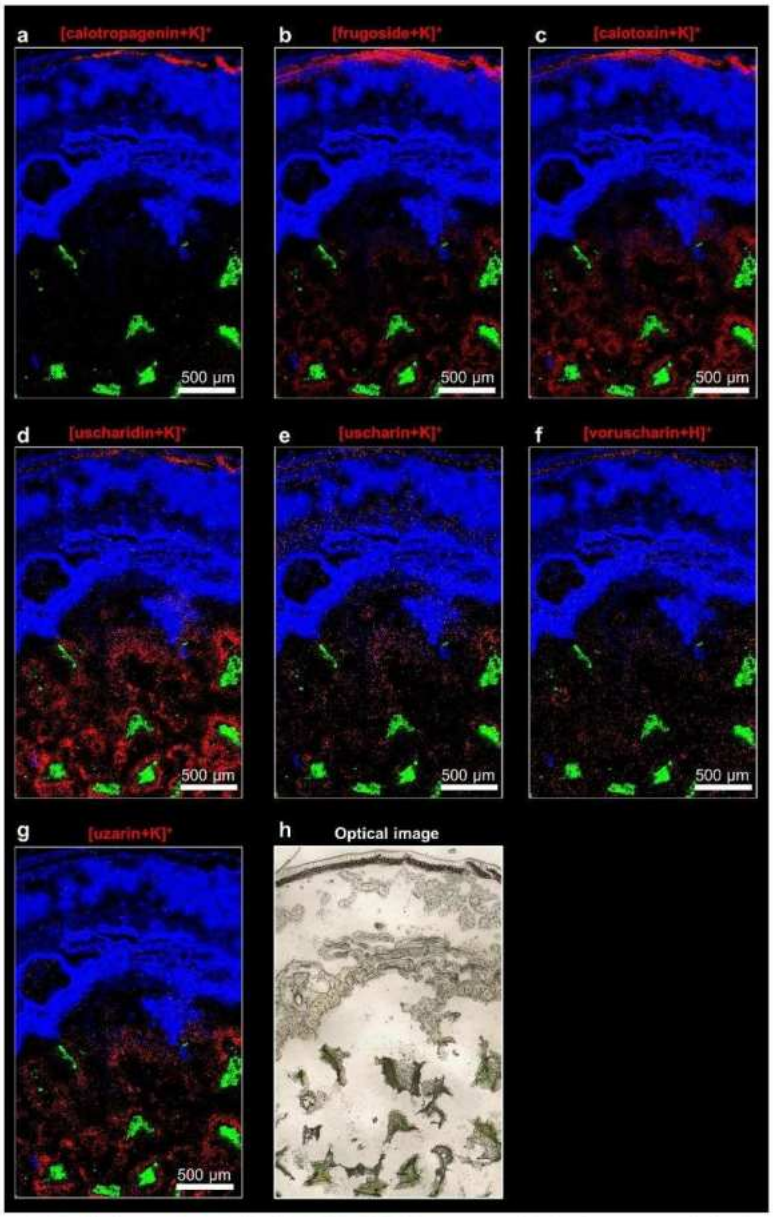


**Figure S25.** High-resolution AP-SMALDI MSI (5 µm step size) of transversal *D. plexippus* (biological replicate 7) section. RGB images showing the spatial distribution of (**a**) calotropagenin ($[M+K]^+$, red) at *m/z* 443.1829, (**b**) frugoside ($[M+K]^+$, red) at *m/z* 575.2616, (**c**) calotoxin ($[M+K]^+$, red) at *m/z* 587.2253, (**d**) uscharidin ($[M+K]^+$, red) at *m/z* 569.2146, (**e**) uscharin ($[M+K]^+$, red) at *m/z* 626.2159, (**f**) voruscharin ($[M+H]^+$, red) at *m/z* 590.2770, (**g**) uzarin ($[M+K]^+$, red) at *m/z* 737.3149. Additionally, (**a-g**) pheophytin a ($[M+K]^+$, green) at *m/z* 909.5290 and PE(36:3) ($[M+K]^+$, blue) at *m/z* 780.4940 were used to highlight ingested plant tissue and insect morphology. (**h**) Optical image of the analyzed region of interest.

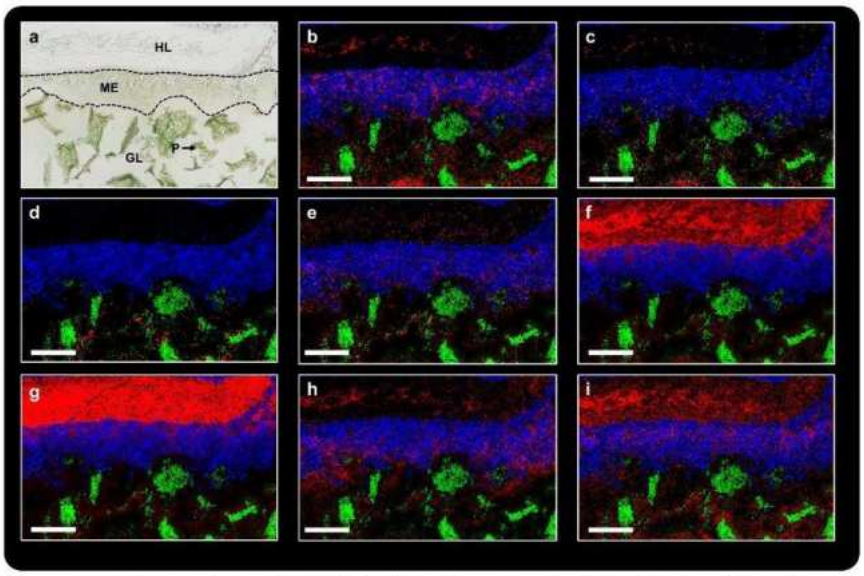


**Figure S26**. High-resolution AP-SMALDI MSI (10 µm step size) of midgut epithelium tissue in a longitudinal *Danaus plexippus* (biological replicate 3) section to investigate transport of selected cardenolide and other primary- and secondary metabolites. (**a**) Optical image of the analyzed region of interest. P: *Asclepias curassavica* plant material, GL: gut lumen, ME: midgut epithelium tissue, HL: hemolymph. (**b-i**) RGB overlay images showing the spatial distribution for (**b**) frugoside ($[M+K]^+$, red) at *m/z* 575.2616, (**c**) calotoxin ($[M+K]^+$, red) at *m/z* 587.2253, (**d**) asclepin ($[M+K]^+$, red) at *m/z* 613.2415, (**e**) kaempferol-glucopyranoside ($[M+Na]^+$, red) at *m/z* 471.0898, (**f**) malvidin-glucoside ($[M+Na]^+$, red) at *m/z* 515.1160, (**g**) N-(1-deoxy-1-fructosyl)tyrosine ($[M+K]^+$, red) at *m/z* 382.0899, (**h**) guanosine ($[M+K]^+$, red) at *m/z* 322.0548, (**i**) disaccharide ($[M+K]^+$, red) at *m/z* 381.0793. Additionally, (**b-i**) pheophytin a ($[M+K]^+$, green) at *m/z* 909.5290 and PE(36:3) ($[M+K]^+$, blue) at *m/z* 780.4940 were used to highlight ingested plant tissue and midgut epithelium tissue. Scale bars, 500 µm.

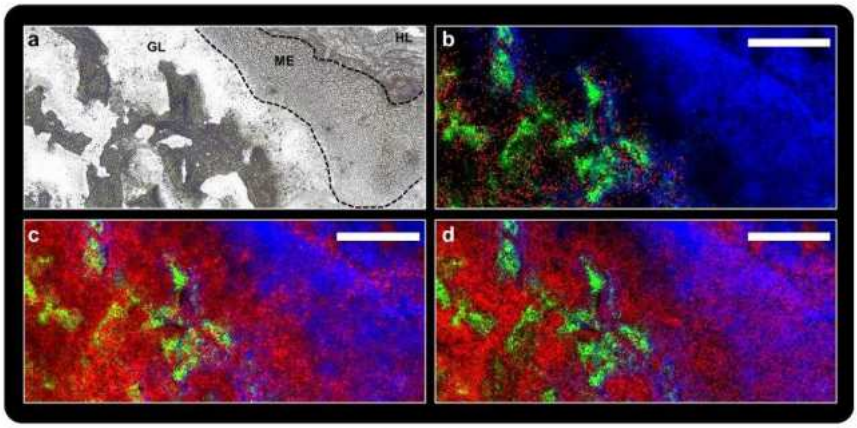


**Figure S27**. High-resolution AP-SMALDI MSI (10 µm step size) of midgut epithelium tissue of a longitudinal *Euploea core* (biological replicate 3) section to investigate various primary- and secondary metabolites. (**a**) Optical image of the analyzed region of interest. GL: gut lumen, ME: midgut epithelium tissue, HL: hemolymph. (**b-d**) RGB overlay images showing the spatial distribution for (**b**) calotropin/calactin ($[M+K]^+$, red) at *m/z* 571.2305, (**c**) guanosine ($[M+K]^+$, red) at *m/z* 322.0547, (**d**) disaccharide ($[M+K]^+$, red) at *m/z* 381.0793 and (**b-d**) pheophytin a ($[M+K]^+$, green) at *m/z* 909.5290 and PE(36:3) ($[M+K]^+$, blue) at *m/z* 780.4940. Scale bars, 500 µm.

# CHAPTER III

## Molecular Networking and On-Tissue Chemical Derivatization for Enhanced Identification and Visualization of Steroid Glycosides by MALDI Mass Spectrometry Imaging

**Domenic Dreisbach[1], Sven Heiles[1,2], Dhaka R. Bhandari[1], Georg Petschenka[3], Bernhard Spengler[1]**

[1]Institute for Inorganic and Analytical Chemistry, Justus Liebig University Giessen, Heinrich-Buff-Ring 17, 35392 Giessen, Germany

[2]Leibniz Institute for Analytical Sciences, ISAS – e.V., Otto-Hahn-Straße 6b, 44139 Dortmund, Germany

[3]Institute of Phytomedicine, University of Hohenheim, Otto-Sander-Straße 5, 70599 Stuttgart, Germany

*Anal. Chem*. **2022**, 94, 46, 15971-15979

analytical chemistry

pubs.acs.org/ac Article

# Molecular Networking and On-Tissue Chemical Derivatization for Enhanced Identification and Visualization of Steroid Glycosides by MALDI Mass Spectrometry Imaging

Domenic Dreisbach, Sven Heiles, Dhaka R. Bhandari, Georg Petschenka, and Bernhard Spengler*

Cite This: Anal. Chem. 2022, 94, 15971−15979 Read Online

ACCESS | Metrics & More | Article Recommendations | Supporting Information



**ABSTRACT:** Spatial metabolomics describes the spatially resolved analysis of interconnected pathways, biochemical reactions, and transport processes of small molecules in the spatial context of tissues and cells. However, a broad range of metabolite classes (e.g., steroids) show low intrinsic ionization efficiencies in mass spectrometry imaging (MSI) experiments, thus restricting the spatial characterization of metabolic networks. Additionally, decomposing complex metabolite networks into chemical compound classes and molecular annotations remains a major bottleneck due to the absence of repository-scaled databases. Here, we describe a multimodal mass-spectrometry-based method combining computational metabolome mining tools and high-resolution on-tissue chemical derivatization (OTCD) MSI for the spatially resolved analysis of metabolic networks at the low micrometer scale. Applied to plant toxin sequestration in *Danaus plexippus* as a model system, we first utilized liquid chromatography (LC)−MS-based molecular networking in combination with artificial intelligence (AI)-driven chemical characterization to facilitate the structural elucidation and molecular identification of 32 different steroidal glycosides for the host-plant *Asclepias curassavica*. These comprehensive metabolite annotations guided the subsequent matrix-assisted laser desorption/ionization mass spectrometry imaging (MALDI MSI) analysis of cardiac-glycoside sequestration in *D. plexippus*. We developed a spatial-context-preserving OTCD protocol, which improved cardiac glycoside ion yields by at least 1 order of magnitude compared to results with untreated samples. To illustrate the potential of this method, we visualized previously inaccessible (sub)cellular distributions (2 and 5 μm pixel size) of steroidal glycosides in *D. plexippus*, thereby providing a novel insight into the sequestration of toxic metabolites and guiding future metabolomics research of other complex sample systems.

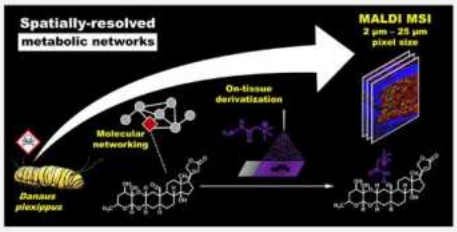


## INTRODUCTION

Metabolic networks describe interconnected pathways of biochemical reactions and transport processes of low-molecular-weight chemical species (metabolic intermediates, hormones, signaling molecules, secondary metabolites) within living organisms.[1−3] The processes within metabolic networks can be temporally and spatially organized.[4] In this context, the interest and ever-growing need to spatially characterize biological phenomena *in situ* have grown rapidly, which stimulated the development of enabling technologies. In particular, mass spectrometry imaging (MSI) methods have emerged as one of the fastest-growing mass spectrometry (MS) fields over the past decade.[5,6] MSI provides for nontargeted spatially resolved analysis of molecular species. Not only the analytes of interest but also hundreds of other chemical species can be detected, identified, and visualized simultaneously, thereby aiming to link molecular structures to biological functions and origin.[7,8] Among the different MSI methods, MALDI MSI is the predominant bioanalytical tool in chemistry, biology, and medicine, and recent technical advances have considerably improved the performance characteristics regarding molecular coverage, sensitivity, and spatial resolution. For instance, Kompauer *et al.* combined a coaxial ion source geometry (MS-inlet and laser beam path coaxially aligned to the sample-surface normal) with a custom-made long-working-distance objective lens, allowing the visualization of lipid, metabolite, and peptide distributions in complex biological samples at atmospheric pressure with an effective lateral resolution of 1.4 μm.[9] However, sensitivity is a significant barrier for visualizing metabolic networks via MALDI MSI.[10] The problem of generally low MALDI ionization efficiencies (ion yields down to $10^{-6}$ for some analyte classes[11,12]) is exacerbated by the decreasing amount of

Received: June 23, 2022
Accepted: October 11, 2022
Published: November 8, 2022





https://doi.org/10.1021/acs.analchem.2c02694
Anal. Chem. 2022, 94, 15971−15979

ablated material in high-resolution MSI. Multiple approaches to increase the MALDI ion yield have been reported, including optimized MALDI laser wavelength[13,14] and laser-induced post-ionization (MALDI-2).[15] For example, Niehaus *et al.* developed an ion source for transmission-mode MALDI-2 MSI, demonstrating improved analytical sensitivity by several orders of magnitude for phospho- and glycolipids with pixel sizes of 1 $\mu$m.[16] However, this approach requires novel and complex instrumentation, and the limited availability of commercial MALDI-2 MSI instruments prevents broader applicability.[17,18]

As a powerful alternative, on-tissue chemical derivatization (OTCD) of target analytes with precharged moieties can counteract isobaric matrix interferences, ion suppression, and low intrinsic ionization efficiencies.[19] Introduced in 2013 by Cobice *et al.*, hydrazine-forming reagents have been used to target ketone-containing substrates and products of the glucocorticoid amplifying enzyme 11$\beta$-HSD1 in rat adrenal gland and mouse brain.[20] Afterward, various studies utilized OTCD-MSI to gain additional or previously inaccessible insight into spatial distributions and molecular structures in the field of biological and medical research.[21−25] Despite all of these studies that demonstrate the potential of selectively enhancing ion yields, OTCD methods can be limited by spatial artifacts and analyte washing effects, thus preventing the visualization of (sub)cellular metabolite distributions.

To comprehensively explore and interpret metabolic networks, the corresponding individual chemical components have to be discovered and identified. However, molecular identification and elucidating chemical structures are mostly restricted to compounds for which mass spectrometric reference data are archived in spectral libraries (e.g., commercially available chemicals).[26−28] Since its introduction in 2012, molecular networking from the Global Natural Products Social Molecular Networking (GNPS) infrastructure has become a key method to organize and annotate nontargeted LC−$MS^1$ and $-MS^2$ data.[29−31] Utilizing spectral similarity (with the assumption of structural similarity), related molecular species are connected, and annotations from spectral library matching can be propagated through generated molecular networks, thereby pushing the frontier of conventional database search and facilitating the structural elucidation of unknown chemical compounds. Dührkop *et al.* developed the computational method CSI (Compound Structure Identification):FingerID,[32] which combines fragmentation-tree calculations and machine-learning techniques for *in silico* annotations of $MS^2$ spectra based on substantially larger molecular structure databases. This method tackled the major bottleneck of the limited availability of chemical compounds represented in mass spectral libraries. Very recently, the same authors described CANOPUS (class assignment and ontology prediction using mass spectrometry), a computational tool that utilizes a deep neural network to predict chemical compound classes and to perform structural analysis of unknown metabolites using high-resolution $MS^2$ data.[33−35] Therefore, combining these different computational metabolome mining tools could provide a powerful platform to comprehensively explore metabolic networks and identify their respective chemical species. Here, we combined LC−MS-based molecular networking and artificial intelligence (AI)-driven chemical classification with OTCD MALDI MSI for the unbiased spatial-metabolomic characterization of plant toxin sequestration in the monarch butterfly (*Danaus plexippus*) (Figure S1). In this fascinating antagonistic interaction, the monarch butterfly absorbs and accumulates steroidal plant toxins (cardiac glycosides) from milkweed host plants (*Asclepias* spp.) into its own body tissues to obtain a chemical defense against predators.[36−38]

First, we generated a metabolomic "in-house" database of *A. curassavica* consisting of 32 steroidal glycosides. Next, these annotations were utilized to guide the spatially resolved MSI-based analysis of cardiac glycoside sequestration in monarch caterpillar tissues and cells. We mitigated the problem of low intrinsic ionization efficiencies by the selective chemical tagging of carbonyl-containing cardiac glycosides with pre-charged moieties while retaining spatial information. To illustrate the potential of our methodology, we imaged (sub)cellular distributions of derivatized cardiac glycosides in epithelial cells, Malpighian tubules, and various body tissues in unprecedented detail.

## ■ EXPERIMENTAL SECTION

**Chemicals.** Acetonitrile and water (HiPerSolv) were purchased from VWR International GmbH (Darmstadt, Germany). 2,5-Dihydroxybenzoic acid (DHB) was purchased from Merck (Darmstadt, Germany). Trifluoroacetic acid (TFA) was purchased from AppliChem GmbH (Darmstadt, Germany). Girard's reagent T (GirT) was purchased from Merck (Darmstadt, Germany). Formic acid (FA) was purchased from Fisher Scientific (Schwerte, Germany).

**Plants and Insects.** Samples of *Asclepias curassavica* were obtained from plants cultivated at the Institute of Insect Biotechnology (Justus Liebig University, Giessen, Germany). Caterpillars of *D. plexippus* were raised on *A. curassavica* under controlled conditions at the same institute.

**Sample Preparation for LC−MS.** *A. curassavica* leaf samples were harvested, immediately freeze-dried, ground to a fine powder, and subsequently extracted for nontargeted LC−$MS^2$ experiments. The detailed experimental procedure is provided in Supplementary Note 1.

**Sample Preparation for OTCD MALDI MSI.** The established cryosectioning protocol to obtain longitudinal tissue sections for final instar larvae (Figure S2) of excellent quality regarding morphological preservation is reported elsewhere.[39] Prior to on-tissue chemical derivatization, tissue sections were brought to room temperature in a desiccator for 45 min to avoid condensation of humidity on the sample surface. Optical microscopic images of tissue sections before and after OTCD, after matrix application, and after MSI analysis and of hematoxylin−eosin (H&E)-stained tissue sections were obtained using a Keyence VHX-5000 digital microscope (Keyence Deutschland GmbH, Neu-Isenburg, Germany) equipped with a VH-Z250R objective lens. A volume of 35 $\mu$L of GirT solution (15 mg/mL in MeOH/water 7:3 v/v adding 0.2% TFA) was sprayed onto the tissue section at a flow rate of 7 $\mu$L/min using an ultrafine pneumatic sprayer system (SMALDIPrep, TransMIT GmbH, Giessen, Germany). The nebulizing nitrogen gas pressure was 1 bar, and the rotation was set to 500 rpm. After derivatization, samples were kept at room temperature in a desiccator for 2 h without any further incubation. A volume of 100 $\mu$L DHB matrix solution (30 mg/mL in MeOH/water 1:1 v/v adding 0.1% TFA) was sprayed onto the tissue section at a flow rate of 5 $\mu$L/min using the same ultrafine pneumatic sprayer system. After MSI analysis, tissue sections were washed with ethanol (70%) for 2 min to remove the matrix layer followed by H&E



https://doi.org/10.1021/acs.analchem.2c02694
Anal. Chem. 2022, 94, 15971−15979

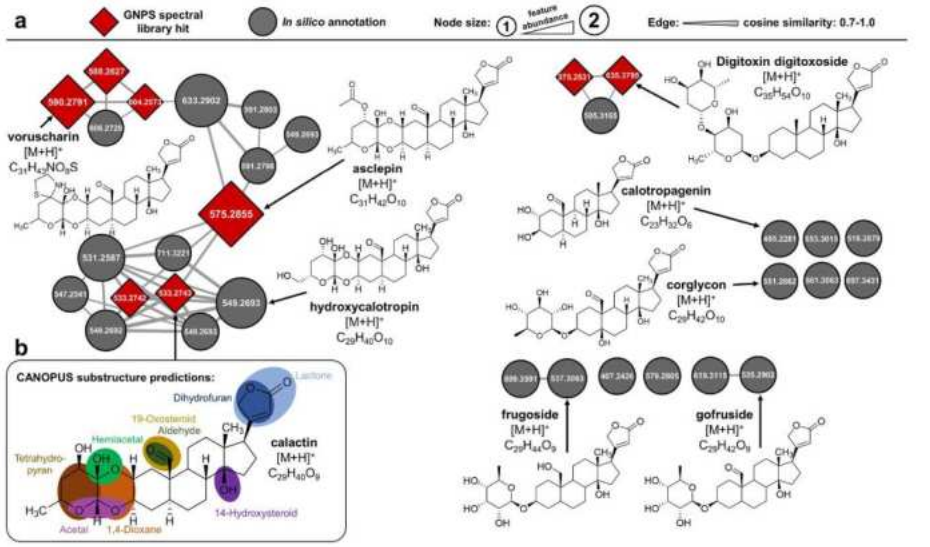


**Figure 1.** Feature-based molecular networking and *in silico* systematic classification, substructure prediction, and annotation for cardiac glycosides in *A. curassavica*. (a) FBMN results for nontargeted LC−MS$^2$ data of *A. curassavica* leaf showing molecular networks related to cardiac glycosides. The node size proportionally represents the LC−MS feature abundance (peak area), and the increased edge thickness corresponds to the higher cosine similarity (0.7 to 1.0). CANOPUS was used for compound classification to discover additional candidates that were not part of the original molecular network. In total, 32 different cardiac glycosides were identified based on 8 GNPS spectral library hits (red nodes) and 24 *in silico* annotations (gray nodes) using SIRIUS (CSI:FingerID). *In silico* annotations were also manually evaluated (Supplementary Data 1). (b) CANOPUS substructure predictions (posterior probability > 75%) for calactin to facilitate structural elucidation and fragmentation pathway analysis.

staining for histological classification (see Supplementary Protocol 1).

**Instrumentation for MSI.** High-resolution (5 to 25 $\mu$m step size) MALDI MSI and MALDI MS$^2$ experiments were performed using an autofocusing AP-SMALDI$^5$ AF ion source[40] (TransMIT GmbH, Giessen, Germany) coupled to an orbital trapping mass spectrometer (Q Exactive HF, Thermo Fisher Scientific GmbH, Bremen, Germany). For higher-resolution (2 $\mu$m step size) MALDI MSI experiments, a prototype AP-SMALDI AF ion source coupled to a Q Exactive Orbitrap mass spectrometer (Thermo Fisher Scientific GmbH, Bremen, Germany) was used. Detailed experimental parameters are provided in Supplementary Note 2.

**Instrumentation for HPLC−MS.** All HPLC−MS experiments were performed using a Dionex UltiMate 3000 HPLC instrument (Thermo Fisher Scientific, Massachusetts, USA) coupled to a Q Exactive HF-X Orbitrap mass spectrometer (Thermo Fisher Scientific, Bremen, Germany). Analytes were separated on a Kinetex C18 reversed-phase column (2.6 $\mu$m, 100 × 2.1 mm, Phenomenex, Torrance, USA). Detailed experimental parameters for HPLC−MS/MS analysis are provided in Supplementary Note 3.

**MSI Data Analysis.** The Xcalibur Qual Browser (Thermo Fisher Scientific, Massachusetts, USA) was used to display mass spectra. Ion images of selected $m/z$ values were generated using the MIRION[41] imaging software (v3.3.64.20, TransMIT GmbH, Giessen, Germany). All MS images were generated without the use of image processing steps such as smoothing or interpolation. Ion images were normalized to the total ion count (TIC) per pixel. The resulting ion images were finally adjusted in brightness for optimal visualization. MSiReader[42] was used to extract intensity profiles for defined regions of interest. Lipids and metabolites were assigned based on exact mass measurements, LC−MS$^2$ experiments, on-tissue MALDI MS$^2$, and METASPACE[43] annotations.

**Molecular Networking and *In Silico* Molecular Characterization.** Raw mass spectra were converted to mzXML files using MSConvert (Proteo Wizard, v.3.0.11579). MS$^1$ feature extraction and MS$^2$ processing were performed using MZmine 2[44] (see Supplementary Note 4 for detailed information). Feature-based molecular networks (FBMNs) were generated using the FBMN workflow from the GNPS analysis infrastructure (see Supplementary Note 5 for detailed information) and visualized with Cytoscape[45] (v.3.8.0). SIRIUS (v.4.5.3) and the included CSI:FingerID and CANOPUS tools were used for *in silico* characterization of LC−MS$^2$ data.

## ■ RESULTS AND DISCUSSION

**Molecular Networking Combined with AI-Driven Molecular Characterization Defines the Steroidal Glycoside Composition of *A. curassavica*.** First, we performed nontargeted LC−MS$^2$ experiments of leaf extracts and utilized state-of-the-art molecular networking tools in combination



https://doi.org/10.1021/acs.analchem.2c02694
Anal. Chem. 2022, 94, 15971−15979

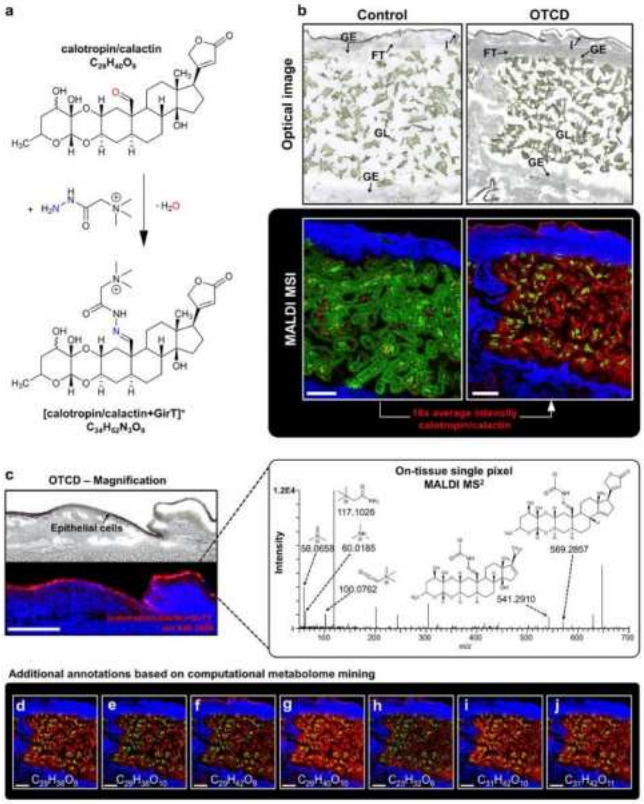


**Figure 2.** High-resolution MALDI MSI (25 $\mu$m step size) for chemically derivatized cardiac glycosides in longitudinal *D. plexippus* sections. (a) Schematic of the reaction between calotropin/calactin and the GirT reagent. (b) Optical images showing the analyzed area for conventional MALDI (left) and OTCD MALDI MSI (right). The corresponding RGB overlay images were normalized to the same intensity scale and show the spatial distribution of calotropin/calactin in red as $[M + K]^+$ at $m/z$ 571.2306 for control (left) and $[M + GirT]^+$ at $m/z$ 646.3699 for OTCD (right), pheophytin a as $[M + K]^+$ at $m/z$ 909.5291 in green, and PS(36:3) as $[M + K]^+$ at $m/z$ 810.5046 in blue. (c) Magnified view for the integument area of the OTCD experiment highlighting the accumulation of the toxin in the epithelial cells of the integument. Corresponding OTCD MALDI MS$^2$ spectrum of calotropin/calactin as $[M + GirT]^+$ at $m/z$ 646.3699 acquired from a single pixel at the *D. plexippus* integument. (d–j) RGB overlay images showing additional derivatized cardiac glycosides in red. (d) Uscharidin ($[M + GirT]^+$, $m/z$ 644.3541), (e) hydroxyuscharidin ($[M + GirT]^+$, $m/z$ 660.3489), (f) gofrugoside ($[M + GirT]^+$, $m/z$ 648.3828), (g) calotoxin/hydroxycalactin/hydroxycalotropin ($[M + GirT]^+$, $m/z$ 662.3648), (h) calotropagenin ($[M + GirT]^+$, $m/z$ 518.3233), (i) asclepin ($[M + GirT]^+$, $m/z$ 688.3806), and (j) hydroxyasclepin ($[M + GirT]^+$, $m/z$ 704.3756). Scale bars: (b, d–j) 1 mm and (c) 500 $\mu$m.

with AI-driven molecular characterization to acquire a metabolomic profile for the host plant *A. curassavica*. Figure S3 shows the comprehensive FBMN results that consisted of 1175 mass spectral nodes organized into 89 independent molecular families. In total, we obtained 145 spectral library hits (red nodes), allowing the classification of the corresponding molecular networks. Figure 1a shows the molecular network for cardiac glycosides, which are potent inhibitors for $Na^+/K^+$-ATPase, a cation carrier ubiquitously expressed in animal cells. Utilizing AI-driven compound class prediction, 12 additional LC–MS$^2$ features were classified as cardiac glycosides (Figure 1a, bottom right), which were not part of the original molecular network due to different fragments in the MS$^2$ spectra (Supplementary Note 3). In total, 32 different cardiac glycosides were identified based on 8 GNPS spectral library hits (red nodes) and 24 *in silico* annotations (gray nodes) (Table S1). To evaluate *in silico* annotations, we manually investigated the respective fragmentation spectra (Supplementary Data 1). Compared to the most recent studies[46,47] regarding toxic steroidal glycoside composition in *A. curassavica*, we found 20 additional cardiac glycosides that were also absent from mass spectral libraries. Computational substructure predictions (as depicted in Figure 1b for calotropin) facilitated the structural elucidation of annotated



https://doi.org/10.1021/acs.analchem.2c02694
Anal. Chem. 2022, 94, 15971–15979

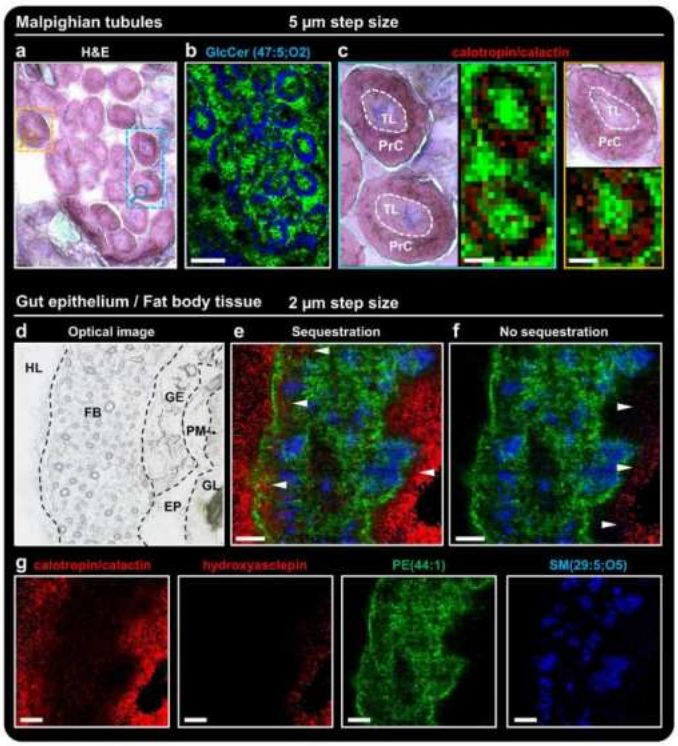


**Figure 3.** OTCD MALDI MSI of derivatized cardiac glycosides, nucleotides, and lipids at subcellular resolution in various tissue types and cells of *D. plexippus*. (a) Optical image of H&E-stained Malpighian tubules after MSI analysis. (b) Corresponding green−blue overlay image obtained with 5 µm step size showing the spatial distribution of thymidine 3′,5′-hydrogen phosphate ($[M + K]^+$, $m/z$ 343.0092, green) in the tubule lumen and GlcCer(47:5;O2) ($[M + H]^+$, $m/z$ 874.7130, blue) in the principal cell of the tubule. (c) Magnifications of the color-coded areas in (a) displaying the morphology for transverse-sectioned Malpighian tubules (PrC: principal cell; TL: tubule lumen) and their corresponding red−green overlay images obtained with 5 µm step size showing the spatial distribution of calotropin/calactin ($[M + GirT]^+$, $m/z$ 646.3699, red) and thymidine 3′,5′-hydrogen phosphate ($[M + K]^+$, $m/z$ 343.0092, green). (d) Optical image of the analyzed region of interest showing the hemolymph (HL), fat body (FB), gut epithelium (GE), ectoperitrophic space (EP), peritrophic membrane (PM), and gut lumen (GL). (e, f) Corresponding RGB overlay images obtained with 2 µm step size showing the spatial distribution of calotropin/calactin ($[M + GirT]^+$, $m/z$ 646.3699, red) for (e), hydroxyasclepin ($[M + GirT]^+$, $m/z$ 704.3754, red) for (f), and PE(44:1) ($[M + H]^+$, $m/z$ 858.6927, green) and SM(29:5;O5) ($[M + Na]^+$, $m/z$ 695.3991, blue) for (e) and (f). (g) Single ion images for the molecular compounds shown in the RGB overlays. Scale bars: (b) 100 µm, (c) 25 µm, and (e−g) 60 µm.

cardiac glycosides. Whereas all detected and classified cardiac glycosides are 19-oxosteroids (besides digitoxigenin ($m/z$ 375.2531) and two derivatives (Figure 1a), the molecular network exclusively contains cardiac glycoside with an aldehyde group. Therefore, cardiac glycosides having a hydroxyl function at C19 (frugoside, $C_{29}H_{44}O_9$ at $m/z$ 537.3063; antiaroside B, $C_{35}H_{54}O_{14}$ at $m/z$ 699.3591; strophanthidol, $C_{23}H_{34}O_6$ at $m/z$ 407.2426) were not part of the cardiac glycoside network due to different characteristic fragments (Figure S4 and Supplementary Note 5). Despite having an aldehyde group at C19, gofruside ($m/z$ 535.2902, $C_{29}H_{42}O_9$) and corglycone ($m/z$ 551.2860, $C_{29}H_{42}O_{10}$) were also excluded from the molecular network due to ether-bond-linkage between the aglycone and glycoside unit (instead of 1,4-dioxane linkage), and the precursor calotropagenin ($m/z$ 405.2281, $C_{23}H_{32}O_6$) was excluded due to the absence of a glycoside unit. Importantly, FBMN resolved several isomers for $m/z$ 533.2741 ($C_{29}H_{40}O_9$), $m/z$ 549.2693 ($C_{29}H_{40}O_{10}$), and $m/z$ 591.2803 ($C_{31}H_{42}O_{11}$) that have similar $MS^2$ spectra but distinct retention times and thus would have remained hidden in classical molecular networking. The molecular network can be divided into subnetworks depending on different chemical subgroups (thiazolidine/thiazoline, acetyloxy, and hydroxy/ketone group) in the glycoside unit, which is represented by the spectral library annotations for voruscharin, asclepin, and calotropin in Figure 1a. In addition, FBMN enabled quantitative analysis by using the LC−MS feature abundance (peak area) showing that asclepin ($C_{31}H_{42}O_{10}$ at $m/z$



https://doi.org/10.1021/acs.analchem.2c02694
Anal. Chem. 2022, 94, 15971−15979

575.2855), 16α-acetoxyasclepin ($C_{33}H_{44}O_{12}$ at $m/z$ 633.2902), uscharidin ($C_{29}H_{38}O_9$ at $m/z$ 531.2587), and voruscharin ($C_{31}H_{43}NO_8S$ at $m/z$ 590.2791) are the most abundant cardiac glycosides in *A. curassavica*.

**Visualizing Metabolic Networks of Cardiac Glycoside Sequestration in *D. plexippus*.** Next, we utilized our metabolomic "in-house" database to guide *in situ* visualization of metabolic networks related to cardiac glycoside sequestration in fifth instar longitudinal *D. plexippus* caterpillar sections. However, previous studies showed that detecting and visualizing steroidal compounds using MSI coupled with soft ionization techniques are exceptionally difficult due to poor ion yields and the presence of interfering molecules in the low mass-to-charge-number range ($m/z$ < 500).[20−25] Therefore, we used Girard's reagent T (GirT) to enhance detection sensitivity while retaining spatial information. We developed an ultrafine OTCD method by utilizing a high reagent concentration combined with a low total spray volume and flow rate that was followed by incubation without increased humidity and optimized matrix application (Figures S5−S9 and Supplementary Note 6 for details regarding method development). Girard's reagent T reacted with carbonyl-containing cardiac glycosides, resulting in hydrazone formation and a positively charged triethylamine function (Figure 2a). To analyze and demonstrate the ion signal boost provided by the covalent charge-tagging approach, we also performed MSI experiments without OTCD, but with identical experimental parameters, of the adjacent section.

The optical images (Figure 2b) display the analyzed area consisting of the gut lumen (GL) that contains the *A. curassavica* plant material and is surrounded by the gut epithelium (GE), fat tissue (FT), and integument (I). The corresponding MSI results for three selected ion signals are shown in red−green−blue overlay (RGB) images obtained with a 25 μm step size (Figure 2b). The red color channel highlights the spatial distribution of the toxic cardiac glycoside isomers calotropin/calactin ($[M + K]^+$ and $[M + GirT]^+$, respectively). The green color channel represents pheophytin a ($[M + K]^+$), which is characterized as a chlorophyll A molecule without the central $Mg^{2+}$ cation and serves as a marker for the plant material. The spatial distribution of PS(36:3) ($[M + K]^+$) is shown in blue, highlighting the gut epithelium and fat tissue. In general, for OTCD, no additional adducts ($H^+$, $Na^+$, $K^+$) of cardiac glycosides were detected, and derivatized ions were exclusively detected as GirT-carrying ions. For comparison, both RGB images were normalized to the same intensity scale, thereby demonstrating that the average signal intensity of calotropin/calactin was increased by 16-fold ($[M + GirT]^+$ relative to the dominant non-OTCD adduct $[M + K]^+$, see Figure S10 for box plots), also increasing the pixel coverage to 72% (35% for the control). Hence, OTCD MALDI MSI significantly improved the extracted biological information and vividly revealed that steroidal glycosides are extracted from the *A. curassavica* plant material, absorbed into the gut epithelium, and stored in the integument of the caterpillar. Importantly, derivatized species preserved their fidelity and spatial integrity, therefore allowing us to spatially resolve the fine distribution of accumulated cardiac glycosides in the single layer of epithelial cells in the integument, as shown in Figure 2c for calotropin/calactin. The corresponding single-pixel mass spectrum (Figure S11) demonstrates that $[calotropin/calactin+GirT]^+$ is one of the most abundant signals (ion intensities of ~$1 \times 10^5$), thus enabling *in situ* identification by on-tissue single-pixel MALDI $MS^2$ (Figure 2c). In total, we detected and annotated 19 derivatized cardiac glycosides in *D. plexippus*, demonstrating that our LC−MS-based molecular networking/AI-classification approach successfully guided and facilitated the spatial molecular characterization using MSI. Our OTCD MALDI MSI results determined that the majority of cardiac glycosides are taken up and stored in the integument of the caterpillar (e.g., calotropin/calactin (Figure 2b), low amounts of uscharidin (Figure 2d) and hydroxyuscharidin (Figure 2e), gofrugoside (Figure 2f), calotoxin/hydroxycalactin/hydroxycalotropin (Figure 2g), and calotropagenin (Figure 2h)). In contrast, asclepin (Figure 2i) and hydroxyasclepin (Figure 2j) belong to the most abundant toxic glycosides in *A. curassavica* (Figure 1a) and were exclusively located in the gut lumen. Thus, our MSI results demonstrate that small incremental changes in the chemical structure directly correlate to the selectivity of plant toxin sequestration in *D. plexippus*.

**Visualizing (Sub)Cellular Distributions of Derivatized Cardiac Glycosides.** To elucidate specific molecular events and transport processes involved in cardiac glycoside sequestration, the spatially resolved analysis has to approach (sub)cellular resolution. We performed OTCD-MSI experiments with 5 μm step size of Malpighian tubules, which are multifunctional tissues involved in osmoregulation, renal excretion of nitrogenous waste, and elimination of xenobiotics and metabolic waste from the hemolymph.[48] We note that the MSI experiments were performed without oversampling, as demonstrated in Figure S12, showing the matrix-coated sample surface after measurement and laser ablation craters with a diameter of ~3 μm onto the penetrated tissue.

Figure 3a shows the optical image of H&E-stained Malpighian tubules after MSI analysis (Figure S2 for the whole longitudinal *D. plexippus* larva section and Figure S13 before MSI analysis). The morphology of transverse-sectioned tubules (Figure S14) can be reproduced by the MSI green−blue overlay image (Figure 3b) showing the spatial distribution of thymidine 3′,5′-hydrogen phosphate ($[M + K]^+$ at $m/z$ 343.0092) in green and GlcCer(47:5;O2) ($[M + H]^+$ at $m/z$ 874.7130) in blue. The nucleotide derivative was primarily located in the tubule lumen (TL) and the surrounding tissue, whereas a broad variety of lipids (Figure S15 for additional examples of different lipid classes) were exclusively detected in the principal cell (PrC).

Figure 3c displays detailed MSI results for two defined regions of interest (highlighted in Figure 3a), with the red color channel representing the spatial distribution of derivatized calotropin/calactin ($[M + GirT]^+$ at $m/z$ 646.3699). Interestingly, the cardiac glycoside was exclusively detected in the principal cell and not in the lumen of the tubules. However, the transepithelial fluid secretion to produce urine in the Malpighian tubules includes an osmotic gradient that causes water-soluble xenobiotics and metabolic waste from the hemolymph to diffuse. Thus, our OTCD MALDI MSI results suggest that cardiac glycosides are not part of the transcellular and paracellular excretion pathways and indicate that they may instead be actively transported back to the hemolymph and subsequently stored in the integument. Therefore, toxic glycosides that were already absorbed and transported through the gut epithelium are not excreted, which enhance the efficiency of the sequestration mechanism.

To demonstrate the potential of OTCD MALDI MSI for investigating the spatial organization of metabolic networks with sampling areas below 5 $\mu m^2$, we next analyzed different



https://doi.org/10.1021/acs.analchem.2c02694
Anal. Chem. 2022, 94, 15971−15979

physiological layers regarding cardiac glycoside uptake with 2 μm step size. We detected and spatially resolved various derivatized cardiac glycosides primarily located in the gut lumen (GL), ectoperitrophic space (EP), fat body (FB), and hemolymph (Figure 3d−g and Figure S16, red color channel). We utilized the distribution of the lipids $[PE(44:1) + H]^+$ at $m/z$ 858.6927 in green as a tissue marker for the gut epithelium and fat body and $[SM(29:5;O5) + Na]^+$ at $m/z$ 695.3991 in blue showing specific enrichments in the gut epithelium and fat body, which would most likely remain hidden with larger step sizes. The low cardiac glycoside abundance in the gut epithelium may suggest fast and efficient transport across the tissue into the hemolymph. However, different ionization efficiencies due to different sample matrix backgrounds (i.e., gut epithelium tissue and gut lumen) have to be considered. In previous studies,[39] it was not possible to visualize cardiac glycoside distributions in the fat body of the larvae. However, we observed the accumulation of calotropin/calactin, calotoxin/hydroxycalotropin/hydroxycalactin, and the precursor calotropagenin in the fat body with an increased accumulation in the outer layer of the fat tissue (Figure 3e and Figure S16a). Notably, this observation was not made for other derivatized metabolites with similar polarity (e.g., futalosine derivative; Figure S16b), thus suggesting that this specific pattern along with other (sub)cellular cardiac glycoside distributions is not caused by analyte diffusion effects during sample preparation. Figure 3f shows the spatial distribution for hydroxyasclepin, which is not sequestered by *D. plexippus* (as determined in the previous MSI experiment). Instead, hydroxyasclepin, which belongs to one of the most abundant cardiac glycosides in *A. curassavica*, was exclusively detected in the gut lumen and ectoperitrophic space with similar intensity to calotropin/calactin but not located in the gut epithelium tissue (despite being in direct contact). Thus, our MSI data demonstrate that the peritrophic membrane (PM), which was shown to restrict the cardenolide digitoxin to the gut lumen of locusts,[49] has no function regarding the selectivity of cardiac glycoside sequestration in our system.

## CONCLUSIONS

Our workflow combines novel computational methods for *in silico* annotation, classifying chemical compounds and generating molecular networks based on LC−MS bulk analysis with high-resolution OTCD MALDI MSI in a robust way to comprehensively analyze metabolic networks in the spatial context of tissues and cells. Utilizing plant toxin sequestration in *D. plexippus* as a model system, we were able to structurally characterize and identify 32 different steroidal glycosides in the host plant *A. curassavica*. To the best of our knowledge, this is the highest number of detected cardiac glycosides for this milkweed species, thereby demonstrating the enormous potential of computational metabolomics approaches to decompose metabolic networks into compound classes and molecule annotations. However, no available *in silico* molecular fingerprint-based annotation method can distinguish between correct and incorrect annotations, making manual evaluation necessary. Our covalent charge-tagging approach using the GirT reagent substantially improved the sensitivity and enabled the spatial visualization of carbonyl-containing cardiac glycosides in the fat body, gut epithelium, Malpighian tubules, and epidermal integument cells of *D. plexippus* with pixel sizes of 2, 5, and 25 μm. In this context, the optimized OTCD sample preparation protocol preserved spatial integrity to ensure that the effective lateral resolution was defined by the laser spot size rather than the analyte diffusion radius. Although primarily demonstrated here for carbonyl-containing steroidal glycosides, many functional groups (phenols,[50,51] thiols,[52] amines,[53,54] carboxylic acids,[55] phosphate monoesters,[56] and alkenes[57,58]) can be targeted with different OTCD reagents to achieve increased ion yields and to force specific fragmentation patterns. Thus, our generic workflow represents a customizable and expandable method and can readily be applied to a wide range of spatially resolved small-molecule studies in the fields of chemistry, biology, and medicine.

## ASSOCIATED CONTENT

### Supporting Information

The Supporting Information is available free of charge at https://pubs.acs.org/doi/10.1021/acs.analchem.2c02694.

More detailed descriptions regarding experimental parameters and data analysis (Supplementary Notes 1−6); overview for all annotated cardiac glycosides (Table S1); experimental design of this study (Figure S1); optical image of final instar longitudinal *D. plexippus* section (Figure S2); comprehensive FBMN results (Figure S3); LC−$MS^2$ spectra for calotropin and frugoside highlighting different fragmentation pathways (Figure S4); additional results for OTCD method development (Figures S5−S9); box plots for *in silico* quantification of MSI data (Figure S10), MS spectra for control and OTCD MSI obtained at *D. plexippus* integument (Figure S11); optical images of *D. plexippus* Malpighian tubules before OTCD and matrix application and after MSI and H&E staining (Figures S12 and S13); simplified scheme showing Malpighian tubule morphology (Figure S14); OTCD MALDI MSI results showing subcellular lipid distributions in Malpighian tubules (Figure S15); OTCD MALDI MSI results obtained with 2 μm step size showing various derivatized metabolites (Figure S16); and LC−$MS^2$ spectra for all detected cardiac glycosides including fragmentation pathways (Supplementary Data 1) (PDF)

## AUTHOR INFORMATION


### Corresponding Author

**Bernhard Spengler** − *Institute for Inorganic and Analytical Chemistry, Justus Liebig University Giessen, 35392 Giessen, Germany;* orcid.org/0000-0003-0179-5653; Email: bernhard.spengler@anorg.chemie.uni-giessen.de

### Authors

**Domenic Dreisbach** − *Institute for Inorganic and Analytical Chemistry, Justus Liebig University Giessen, 35392 Giessen, Germany*

**Sven Heiles** − *Institute for Inorganic and Analytical Chemistry, Justus Liebig University Giessen, 35392 Giessen, Germany; Leibniz Institute for Analytical Sciences, ISAS−e.V., 44139 Dortmund, Germany; Lipidomics, Faculty of Chemistry, University of Duisburg-Essen, 45141 Essen, Germany;* orcid.org/0000-0003-3779-8071

**Dhaka R. Bhandari** − *Institute for Inorganic and Analytical Chemistry, Justus Liebig University Giessen, 35392 Giessen, Germany*

**Georg Petschenka** – *Institute of Phytomedicine, University of Hohenheim, 70599 Stuttgart, Germany*

Complete contact information is available at: https://pubs.acs.org/10.1021/acs.analchem.2c02694

### Author Contributions

B.S. supervised the project; D.D, S.H, D.B., and B.S. conceived this study; G.P. provided monarch larvae samples and gave biological insight; D.D. performed all experiments; D.D. performed data analysis; all authors discussed the findings; D.D. wrote the original draft; and all authors reviewed and edited the manuscript. All authors have approved the final version of the manuscript.

### Notes

The authors declare the following competing financial interest(s): B.S. is a consultant and D.D. is a part-time employee of TransMIT GmbH, Giessen, Germany.

## ■ ACKNOWLEDGMENTS

This research was funded by DFG grant PE 2059/3-1 to G.P. and the LOEWE Program of the State of Hesse by funding the LOEWE Center for Insect Biotechnology and Bioresources. Financial support by the German Research Foundation [Deutsche Forschungsgemeinschaft (DFG) under grants Sp314/13-1, Sp314/23-1, and INST 162/500-1 FUGG] and by the Federal State of Hesse LOEWE Center DRUID (Novel Drug Targets against Poverty-Related and Neglected Tropical Diseases) is gratefully acknowledged. S.H. acknowledges the support by the "Ministerium für Kultur und Wissenschaft des Landes Nordrhein-Westfalen" and the German Ministry of Research and Education (BMBF).

## ■ REFERENCES

(1) Jeong, H.; Tombor, B.; Albert, R.; Oltvai, Z. N.; Barabási, A.-L. *Nature* **2000**, *407*, 651−654.
(2) Wagner, A.; Fell, D. A. *Proc. R. Soc. London. Ser. B Biol. Sci.* **2001**, *268*, 1803−1810.
(3) Ma, H.; Zeng, A.-P. *Bioinformatics* **2003**, *19*, 270−277.
(4) Dräger, A.; Planatscher, H. *Metabolic Networks BT - Encyclopedia of Systems Biology*; Dubitzky, W., Wolkenhauer, O., Cho, K.-H., Yokota, H., Eds.; Springer New York: New York, NY, 2013; pp. 1249−1251. DOI: 10.1007/978-1-4419-9863-7_1277.
(5) Spengler, B. *Anal. Chem.* **2015**, *87*, 64−82.
(6) Buchberger, A. R.; DeLaney, K.; Johnson, J.; Li, L. *Anal. Chem.* **2018**, *90*, 240−265.
(7) Alexandrov, T. *Annu. Rev. Biomed. Data Sci.* **2020**, *3*, 61−87.
(8) Petras, D.; Jarmusch, A. K.; Dorrestein, P. C. *Curr. Opin. Chem. Biol.* **2017**, *36*, 24−31.
(9) Kompauer, M.; Heiles, S.; Spengler, B. *Nat. Methods* **2017**, *14*, 90−96.
(10) Gilmore, I. S.; Heiles, S.; Pieterse, C. L. *Annu. Rev. Anal. Chem.* **2019**, *12*, 201−224.
(11) Dreisewerd, K. *Chem. Rev.* **2003**, *103*, 395−426.
(12) Chu, K. Y.; Lee, S.; Tsai, M.-T.; Lu, I.-C.; Dyakov, Y. A.; Lai, Y. H.; Lee, Y.-T.; Ni, C.-K. *J. Am. Soc. Mass Spectrom.* **2014**, *25*, 310−318.
(13) Niehaus, M.; Schnapp, A.; Koch, A.; Soltwisch, J.; Dreisewerd, K. *Anal. Chem.* **2017**, *89*, 7734−7741.
(14) Soltwisch, J.; Jaskolla, T. W.; Hillenkamp, F.; Karas, M.; Dreisewerd, K. *Anal. Chem.* **2012**, *84*, 6567−6576.
(15) Soltwisch, J.; Kettling, H.; Vens-Cappell, S.; Wiegelmann, M.; Müthing, J.; Dreisewerd, K. *Science* **2015**, *348*, 211−215.
(16) Niehaus, M.; Soltwisch, J.; Belov, M. E.; Dreisewerd, K. *Nat. Methods* **2019**, *16*, 925−931.
(17) Spraggins, J. M.; Djambazova, K. V.; Rivera, E. S.; Migas, L. G.; Neumann, E. K.; Fuetterer, A.; Suetering, J.; Goedecke, N.; Ly, A.; Van de Plas, R. *Anal. Chem.* **2019**, *91*, 14552−14560.
(18) Soltwisch, J.; Heijs, B.; Koch, A.; Vens-Cappell, S.; Höhndorf, J.; Dreisewerd, K. *Anal. Chem.* **2020**, *92*, 8697−8703.
(19) Harkin, C.; Smith, K. W.; Cruickshank, F. L.; Logan Mackay, C.; Flinders, B.; Heeren, R. M. A.; Moore, T.; Brockbank, S.; Cobice, D. F. *Mass Spectrom. Rev.* **2021**, *41*, 662−694.
(20) Cobice, D. F.; Mackay, C. L.; Goodwin, R. J. A.; McBride, A.; Langridge-Smith, P. R.; Webster, S. P.; Walker, B. R.; Andrew, R. *Anal. Chem.* **2013**, *85*, 11576−11584.
(21) Cobice, D. F.; Livingstone, D. E. W.; Mackay, C. L.; Goodwin, R. J. A.; Smith, L. B.; Walker, B. R.; Andrew, R. *Anal. Chem.* **2016**, *88*, 10362−10367.
(22) Barré, F. P. Y.; Flinders, B.; Garcia, J. P.; Jansen, I.; Huizing, L. R. S.; Porta, T.; Creemers, L. B.; Heeren, R. M. A.; Cillero-Pastor, B. *Anal. Chem.* **2016**, *88*, 12051−12059.
(23) Takeo, E.; Sugiura, Y.; Uemura, T.; Nishimoto, K.; Yasuda, M.; Sugiyama, E.; Ohtsuki, S.; Higashi, T.; Nishikawa, T.; Suematsu, M.; Fukusaki, E.; Shimma, S. *Anal. Chem.* **2019**, *91*, 8918−8925.
(24) Angelini, R.; Yutuc, E.; Wyatt, M. F.; Newton, J.; Yusuf, F. A.; Griffiths, L.; Cooze, B. J.; El Assad, D.; Frache, G.; Rao, W. *Anal. Chem.* **2021**, *93*, 4932−4943.
(25) Zecchi, R.; Franceschi, P.; Tigli, L.; Amidani, D.; Catozzi, C.; Ricci, F.; Salomone, F.; Pieraccini, G.; Pioselli, B.; Mileo, V. *Anal. Bioanal. Chem.* **2021**, 4363.
(26) Vinaixa, M.; Schymanski, E. L.; Neumann, S.; Navarro, M.; Salek, R. M.; Yanes, O. *TrAC, Trends Anal. Chem.* **2016**, *78*, 23−35.
(27) Kind, T.; Tsugawa, H.; Cajka, T.; Ma, Y.; Lai, Z.; Mehta, S. S.; Wohlgemuth, G.; Barupal, D. K.; Showalter, M. R.; Arita, M.; Fiehn, O. *Mass Spectrom. Rev.* **2018**, *37*, 513−532.
(28) Montenegro-Burke, J. R.; Guijas, C.; Siuzdak, G. METLIN: A Tandem Mass Spectral Library of Standards. In *Computational Methods and Data Analysis for Metabolomics*; Springer, 2020; pp. 149−163, DOI: 10.1007/978-1-0716-0239-3_9.
(29) Watrous, J.; Roach, P.; Alexandrov, T.; Heath, B. S.; Yang, J. Y.; Kersten, R. D.; van der Voort, M.; Pogliano, K.; Gross, H.; Raaijmakers, J. M. *Proc. Natl. Acad. Sci.* **2012**, *109*, E1743−E1752.
(30) Wang, M.; Carver, J. J.; Phelan, V. V.; Sanchez, L. M.; Garg, N.; Peng, Y.; Nguyen, D. D.; Watrous, J.; Kapono, C. A.; Luzzatto-Knaan, T.; Porto, C.; Bouslimani, A.; Melnik, A. V.; Meehan, M. J.; Liu, W. T.; Crüsemann, M.; Boudreau, P. D.; Esquenazi, E.; Sandoval-Calderón, M.; Kersten, R. D.; Pace, L. A.; Quinn, R. A.; Duncan, K. R.; Hsu, C. C.; Floros, D. J.; Gavilan, R. G.; Kleigrewe, K.; Northen, T.; Dutton, R. J.; Parrot, D.; Carlson, E. E.; Aigle, B.; Michelsen, C. F.; Jelsbak, L.; Sohlenkamp, C.; Pevzner, P.; Edlund, A.; McLean, J.; Piel, J.; Murphy, B. T.; Gerwick, L.; Liaw, C. C.; Yang, Y. L.; Humpf, H. U.; Maansson, M.; Keyzers, R. A.; Sims, A. C.; Johnson, A. R.; Sidebottom, A. M.; Sedio, B. E.; Klitgaard, A.; Larson, C. B.; Boya P, C. A.; Torres-Mendoza, D.; Gonzalez, D. J.; Silva, D. B.; Marques, L. M.; Demarque, D. P.; Pociute, E.; O'Neill, E. C.; Briand, E.; Helfrich, E. J. N.; Granatosky, E. A.; Glukhov, E.; Ryffel, F.; Houson, H.; Mohimani, H.; Kharbush, J. J.; Zeng, Y.; Vorholt, J. A.; Kurita, K. L.; Charusanti, P.; McPhail, K. L.; Nielsen, K. F.; Vuong, L.; Elfeki, M.; Traxler, M. F.; Engene, N.; Koyama, N.; Vining, O. B.; Baric, R.; Silva, R. R.; Mascuch, S. J.; Tomasi, S.; Jenkins, S.; Macherla, V.; Hoffman, T.; Agarwal, V.; Williams, P. G.; Dai, J.; Neupane, R.; Gurr, J.; Rodríguez, A. M. C.; Lamsa, A.; Zhang, C.; Dorrestein, K.; Duggan, B. M.; Almaliti, J.; Allard, P. M.; Phapale, P.; Nothias, L. F.; Alexandrov, T.; Litaudon, M.; Wolfender, J. L.; Kyle, J. E.; Metz, T. O.; Peryea, T.; Nguyen, D. T.; VanLeer, D.; Shinn, P.; Jadhav, A.; Müller, R.; Waters, K. M.; Shi, W.; Liu, X.; Zhang, L.; Knight, R.; Jensen, P. R.; Palsson, B. Ø.; Pogliano, K.; Linington, R. G.; Gutiérrez, M.; Lopes, N. P.; Gerwick, W. H.; Moore, B. S.; Dorrestein, P. C.; Bandeira, N. *Nat. Biotechnol.* **2016**, *34*, 828−837.
(31) Nothias, L.-F.; Petras, D.; Schmid, R.; Dührkop, K.; Rainer, J.; Sarvepalli, A.; Protsyuk, I.; Ernst, M.; Tsugawa, H.; Fleischauer, M.; Aicheler, F.; Aksenov, A. A.; Alka, O.; Allard, P. M.; Barsch, A.; Cachet, X.; Caraballo-Rodriguez, A. M.; da Silva, R. R.; Dang, T.;

Garg, N.; Gauglitz, J. M.; Gurevich, A.; Isaac, G.; Jarmusch, A. K.; Kameník, Z.; Kang, K. B.; Kessler, N.; Koester, I.; Korf, A.; le Gouellec, A.; Ludwig, M.; Martin, H. C.; McCall, L. I.; McSayles, J.; Meyer, S. W.; Mohimani, H.; Morsy, M.; Moyne, O.; Neumann, S.; Neuweger, H.; Nguyen, N. H.; Nothias-Esposito, M.; Paolini, J.; Phelan, V. V.; Pluskal, T.; Quinn, R. A.; Rogers, S.; Shrestha, B.; Tripathi, A.; van der Hooft, J. J. J.; Vargas, F.; Weldon, K. C.; Witting, M.; Yang, H.; Zhang, Z.; Zubeil, F.; Kohlbacher, O.; Böcker, S.; Alexandrov, T.; Bandeira, N.; Wang, M.; Dorrestein, P. C. *Nat. Methods* **2020**, *17*, 905−908.
(32) Dührkop, K.; Shen, H.; Meusel, M.; Rousu, J.; Böcker, S. *Proc. Natl. Acad. Sci.* **2015**, *112*, 12580−12585.
(33) Dührkop, K.; Fleischauer, M.; Ludwig, M.; Aksenov, A. A.; Melnik, A. V.; Meusel, M.; Dorrestein, P. C.; Rousu, J.; Böcker, S. *Nat. Methods* **2019**, *16*, 299−302.
(34) Feunang, Y. D.; Eisner, R.; Knox, C.; Chepelev, L.; Hastings, J.; Owen, G.; Fahy, E.; Steinbeck, C.; Subramanian, S.; Bolton, E. *Aust. J. Chem.* **2016**, *8*, 1−20.
(35) Dührkop, K.; Nothias, L.-F.; Fleischauer, M.; Reher, R.; Ludwig, M.; Hoffmann, M. A.; Petras, D.; Gerwick, W. H.; Rousu, J.; Dorrestein, P. C.; Böcker, S. *Nat. Biotechnol.* **2021**, *39*, 462−471.
(36) Petschenka, G.; Agrawal, A. A. *Proc. R. Soc. B Biol. Sci.* **1818**, *2015*, 20151865.
(37) Petschenka, G.; Agrawal, A. A. *Curr. Opin. insect Sci.* **2016**, *14*, 17−24.
(38) Jones, P. L.; Petschenka, G.; Flacht, L.; Agrawal, A. A. *J. Chem. Ecol.* **2019**, *45*, 264−277.
(39) Dreisbach, D.; Bhandari, D. R.; Betz, A.; Tenbusch, L.; Vilcinskas, A.; Spengler, B.; Petschenka, G. *bioRxiv* **2022**, DOI: 10.1101/2022.06.02.494161.
(40) Kompauer, M.; Heiles, S.; Spengler, B. *Nat. Methods* **2017**, *14*, 1156−1158.
(41) Paschke, C.; Leisner, A.; Hester, A.; Maass, K.; Guenther, S.; Bouschen, W.; Spengler, B. *J. Am. Soc. Mass Spectrom.* **2013**, *24*, 1296−1306.
(42) Robichaud, G.; Garrard, K. P.; Barry, J. A.; Muddiman, D. C. *J. Am. Soc. Mass Spectrom.* **2013**, *24*, 718−721.
(43) Palmer, A.; Phapale, P.; Chernyavsky, I.; Lavigne, R.; Fay, D.; Tarasov, A.; Kovalev, V.; Fuchser, J.; Nikolenko, S.; Pineau, C.; Becker, M.; Alexandrov, T. *Nat. Methods* **2017**, *14*, 57−60.
(44) Pluskal, T.; Castillo, S.; Villar-Briones, A.; Orešič, M. *BMC Bioinf.* **2010**, *11*, 395.
(45) Shannon, P.; Markiel, A.; Ozier, O.; Baliga, N. S.; Wang, J. T.; Ramage, D.; Amin, N.; Schwikowski, B.; Ideker, T. *Genome Res.* **2003**, *13*, 2498−2504.
(46) Zhang, R.-R.; Tian, H.-Y.; Tan, Y.-F.; Chung, T.-Y.; Sun, X.-H.; Xia, X.; Ye, W.-C.; Middleton, D. A.; Fedosova, N.; Esmann, M.; Tzen, J. T. C.; Jiang, R.-W. *Org. Biomol. Chem.* **2014**, *12*, 8919−8929.
(47) Agrawal, A. A.; Böröczky, K.; Haribal, M.; Hastings, A. P.; White, R. A.; Jiang, R.-W.; Duplais, C. *Proc. Natl. Acad. Sci.* **2021**, *118*, No. e2024463118.
(48) Beyenbach, K. W.; Skaer, H.; Dow, J. A. T. *Annu. Rev. Entomol.* **2010**, *55*, 351−374.
(49) Barbehenn, R. V. *Arch. Insect Biochem. Physiol.* **1999**, *42*, 130−137.
(50) Chacon, A.; Zagol-Ikapitte, I.; Amarnath, V.; Reyzer, M. L.; Oates, J. A.; Caprioli, R. M.; Boutaud, O. *J. Mass Spectrom.* **2011**, *46*, 840−846.
(51) Beasley, E.; Francese, S.; Bassindale, T. *Anal. Chem.* **2016**, *88*, 10328−10334.
(52) Fülöp, A.; Bausbacher, T.; Rizzo, S.; Zhou, Q.; Gillandt, H.; Hopf, C.; Rittner, M. *Anal. Chem.* **2020**, *92*, 6224−6228.
(53) Djidja, M.; Francese, S.; Loadman, P. M.; Sutton, C. W.; Scriven, P.; Claude, E.; Snel, M. F.; Franck, J.; Salzet, M.; Clench, M. R. *Proteomics* **2009**, *9*, 2750−2763.
(54) Shariatgorji, M.; Nilsson, A.; Goodwin, R. J. A.; Källback, P.; Schintu, N.; Zhang, X.; Crossman, A. R.; Bezard, E.; Svenningsson, P.; Andren, P. E. *Neuron* **2014**, *84*, 697−707.
(55) Wu, Q.; Comi, T. J.; Li, B.; Rubakhin, S. S.; Sweedler, J. V. *Anal. Chem.* **2016**, *88*, 5988−5995.
(56) Iwama, T.; Kano, K.; Saigusa, D.; Ekroos, K.; van Echten-Deckert, G.; Vogt, J.; Aoki, J. *Anal. Chem.* **2021**, *93*, 3867−3875.
(57) Wäldchen, F.; Spengler, B.; Heiles, S. *J. Am. Chem. Soc.* **2019**, *141*, 11816−11820.
(58) Wäldchen, F.; Mohr, F.; Wagner, A. H.; Heiles, S. *Anal. Chem.* **2020**, *92*, 14130−14138.





https://doi.org/10.1021/acs.analchem.2c02694
*Anal. Chem.* 2022, 94, 15971−15979

**Supplementary Information**

# Supplementary Information

## Molecular Networking and On-Tissue Chemical Derivatization for Enhanced Identification and Visualization of Steroid Glycosides by MALDI Mass Spectrometry Imaging

**Domenic Dreisbach[1], Sven Heiles[1,2,3], Dhaka R. Bhandari[1], Georg Petschenka[4], Bernhard Spengler*[1]**

[1]Institute for Inorganic and Analytical Chemistry, Justus Liebig University Giessen, Heinrich-Buff-Ring 17, 35392 Giessen, Germany

[2]Leibniz Institute for Analytical Sciences, ISAS – e.V., Otto-Hahn-Straße 6b, 44139 Dortmund, Germany

[3]Lipidomics, Faculty of Chemistry, University of Duisburg-Essen, Universitätsstraße 5, 45141 Essen, Germany

[4]Institute of Phytomedicine, University of Hohenheim, Otto-Sander-Straße 5, 70599 Stuttgart, Germany

* corresponding author: bernhard.spengler@anorg.chemie.uni-giessen.de

# Table of Content

**Supplementary Protocol 1: H&E staining protocol**

1. Dehydration in ethanol and set to demineralized water
   - 100 % ethanol: 2 min
   - 70% ethanol: 2 min
   - 40% ethanol: 2 min
   - Demineralized water: 2 min
2. Hematoxylin: 12 min
3. Washing steps
   - Tap water: 10 min
   - Demineralized water: 5 min
4. 1% aqueous eosin Y solution: 1 min
5. Differentiation in ethanol
   - Demineralized water: 2 min
   - 40% ethanol: 2 min
   - 70% ethanol: 2 min
   - 100 % ethanol: 2 min
6. Xylol
7. Eukitt fixation

**Supplementary Note 1: Sample preparation for LC-MS**

*A. curassavica* leaf samples were harvested, immediately freeze-fried in liquid nitrogen, ground to a fine powder and subsequently extracted for LC-$MS^2$ experiments. An amount of 50 mg of dry leaf powder was transferred into 2 mL screw-cap vials (Sarstedt, Nümbrecht, Germany) and after the addition of 900 mg zirconia beads (Roth, Karlsruhe, Germany), samples were homogenized in a Fast-Prep-24 instrument (MP Biomedicals, Germany) for two 45 sec cycles at a speed of 6.5 m/sec. Subsequently, samples were centrifuged at 16,100 rpm and supernatants were transferred into fresh vials. After evaporating samples to dryness under a stream of $N_2$, dry residues were dissolved in 1 mL methanol by agitation in the Fast-Prep-24 instrument (without the addition of beads). Before LC-MS analysis, samples were filtered via Rotilabo®-syringe filters (nylon, 0.45 µm, Roth, Karlsruhe, Germany) and diluted (1:20) using MeOH.

**Supplementary Note 2: Experimental parameters for MSI analysis**

All MSI measurements were conducted in the positive-ion mode in mass-to-charge ($m/z$) range of 250 to 1000 at a mass resolution of 240,000 for Q Exactive HF (120,000 for Q Exactive) at

*m/z* 200. Internal lock-mass calibration was performed by using the DHB matrix cluster ion signal at *m/z* 716.12461 ([5DHB−4$H_2O$+$NH_4$]$^+$), resulting in a high mass accuracy of ±1 ppm. For desorption/ionization, 50 laser pulses per pixel at a wavelength of 343 nm were focused perpendicular to the sample surface. The step size of the XYZ-sample stage was set to the desired pixel size. The full-pixel mode was used for MALDI MSI experiments conducted with 25 µm step size. In full-pixel mode, the pixel area is ablated by multiple laser pulses by a meandering movement to improve the ion signal intensities of the MSI experiment. The scan speed for all MSI experiments was 1.6 pixel/s. The acceleration voltage was set to 3 kV. The ion injection time was set to 500 ms. The capillary temperature was 250 °C, and the S-lens level was set to 100 arbitrary units.

**Supplementary Note 3: Experimental parameters for HPLC-MS analysis**

The injection volume was 15 µL, and the column compartment was set to 50 °C. Mobile phase A was water (0.1 % FA). Mobile phase B was acetonitrile (0.1 % FA). A flow rate of 0.5 mL/min applying the following gradient: 0−2 min, 10% B; 2−20 min, 20−70% B; 20−25 min, 70−95% B; 25−30 min, 95% B; 30−35 min, 95−10% B. The mass spectrometer was operated in positive-ion mode in a mass-to-charge (*m/z*) range of 250 to 1000 at a mass resolution of 240,000 at *m/z* 200. Data-dependent acquisition (DDA) for $MS^2$ spectra was performed. Up to 7 $MS^2$ spectra per $MS^1$ survey scan were recorded. The maximum ion injection time for $MS^2$ scans was set to 100 ms with an AGC target of 1E5 ions and a minimum of 5% AGC. The $MS^2$ precursor isolation window was set to $\Delta m/z$ = ±1. Normalized collision energy (NCE) of 25 % was used for fragmentation with $z$ = 1 as the default charge state. Dynamic precursor exclusion was set to 6s. Following HESI-source parameters were applied: spray voltage (+), 3.5 kV; capillary temperature, 300 °C; sheath gas flow rate, 35 psi; aux gas flowrate, 12 psi; aux gas heater temperature, 150 °C.

**Supplementary Note 4: LC-MS data pre-processing using MZmine 2**

The mzXML files were imported and following parameters were applied: an initial threshold of 1E6 for $MS^1$ spectra and 1E4 for $MS^2$ spectra was used. For feature-detection, the ADAP chromatogram builder was used with a minimum signal intensity and group intensity threshold of 3E6 and with ± 3 ppm mass tolerance. A minimum mass appearance over 5 consecutive scans was set. The extracted ion chromatograms were deconvoluted using the local minimum search algorithm with a chromatographic threshold of 10%, search minimum in RT range of 0.3 min, minimum relative height of 10%, minimum absolute height of 3E6, minimum ratio of peak top/edge 0.5 and peak duration between 0.02 min and 3 min. For $MS^1$-$MS^2$ pairing, a

mass range of 0.01 Da for median m/z centre calculation and RT range of 0.2 min was used. Isotope signals were grouped with m/z tolerance of ± 3 ppm and RT tolerance of 0.1 min.

**Supplementary Note 5: Feature-based molecular networking from the GNPS analysis infrastructure**

The .mgf files were uploaded into the GNPS ecosystem and for FBMN following parameters were applied: precursor ion mass tolerance: 0.01 Da, fragment ion mass tolerance: 0.01 Da. The minimum cosine score between a pair of MS2 spectra in order to form an edge in the molecular network was 0.7. The maximum amount of neighbour nodes from a single node was 10. The minimum number of fragment ions that were shared between pairs of related $MS^2$ spectra was 5. The maximum precursor ion mass difference between two nodes was 600 Da. For spectral library annotations, the $MS^2$ spectra contained a minimum number of 6 matched fragment ions. Additionally, the minimum cosine score after spectral matching of experimental $MS^2$ spectra with spectral library $MS^2$ spectra was 0.7. The molecular networking results were imported into Cytoscape (v.3.8.0). For optimal visualization, $H^+$-adducts were exclusively shown.

**Supplementary Note 6: Method development for high-resolution OTCD MALDI MSI of cardiac glycosides**

We optimized the sample preparation protocol to achieve high sensitivity while retaining spatial information. In summary, the solvent composition of methanol/water (7:3) v/v enabled high GirT-concentration (15 mg/mL), which subsequently allowed us to use a low spray volume (35 µL) combined with a low flowrate (7 µl/min) to prevent analyte delocalization and washing-effects (as shown in Figure S5 for 50 µL spray volume and 10 µL/min flow rate). Between OTCD and matrix application, the sample tissue was transferred into a desiccator for two hours at room temperature to increase reaction yield (Figure S6) and to prevent spatial artefacts due to hydroscopic properties of the GirT reagent. Any further incubation step that included increased humidity and temperature resulted in analyte delocalization and washing effects (Figure S7) and was thus avoided. Next, OTCD was quenched by matrix application, which also provides chemical preservation and inhibits oxidation of derivatized cardiac glycosides (Figure S6). Using an ultrafine pneumatic spraying protocol for DHB as a matrix with methanol/water (1:1) v/v as solvent showed excellent results regarding homogenous matrix crystallization (crystal sizes ≤ 10 µm) for different surface characteristics of *D. plexippus* tissue sections, including fat body tissue, digested plant material and integument (Figure S8 and Figure S9 for comparison with DHB matrix layer without OTCD).

**Supplementary Table 1**. Overview of the cardiac glycoside composition in *A. curassavica*, determined via LC-MS-based feature-based molecular networking and *in silico* molecular characterization.

| m/z (exp.) | mass error (ppm) | sum formula | RT (min) | annotation |
|---|---|---|---|---|
| 375.2530 | 1.2 | $C_{23}H_{34}O_4$ | 12.91 | digitoxigenin |
| 405.2280 | 1.1 | $C_{23}H_{34}O_4$ | 5.24 | calotropagenin |
| 407.2433 | 1.3 | $C_{23}H_{34}O_6$ | 4.90 | strophanthidol |
| 505.3165 | 1.0 | $C_{29}H_{44}O_7$ | 11.07 | digitoxigenin digitoxoside |
| 519.2879 | 1.1 | $C_{29}H_{42}O_8$ | 12.20 | strobosid |
| 531.2587 | 1.2 | $C_{29}H_{38}O_9$ | 10.42 | uscharidin |
| 533.2742 | 1.5 | $C_{29}H_{40}O_9$ | 8.47 | calactin |
| 533.2742 | 1.5 | $C_{29}H_{40}O_9$ | 9.18 | calotropin |
| 535.2902 | 0.9 | $C_{29}H_{42}O_9$ | 8.26 | gofruside |
| 537.3060 | 0.7 | $C_{29}H_{44}O_9$ | 7.94 | frugoside |
| 547.2541 | 0.8 | $C_{29}H_{38}O_{10}$ | 9.53 | hydroxyuscharidin |
| 549.2692 | 1.0 | $C_{29}H_{40}O_{10}$ | 6.20 | calactinic acid |
| 549.2692 | 1.0 | $C_{29}H_{40}O_{10}$ | 7.24 | calotoxin |
| 549.2693 | 1.0 | $C_{29}H_{40}O_{10}$ | 8.38 | hydroxycalactin |
| 549.2693 | 1.0 | $C_{29}H_{40}O_{10}$ | 9.27 | hydroxycalotropin |
| 551.2860 | 0.6 | $C_{29}H_{42}O_{10}$ | 6.33 | corglycon |
| 553.3015 | 0.7 | $C_{29}H_{44}O_{10}$ | 6.16 | periplogenin glycoside |
| 561.3063 | 0.9 | $C_{31}H_{44}O_9$ | 11.95 | gomphoside-acetate |
| 575.2855 | 0.5 | $C_{31}H_{42}O_{10}$ | 10.70 | asclepin |
| 579.2805 | 1.1 | $C_{30}H_{42}O_{11}$ | 8.14 | hydroxycalactinic acid methylester |
| 588.2627 | 0.8 | $C_{31}H_{41}NO_8S$ | 11.56 | uscharin |
| 590.2791 | 0.5 | $C_{31}H_{43}NO_8S$ | 10.92 | voruscharin |
| 591.2798 | 1.1 | $C_{31}H_{42}O_{11}$ | 8.19 | acetoxycalotropin |
| 591.2803 | 0.9 | $C_{31}H_{42}O_{11}$ | 8.56 | hydroxyasclepin |
| 604.2573 | 1.1 | $C_{31}H_{41}NO_9S$ | 7.76 | hydroxyuscharin |
| 606.2729 | 0.9 | $C_{31}H_{43}NO_9S$ | 10.78 | hydroxyvoruscharin |
| 619.3115 | 0.8 | $C_{33}H_{46}O_{11}$ | 11.37 | diacetylgofruside |
| 633.2902 | 1.0 | $C_{33}H_{44}O_{12}$ | 10.43 | acetoxyasclepin |
| 635.3795 | 0.7 | $C_{35}H_{54}O_{10}$ | 12.01 | digitoxin bisdigitoxoside |
| 697.3430 | 0.9 | $C_{35}H_{52}O_{14}$ | 7.13 | cannogenin diglycoside |
| 699.3591 | 0.6 | $C_{35}H_{54}O_{14}$ | 6.83 | antiaroside B |
| 711.3220 | 0.8 | $C_{35}H_{50}O_{16}$ | 5.91 | calotoxin-glycoside |

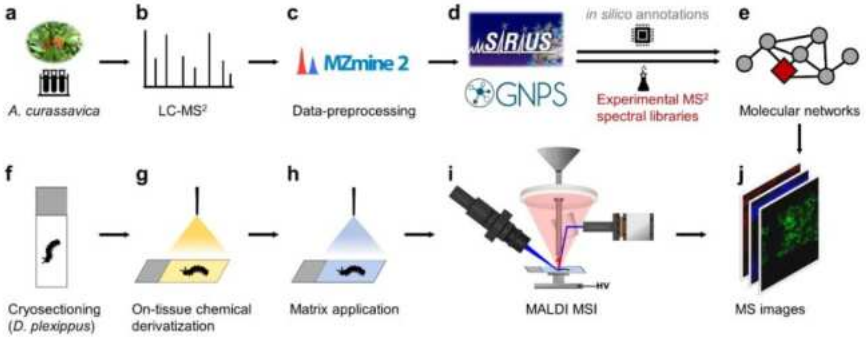


**Figure S1. Experimental design for the FBMN-based annotation and structural characterization of cardiac glycosides in *A. curassavica*, followed by *in situ* visualization of metabolic networks related to sequestration in *D. plexippus* using OTCD MALDI MSI.** (**a**) Metabolite extraction for *A. curassavica* leaf samples. (**b**) Performing non-targeted LC-MS$^2$ experiments. (**c**) LC-MS feature detection and data-preprocessing using MZmine 2. (**d**) FBMN workflow from the GNPS ecosystem in combination with SIRIUS for increased annotation rate, compound classification and structural elucidation. (**e**) Visualizing molecular networking results using Cytoscape and generate internal database to facilitate metabolite identification for subsequent MSI experiments. (**f**) Cryo-sectioning of last instar *D. plexippus* larvae. (**g**) Optimized pneumatic spraying protocol for OTCD using GirT reagent. (**h**) Optimized pneumatic spraying protocol for DHB matrix solution. (**i**) Performing high-resolution MALDI MSI experiments. (**j**) Identification of derivatized metabolites and generating the respective MS ion images.

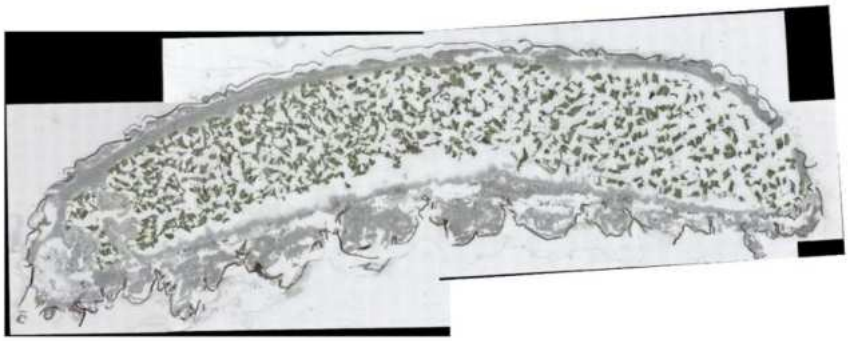

**Figure S2**. Optical image of longitudinal last instar *D. plexippus* caterpillar section.

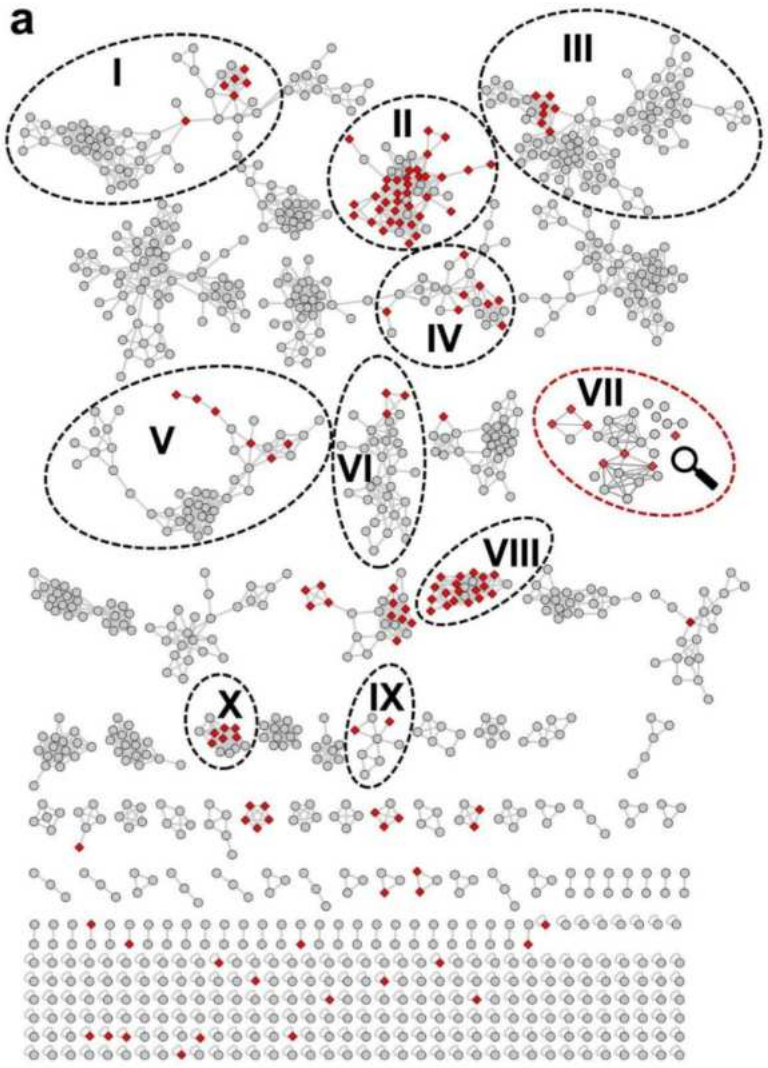


**Figure S3**. Comprehensive FBMN results consisting of 1175 mass spectral nodes, that were organized into 89 independent molecular families. In total, 145 spectral library hits (red nodes) were obtained allowing to classify the corresponding molecular networks. For instance, the molecular networks I to III (MN I-III) were composed of fatty acids, phosphatidylcholines (PC), sphingomyelins (SM) and arachidonoylthio-PCs; MN IV contains flavonoid glycosides, MN V contains phosphatidylethanolamines (PE), MN VI contains carotenoids, MN VII contains

cardiac glycosides, MN VIII contains flavonoids, MN IX contains polysaccharides and MN X contains isoflavonoids.

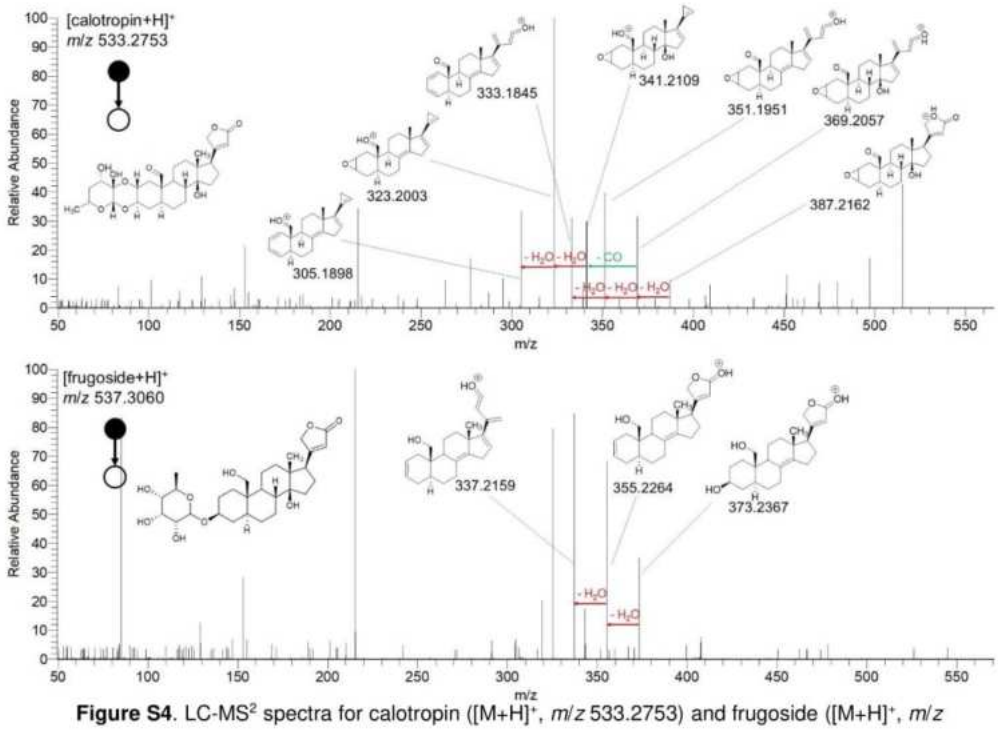


**Figure S4**. LC-MS$^2$ spectra for calotropin ([M+H]$^+$, *m/z* 533.2753) and frugoside ([M+H]$^+$, *m/z* 537.3060) highlighting the differences regarding characteristic fragments. Thus, frugoside was not part of the molecular network, which is based on the characteristic fragmentation pathway of calotropin, calactin and asclepin.

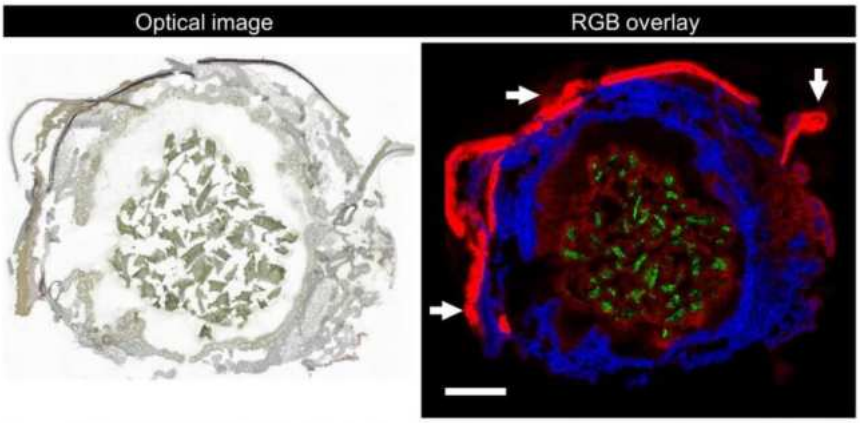


**Figure S5**. OTCD MALDI MSI of derivatized cardiac glycosides in *D. plexippus*. After GirT-reagent application (10 mg/ml in MeOH/water 7:3 v/v, 50 µl spray volume, 10 µl/min flowrate), the sample was transferred in a desiccator for 2 hours. (**a**) Optical image of transversal *D. plexippus* section before OTCD and matrix application. (**b**) Corresponding RGB overlay image obtained with 25 µm step size showing the spatial distribution of calotropin/calactin in red ($[M+GirT]^+$ at *m/z* 646.3699), pheophytin a ($[M+K]^+$ at *m/z* 909.5291) in green and PS(18:1/18:2) ($[M+K]^+$ at *m/z* 810.5046) in blue. The extensive cardiac glycoside distribution at the integument indicates washing-out effects and analyte delocalization. Scale bar, 1 mm.

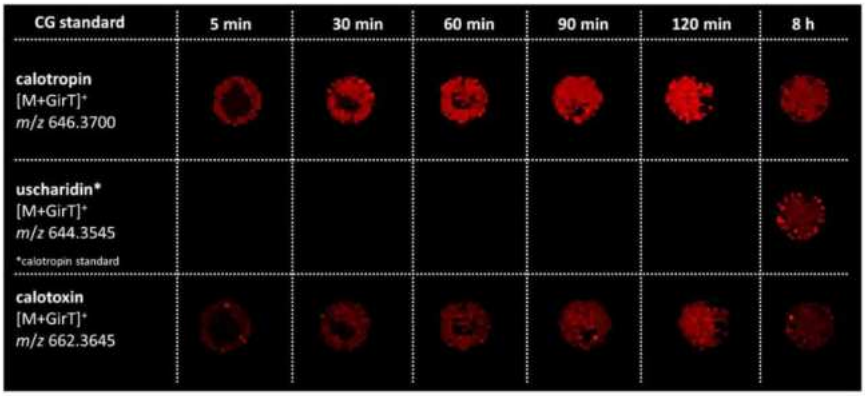


**Figure S6**. Dried-droplet MALDI MSI experiments of two derivatized cardiac glycoside standards (calotropin and calotoxin). A volume of 1 µL cardiac glycoside standard was spotted into reaction holes of a PTFE-coated glass slide. Subsequently, 1 µL of GirT-reagent (15 mg/mL) was added. After specific time intervals, the reaction was quenched by adding 1 µL of DHB-matrix solution (30 mg/mL). The highest reaction yield was obtained after 120 minutes of incubation. After 8 hours, uscharidin was detected for the calotropin standard measurement indicating oxidation of the respective species. Note that all reaction holes were measured simultaneously after the longest incubation time interval (8 hours). Thus, our data suggests that the chemical reaction is successfully quenched by adding the DHB matrix solution, which subsequently provides chemical preservation and inhibits the oxidation of derivatized cardiac glycosides (see time incubation intervals of ≤ 2 hours).

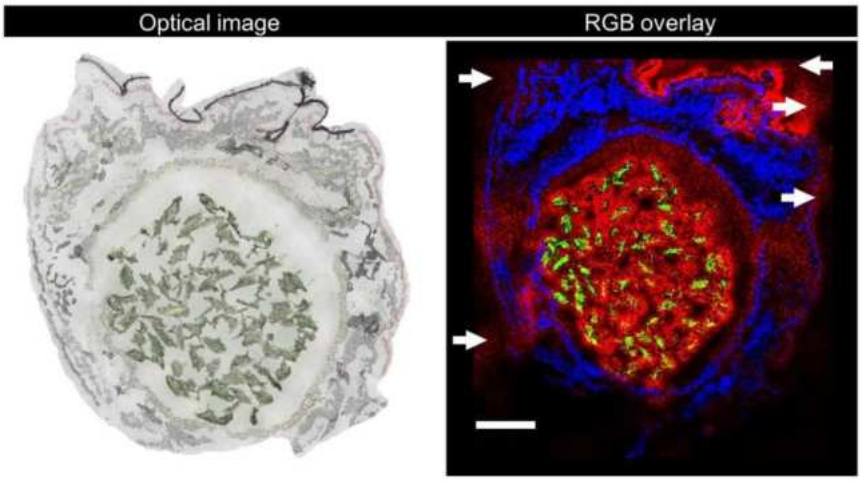


**Figure S7**. OTCD MALDI MSI of derivatized cardiac glycosides in *D. plexippus*. After GirT-reagent application (10 mg/ml in MeOH/water 7:3 v/v, 50 µL spray volume, 10 µL/min flowrate), the sample was incubated in a cell culture incubator (38°C, 100% relative humidity) for 2 hours. (**a**) Optical image of transversal *D. plexippus* section before OTCD and matrix application. (**b**) Corresponding RGB overlay image obtained with 25 µm step size showing the spatial distribution of calotropin/calactin in red ($[M+GirT]^+$ at *m/z* 646.3699), pheophytin a ($[M+K]^+$ at *m/z* 909.5291) in green and PS(18:1/18:2) ($[M+K]^+$ at *m/z* 810.5046) in blue. The extensive and leaked-out cardiac glycoside distribution at the integument indicate washing-out effects and analyte delocalization. Scale bar, 1 mm.

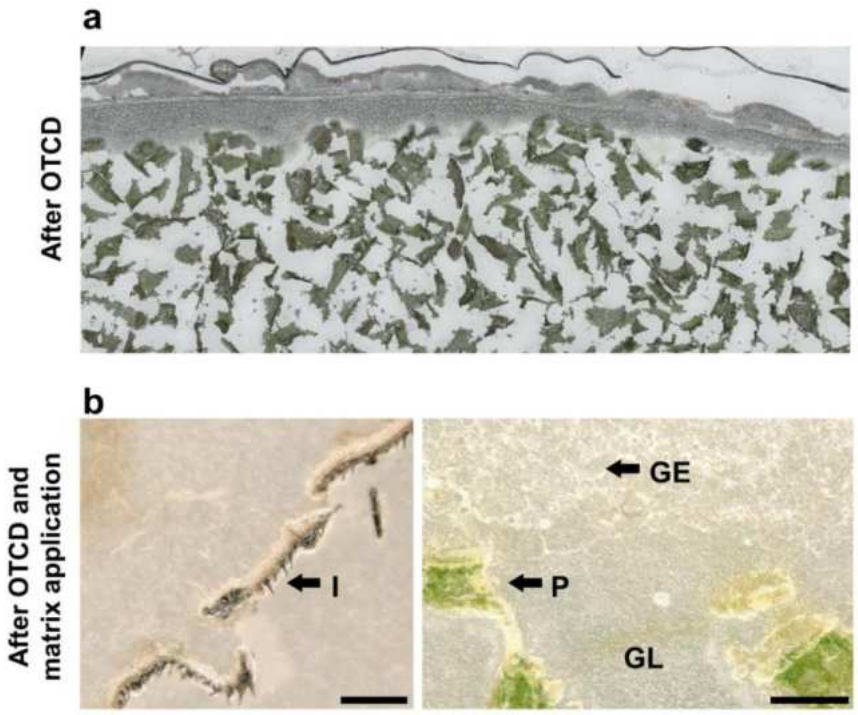


**Figure S8**. Optical images of longitudinal *D. plexippus* section (**a**) after OTCD and (b) after OTCD and matrix application. The optimized sample preparation protocol for OTCD (15 mg/ml GirT in MeOH/water 7:3 v/v, 35 µL spray volume, 7 µL/min flowrate) and matrix application (30 mg/ml DHB in MeOH/water 1:1 v/v, 100 µL spray volume, 5 µL/min flowrate) provides a homogenous matrix layer with crystal sizes of ≤ 10 µm, which is demonstrated for different surface characteristics including integument (I) plant material (P), gut lumen (GL) and gut epithelium (GE). Scale bars, 100 µm.

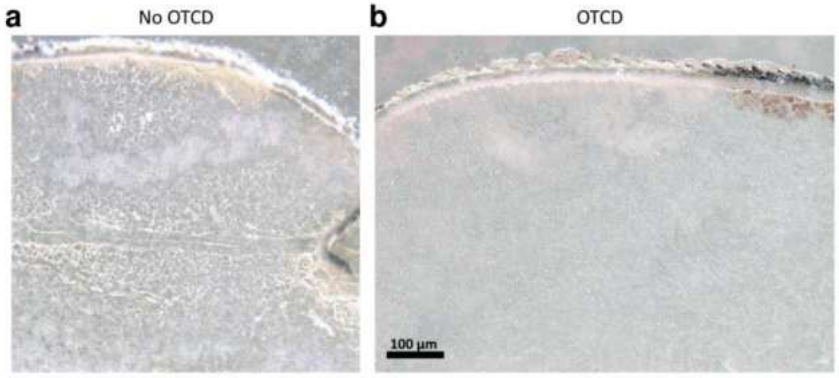


**Figure S9**. Optical images of longitudinal *D. plexippus* section for matrix layer comparison of (**a**) control experiment (conventional MALDI MSI without OTCD) and (**b**) OTCD MALDI MSI.

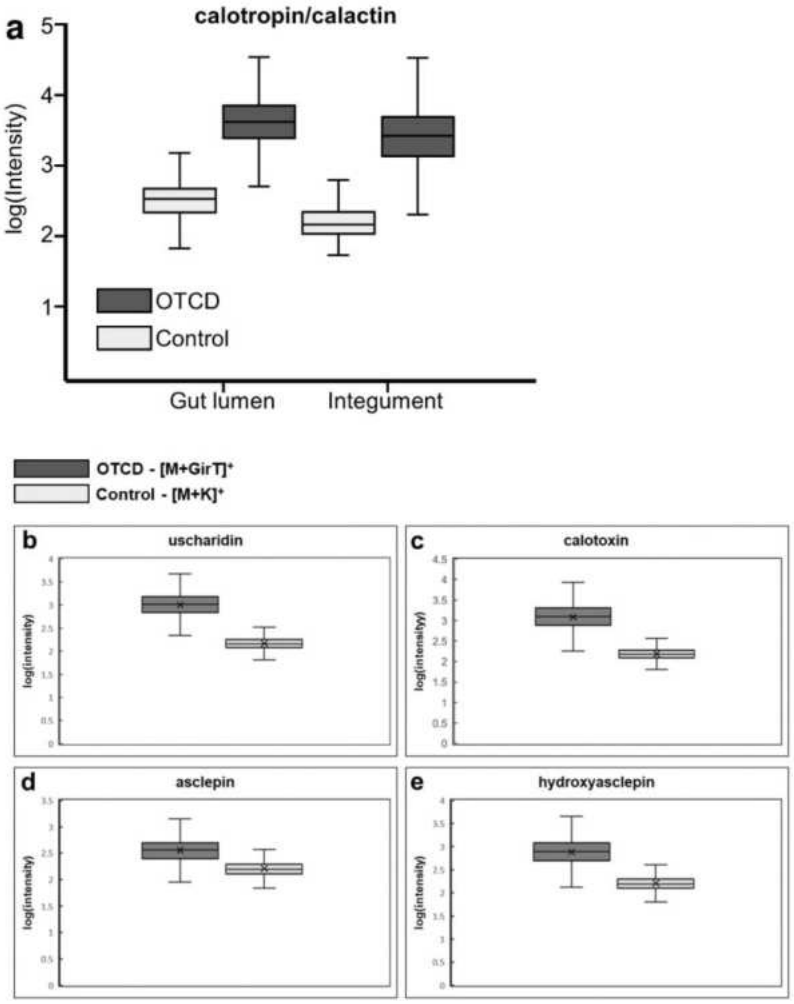


**Figure S10**. Box plots showing *in silico* extracted ion intensities of cardiac glycosides for OTCD and control MALDI MSI. Utilizing OTCD, cardiac glycoside ion intensities were increased by (**a**) 16-fold for calotropin/calactin (**b**) 13.9-fold for uscharidin, (**c**) 14.3-fold for calotoxin, (**d**) 11.5-fold for asclepin and (**e**) 13.1-fold for hydroxyasclepin.

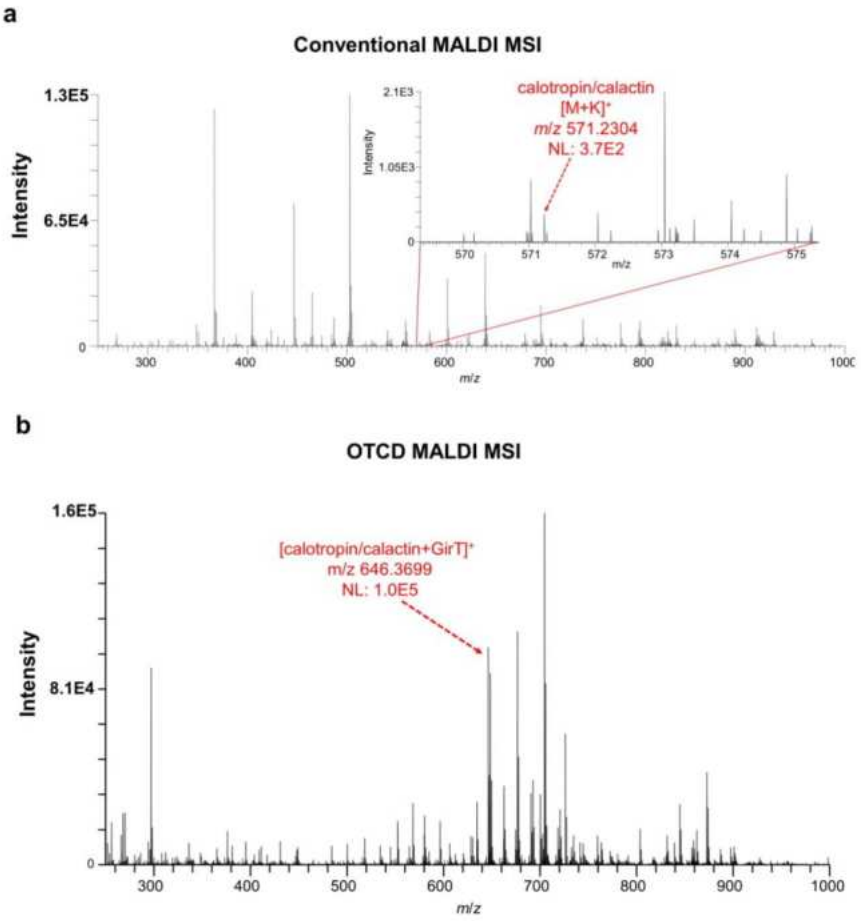


**Figure S11**. Representative MALDI MSI spectrum for (**a**) conventional MALDI (control) and (**b**) OTCD MALDI MSI (MSI data shown in Figure 2b) acquired from a single pixel at *D. plexippus* integument. For the control experiment, the ion signal of $[M+K]^+$ is the predominant adduct signal of calotropin/calactin with an ion intensity of 3.7E2. For OTCD MALDI MSI, the derivatized calotropin/calactin signal is one of the most abundant signals with an ion intensity of 1.0E5.

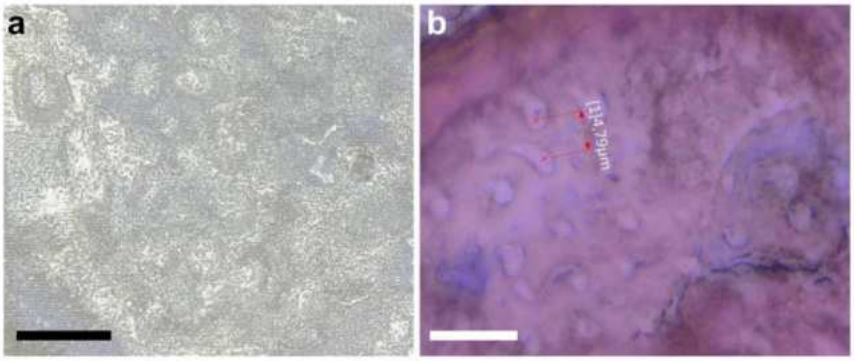


**Figure S12**. Optical images of Malpighian tubules after OTCD MALDI MSI performed with 5 µm step size using the AP-SMALDI$^5$ AF ion source. (**a**) Matrix-coated sample surface after measurement showing laser ablation craters of ≤ 5 µm. Thus, MSI analysis was performed without oversampling. (**b**) Magnification of a single H&E-stained malpighian tubule after measurement demonstrating 5 µm step size and laser ablation craters of ≤ 5 µm onto the penetrated tissue. Scale bars, (a) 100 µm (b) 10 µm.

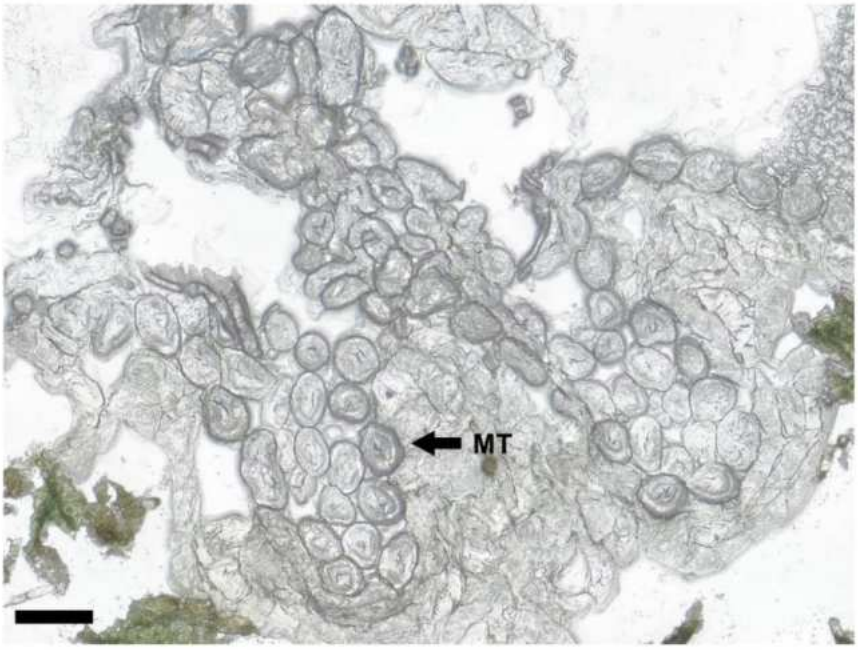


**Figure S13**. Optical image of longitudinal *D. plexippus* section (before OTCD and matrix application) highlighting transversal-sectioned Malpighian tubules (MT). Scale bar, 100 µm.

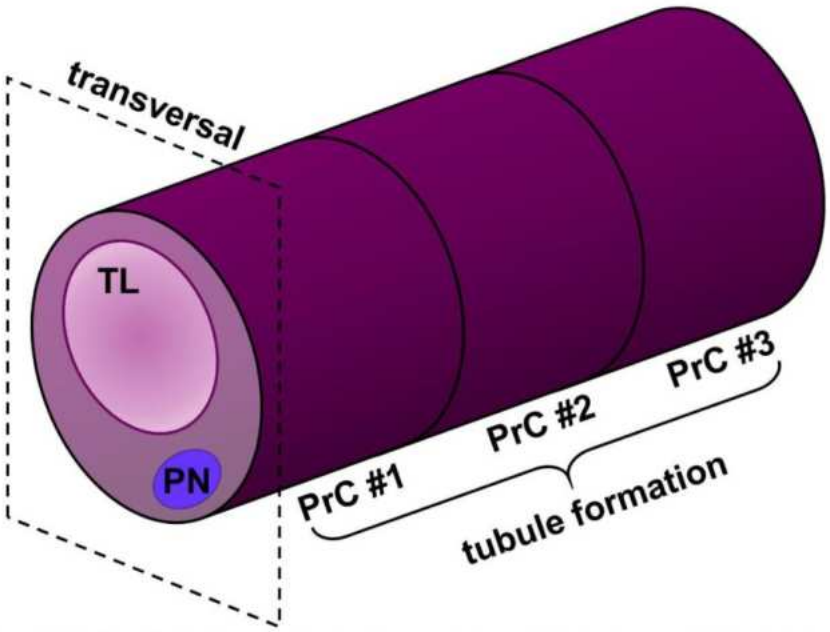


**Figure S14**. Simplified schematic showing the morphology of *D. plexippus* malpighian tubules. The principal cells fold upon itself to form a tubule lumen. PrC: principal cell; PN: principal cell nucleus; TL: tubule lumen.

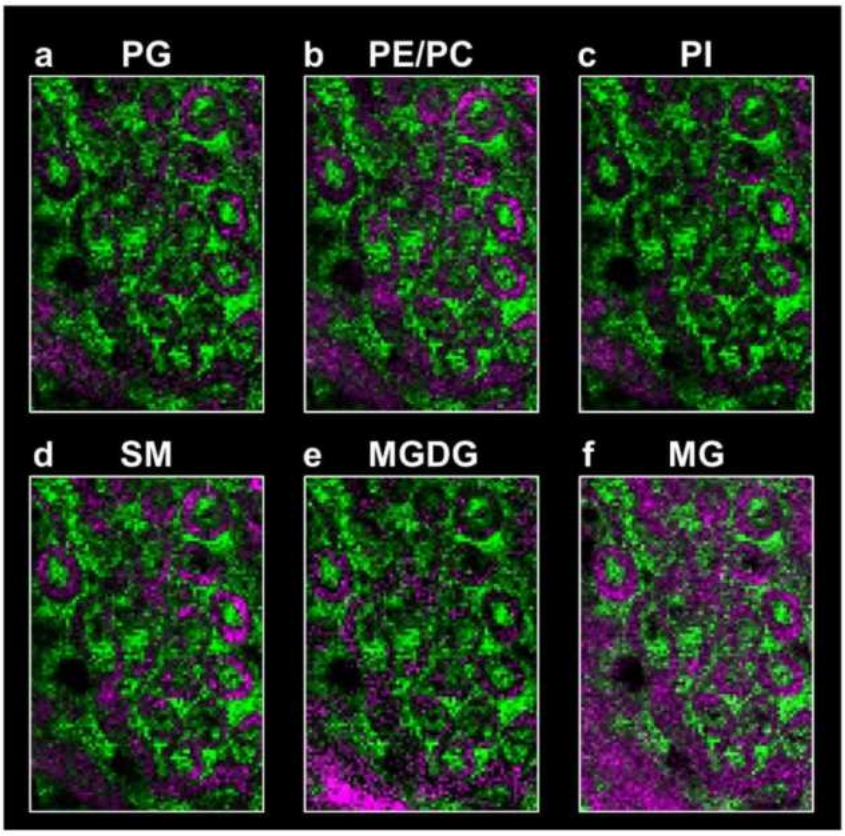


**Figure S15**. OTCD MALDI MSI of *D. plexippus* malpighian tubules. Dual ion channel images obtained with 5 µm step size showing the spatial distribution for different lipid classes in pink. (**a**) $[PG(22:3/14:0)+Na]^+$ at *m/z* 795.5146, (**b**) $[PE(P\text{-}18:2/24:6)+Na]^+$ at *m/z* 822.5408 (**c**) $[PI(16:0/26:0)+H]^+$ at *m/z* 951.6896 (**d**) $[SM(16:0/34:6)+Na]^+$ at *m/z* 955.7238 (**e**) $[MGDG(16:2/20:3)+H]^+$ at *m/z* 777.5511 (**f**) $[MG(19:0)+Na]^+$ at *m/z* 395.3132. The nucleotide derivative thymidine 3',5'-hydrogen phosphate ($[M+K]^+$, *m/z* 343.0092) is shown in green.

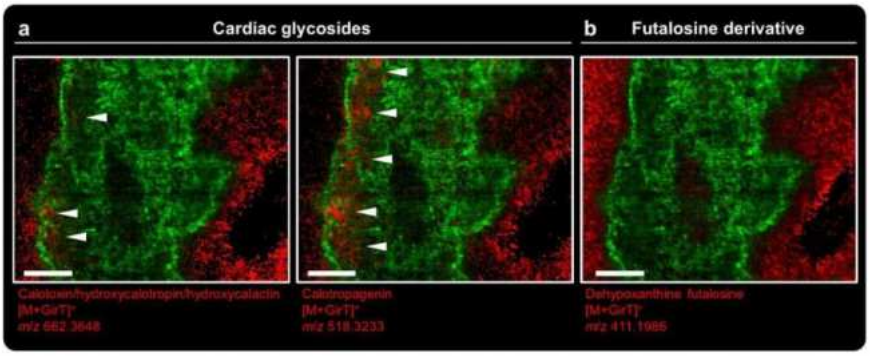


**Figure S16. OTCD MALDI MSI (2 µm step size) of derivatized cardiac glycosides and futalosine derivative uptake in *D. plexippus*.** Red-green overlay images showing the spatial distribution for (**a**) the derivatized isomers calotoxin/hydroxycalotropin/hydroxycalactin ([M+GirT]$^+$, *m/z* 662.3648) and calotropagenin ([M+GirT]$^+$, *m/z* 518.3233) in red, (**b**) dehypoxanthine futalosine ([M+GirT]+, m/z 411.1986) in red and (**a**,**b**) PE(46:3) ([M+H]$^+$, *m/z* 882.6922) in green. In contrast to both cardiac glycosides, the derivatized futalosine species is not accumulated in the outer layer of the fat body tissue of the caterpillar. Scale bar, 80 µm.

**Supplementary Data 1: Structure and LC-MS$^2$ spectra for all detected cardiac glycosides. Red arrows indicate water loss and green arrows indicate carbon monoxide loss.**

**uzarigenin**

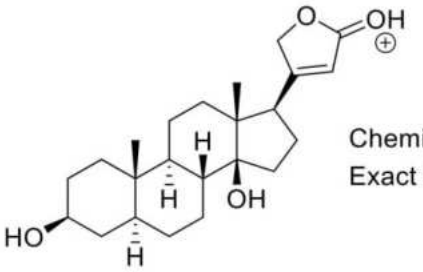


Chemical Formula: $C_{23}H_{35}O_4^+$
Exact Mass: 375.25

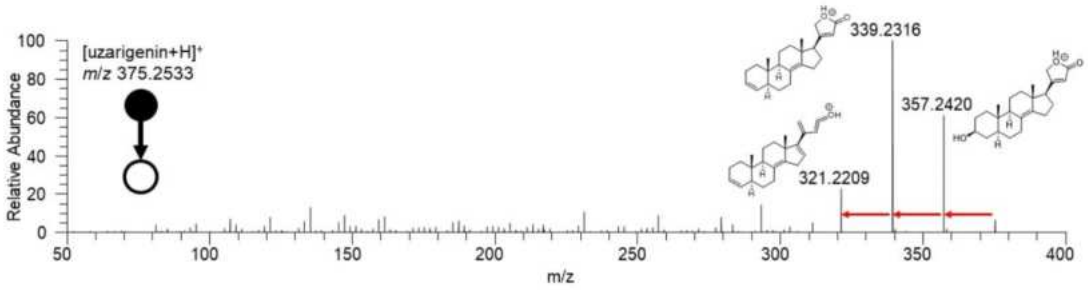


**calotropagenin**

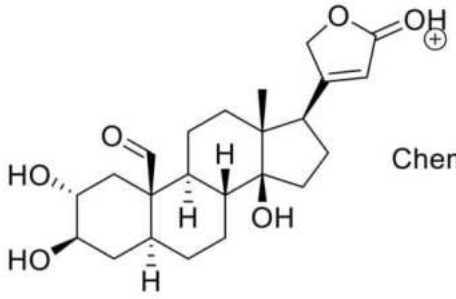


Chemical Formula: $C_{23}H_{33}O_6^+$
Exact Mass: 405.23

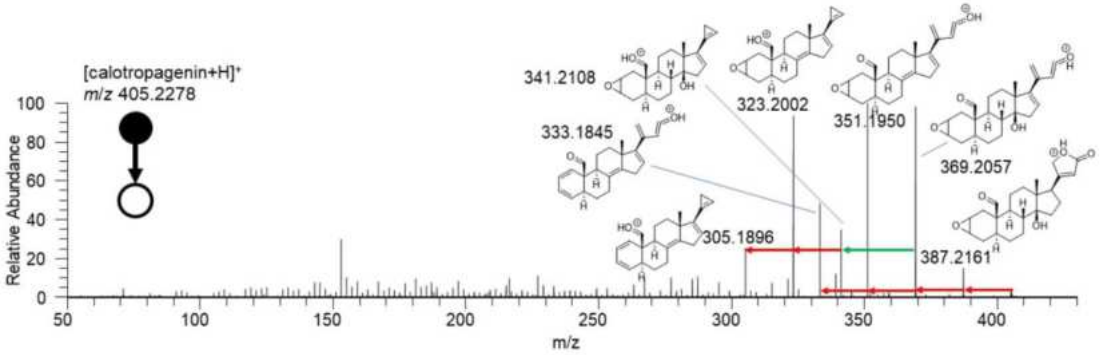

**strophanthidol**

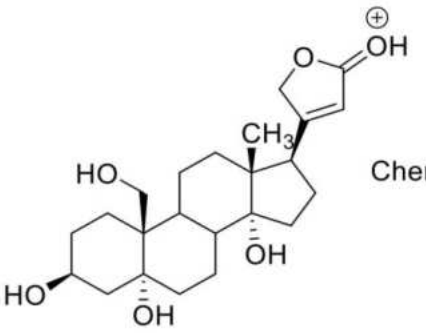


Chemical Formula: $C_{23}H_{35}O_6^+$
Exact Mass: 407.24

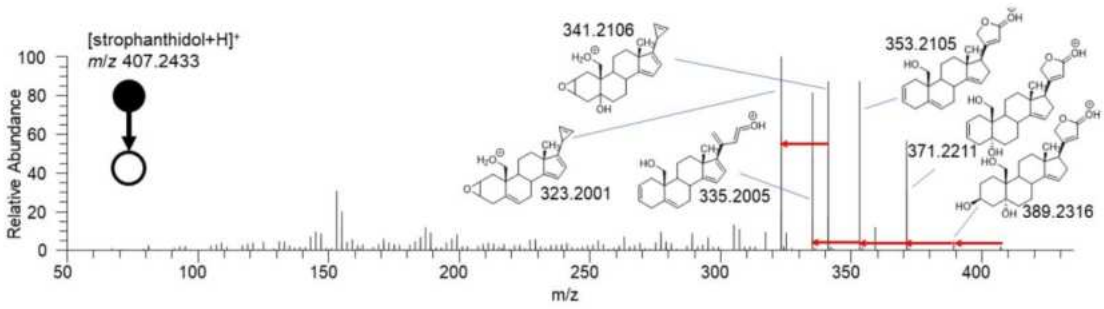


**digitoxigenin digitoxoside**

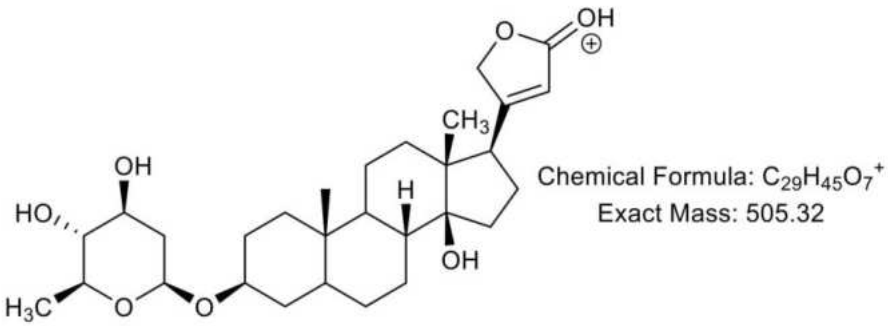


Chemical Formula: $C_{29}H_{45}O_7^+$
Exact Mass: 505.32

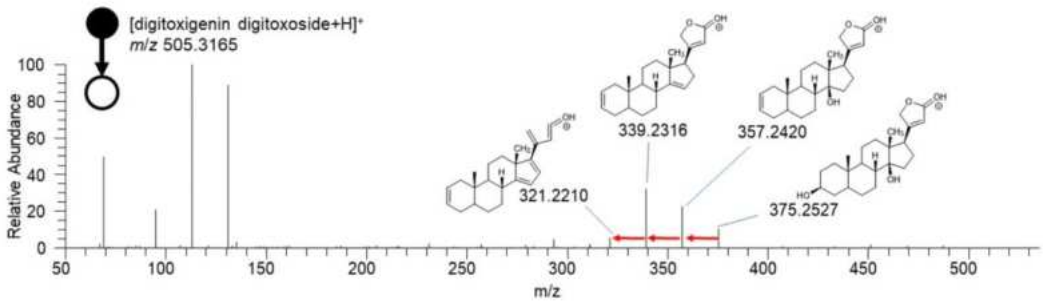

**strobosid**

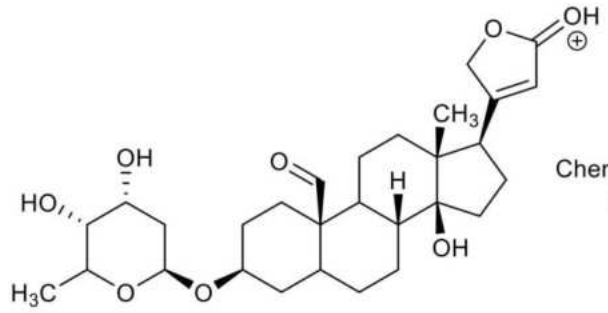


Chemical Formula: $C_{29}H_{43}O_8^+$
Exact Mass: 519.30

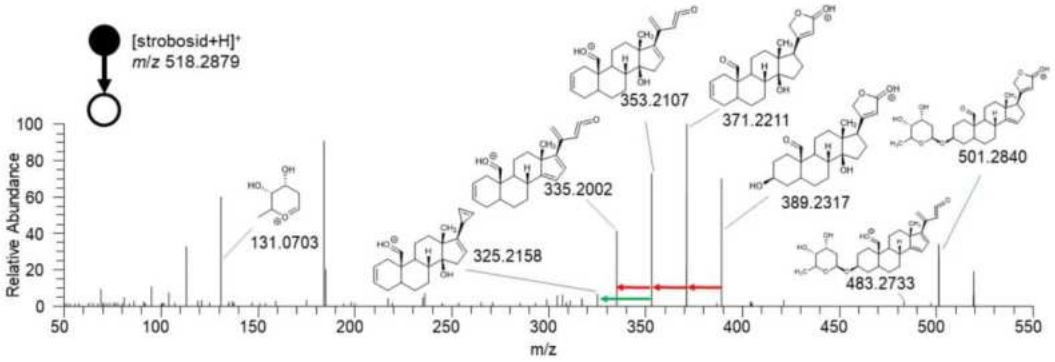


**uscharidin**

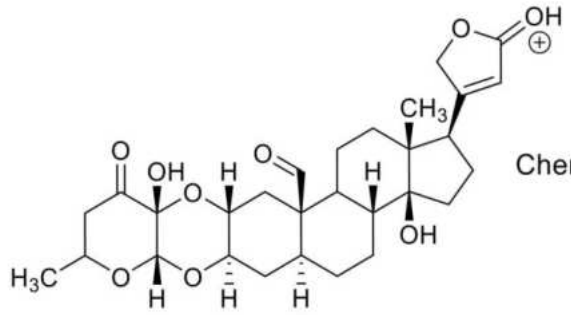


Chemical Formula: $C_{29}H_{39}O_9^+$
Exact Mass: 531.26

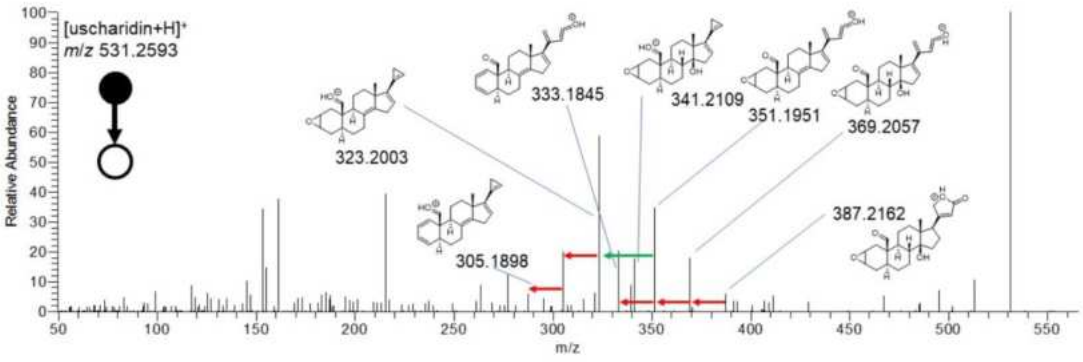

**calotropin**

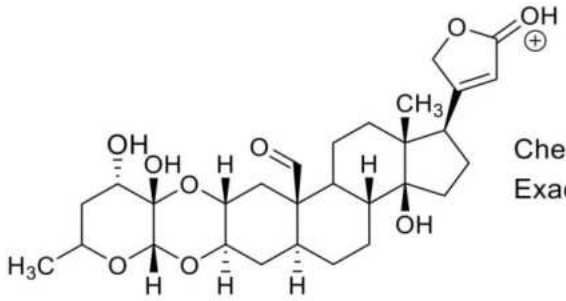

Chemical Formula: $C_{29}H_{41}O_9^+$
Exact Mass: 533.27

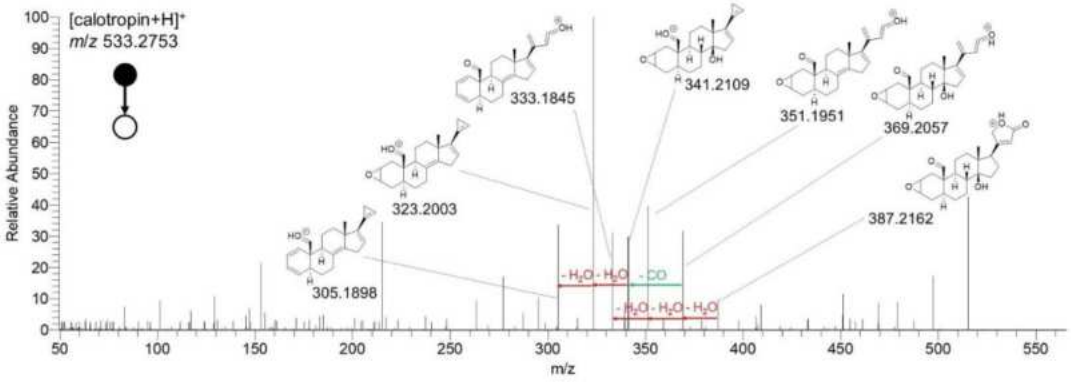


**calactin**

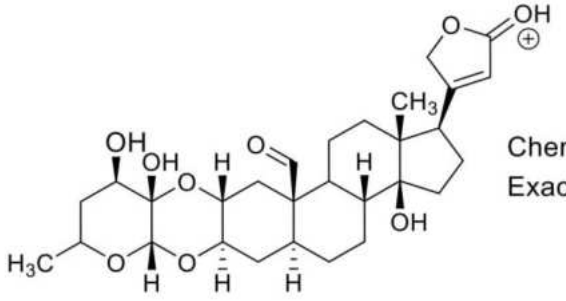

Chemical Formula: $C_{29}H_{41}O_9^+$
Exact Mass: 533.27

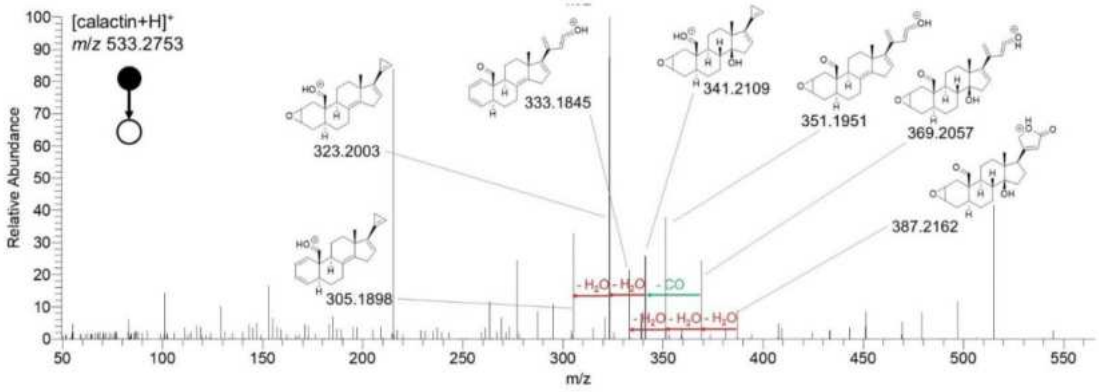

**gofruside**

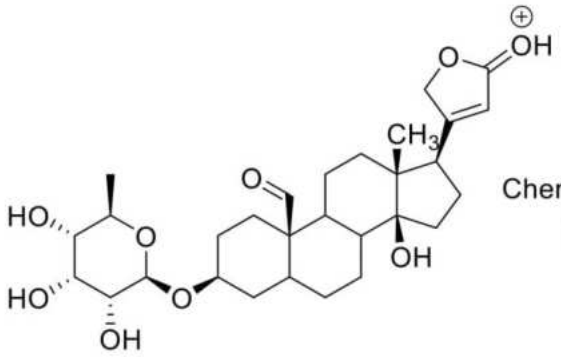

Chemical Formula: $C_{29}H_{43}O_9^+$
Exact Mass: 535.29

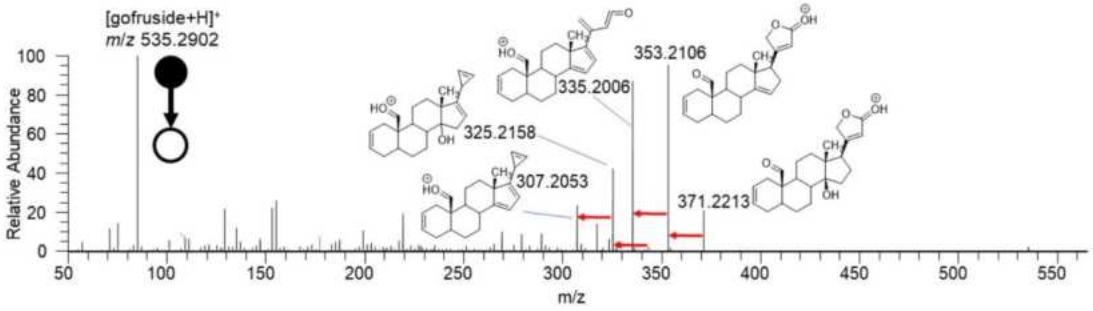


**frugoside**

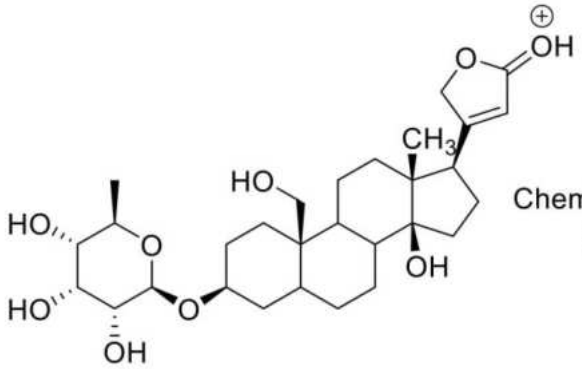

Chemical Formula: $C_{29}H_{45}O_9^+$
Exact Mass: 537.31

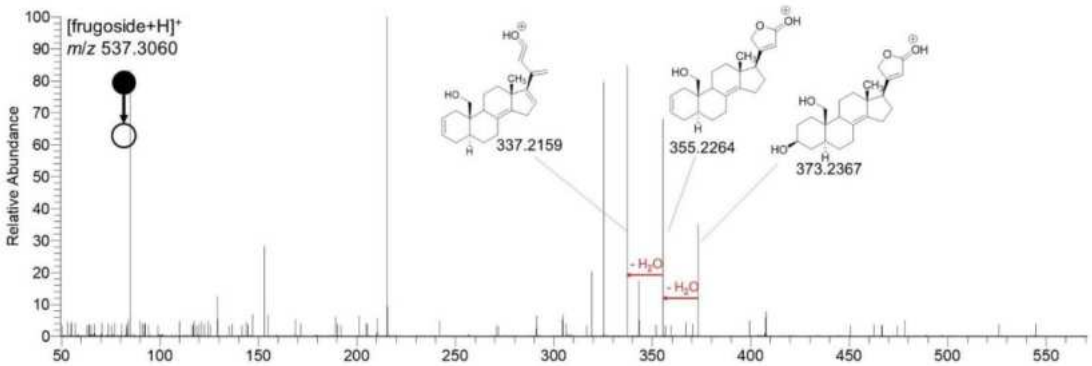

**hydroxyuscharidin**

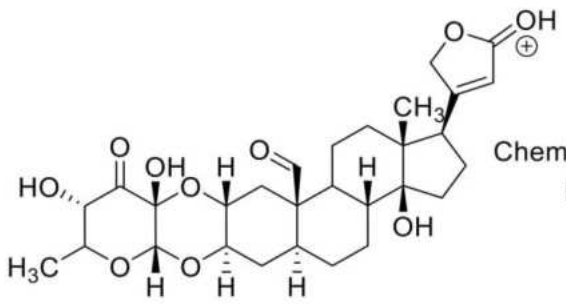


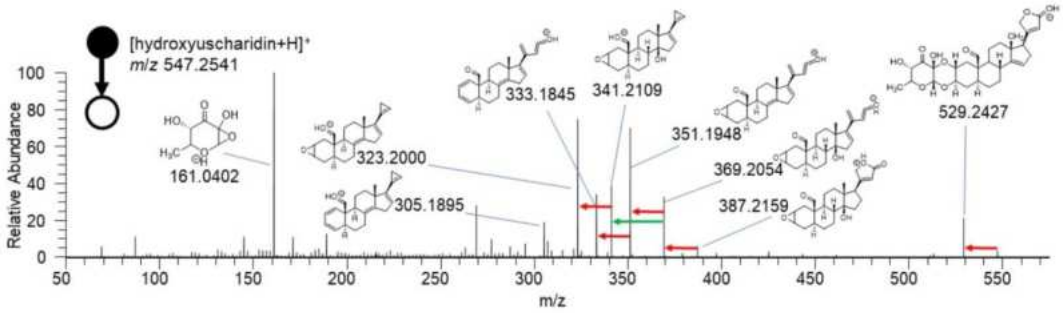


**calotoxin**

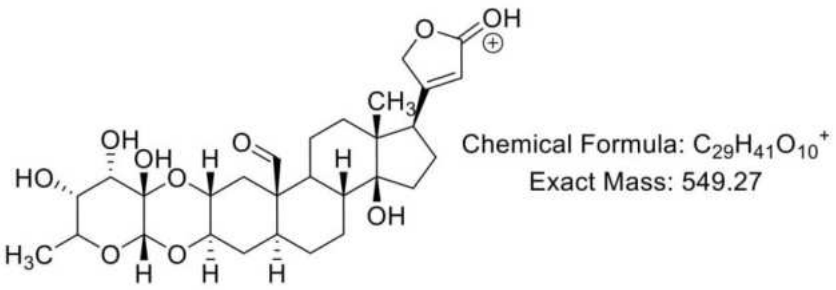


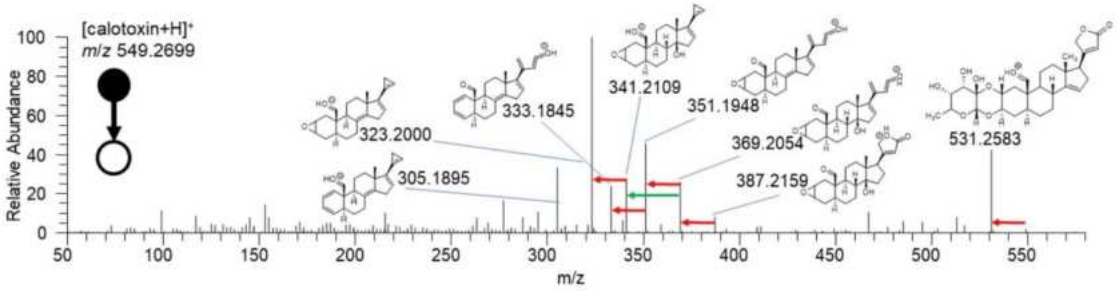

**hydroxycalotropin**

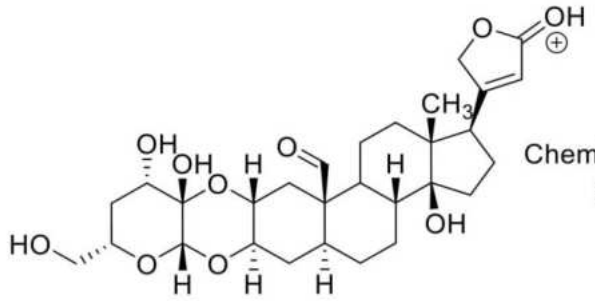


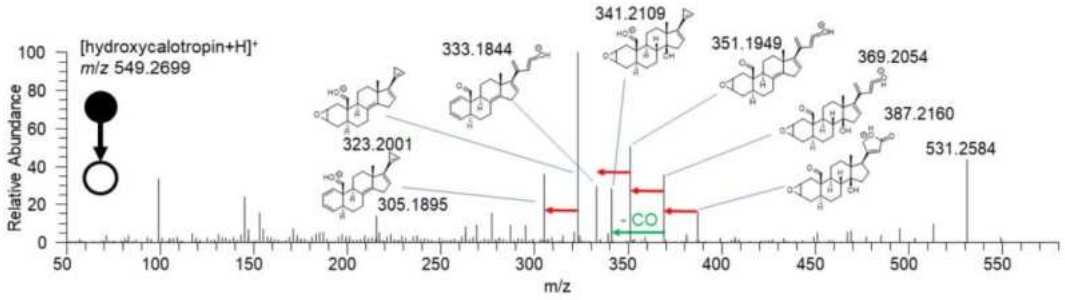


**hydroxycalactin**

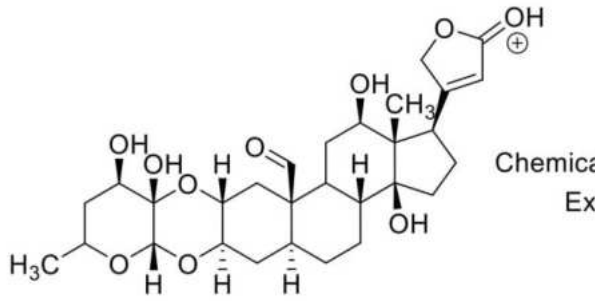


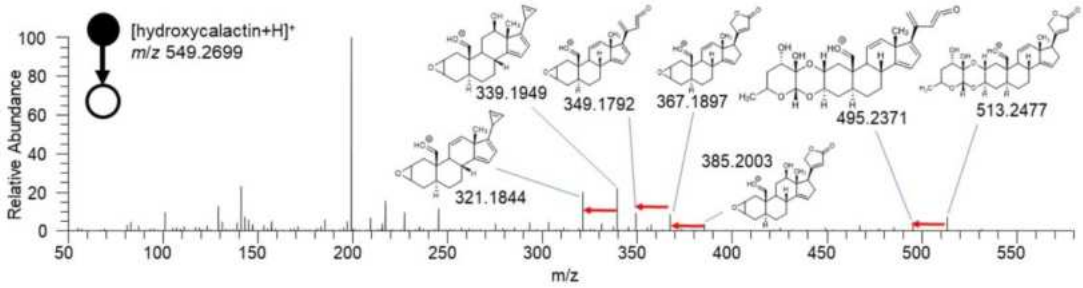

**calactinic acid**

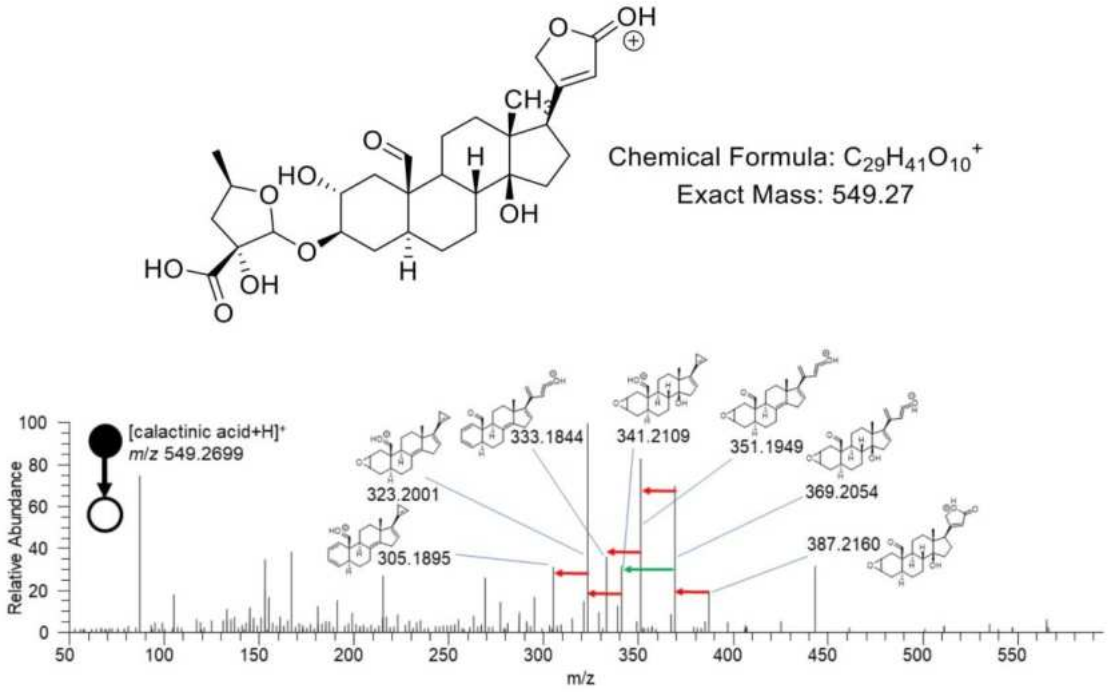


**corglycon**

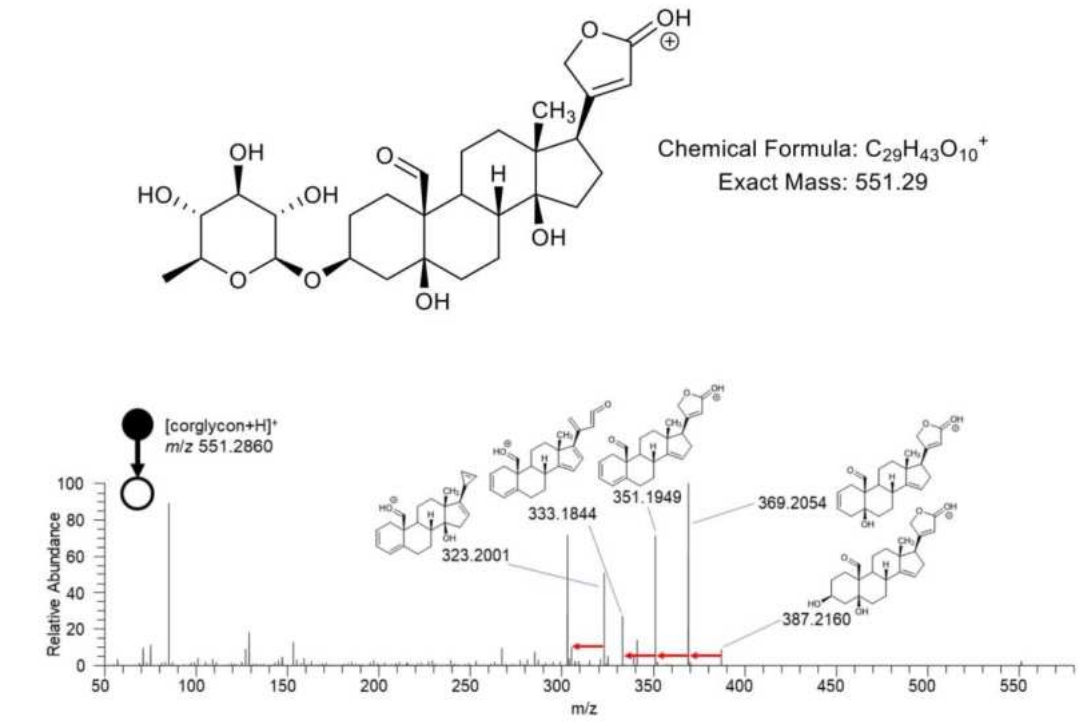

**periplogenin-glycoside**

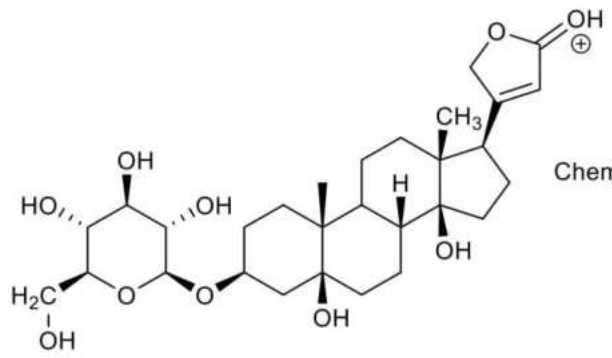


Chemical Formula: $C_{29}H_{45}O_{10}^{+}$
Exact Mass: 553.30

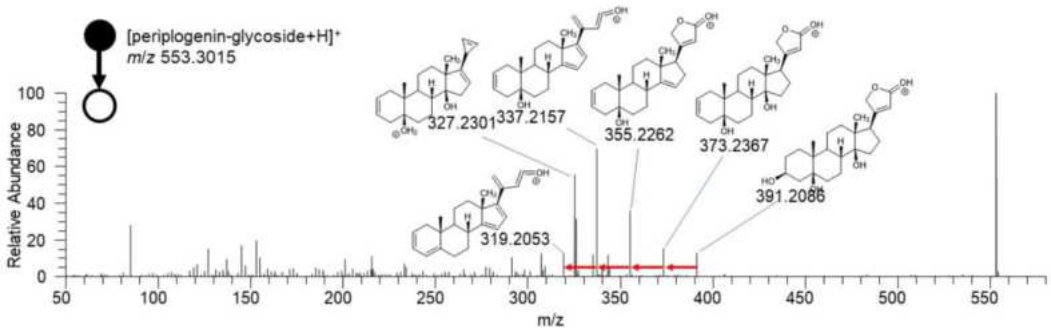


**gomphoside-acetate**

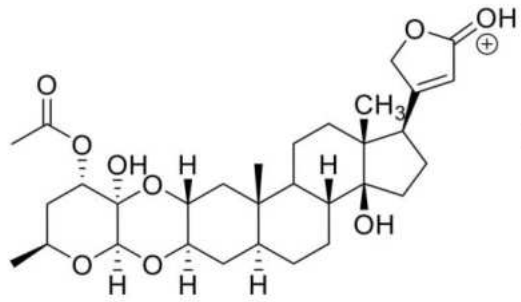


Chemical Formula: $C_{31}H_{45}O_{9}^{+}$
Exact Mass: 561.31

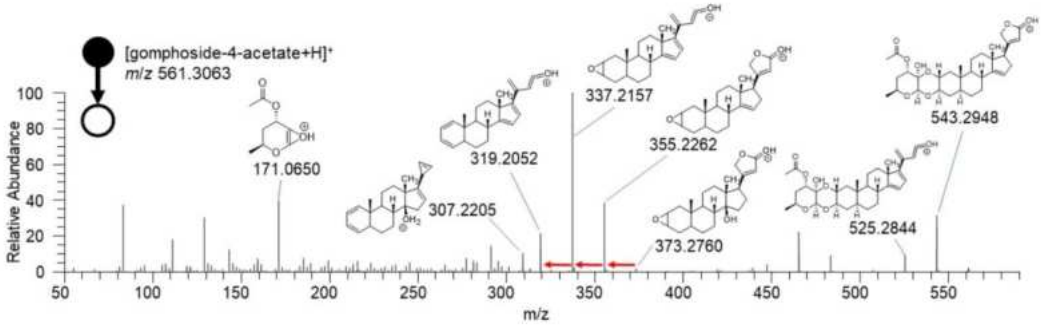

**asclepin**

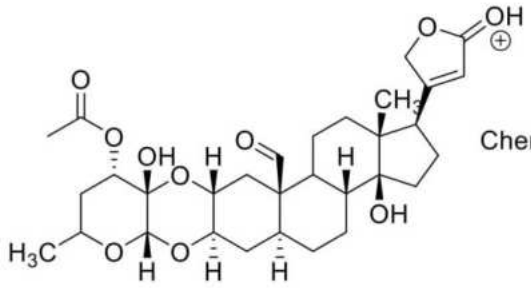

Chemical Formula: $C_{31}H_{43}O_{10}^{+}$
Exact Mass: 575.29

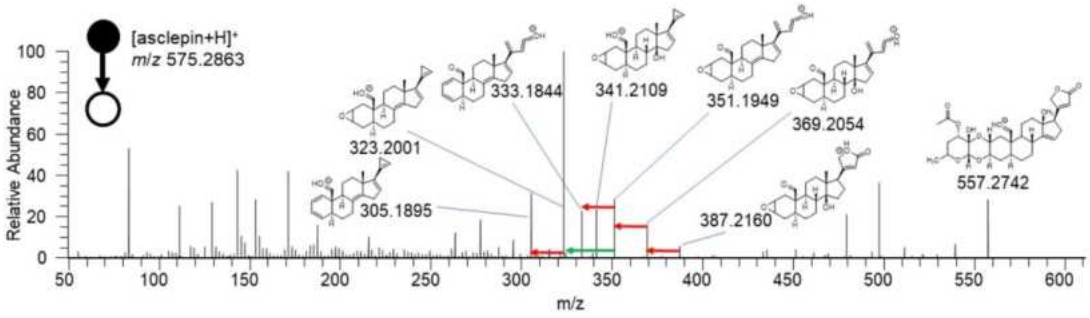


**hydroxycalactinic acid methylester**

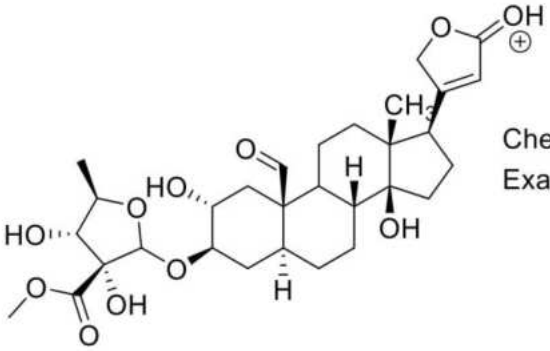

Chemical Formula: $C_{30}H_{43}O_{11}^{+}$
Exact Mass: 579.28

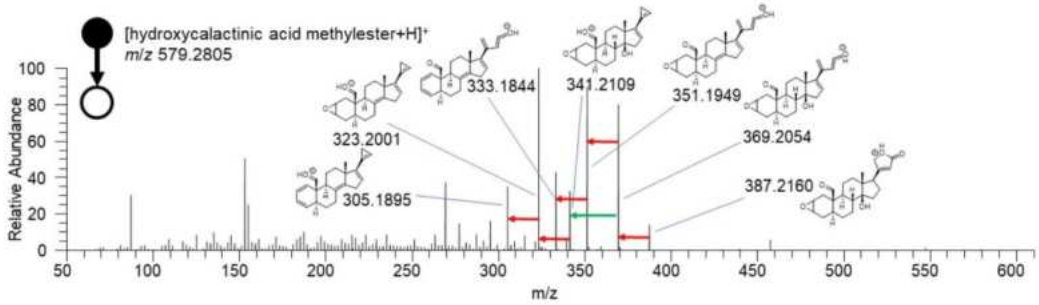

**uscharin**

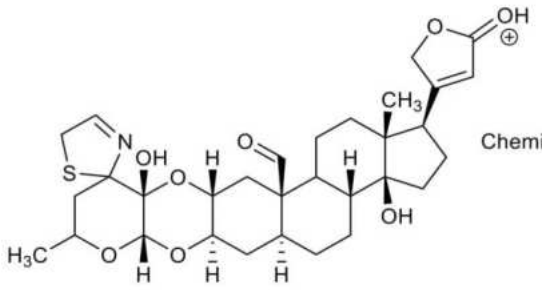


Chemical Formula: $C_{31}H_{42}NO_8S^+$
Exact Mass: 588.26

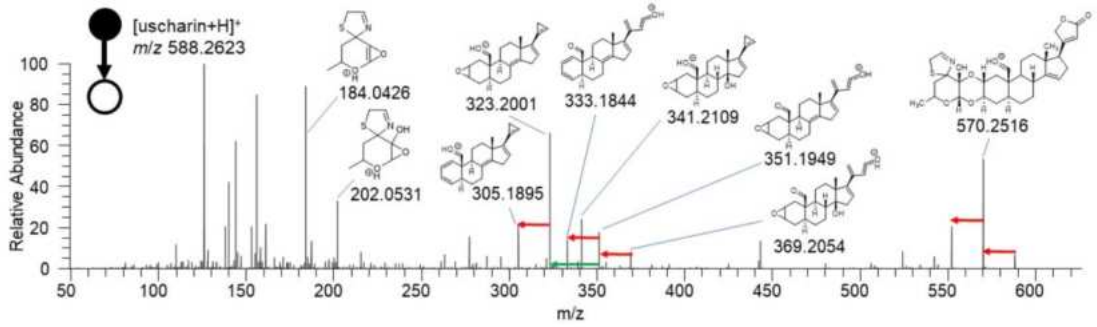


**voruscharin**

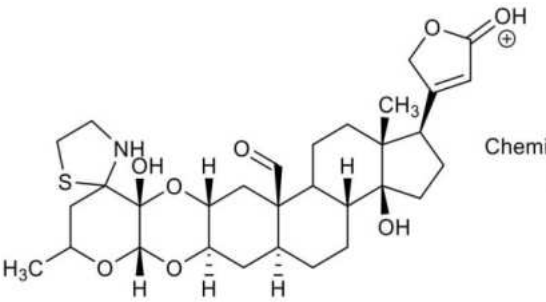


Chemical Formula: $C_{31}H_{44}NO_8S^+$
Exact Mass: 590.28

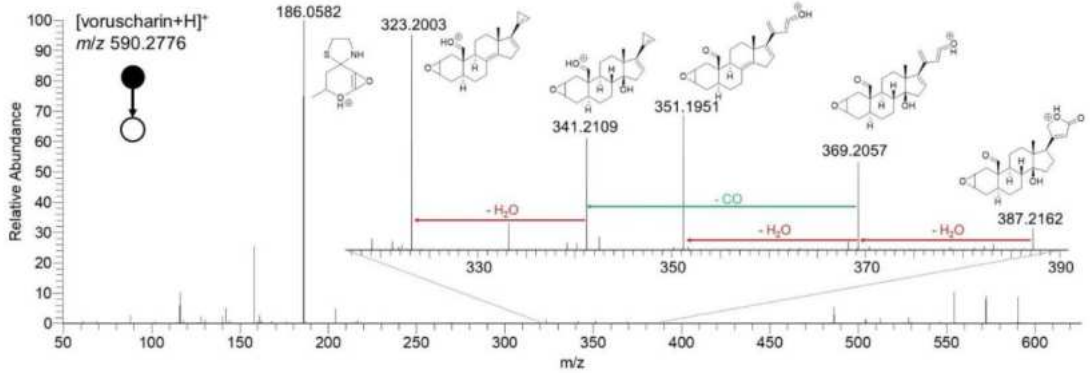

**acetoxycalotropin**

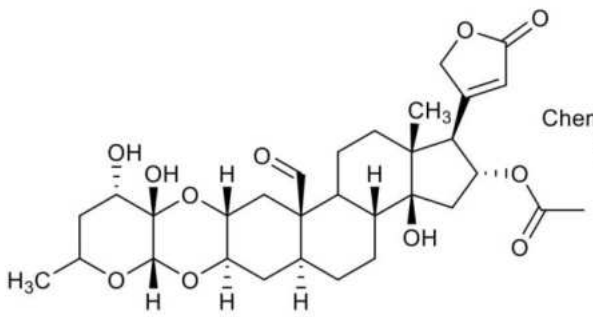

Chemical Formula: $C_{31}H_{42}O_{11}$
Exact Mass: 590.27

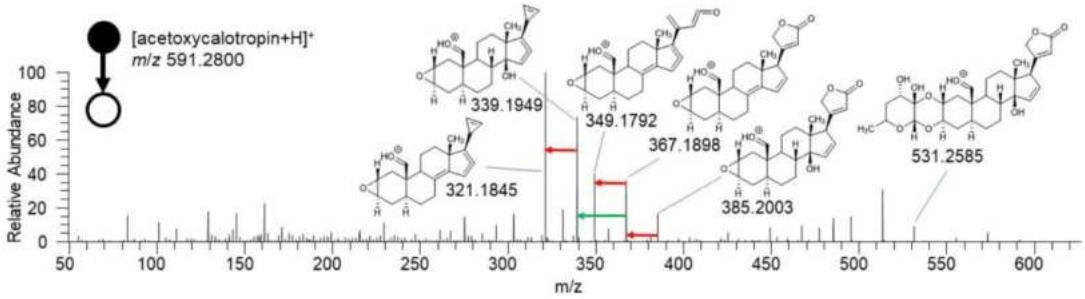


**hydroxyasclepin**

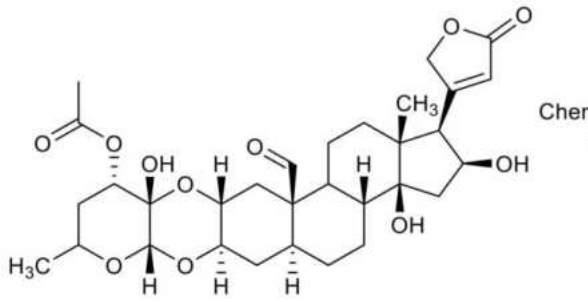

Chemical Formula: $C_{31}H_{42}O_{11}$
Exact Mass: 590.27

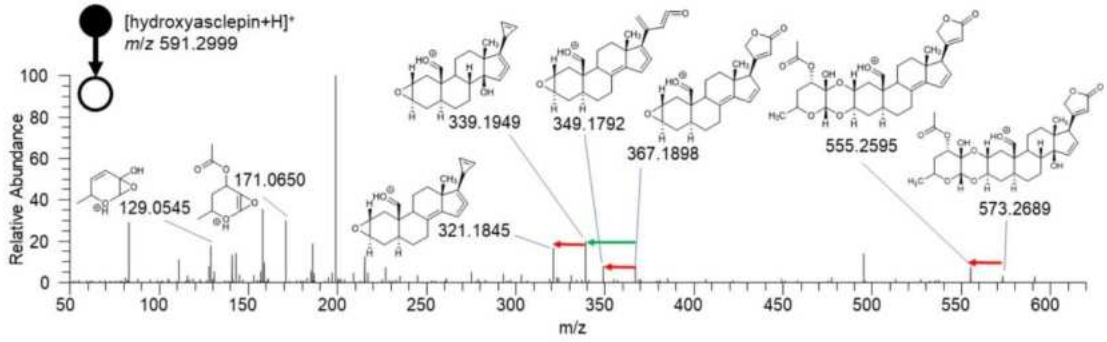

**hydroxyuscharin**

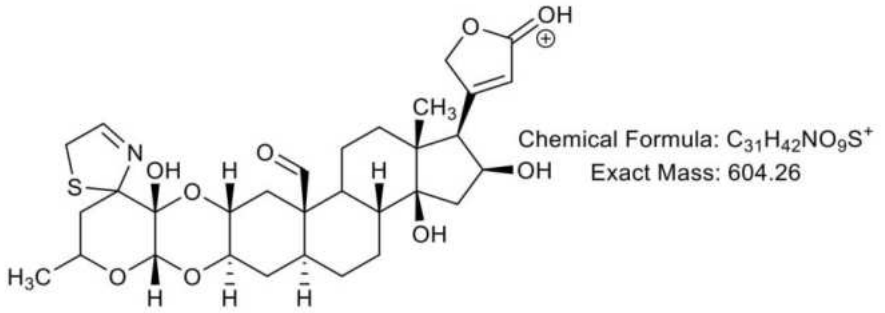


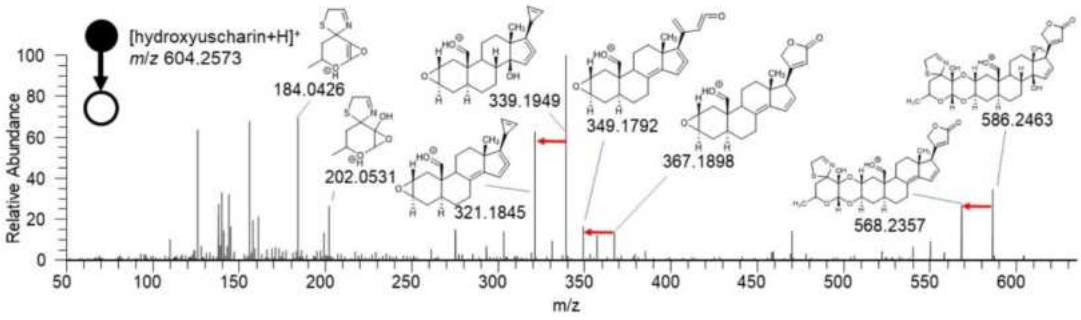


**hydroxyvoruscharin**

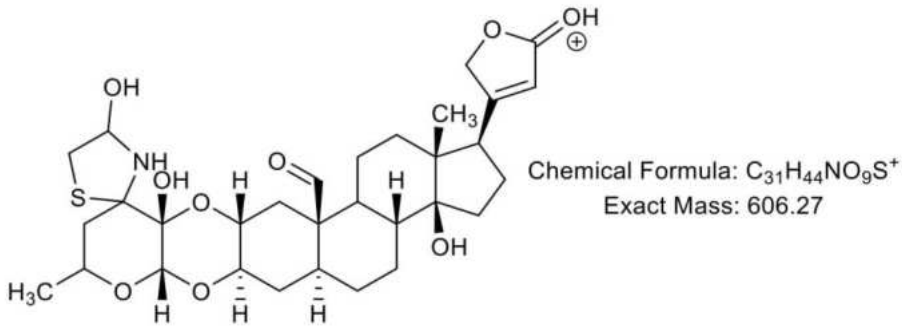


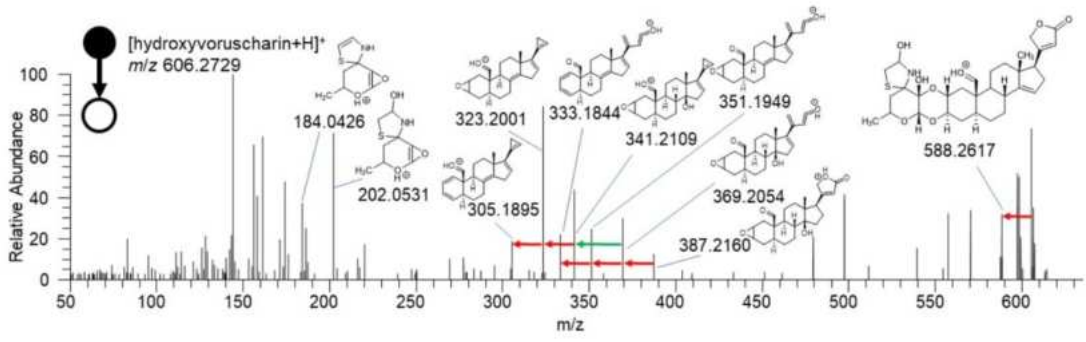

**diacetylgofruside**

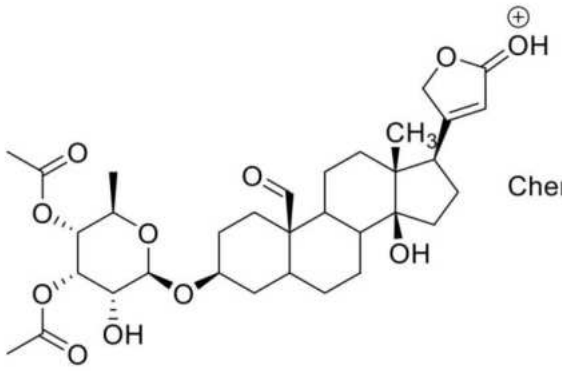

Chemical Formula: $C_{33}H_{47}O_{11}^{+}$
Exact Mass: 619.31

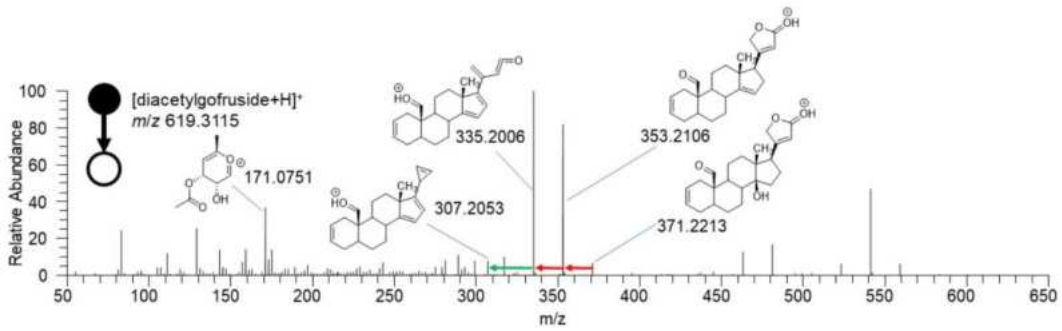


**acetoxyasclepin**

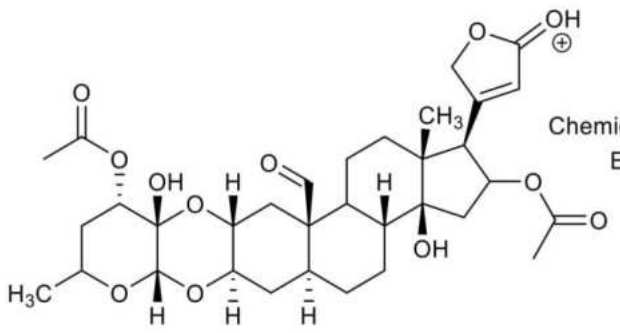

Chemical Formula: $C_{33}H_{45}O_{12}^{+}$
Exact Mass: 633.29

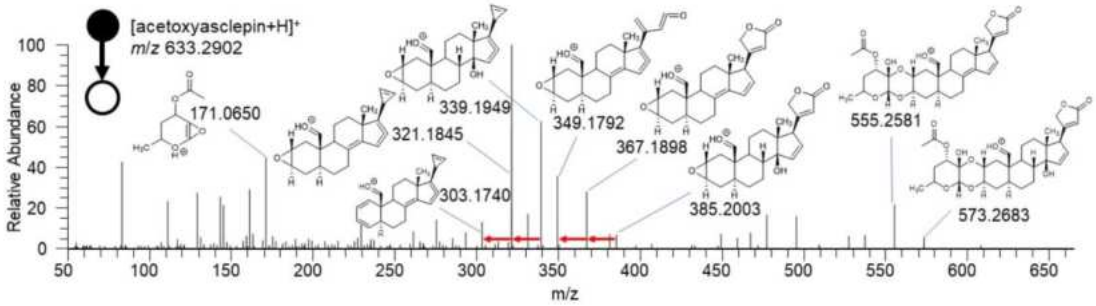

**digitoxin bisdigitoxoside**

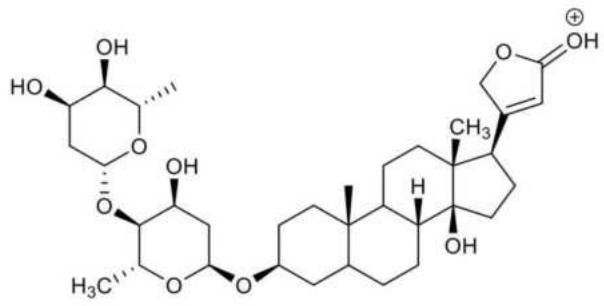

Chemical Formula: $C_{35}H_{55}O_{10}^{+}$
Exact Mass: 635.38

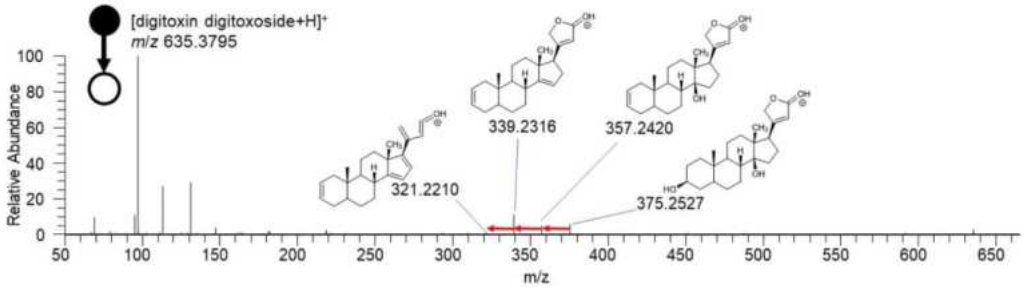


**cannogenin-diglycoside**

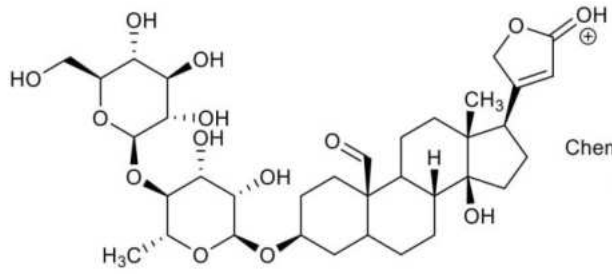

Chemical Formula: $C_{35}H_{53}O_{14}^{+}$
Exact Mass: 697.34

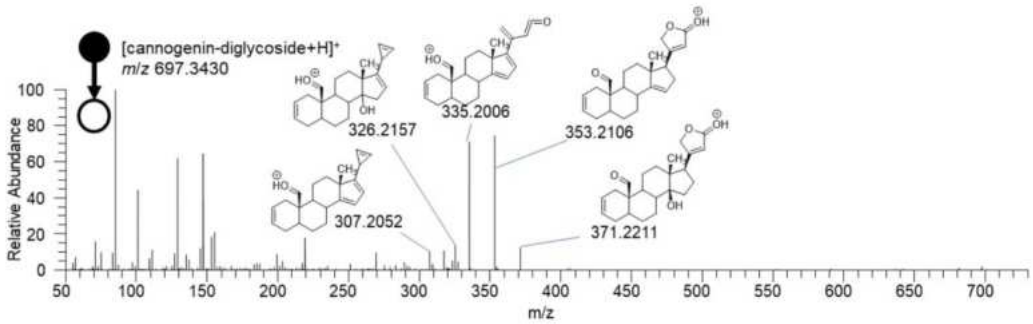

**antiaroside B**

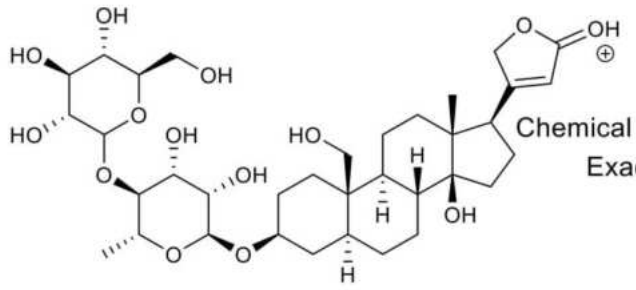

Chemical Formula: $C_{35}H_{55}O_{14}^{+}$
Exact Mass: 699.36

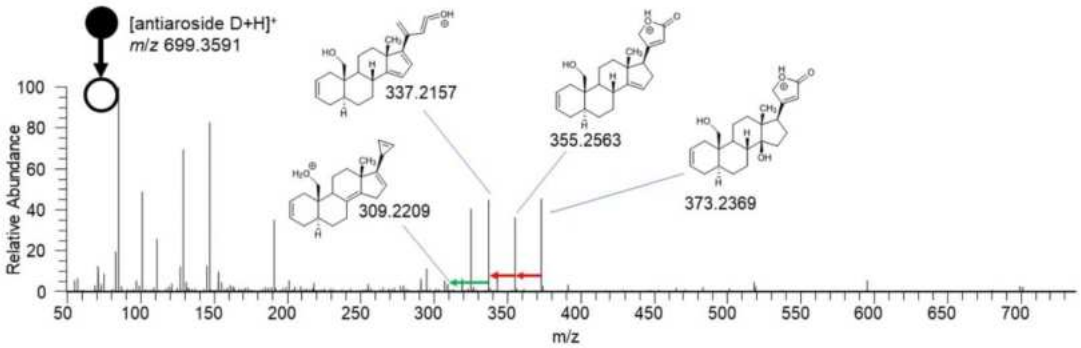


**calotoxin-glycoside**

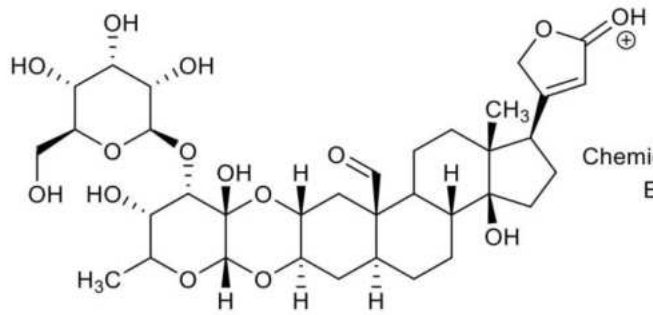

Chemical Formula: $C_{35}H_{51}O_{15}^{+}$
Exact Mass: 711.32

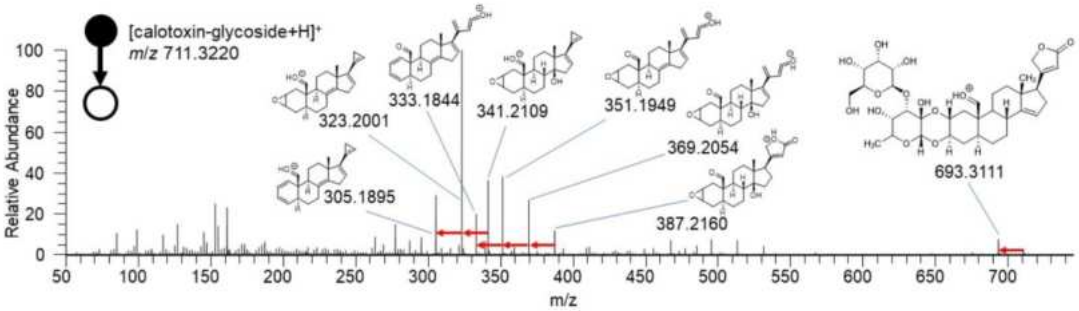

# ACKNOWLEDGEMENTS

First and foremost, I will express my sincere gratitude to my supervisors Prof. Dr. Bernhard Spengler and Prof. Dr. Georg Petschenka. Without their guidance and dedicated involvement in every step throughout the last four years, this thesis would have never been accomplished. I would like to thank you very much for your support and the given opportunity to be a part of your research groups.

A special thanks to Dr. Dhaka R. Bhandari and Prof. Dr. Sven Heiles for valuable discussions, reviewing my progress constantly and supporting me since my time as an undergraduate.

Many thanks to all staff members at the Institute of Inorganic and Analytical Chemistry, and the Institute of Insect Biotechnology by representing such a friendly and fruitful working environment. I always appreciated the strong collaboration and for making the past four years a much more enjoyable experience. I want to thank Dr. Stefanie Gerbig, Dr. Karl-Christian Schäfer, and David Luh for their valuable support in the laboratory.

Finally, but most importantly, I would like to thank my family and my girlfriend for their continuous support, encouragement and unconditional love.

# DECLARATION

I declare that I have completed this dissertation without the unauthorized help of a second party and only with the assistance acknowledged therein. I have appropriately acknowledged and referenced all text passages that are derived literally from or are based on the content of published or unpublished work of others, and all information that relates to verbal communications. I have abided by the principles of good scientific conduct laid down in the charter of the Justus Liebig University of Giessen in carrying out the investigations described in the dissertation.

_____

Place, date and signature

Versicherung:

„Ich erkläre: Ich habe die vorgelegte Dissertation selbständig und ohne unerlaubte fremde Hilfe und nur mit den Hilfen angefertigt, die ich in der Dissertation angegeben habe. Alle Textstellen, die wörtlich oder sinngemäß aus veröffentlichten Schriften entnommen sind, und alle Angaben, die auf mündlichen Auskünften beruhen, sind als solche kenntlich gemacht. Bei den von mir durchgeführten und in der Dissertation erwähnten Untersuchungen habe ich die Grundsätze guter wissenschaftlicher Praxis, wie sie in der „Satzung der Justus-Liebig-Universität Gießen zur Sicherung guter wissenschaftlicher Praxis“ niedergelegt sind, eingehalten.“

_____

Ort, Datum und Unterschrift

Der Lebenslauf wurde aus der elektronischen Version der Arbeit entfernt.

The curriculum vitae was removed from the electronic version of the paper.